

# Classical and Quantum Bosonic Fields on the Spacetimes of Black Holes and Stars

Jake N. Percival

Supervisor: Dr Sam Dolan



A thesis in partial fulfillment of the requirements for a Doctorate of Philosophy  
in the School of Mathematics and Statistics  
The University of Sheffield

January 2022



# Acknowledgments

First and foremost I would like to thank my supervisor Sam Dolan for all of his guidance, advice and, perhaps most of all, his incredible patience over the past five years. It took me longer than most to get to where I am now, but all throughout he always managed to find the time to help. His support and encouragement has been essential and I couldn't have done this without him.

My learning mentor, Helen, has also been an invaluable source of advice and encouragement this past year. She helped me realise that there's always less to worry about than I think, even on the days when I can't make myself believe it!

I acknowledge the financial support of the School of Mathematics and Statistics at the University of Sheffield, for providing me the opportunity to undertake this PhD and to attend conferences both inside and outside the country. In addition, I wish to thank the MASH crew for allowing me to gain valuable experience in teaching. I found my time there incredibly fulfilling and it has helped me decide how I want to apply the skills I have learned going forward.

I also want to thank the entirety of Sheffield's CRAG research group for being such an open and welcoming environment. It's wonderful to have seen the group multiply in size in the time that I've been there, even if I've not been able to meet a lot of the new members due to the pandemic! I would especially like to thank those who were my office mates the longest, Jake, Tom M, Tom S, and Vis, for never failing to make my day better even when the work was hard.

To my closest friends, Luna, Tom B, Matrim, Jasmin, Callum and Brett: thanks for giving me something to look forward to each and every week with your company, especially online these past couple of years. The pandemic has hit us all hard, but it is friendships like yours that have made life under Covid bearable.

Finally, I would like to thank my family for their unwavering love and commitment to my well-being. Without my mum's advice I wouldn't have taken the time away from work that I needed to keep myself going, nor would I have had the head-space to finish this thesis while looking after myself. Their help means so much to me and I hope some day that I can repay at least a fraction of that kindness.



# Summary

This thesis consists of two parts. Part I, containing chapters 2, 3 and 4, concerns *classical*, massive, scalar and vector (Proca) fields on static and rotating black hole spacetimes. Part II, containing chapters 5, 6 and 7, concerns *quantum*, massless, scalar fields on static black hole spacetimes and the spacetimes of spherically symmetric stars.

The goal of Part I is to present our numerical calculation of the quasinormal modes (QNMs) of the odd-parity, charged Proca field on the Reissner-Nordström spacetime and all three polarization states of the uncharged Proca field on the Kerr and Kerr-Newman spacetimes. In chapter 2 we introduce the static and rotating black hole spacetimes we will be concerned with and the formalism used to describe the propagation of scalar and vector fields on these spacetimes. Then, in chapter 3, we discuss the known methods of solving the equations of motion of these fields on static spacetimes and how this leads to the concept of QNMs, including our new application of Leaver's method [96] to the odd-parity, charged Proca field on the Reissner-Nordström spacetime. Finally, chapter 4 details the much more recent method (the LFKK ansatz [66]) used to solve the Proca equation of motion on rotating black hole spacetimes and our new application of Leaver's method to the uncharged Proca field on the Kerr and Kerr-Newman spacetimes.

The focus of Part II is on our numerical exploration of the method of taking differences between quantum expectation values (QEVs) evaluated in the same vacuum state, but on different background spacetimes. In chapter 5 we introduce the concept of semiclassical gravity and the method of Levi and Ori [100] for calculating QEVs, including the results of our own numerical implementation of said method that are consistent with the literature. Then, in chapter 6, we discuss the method of Anderson and Fabbri [7] to find the differences  $\Delta \langle \phi^2 \rangle$  and  $\Delta \langle T^\mu{}_\nu \rangle$  of the vacuum polarization and stress-energy tensor of a scalar field between the spacetimes of a Newtonian star and a black hole in the Boulware vacuum state. We apply this method to a toy model consisting of an infinitesimally thin shell on a flat background spacetime. In chapter 7, we extend this method to more general spherically symmetric stellar models and verify our new results numerically. We also present a new numerical analysis of  $\Delta \langle \phi^2 \rangle$  and  $\Delta \langle T^\mu{}_\nu \rangle$  near the star surface and consider its dependence on the star structure and the coupling  $\xi$  to the scalar curvature.

Finally, chapter 8 contains our conclusions and ideas for possible extensions to the work presented here.



# Contents

<b>1</b>	<b>Introduction</b>	<b>13</b>
<b>I</b>	<b>Classical Fields</b>	<b>19</b>
<b>2</b>	<b>Black Hole Spacetimes and Classical Fields</b>	<b>21</b>
2.1	Fields Propagating on Curved Spacetimes . . . . .	21
2.1.1	Principle of Least Action and Lagrangians . . . . .	21
2.1.2	The Equations of Motion . . . . .	23
2.1.3	Gauge Freedom . . . . .	25
2.1.4	The Eikonal Approximation . . . . .	26
2.1.4.1	From Fields to Particles . . . . .	26
2.1.4.2	Lagrangians and Hamiltonians . . . . .	27
2.1.5	Symmetries and Killing Vectors . . . . .	28
2.1.6	Killing Tensors and the Principal Tensor . . . . .	29
2.2	Black Hole Solutions of the Einstein Field Equations . . . . .	32
2.2.1	Finding the Solutions . . . . .	32
2.2.2	The Kinnersley Tetrad and the Principal Tensor . . . . .	35
2.2.3	The Existence and Nature of Horizons . . . . .	36
2.2.3.1	Static, Spherically Symmetric Black Holes . . . . .	36
2.2.3.2	Stationary, Axisymmetric Black Holes . . . . .	38
2.3	Geodesic Orbits . . . . .	38
2.3.1	Conserved Quantities and Equations of Motion on Kerr-Newman . . . . .	40
2.3.2	Geodesic Orbits . . . . .	41
2.3.2.1	Geodesic Effective Potential . . . . .	41
2.3.2.2	Stable and Unstable Orbits, Photon Orbits and the ISCO . . . . .	42

2.3.3	Relation to Energy Extraction . . . . .	45
2.4	Solving Recurrence Relations . . . . .	46
2.4.1	Gaussian Elimination . . . . .	46
2.4.2	Continued Fractions . . . . .	47
<b>3</b>	<b>Bosonic Fields on Static Black Hole Spacetimes</b>	<b>49</b>
3.1	Solving the Perturbation Field Equations . . . . .	50
3.1.1	Scalar Fields . . . . .	50
3.1.1.1	Superradiance . . . . .	53
3.1.2	Vector Fields . . . . .	54
3.1.2.1	Electromagnetic Field . . . . .	54
3.1.2.2	Uncharged Proca Field . . . . .	55
3.1.2.3	The Massless Limit . . . . .	57
3.1.2.4	Charged Proca Field . . . . .	58
3.2	Quasinormal Modes and Quasibound States . . . . .	60
3.2.1	Introduction and Motivation . . . . .	60
3.2.1.1	Massless Quasinormal Modes . . . . .	60
3.2.1.2	Quasibound States . . . . .	61
3.2.1.3	Massive Quasinormal Modes . . . . .	63
3.2.1.4	QNMs and Geodesics . . . . .	64
3.2.1.5	Unifying QNMs and QBSs . . . . .	65
3.2.2	QNMs and QBSs of a Scalar Field . . . . .	66
3.2.3	QNMs and QBSs of a Vector Field . . . . .	67
3.3	Analytical Approximations for Quasibound States . . . . .	68
3.3.1	Scalar Field . . . . .	68
3.3.2	Vector Field . . . . .	69
3.4	Numerical Methods and Results . . . . .	70
3.4.1	Direct Integration . . . . .	70
3.4.2	Recurrence Relations and Leaver's Method . . . . .	71
3.4.2.1	How many terms? . . . . .	71
3.4.2.2	A Recurrence Relation for Odd-Parity, Charged, Massive Vector Fields in Reissner-Nordström . . . . .	72

<i>CONTENTS</i>	9
<b>4 Bosonic Fields on Rotating Black Hole Spacetimes</b>	<b>81</b>
4.1 Massless Fields on the Kerr Spacetime . . . . .	81
4.2 Vector Fields on Kerr Spacetime . . . . .	83
4.2.1 The Electromagnetic Field . . . . .	83
4.2.2 The Separability of the Proca Equation on Kerr Spacetime . . . . .	85
4.2.2.1 The LFKK Ansatz . . . . .	85
4.2.2.2 The Maxwell Scalars . . . . .	88
4.2.2.3 The Three Polarization States . . . . .	88
4.2.3 Analytical Approximations for QBSs . . . . .	90
4.2.4 Solving the Proca Equation . . . . .	92
4.2.4.1 The Angular Eigenvalue: Spectral Decomposition . . . . .	92
4.2.4.2 The Radial Equation via Direct Integration . . . . .	94
4.2.4.3 The Radial Equation via Leaver's Method . . . . .	94
4.2.5 Numerical Results . . . . .	96
4.2.5.1 Consistency Checks and QBSs . . . . .	96
4.2.5.2 QNM Data . . . . .	99
4.3 QNMs in the Kerr-Newman Spacetime . . . . .	105
4.3.1 Scalar Field . . . . .	107
4.3.2 Proca Field Numerical Results . . . . .	108
<b>II Quantum Fields</b>	<b>115</b>
<b>5 Quantum Field Theory on Curved Spacetime</b>	<b>117</b>
5.1 Quantisation of a Scalar Field . . . . .	117
5.1.1 Canonical Quantisation . . . . .	117
5.1.2 Non-Uniqueness of the Vacuum State . . . . .	119
5.2 Calculating Vacuum Polarization . . . . .	120
5.2.1 The Two Point Function and Counterterms . . . . .	120
5.2.2 Evaluation Methods . . . . .	123
5.2.2.1 WKB Methods . . . . .	123
5.2.2.2 Counterterm Mode Sum Prescriptions . . . . .	124
5.2.3 The Pragmatic Mode Sum Regularisation (PMR) of Levi and Ori . . . . .	125
5.2.3.1 Generalised Sums and Integrals . . . . .	126
5.2.3.2 PMR by Angular-Splitting in a Static Spacetime . . . . .	126

5.2.3.3	Application to Schwarzschild . . . . .	130
5.2.3.4	Error Estimation . . . . .	135
5.2.3.5	Results . . . . .	136
<b>6</b>	<b>QFT Differences on Locally Equivalent Spacetimes</b>	<b>139</b>
6.1	Mode Sum Expressions for $\Delta \langle \phi^2 \rangle$ and $\Delta \langle T^\mu_\nu \rangle$ . . . . .	139
6.1.1	Vacuum Polarization . . . . .	139
6.1.2	Extension to the Stress-Energy Tensor . . . . .	141
6.1.2.1	Stress Energy Conservation . . . . .	142
6.1.3	Far Field Limit for Newtonian Stars . . . . .	143
6.2	Toy Model: Spherical Shell on Flat Spacetime . . . . .	144
6.2.1	Outside the Shell . . . . .	145
6.2.1.1	The Far Field Limit . . . . .	148
6.2.2	Inside the Shell . . . . .	150
6.2.3	The Total Energy Difference . . . . .	151
6.2.3.1	Analytical Calculation: $\ell = 0$ . . . . .	151
6.2.3.2	Numerical Verification: $\ell = 0$ . . . . .	152
6.2.3.3	Numerical Calculation: $\ell > 0$ . . . . .	154
<b>7</b>	<b>Numerical Analysis of QFT Differences</b>	<b>157</b>
7.1	Approximation in the Far Field Limit . . . . .	157
7.1.1	Constant Density Stars . . . . .	157
7.1.2	Ultra Compact Objects . . . . .	160
7.1.3	Different Stellar Models . . . . .	161
7.2	Outline of the Numerical Method . . . . .	163
7.3	Numerical Analysis Near the Star Surface . . . . .	167
7.3.1	Vacuum Polarization Near a Compact Object . . . . .	167
7.3.1.1	$R = 4M$ (Compact Neutron Star) . . . . .	167
7.3.1.2	$R = 2.26M$ (Ultra Compact Object) . . . . .	169
7.3.2	Stress-Energy Tensor Near a Compact Object . . . . .	172
7.3.2.1	$R = 4M$ (Compact Neutron Star) . . . . .	172
7.3.2.2	$R = 2.26M$ (Ultra Compact Object) . . . . .	174
7.3.2.3	Comparison . . . . .	177
7.4	Numerical Analysis Far From the Star Surface . . . . .	178

<i>CONTENTS</i>	11
7.4.1 Vacuum Polarization . . . . .	178
7.4.2 Stress-Energy Tensor . . . . .	182
<b>8 Conclusion and Outlook</b>	<b>187</b>
8.1 Summary of Results . . . . .	187
8.1.1 Classical Fields . . . . .	187
8.1.2 Quantum Fields . . . . .	188
8.2 Further Study . . . . .	189
<b>A Quasibound States of a Scalar Field</b>	<b>191</b>
A.1 Non-rotating Spacetimes . . . . .	191
A.2 Rotating Spacetimes . . . . .	193
A.2.1 Analytical Methods . . . . .	193
A.2.1.1 Leading Order . . . . .	194
A.2.1.2 Higher Orders . . . . .	195
A.2.2 Numerical Methods . . . . .	196



# Chapter 1

## Introduction

Einstein's theory of General Relativity (GR), completed in 1915, is the most experimentally verified theory of gravity that currently exists, refining the prior Newtonian theory that had been the consensus for centuries. It was able to predict new phenomena, the most startling of which being the existence of black holes, the effects of which were recently observed in gravitational wave experiments [3]. Prior to that, GR explained a long-standing discrepancy between the Newtonian theory and experimental observation, namely, the perihelion shift of the planet Mercury (for a review of experimental tests of GR see [147]). GR also forms the theoretical foundations of modern cosmology [31] and is the basis for many technologies that we today take for granted, such as GPS [9].

Broadly speaking, GR consists of two components that are constantly interacting with each other: matter and spacetime. This interaction is governed by a system of partial differential equations (PDEs) called Einstein's field equations. These equations read [104]

$$G_{\mu\nu} + \Lambda g_{\mu\nu} = \kappa T_{\mu\nu}. \quad (1.0.1)$$

On the left-hand side,  $g_{\mu\nu}$  is the spacetime *metric*,  $G_{\mu\nu}$  is the *Einstein tensor*, containing all the information about how the spacetime geometry is curved and  $\Lambda$  is the *cosmological constant*, currently theorised to be small and positive due to the observed accelerating expansion of the universe [62]. Throughout this work we will set  $\Lambda = 0$ , as current estimates indicate  $\Lambda$  to be of the order  $10^{-122} \ell_P^{-2}$  (where  $\ell_P$  is the Planck length) and so it will not produce observable effects at non-cosmological scales. On the right-hand side,  $T_{\mu\nu}$  is the *stress-energy tensor* containing all the information about how the various matter fields are distributed. As such, the Einstein field equations in a vacuum are Eq. (1.0.1) with the right hand side set to zero. The constant of proportionality is  $\kappa = 8\pi G/c^4$  where  $G$  is Newton's gravitational constant and  $c$  is the speed of light in a vacuum. Let's consider these two ingredients, spacetime and matter, in more detail.

A *spacetime* is a differentiable manifold endowed with a Lorentzian metric, which in four dimensions and under the conventions we shall use is a metric with the signature  $(-, +, +, +)$ . As such, one dimension is designated as *timelike* and the remaining dimensions are designated as *spacelike*. Due to the Lorentzian signature, spacetime intervals as calculated with the metric can be positive, negative or zero. If two spacetime points (*events*) are separated by a positive spacetime interval (that is, if they are *spacelike separated*) then they cannot communicate with one another: they are not causally connected.

Shortly after the theory of GR was completed, Schwarzschild published his static, spherically symmetric solution of the vacuum Einstein equations [132]. This Schwarzschild spacetime has the startling property that it contains a *singularity*, a point at which the spacetime curvature (the “square” of the Riemann tensor) diverges. Fortunately, the singularity exists behind an *event horizon*. Events within the event horizon are spacelike separated from those without and so no information that crosses the event horizon can ever again reach the outside world. Spacetimes that have an event horizon, whether or not they have a curvature singularity shrouded behind them, are called *black holes*.

Within a few years of the Schwarzschild solution being found (between 1916 and 1918), the solution was generalised to that of a spherically symmetric, electrically charged black hole (a solution of the electrovacuum Einstein-Maxwell equations) that we today call the Reissner-Nordström solution [124, 110]. However, it took over four decades before Schwarzschild’s solution could be generalised to the rotating case, in work done by Kerr in 1963 [87]. This in turn was swiftly generalised to the solution of a charged and rotating black hole (named the Kerr-Newman solution) in 1965 [109]. This solution is specified by just three parameters: the mass, charge and angular momentum of the black hole. Black holes may have accrued a reputation for being mysterious in the century or so since their existence was first proposed, but from a mathematical perspective they are remarkably simple objects, requiring only these three parameters to fully describe [125].

When two black holes are about to collide and spiral around each other in what is called a black hole merger, ripples in spacetime called *gravitational waves* are released [3]. Even after the merge, the resulting object continues to release gravitational waves at resonant frequencies (called *quasinormal modes* (QNMs) [95] a concept that we will elaborate on soon) as it returns to an undisturbed, latent state. The advent of gravitational wave astronomy has allowed these ripples to be observed, providing the strongest evidence to-date of the existence of black holes. Gravitational wave astronomy has advanced rapidly since the first gravitational wave detection in 2015: the GWTC-2 [4] is a catalog of 39 gravitational wave events that are either the result of the merger of two black holes, or a black

hole and a neutron star. Together, these are referred to as compact binary coalescences, where a *compact object* is the general term for the final state of collapse of a stellar object, be that a white dwarf, a neutron star, or a black hole.

Now let's consider the topic of matter fields. The most complete and well-verified theory of matter fields that exist in Nature is the Standard Model (SM) of particle physics, which encapsulates every fundamental particle known to exist and three of the four fundamental forces [102] (the convention that we will adopt in this work is that all SM fields will be referred to as “matter” fields, even those such as the photon that mediate force interactions). The fourth force, gravity, is described in classical field theory by GR. Although the SM has survived every experimental test it has been put under, the theory is incomplete because it does not provide a quantum description of the gravitational force.

Matter fields can be categorised by their *spin*, which is either an integer (in which case the field is referred to as a *boson*) or a half-integer (in which case the field is referred to as a *fermion*). We will begin with an entirely *classical* description of these fields, where they are all given by tensorial functions of the spacetime coordinates.

The only fundamental spin-0 field (described by a scalar function of the spacetime coordinates and obeying a *Klein-Gordon* equation) known to exist is the Higgs boson, which has only been observed in high energy particle physics experiments [2]. However, modern cosmological models of inflation in the early universe often make use of additional hypothetical scalar fields [107]. Regardless of their physical relevance, scalar fields are useful for theoreticians as they are the most simple to handle and so can be used in the construction of toy models. Spin-1/2 fields (obeying the *Dirac* equation and described by spinor functions) model, among others, neutrinos in the massless case and electrons in the massive case. Spin-1 fields (described by vector functions) model the electromagnetic field in the massless case. A massive spin-1 field obeys the *Proca* equation and massive spin-1 bosons govern the weak and strong nuclear interactions in the SM. There are many proposed extensions to the SM, including a spin-2 boson that would govern gravitational interactions (the graviton) and supersymmetric partners to every existing SM particle [146].

The hypothetical particles we will focus on in this work are *ultra-light* vector bosons which have been proposed as potential candidates for dark matter [58, 11, 86]. With very long Compton wavelengths, these particles have the potential to gather in “clouds” around black holes, with certain frequencies called *quasibound state* frequencies. Like quasinormal modes, we will discuss quasibound states in more detail shortly.

Now that we have discussed both spacetime and the matter fields that will live in that spacetime, let's return to describing how these two aspects interact with each other. To understand how

these fields propagate on spacetime, and thus make predictions that can be tested, we must study their equations of motion. These equations are systems of coupled PDEs that can be technically challenging to solve. However, in many situations these PDEs can be separated into systems of much less daunting ordinary differential equations (ODEs). Whether or not such a separation can be performed depends both on the symmetries of the spacetime being considered and on the nature of the perturbing matter field. Work done by Teukolsky [137] allowed the equations of motion of massless fields of integer spin to be separated on rotating black hole spacetimes and similar work by Unruh [140] did the same for the massless spin-1/2 Dirac field. In the cases of scalar fields and the Dirac field, this was extended to the case of non-zero mass by Brill *et al.*, [26] and Chandrasekhar [42] respectively, but for massive vector fields the equation of motion proved much more resistant to attempts to separate it. For the decades that followed, it was widely believed that the equation of motion of the Proca field could not be separated on a rotating black hole spacetime, forcing researchers to tackle the PDEs directly. This limited the results that could be obtained to various approximations, such as the slowly rotating black hole [113].

It wasn't until 2018 that this problem was solved. Rotating black hole spacetimes have *hidden symmetries*, symmetries that can be seen when one considers the phase space of a particle moving on that spacetime [64]. This can be contrasted with *explicit symmetries*, such as time translation and axial rotation, that are described by Killing vectors. Hidden symmetries are described by higher rank Killing objects and, in the case of a rotating black hole, can be encapsulated in an object called the *principal tensor*. It was the work of Frolov *et al.* [66], building on the prior work of Lunin [101], that showed how the principal tensor could be applied to separate the equation of motion of the massive vector field. This immediately paved the way for detailed calculations of the interactions between massive vector fields and rotating black holes that could have experimentally observable effects. Two effects that have drawn attention, and those that we will be interested in, have already been mentioned: quasinormal modes (QNMs) and quasibound states (QBSs).

On a black hole spacetime, quasibound state frequencies are the special frequencies of a massive field where two boundary conditions are met: the field is regular on the future event horizon and decays away far from the black hole. If the black hole is charged or rotating, then it is possible for the field to be reflected off the gravitational potential of the hole with more energy than it impacted with (an effect called *superradiance* [28]), but at the same time, if the field is in a quasibound state, the mass of the field could prevent it from then escaping the black hole allowing it to be pulled in and amplified again. As such, the amplitude of the field will continue to grow in a phenomenon called a *superradiant instability* [27]. This allows the field to form a “cloud” around the black hole,

which could potentially be observed as the black hole having bosonic hair [82], but can also be used to constrain the mass of these hypothetical particles [33, 112]. The QBSs of the Proca field around a rotating black hole were found using the newly-found separation of the equations of motion in [54].

Quasinormal modes were mentioned earlier in the context of the gravitational waves emitted by black hole mergers, but they are also relevant whenever a matter field, massive or not, interacts with a black hole. Any perturbing field will cause the black hole to emit radiation at quasinormal mode frequencies as it relaxes back to a quiescent state. In this case, the spectrum of observed frequencies depends on the field parameters (mass and spin) as well as the black hole parameters (mass, charge and angular momentum). In the case of a massless spin-2 field this represents a gravitational perturbation, which predicts the existence of the QNMs found in gravitational wave observations described earlier. The field of *black hole spectroscopy* aims to spot these QNMs within the broader gravitational wave signal [10] and if higher overtones can be observed [72] then this can either constrain the black hole parameters, or be used to test the theory of GR itself. QNMs of massless fields in general are well studied, in part due to the separability of their equations of motion, but there are larger gaps in the literature when it comes to the QNMs of massive fields. Now that the equation of motion of the Proca field has been shown to be separable, one of those gaps can be filled, which we did with Dolan in [117] and which will be described in the first half of this thesis.

So far, we have considered only *classical* fields propagating on various background spacetimes, described by functions of the spacetime coordinates. The current consensus is that the universe, at a fundamental level, is *quantum mechanical*. Hence, any classical theory can only be an approximation of the fundamental physics and a theory of quantum gravity is required to describe the universe fully. Such a theory would most certainly be needed in situations where both gravity and quantum mechanics play a leading role, such as in the very early universe, or near spacetime curvature singularities such as those in the centre of black holes.

Unfortunately a complete theory of quantum gravity that agrees with experimental observation is still unknown, though there are several promising candidates, with perhaps the most well studied being string theory [19]. The central problem is that it is known how to describe the matter fields on the spacetime quantum mechanically, but not the spacetime itself. The former is done by treating the fields no longer as functions, but as *operators* acting on a Hilbert space of state vectors. As such, an approximate theory of quantum gravity presents itself, that of *semiclassical gravity*, in which the matter fields are quantised, but spacetime is still treated classically. At the heart of this theory is

the *semiclassical Einstein equation* (cf. Eq. (1.0.1), with the cosmological constant set to zero),

$$G_{\mu\nu} = \kappa \langle T_{\mu\nu} \rangle, \quad (1.0.2)$$

where on the right-hand side, the source term of the classical Einstein equation has been replaced with the *expectation value* of the stress-energy tensor  $T_{\mu\nu}$  in a chosen quantum state.

Semiclassical gravity has been studied for several decades and has produced some fascinating results. Perhaps the most well known is Hawking’s famous conclusion that black holes cannot exist forever. They will evaporate away over time by the emission of thermal Hawking radiation [78]. Other results concern the properties of  $\langle T_{\mu\nu} \rangle$  itself, in particular that it violates many of the energy conditions satisfied by its classical counterpart [142]. In essence, this means there exist reference frames where an observer could measure that the quantum field has a negative energy density. This has consequences for the potential existence of exotic spacetimes, such as wormholes [105].

However, semiclassical gravity comes with its own share of challenges that need to be overcome. Quantum expectation values (QEVs) are constructed out of products of operator valued distributions and as such, they are divergent. This isn’t unique to semiclassical gravity: quantum field theory in flat spacetimes also encounters this problem. The process known as *renormalisation* allows us to make sense of these divergences. There are many different schemes that can be used to carefully isolate the divergent terms of a QEV and remove them (for example, the methods we will discuss in this work are based on Hadamard renormalisation, [76]), but there are also ways to arrive at a finite quantity while avoiding renormalisation entirely. One such way is to calculate the QEV of interest in two different quantum states where it happens to diverge in the same manner and then take the difference between the two. This method has been well studied in the literature for decades [32].

Another method, described by Anderson and Fabbri in [7] much more recently, is to calculate the QEV in the same quantum state, but in two different spacetimes that are locally equivalent. By this, it is meant that the two spacetimes are identical within a neighbourhood of the point the QEV is to be measured and hence it is guaranteed to diverge in the same manner on both of them.

In the second half of this thesis, we will explore potential numerical applications of this method. The two spacetimes we will focus on are those of a non-rotating, uncharged black hole (where multiple QEVs have already been calculated fully and renormalised, [8]) and a spherically symmetric star with some specified internal structure (where QEVs are much less well studied, especially near the star surface). We know that outside the gravitational source these two spacetimes are equivalent due to Birkhoff’s theorem [63]. Hence, we hope to construct QEVs on a spacetime that is globally more complicated (that of a star) by exploiting its local similarity to a spacetime that is much simpler (that of a black hole).

## Part I

# Classical Fields



## Chapter 2

# Black Hole Spacetimes and Classical Fields

### Introduction and Overview

In this chapter, we introduce the formalism required to describe classical scalar and vector fields propagating on black hole spacetimes. We begin by introducing the fields, specifying the action and finding the equations of motion. We cover some general properties of fields on curved spacetimes including gauge freedom, symmetries and conservation laws. We then introduce the black hole spacetimes on which the fields will propagate and describe some of their features, such as their circular geodesic orbits. Finally, we outline the primary method we will be using in chapters 3 and 4 to find the quasinormal modes and quasibound states of these fields: the continued fraction method [95, 96].

Throughout the chapter we will use natural units, in which the gravitational constant  $G$  and the speed of light  $c$  are set to unity.

## 2.1 Fields Propagating on Curved Spacetimes

### 2.1.1 Principle of Least Action and Lagrangians

Throughout the next three chapters of this work, we will be primarily discussing the theory of massive, charged scalar and vector fields (as well as massless, uncharged electromagnetic fields) propagating in a curved spacetime. In classical field theory, the equations of motion of all these fields are found via the *principle of least action* [37], which states that the classical trajectory of these fields in phase space will be one that gives an extremum of the *action*  $S$ . The action is a

functional of all the fields, written as an integral over spacetime of the *Lagrangian density*  $\mathcal{L}$ . More specifically,

$$S = \int \sqrt{-g} \mathcal{L} d^4x, \quad (2.1.1)$$

$$\mathcal{L} = \mathcal{L}_G + \mathcal{L}_F + \mathcal{L}_\Phi + \mathcal{L}_W, \quad (2.1.2)$$

where  $\mathcal{L}_G, \mathcal{L}_F, \mathcal{L}_\Phi$  and  $\mathcal{L}_W$  are the Lagrangian densities of the gravitational, electromagnetic, massive scalar and massive vector (i.e., Proca) fields respectively and  $g$  is the determinant of the spacetime metric  $g_{\mu\nu}$ . Throughout this work, the connection defined on a metric  $\nabla_\mu$  will be the unique, torsion-free connection that is compatible with the metric, i.e.,  $\nabla_\rho g_{\mu\nu} = 0$ .

The four Lagrangian densities are given by [63, 37, 80]

$$\mathcal{L}_G = \frac{R}{16\pi}, \quad (2.1.3)$$

$$\mathcal{L}_F = -\frac{1}{4} F_{\mu\nu} F^{\mu\nu}, \quad (2.1.4)$$

$$\mathcal{L}_\Phi = -\frac{1}{2} \left( g^{\mu\nu} \left( \tilde{\nabla}_\mu \Phi \right)^* \tilde{\nabla}_\nu \Phi + \mu^2 \Phi^* \Phi \right), \quad (2.1.5)$$

$$\mathcal{L}_W = - \left( \frac{1}{4} W_{\mu\nu}^\dagger W^{\mu\nu} + \frac{1}{2} \mu^2 W_\nu^* W^\nu + 2ie W_\mu^* W_\nu F^{\mu\nu} \right). \quad (2.1.6)$$

We will now describe these terms in order. In  $\mathcal{L}_G$ ,  $R$  is the Ricci scalar defined according to  $R = g^{\mu\nu} R_{\mu\nu} = g^{\mu\alpha} g^{\nu\beta} R_{\mu\nu\alpha\beta}$ , where  $R_{\mu\nu}$  is the *Ricci tensor* and  $R_{\mu\nu\alpha\beta}$  is the *Riemann tensor* [63]. The Riemann tensor is constructed from the metric and its derivatives through the *Christoffel Symbols*  $\Gamma_{\alpha\beta}^\mu$ ,

$$R^\mu_{\nu\alpha\beta} = g^{\mu\rho} R_{\rho\nu\alpha\beta} = \partial_\alpha \Gamma^\mu_{\nu\beta} - \partial_\beta \Gamma^\mu_{\nu\alpha} + \Gamma^\mu_{\sigma\alpha} \Gamma^\sigma_{\nu\beta} - \Gamma^\mu_{\sigma\beta} \Gamma^\sigma_{\nu\alpha}, \quad (2.1.7)$$

$$\Gamma^\mu_{\alpha\beta} = \frac{1}{2} g^{\mu\nu} (\partial_\beta g_{\nu\alpha} + \partial_\alpha g_{\nu\beta} - \partial_\nu g_{\alpha\beta}). \quad (2.1.8)$$

In  $\mathcal{L}_F$ ,  $F_{\mu\nu}$  is the *Faraday tensor* of the electromagnetic field. This tensor is antisymmetric and consists of six real component functions describing the electric and magnetic fields in each of the three spatial directions. By construction, it satisfies the identity

$$\nabla_{[\alpha} F_{\mu\nu]} = 0, \quad (2.1.9)$$

where the square brackets around the indices indicate antisymmetrisation. Written in terms of the electric and magnetic fields, this contains two of the four of *Maxwell's equations*. It follows that  $F_{\mu\nu}$ , at least locally, can be written in terms of a vector potential  $A_\mu$

$$F_{\mu\nu} = \nabla_\mu A_\nu - \nabla_\nu A_\mu. \quad (2.1.10)$$

In  $\mathcal{L}_\Phi$ ,  $\Phi$  is a complex scalar field of mass  $\mu$  and charge  $e$ , with complex conjugate  $\Phi^*$ . The derivative  $\nabla_\mu$  is modified to include the charge,

$$\tilde{\nabla}_\mu = \nabla_\mu - ieA_\mu. \quad (2.1.11)$$

Similarly, in  $\mathcal{L}_W$ ,  $W_\mu$  is a complex vector field of mass  $\mu$  and charge  $e$  (we will adopt the same symbols for mass and charge for both the scalar and vector fields as we will not be considering both of these fields at the same time).  $W_{\mu\nu}$  is a tensor constructed from the vector field

$$W_{\mu\nu} = \nabla_\mu W_\nu - \nabla_\nu W_\mu \quad (2.1.12)$$

and  $W_{\mu\nu}^\dagger$  is its Hermitian conjugate.

### 2.1.2 The Equations of Motion

The condition that the action  $S$  in (2.1.1) be extremised is equivalent to the requirement that the action be invariant under a small variation of each of the fields  $\Phi$ ,  $W_\mu$ ,  $A_\mu$  and  $g_{\mu\nu}$ . In other words, the functional derivative of  $S$  with respect to these fields is zero.

We demonstrate the general procedure on a Lagrangian  $\mathcal{L}(\Psi^i, \partial_\mu \Psi^i)$  of a set of fields and their derivatives labeled by the index  $i$ . We can add a small variation  $\delta\Psi^i$  to the field, add the derivative of this variation to the derivative of the field and then Taylor expand, as follows,

$$\sqrt{-g}\mathcal{L}(\Psi^i + \delta\Psi^i, \partial_\mu \Psi^i + \partial_\mu \delta\Psi^i) = \sqrt{-g}\mathcal{L}(\Psi^i, \partial_\mu \Psi^i) + \frac{\partial(\sqrt{-g}\mathcal{L})}{\partial\Psi^i} \delta\Psi^i + \frac{\partial(\sqrt{-g}\mathcal{L})}{\partial(\partial_\mu \Psi^i)} \partial_\mu \delta\Psi^i + O(\delta^2).$$

Hence, the total variation in the action is the spacetime integral of the last two terms

$$\delta S = \int d^4x \left[ \frac{\partial(\sqrt{-g}\mathcal{L})}{\partial\Psi^i} \delta\Psi^i + \frac{\partial(\sqrt{-g}\mathcal{L})}{\partial(\partial_\mu \Psi^i)} \partial_\mu \delta\Psi^i \right].$$

The second term can be integrated by parts to get

$$\int d^4x \frac{\partial(\sqrt{-g}\mathcal{L})}{\partial(\partial_\mu \Psi^i)} \partial_\mu \delta\Psi^i = - \int d^4x \partial_\mu \left( \frac{\partial(\sqrt{-g}\mathcal{L})}{\partial(\partial_\mu \Psi^i)} \right) \delta\Psi^i + \int d^4x \partial_\mu \left( \frac{\partial(\sqrt{-g}\mathcal{L})}{\partial(\partial_\mu \Psi^i)} \delta\Psi^i \right).$$

The last term here is now the integral of a divergence. Hence, by Stokes' theorem, it is equal to a term dependent only on the value of the variations at the boundary. But the integration is over the entire spacetime, which has no boundary and thus this term vanishes and the variation of the action becomes

$$\delta S = \int d^4x \left[ \frac{\partial(\sqrt{-g}\mathcal{L})}{\partial\Psi^i} - \partial_\mu \left( \frac{\partial(\sqrt{-g}\mathcal{L})}{\partial(\partial_\mu \Psi^i)} \right) \right] \delta\Psi^i.$$

With the  $\delta\Psi^i$  factored out, we can see  $\delta S$  vanishes when the quantity in the square brackets vanishes.

This is the *Euler-Lagrange* equation,

$$\partial_\mu \left( \frac{\partial(\sqrt{-g}\mathcal{L})}{\partial(\partial_\mu\Psi^i)} \right) - \frac{\partial(\sqrt{-g}\mathcal{L})}{\partial\Psi^i} = 0. \quad (2.1.13)$$

This can now be applied to each of the Lagrangian densities in Eqs.(2.1.3)-(2.1.6). We do the calculation explicitly for the case of the complex scalar field, Eq.(2.1.5). The two terms of the Euler-Lagrange equation are

$$\begin{aligned} \frac{\partial(\sqrt{-g}\mathcal{L}_\Phi)}{\partial\Phi^*} &= -\frac{1}{2}\sqrt{-g} \left( ieA_\mu g^{\mu\nu} \tilde{\nabla}_\nu \Phi + \mu^2 \Phi \right), \\ \partial_\mu \left( \frac{\partial(\sqrt{-g}\mathcal{L}_\Phi)}{\partial(\partial_\mu\Phi^*)} \right) &= \partial_\mu \left( -\frac{1}{2}\sqrt{-g} g^{\mu\nu} \tilde{\nabla}_\nu \Phi \right). \end{aligned}$$

Putting these together and dividing by  $-\frac{1}{2}\sqrt{-g}$  gives

$$\frac{1}{\sqrt{-g}} \partial_\mu \left( \sqrt{-g} g^{\mu\nu} \tilde{\nabla}_\nu \Phi \right) - ieA_\mu g^{\mu\nu} \tilde{\nabla}_\nu \Phi - \mu^2 \Phi = 0.$$

Factorising then gives

$$\frac{1}{\sqrt{-g}} (\partial_\mu - ieA_\mu) \left( \sqrt{-g} g^{\mu\nu} \tilde{\nabla}_\nu \Phi \right) - \mu^2 \Phi = 0$$

and now note the divergence formula  $\frac{1}{\sqrt{-g}} \partial_\mu (\sqrt{-g} B^\mu) = \nabla_\mu B^\mu$  for  $B^\mu$  an arbitrary vector

$$\nabla_\mu \left( g^{\mu\nu} \tilde{\nabla}_\nu \Phi \right) - ieA_\mu g^{\mu\nu} \tilde{\nabla}_\nu \Phi - \mu^2 \Phi = 0.$$

Factorising once more leads to the *Klein-Gordon equation*

$$\left( g^{\mu\nu} \tilde{\nabla}_\mu \tilde{\nabla}_\nu - \mu^2 \right) \Phi = 0. \quad (2.1.14)$$

By instead taking derivatives with respect to  $\Phi$  we would get the complex conjugate of this equation satisfied by  $\Phi^*$ .

Applying the Euler-Lagrange equation to the remaining three Lagrangian densities involving  $g_{\mu\nu}$ ,  $A_\mu$  and  $W_\mu$ , one gets the field equations [37, 63, 80]

$$R_{\mu\nu} - \frac{1}{2}g_{\mu\nu}R = 8\pi T_{\mu\nu}, \quad (2.1.15)$$

$$\nabla_\nu F^{\mu\nu} = J^\mu, \quad (2.1.16)$$

$$\nabla_\mu W^{\mu\nu} - \mu^2 W^\nu - ieW_\mu F^{\mu\nu} = 0. \quad (2.1.17)$$

The first of these is the *Einstein field equation*, the second is the remaining pair of *Maxwell's equations* and the third is the (charged) *Proca equation*. On the right hand side of (2.1.15) is the *stress-energy tensor*  $T_{\mu\nu}$  and on the right hand side of Eq.(2.1.16) is the *current distribution*  $J^\mu$ .

As the Einstein equation comes about from the variation of the action with respect to the metric  $g_{\mu\nu}$ , and as the metric is included in  $\mathcal{L}_F$ ,  $\mathcal{L}_W$  and  $\mathcal{L}_\Phi$  through the covariant derivative or the raising and lowering of indices,  $T_{\mu\nu}$  contains contributions from each of the matter fields,

$$T_{\mu\nu} = T_{\mu\nu}^F + T_{\mu\nu}^\Phi + T_{\mu\nu}^W. \quad (2.1.18)$$

Similarly, as the pair of Maxwell's equations (2.1.16) comes from the variation of the action with respect to the vector potential  $A^\mu$ , and  $A^\mu$  is present in both  $\mathcal{L}_W$  and  $\mathcal{L}_\Phi$ ,  $J^\mu$  contains contributions

$$J^\mu = J_\Phi^\mu + J_W^\mu. \quad (2.1.19)$$

In this work, we will be considering massive scalar and vector fields as small perturbations of background black hole spacetimes. The black holes may carry an electromagnetic charge. Hence, the electromagnetic field governed by  $F_{\mu\nu}$  will be large compared to the charge of the scalar and vector fields and we neglect the contributions of  $\Phi$  and  $W_\mu$  to  $T_{\mu\nu}$ . The contribution from the remaining Lagrangian density  $\mathcal{L}_F$  is

$$T_{\mu\nu}^F = F_{\mu\alpha}F_\nu{}^\alpha - \frac{1}{4}g_{\mu\nu}F_{\alpha\beta}F^{\alpha\beta} \quad (2.1.20)$$

and this tensor is traceless,  $g^{\mu\nu}T_{\mu\nu}^F = 0$ .

It is worth noting that, although  $T_{\mu\nu}$  must satisfy the conservation equation  $\nabla_\mu T^{\mu\nu} = 0$ , this is not necessarily true of each term in (2.1.18) individually. This is because energy can be transferred between the electromagnetic field and the charged scalar and vector fields. This energy must be conserved according to the equation

$$\nabla_\nu T_F^{\mu\nu} = -F^\mu{}_\nu J^\nu, \quad (2.1.21)$$

which is derived by applying  $\nabla_\mu$  to (2.1.20) and using Maxwell's equations (2.1.9) and (2.1.16). But, similarly to how we neglected  $T_{\mu\nu}^\Phi$  and  $T_{\mu\nu}^W$ , treating the massive scalar and vector fields as test fields allows us to neglect the contributions  $J_\Phi^\mu$  and  $J_W^\mu$  to the current distribution and so we simply have  $J^\mu = 0$ . Hence,  $\nabla_\nu T_F^{\mu\nu} = 0$  and conservation holds.

### 2.1.3 Gauge Freedom

We can apply *gauge transformations* to the charged scalar field  $\Phi$  and the vector field  $A_\mu$  without altering their equations of motion ((2.1.14) and (2.1.16)) or  $F_{\mu\nu}$ , and hence without changing the underlying physics. These transformations are

$$A_\mu \rightarrow A_\mu - \nabla_\mu \chi, \quad \Phi \rightarrow e^{-ie\chi}\Phi, \quad (2.1.22)$$

where  $\chi$  is an arbitrary scalar function. For the field  $A_\mu$  we typically choose to work in the *Lorenz gauge* defined by the condition

$$\nabla_\mu A^\mu = 0. \quad (2.1.23)$$

This gauge freedom does not exist for the massive vector field  $W_\mu$ . Taking the gradient of Eq. (2.1.17) and rearranging,

$$\begin{aligned} \nabla_\nu W^\nu &= \frac{1}{\mu^2} [\nabla_\nu \nabla_\mu W^{\mu\nu} - ie \nabla_\nu (W_\mu F^{\mu\nu})] \\ &= -\frac{ie}{\mu^2} (F^{\mu\nu} \nabla_\nu W_\mu + W_\mu \nabla_\nu F^{\mu\nu}) = \frac{ie}{\mu^2} F^{\nu\mu} \nabla_\nu W_\mu = \frac{ie}{\mu^2} F^{\nu\mu} W_{\nu\mu}. \end{aligned} \quad (2.1.24)$$

To go from the first line to the second we have used the fact that the double divergence of a two-form is zero. Then we have noted  $\nabla_\nu F^{\mu\nu} = 0$  and then we have applied the antisymmetry of  $F^{\mu\nu}$  and the definition of  $W^{\mu\nu}$  (2.1.12).

From the above it is clear that there is no freedom to choose the form of  $\nabla_\nu W^\nu$ . In the case of a uncharged field  $e = 0$  the Lorenz condition  $\nabla_\nu W^\nu = 0$  is a direct consequence of the Proca equation (2.1.17).

## 2.1.4 The Eikonal Approximation

### 2.1.4.1 From Fields to Particles

We will now introduce a commonly used approximation which, in the limit of large field frequency, relates the equation of motion of a field, such as (2.1.14), to the equation of motion of a particle. This is called the *eikonal approximation* [56, 94] and it will be especially important when we come to discuss quasinormal modes and quasibound states of these fields in Sec. 3.2. We demonstrate this approximation in the case of a charged scalar field.

Let the scalar field be of the form  $\Phi = e^{i\omega\mathcal{S}}$ , for  $\mathcal{S}$  a phase and  $\omega \gg 1$ . We substitute this into the Klein-Gordon equation (2.1.14), assume  $A_\mu$  and  $\mu$  are  $O(\omega)$  and keep only the leading order  $O(\omega^2)$  contribution. If we define  $\pi_\mu = \nabla_\mu \mathcal{S}$  this gives

$$g^{\mu\nu} (\pi_\mu - eA_\mu) (\pi_\nu - eA_\nu) + \mu^2 = 0. \quad (2.1.25)$$

To obtain an equation of motion, we then take the gradient of (2.1.25) and introduce  $p_\mu = \pi_\mu - eA_\mu$

$$(\pi^\mu - eA^\mu) (\nabla_\nu \pi_\mu - e \nabla_\nu A_\mu) = 0, \quad (2.1.26)$$

$$\Rightarrow p^\mu (\nabla_\mu \pi_\nu - e \nabla_\nu A_\mu) = 0, \quad (2.1.27)$$

$$\Rightarrow p^\mu (\nabla_\mu (p_\nu - eA_\nu) - e \nabla_\nu A_\mu) = 0,$$

$$\Rightarrow p^\mu \nabla_\mu p_\nu - e p^\mu F_{\mu\nu} = 0. \quad (2.1.28)$$

Here, in the second line we have used the commutivity of covariant derivatives on scalar functions,  $\nabla_\mu \nabla_\nu \mathcal{S} = \nabla_\nu \nabla_\mu \mathcal{S}$ .

We have thus arrived at the equation of motion for a charged, massive particle

$$p^\mu \nabla_\mu p^\nu = e p_\mu F^{\mu\nu}. \quad (2.1.29)$$

In the case of a uncharged particle, Eq. (2.1.29) reduces to the *timelike geodesic equation*

$$p^\mu \nabla_\mu p^\nu = 0. \quad (2.1.30)$$

Geodesics will be discussed in more detail in Sec. 2.3.

### 2.1.4.2 Lagrangians and Hamiltonians

In the language of Lagrangian and Hamiltonian mechanics, the quantity  $\pi_\mu$  is the *canonical momentum* of a massive, charged particle in an electromagnetic field. This can be shown by considering the Lagrangian of such a particle

$$L = \frac{1}{2} (g_{\mu\nu} \dot{x}^\mu \dot{x}^\nu + 2e A_\mu \dot{x}^\mu), \quad (2.1.31)$$

where  $\dot{x}^\mu = dx^\mu/ds$ , the derivative of  $x^\mu$  with respect to an affine parameter  $s$ . The canonical momentum with respect to  $\dot{x}^\mu$  is

$$\pi_\mu = \frac{\partial L}{\partial \dot{x}^\mu} = g_{\mu\nu} (\dot{x}^\nu + e A^\nu) = p_\mu + e A_\mu, \quad (2.1.32)$$

agreeing with our previous definitions of  $p_\mu$  and  $\pi_\mu$ . The Hamiltonian is a scalar function on the phase space  $H(x^\mu, p_\mu; s)$  found via the Legendre transformation,

$$H = \dot{x}^\mu \pi_\mu - L = \frac{1}{2} (g^{\mu\nu} (\pi_\mu - e A_\mu) (\pi_\nu - e A_\nu)) \quad (2.1.33)$$

and the equations of motion are given by Hamilton's equations

$$\dot{x}^\mu = \frac{\partial H}{\partial \pi_\mu}, \quad \dot{\pi}_\mu = -\frac{\partial H}{\partial x^\mu}. \quad (2.1.34)$$

It is clear that this Hamiltonian is *autonomous*, i.e., it does not depend explicitly on  $s$ . Consequently (after applying Hamilton's equations) the total derivative  $dH/ds$  is zero and so  $H$  is constant along the integral curves of (2.1.34) like so,

$$H = \frac{1}{2} (g^{\mu\nu} (\pi_\mu - e A_\mu) (\pi_\nu - e A_\nu)) = \frac{1}{2} g_{\mu\nu} \dot{x}^\mu \dot{x}^\nu = k, \quad (2.1.35)$$

for  $k$  a constant. To fix the constant, the 4-velocity  $\dot{x}^\mu$  is normalised according to  $g_{\mu\nu} \frac{dx^\mu}{d\tau} \frac{dx^\nu}{d\tau} = -1$  where  $\tau$  is the particle's proper time. The affine parameter  $s$  is related to  $\tau$  by  $d\tau = \mu ds$  and so  $k = -\frac{1}{2}\mu^2$ .

To make the connection between Hamiltonian mechanics and the eikonal approximation, we consider the *Hamilton-Jacobi* equation, in which one tries to find a *characteristic function*  $W(x^\mu, \pi_\mu)$  that satisfies  $H(x^\mu, \partial_\mu W) - k = 0$  (see for example [38] where this analysis is performed in the Kerr spacetime). In full, the equation is

$$g^{\mu\nu} (\partial_\mu W - eA_\mu) (\partial_\nu W - eA_\nu) + \mu^2 = 0 \quad (2.1.36)$$

and this matches precisely with the eikonal equation of motion (2.1.25) if we identify the characteristic function  $W$  with the phase of the field  $\mathcal{S}$  and then, as in the previous subsection, identify  $\pi_\mu$  with  $\nabla_\mu \mathcal{S}$ .

### 2.1.5 Symmetries and Killing Vectors

In this subsection and the next, we will discuss symmetries of spacetimes and the tools used to describe them. This will be vitally important to solving the equations of motion ((2.1.14) and (2.1.17)) of fields propagating on these spacetimes, see in particular Sec. 4.2 on the uncharged Proca field.

The language of *Lie derivatives* and *Killing vectors* can be used to study the symmetries and conserved quantities of a physical theory. The Lie derivative of a general tensor field  $T^{\mu_1 \mu_2 \dots \mu_k}_{\nu_1 \nu_2 \dots \nu_\ell}$  in the direction of a vector field  $V^\mu$  is denoted  $\mathcal{L}_V T$  and is defined by [37]

$$\begin{aligned} \mathcal{L}_V T^{\mu_1 \mu_2 \dots \mu_k}_{\nu_1 \nu_2 \dots \nu_\ell} &= V^\alpha \nabla_\alpha T^{\mu_1 \mu_2 \dots \mu_k}_{\nu_1 \nu_2 \dots \nu_\ell} \\ &- (\nabla_\beta V^{\mu_1}) T^{\beta \mu_2 \dots \mu_k}_{\nu_1 \nu_2 \dots \nu_\ell} - (\nabla_\beta V^{\mu_2}) T^{\mu_1 \beta \dots \mu_k}_{\nu_1 \nu_2 \dots \nu_\ell} - \dots \\ &+ (\nabla_{\nu_1} V^\beta) T^{\mu_1 \mu_2 \dots \mu_k}_{\beta \nu_2 \dots \nu_\ell} + (\nabla_{\nu_2} V^\beta) T^{\mu_1 \mu_2 \dots \mu_k}_{\nu_1 \beta \dots \nu_\ell} + \dots \end{aligned} \quad (2.1.37)$$

In particular the Lie derivative of the metric along a vector field  $V^\mu$  is

$$\mathcal{L}_V g_{\mu\nu} = V^\alpha \nabla_\alpha g_{\mu\nu} + (\nabla_\mu V^\alpha) g_{\alpha\nu} + (\nabla_\nu V^\alpha) g_{\mu\alpha} = \nabla_\mu V_\nu + \nabla_\nu V_\mu = 2\nabla_{(\mu} V_{\nu)}$$

and a Killing vector  $\xi$  is one such that this Lie derivative vanishes

$$\nabla_{(\mu} \xi_{\nu)} = 0. \quad (2.1.38)$$

There is a connection between symmetries in spacetime and conservation laws for fields and particles. Killing vectors can be used to bridge the gap between these two concepts. On the one hand, Killing vectors are the infinitesimal generators of the *isometries* of the metric. If  $\mathcal{M}$  is the underlying manifold, an isometry is a diffeomorphism  $\phi : \mathcal{M} \rightarrow \mathcal{M}$  that leaves the metric invariant, i.e., it defines a map between the tangent spaces at the points  $p$  and  $\phi(p)$ ,  $\phi^* : T_p \rightarrow T_{\phi(p)}$ , such

that  $(\phi^*g)_{\mu\nu} = g_{\mu\nu}$  [144]. The left hand side of this equation is called the *pullback* of the metric, see Appendix A of [37].

On the other hand, Killing vectors can be used to construct quantities that are conserved along particle trajectories. Let's consider the example of a charged scalar particle once more. Suppose we know of a Killing vector  $\xi^\mu$  such that  $\mathcal{L}_\xi g_{\mu\nu} = 0$  and suppose further that the Lie derivative of the vector potential is also zero  $\mathcal{L}_\xi A_\mu = 0$ . It can then be shown that the quantity  $\pi_\mu \xi^\mu$  is conserved on trajectories defined by the equation of motion (2.1.29)

$$\begin{aligned} p^\nu \nabla_\nu (\pi_\mu \xi^\mu) &= \xi^\mu p^\nu \nabla_\nu \pi_\mu + \pi_\mu p^\nu \nabla_\nu \xi^\mu \\ &= e \xi^\mu p^\nu \nabla_\mu A_\nu + e A_\mu p^\nu \nabla_\nu \xi^\mu + p_\mu p^\nu \nabla_\nu \xi^\mu \\ &= e p^\nu (\mathcal{L}_\xi A_\nu) = 0, \end{aligned}$$

where we have applied  $\nabla_\nu \pi_\mu = e \nabla_\mu A_\nu$  from Eq. (2.1.26) and  $\pi_\mu = p_\mu + e A_\mu$ . In addition, we have used the fact that  $p_\mu p^\nu \nabla_\nu \xi^\mu$  vanishes, as  $p_\mu p^\nu$  is symmetric while  $\nabla_\nu \xi^\mu$  is antisymmetric, for  $\xi^\mu$  a Killing vector.

If we return to thinking about scalar particles as modes of a scalar field obeying the Klein-Gordon equation (2.1.14), then the importance of the Killing vector is that it forms a differential operator  $\xi^\mu \nabla_\mu$  that commutes with the d'Alembertian operator  $\square = \nabla^\mu \nabla_\mu$ ,

$$\square (\xi^\mu \nabla_\mu \Phi) = \xi^\mu \nabla_\mu (\square \Phi). \quad (2.1.39)$$

Hence if  $\Phi$  is a solution to the Klein-Gordon equation, then so is  $\xi^\mu \nabla_\mu \Phi$ . Now, consider the eigenmodes of the  $\xi^\mu \nabla_\mu$  operator, such that

$$\xi^\mu \nabla_\mu \Phi = ik \Phi, \quad (2.1.40)$$

for  $k$  a constant. By substituting the eikonal approximation  $\Phi = e^{i\omega \mathcal{S}}$  into (2.1.40) we arrive at  $k = \xi^\mu \nabla_\mu \mathcal{S} = \xi^\mu \pi_\mu$ , which is exactly the quantity that is conserved on a particle trajectory.

When  $\xi_j^\mu = \partial_j^\mu$  is the Killing vector that arises from the metric being independent of a given co-ordinate  $x^j$  (like the time translation and rotational Killing vectors to be discussed in Sec. 2.2.1) this implies that the eigenstate  $\Phi$  depends on  $x^j$  only through a trivial exponential factor  $e^{ikx^j}$ . Hence, in this case we can infer information about the separability of the field from the Killing vector and the separation constant is  $k$ . This relationship between Killing objects and separability of differential equations will now be expanded on further.

### 2.1.6 Killing Tensors and the Principal Tensor

The goal of this section is to introduce the *principal tensor*  $h_{\mu\nu}$ . An understanding of this tensor is vital to successfully applying the method of separation of variables to massive vector perturbations

on the Kerr spacetime, a method that was thought to be ineffective as little as six years ago, before the work of Frolov *et al* in [66], following the work of Lunin in [101]. We will describe this method in Sec. 4.2.

To describe such a tensor, a general discussion of spacetime symmetries is first required. For a comprehensive review of the symmetries of the Kerr-NUT-(A)dS family of spacetimes, see [64]. This will be our primary reference for this subsection.

In the previous subsection we discussed how spacetime symmetries can be encapsulated by Killing vector fields  $\xi^\mu$ . The symmetries that can be described by Killing vectors will be referred to as *explicit symmetries* because they have direct analogues to symmetries of the configuration space. More specifically, the conserved quantity  $I$  that arises from the symmetry is linear in momentum,  $I = \xi^\mu p_\mu$  and so the corresponding Hamiltonian vector field in the phase space [64],

$$X_I = \xi^\mu \frac{\partial}{\partial x^\mu} - (\nabla_\mu \xi^\nu) p_\nu \frac{\partial}{\partial p_\mu}, \quad (2.1.41)$$

loses all reference to momentum after a canonical projection onto the spacetime.

In contrast, there exist symmetries that have no simple expression in the spacetime when projected from the phase space into the configuration space. The conserved quantities from these symmetries contain larger powers of the momenta. These symmetries are only apparent in the phase space itself, i.e., when looking at the trajectories of relativistic particles on the spacetime and are hence referred to as *hidden symmetries*. They are generated by symmetric Killing tensors  $K$  of rank  $s \geq 2$ , that satisfy the Killing equation

$$\nabla_{(\mu_0} K_{\mu_1 \dots \mu_s)} = 0, \quad (2.1.42)$$

of which the corresponding conserved quantity is  $I = K^{\mu_1 \mu_2 \dots} p_{\mu_1} p_{\mu_2} \dots$ . In particular the metric itself,  $g_{\mu\nu}$ , is a Killing tensor of rank 2.

Let's consider the specific case when  $K_{\mu\nu}$  is a rank 2 Killing tensor and derive from that a conserved quantity of the motion of a charged scalar particle. Remarkably, we don't need to use the canonical momentum  $\pi^\mu = p^\mu + eA^\mu$ , rather the 4-momentum of the particle  $p^\mu = \mu u^\mu$  (for  $u^\mu$  the particle's 4-velocity) is sufficient,

$$K \equiv K_{\mu\nu} p^\mu p^\nu, \quad (2.1.43)$$

$$\begin{aligned} \frac{dK}{ds} &= \frac{1}{\mu} p^\mu p^\nu p^\rho \nabla_\rho K_{\mu\nu} + \frac{2}{\mu} K_{\mu\nu} p^\nu p^\rho \nabla_\rho p^\mu \\ &= -\frac{2e}{\mu} K_{\mu\nu} F^{\mu\rho} p_\rho p^\nu = -\frac{2e}{\mu} K_{\mu(\nu} F^{\mu}_{\rho)} p^\rho p^\nu, \end{aligned} \quad (2.1.44)$$

where to get to the third line we have used the equation of motion (2.1.29). This vanishes (and so  $K$  is conserved along particle motion) if the particle has no charge ( $e = 0$ ) or in the absence of

electromagnetic fields ( $F_{\mu\nu} = 0$ ), but also if the symmetry condition

$$K_{\mu(\nu}F^{\mu}_{\rho)} = 0 \quad (2.1.45)$$

is satisfied. We will find in Sec. 2.2.2 that this is indeed true in the spacetime of a charged, rotating black hole.

*Conformal* Killing tensors are similar to Killing tensors, but generate constants of the motion of null particles only. A rank- $s$  conformal Killing tensor satisfies the conformal Killing equation

$$\nabla_{(\mu_0}K_{\mu_1\cdots\mu_s)} = g_{(\mu_0\mu_1}\alpha_{\mu_2\cdots\mu_s)}, \quad (2.1.46)$$

for  $\alpha$  a symmetric tensor of rank  $s - 1$ . In the specific case  $s = 1$  these are conformal Killing vectors  $\xi_\mu$  satisfying

$$\nabla_{(\mu}\xi_{\nu)} = \alpha g_{\mu\nu}, \quad (2.1.47)$$

for  $\alpha$  a scalar function and it is straightforward to show that the quantity  $I = \xi^\mu \ell_\mu$  (with  $\ell_\mu$  the 4-momentum of the null particle) is indeed conserved along null geodesics.

To go further, we can consider more complicated functions of position and momentum  $f(x, p)$  and consider the question, “when are these quantities parallel transported along geodesics”? If a tensor  $K$  satisfies the *generalised* Killing equation

$$\nabla_{(\mu_0}K_{\mu_1\cdots\mu_r)\nu_1\cdots\nu_s} = 0, \quad (2.1.48)$$

then the rank- $s$  tensorial quantity,

$$f_{\mu_1\cdots\mu_s} \equiv K_{\nu_1\cdots\nu_r\mu_1\cdots\mu_s}p^{\nu_1}\cdots p^{\nu_r}, \quad (2.1.49)$$

is parallel transported along geodesics. In the specific case when  $r = 1$  and  $K$  is anti-symmetric, we call the tensor  $K$  a *Killing-Yano* form. In such a case, the rank- $s$  tensorial quantity,

$$f_{\mu_1\cdots\mu_s} = K_{\nu\mu_1\cdots\mu_s}p^\nu, \quad (2.1.50)$$

constructed from  $K$  is perpendicular to each of the  $p^{\nu_j}$  for all  $j$ ,

$$f_{\mu_1\cdots\mu_j\cdots\mu_s}p^{\mu_j} = 0. \quad (2.1.51)$$

Since Killing-Yano forms  $K$  are defined to be anti-symmetric, the covariant derivative  $\nabla K$  belongs to the space of tensors that are anti-symmetric in every index except the first. A subspace of this space of tensors is one in which  $\nabla K$  depends only on the divergence  $\nabla \cdot K$ . We call  $K$  a *closed, conformal Killing-Yano form* if  $\nabla K$  belongs to this particular subspace. The term “closed”

is used because this also implies that the exterior derivative  $dK$  vanishes and the term “conformal” is used because such a tensor behaves nicely under a conformal transformation of the metric. If one were to conformally scale the metric tensor to  $\tilde{g} = \Omega^2 g$ , and  $K$  is a conformal Killing-Yano form of rank  $s$  in  $g$  then  $\tilde{K} = \Omega^{s+1} K$  is a conformal Killing-Yano form in  $\tilde{g}$ . Such a form satisfies the closed, conformal Killing-Yano equation, which in four dimensions reads

$$\nabla_\rho h_{\mu\nu} = g_{\rho\mu} \chi_\nu - g_{\rho\nu} \chi_\mu, \quad \chi_\mu \equiv \frac{1}{3} \nabla_\nu h^\nu{}_\mu. \quad (2.1.52)$$

We are finally able to define the principal tensor  $h_{\mu\nu}$  as a *non-degenerate*, closed, conformal, Killing-Yano 2-form. Non-degenerate, in this context, means it has maximum rank when considered as a matrix and has the maximal number of independent eigenvalues.

If it is known that two Killing-Yano forms  $K_1$  and  $K_2$  (that may or may not be equal) of the same rank exist in a spacetime, then a Killing tensor  $K_{\mu\nu}$  can be constructed from them by taking the symmetrised product

$$K_{1\rho_2\dots\rho_s}^{(\mu} K_2^{\nu)\rho_2\dots\rho_s} = K^{\mu\nu}. \quad (2.1.53)$$

In particular, this can be used to construct a Killing tensor if the principal tensor is known, as the Hodge dual  $(*h)$  of a closed, conformal Killing-Yano form is a Killing-Yano form and so the above equation implies

$$K_{\mu\nu} \equiv (*h)_{\mu\rho} (*h)_\nu{}^\rho \quad (2.1.54)$$

is a Killing tensor. This tensor will be important in the next section when we discuss the conserved quantities of geodesic motion on the Kerr spacetime.

It perhaps isn't surprising that the existence of a principal tensor highly restricts the spacetime metric. In fact, the only family of spacetimes that admit such an object are the family of *off-shell* Kerr-NUT-(A)dS spacetimes [64].

## 2.2 Black Hole Solutions of the Einstein Field Equations

### 2.2.1 Finding the Solutions

We now want to work towards specifying the background metric  $g_{\mu\nu}$  on which our charged scalar and vector fields will propagate. As mentioned in Sec. 2.1.2, we treat these as test fields (i.e., they don't contribute to  $T_{\mu\nu}$  or  $J_\mu$  in Eqs. (2.1.15) and (2.1.16)) and so we require a solution to the electrovacuum equations

$$R_{\mu\nu} - \frac{1}{2} g_{\mu\nu} R = 8\pi T_{\mu\nu}^F, \quad (2.2.1)$$

$$\nabla_\nu F^{\mu\nu} = 0. \quad (2.2.2)$$

We give only a schematic overview, the details of the various methods to solving (2.2.1) and (2.2.2) can be found in [43, 109].

We will be considering black hole spacetimes that are either stationary and axisymmetric (those of rotating black holes) or static and spherically symmetric (those of non-rotating black holes). In addition, all of these spacetimes will be asymptotically flat. As the second set of spacetimes is a special case of the first, we will discuss only the first, weaker pair of assumptions. In a general coordinate system this is the assumed existence of two linearly independent Killing vectors [14]. These are the time-translation Killing vector  $\xi_t^\mu$ , which at infinity is timelike and normalised to  $\xi_t^\mu \xi_\mu^t = -1$  and the rotational Killing vector  $\xi_\phi^\mu$  which has closed integral curves of length  $2\pi$ . Both of these satisfy Killing's equation (2.1.38). These Killing vectors will be used to construct conserved quantities of geodesic motion and will be important when discussing circular geodesic orbits in Sec. 2.3.

We can choose a coordinate system such that these Killing vectors take on a simple form,  $\xi_t^\mu = \partial_t^\mu \equiv [1, 0, 0, 0]$  and  $\xi_\phi^\mu = \partial_\phi^\mu \equiv [0, 0, 0, 1]$ . These coordinates  $(t, r, \theta, \phi)$  are the *Boyer-Lindquist* coordinates. Taking these simple forms for the Killing vectors is equivalent to the condition that all the metric functions  $g_{tr}, g_{r\phi}$  etc... are independent of  $t$  and  $\phi$ . If we also include the condition that the spacetime is invariant under the simultaneous inversion  $t \rightarrow -t$  and  $\phi \rightarrow -\phi$  this requires  $g_{tr} = g_{t\theta} = g_{\phi r} = g_{\phi\theta} = 0$ . As such, what remains is a metric of the form

$$ds^2 = g_{tt}dt^2 + 2g_{t\phi}dtd\phi + g_{\phi\phi}d\phi^2 + [g_{rr}dr^2 + 2g_{r\theta}drd\theta + g_{\theta\theta}d\theta^2]. \quad (2.2.3)$$

The term in the square brackets is the metric of a two dimensional space  $(r, \theta)$  with positive definite signature  $(+, +)$  and so there exists a co-ordinate transformation [43] that reduces it to the form  $e^{2\kappa_1}dr^2 + e^{2\kappa_2}d\theta^2$  where  $\kappa_1$  and  $\kappa_2$  are functions of  $r$  and  $\theta$  only. Hence there are five metric components to find. Full derivations of the form of these five functions can be found in [43] and [109], leading to the *Kerr-Newman* metric,

$$ds^2 = - \left( 1 - \frac{2Mr - Q^2}{\Sigma} \right) dt^2 - \frac{(2Mr - Q^2) 2a \sin^2 \theta}{\Sigma} dtd\phi + \frac{\Sigma}{\Delta} dr^2 + \Sigma d\theta^2 + \frac{h \sin^2 \theta}{\Sigma} d\phi^2, \quad (2.2.4)$$

where

$$\Delta = r^2 - 2Mr + a^2 + Q^2, \quad (2.2.5)$$

$$\Sigma = r^2 + a^2 \cos^2 \theta, \quad (2.2.6)$$

$$h = (r^2 + a^2)^2 - \Delta a^2 \sin^2 \theta \quad (2.2.7)$$

and the corresponding vector potential that satisfies both the Lorenz gauge condition (2.1.23) and

the vacuum field equation (2.2.2) is [63]

$$A^\mu = \frac{Qr}{\Sigma\Delta} [r^2 + a^2, 0, 0, a]. \quad (2.2.8)$$

This is the metric of the spacetime of a charged and rotating black hole. Each of the three constants introduced takes on a physical meaning:  $M$  is the mass of the black hole,  $Q$  is its charge and  $a$  is its angular momentum per unit mass,  $a = J/M$ . Remarkably, these are the only three pieces of information needed to completely specify the metric. In addition, under certain sensible regularity conditions (see theorems 3.2 and 3.3 of [47]), the Kerr-Newman solution is the only stationary, axisymmetric, asymptotically flat solution of the electrovacuum equations with a connected event horizon (event horizons will be discussed in the next subsection). Results of this kind have been known for decades [125] but more recent treatments are given in [47] and [103].

From (2.2.4), various specific cases can be considered. Setting the charge  $Q = 0$  gives the *Kerr* metric of a rotating, uncharged black hole,

$$ds^2 = - \left( 1 - \frac{2Mr}{\Sigma} \right) dt^2 - \frac{4aMr \sin^2 \theta}{\Sigma} dt d\phi + \frac{\Sigma}{\Delta} dr^2 + \Sigma d\theta^2 + \frac{h \sin^2 \theta}{\Sigma} d\phi^2, \quad (2.2.9)$$

(where  $Q$  is set to zero in the definitions of  $\Delta$  and  $h$ ). Setting only  $a = 0$  produces the *Reissner-Nordström* metric of a charged but static black hole,

$$ds^2 = -f_{rn}(r) dt^2 + \frac{dr^2}{f_{rn}(r)} + r^2 (d\theta^2 + \sin^2 \theta d\phi^2), \quad (2.2.10)$$

where we have defined  $f_{rn}(r) = 1 - 2M/r + Q^2/r^2$ . This spacetime is spherically symmetric and has the electromagnetic vector potential,

$$A^\mu = \left[ \frac{Q}{r f_{rn}}, 0, 0, 0 \right]. \quad (2.2.11)$$

Finally, setting both  $a = 0$  and  $Q = 0$  gives the *Schwarzschild* metric of an uncharged, static black hole,

$$ds^2 = -f_{sch}(r) dt^2 + \frac{dr^2}{f_{sch}(r)} + r^2 (d\theta^2 + \sin^2 \theta d\phi^2), \quad (2.2.12)$$

where  $f_{sch}(r) = 1 - 2M/r$ . The Schwarzschild spacetime is, according to Birkhoff's theorem [67], the only spherically symmetric, asymptotically flat solution of the Einstein vacuum field equation (Eq. (2.2.1) with the right hand side equal to zero).

Due to the spherical symmetry, the Reissner-Nordström and Schwarzschild metrics possess additional Killing vectors compared to the Kerr and Kerr-Newman metrics. These vectors are [37]

$$\xi_1^\mu = -\sin \phi \partial_\theta^\mu - \cot \theta \cos \phi \partial_\phi^\mu, \quad (2.2.13)$$

$$\xi_2^\mu = \cos \phi \partial_\theta^\mu - \cot \theta \sin \phi \partial_\phi^\mu, \quad (2.2.14)$$

such that, if we define  $\partial_\phi^\mu = \xi_3^\mu$ , then these three vectors satisfy the commutation relations  $[\xi_i^\mu, \xi_j^\mu] = -\epsilon_{ijk}\xi_k^\mu$ , where  $\epsilon_{ijk}$  is the three dimensional Levi-Civita symbol.

### 2.2.2 The Kinnersley Tetrad and the Principal Tensor

Any Lorentzian spacetime metric can be written in terms of a *null tetrad* and the Kerr-Newman metric is no exception [43]. A null tetrad is a set of four vectors  $\{\ell^\mu, n^\mu, m^\mu, \bar{m}^\mu\}$  (where  $\bar{m}^\mu$  is the complex conjugate of  $m^\mu$ ) with Lorentzian inner products given by

$$-\ell^\mu n_\mu = m^\mu \bar{m}_\mu = 1 \quad (2.2.15)$$

and all other products equal to zero. The inverse metric can be decomposed in terms of these vectors

$$g^{\mu\nu} = -2 \left( \ell^{(\mu} n^{\nu)} - m^{(\mu} \bar{m}^{\nu)} \right). \quad (2.2.16)$$

A natural choice for the four vectors is the *Kinnersley tetrad* given by

$$\begin{aligned} \ell^\mu &= \frac{1}{\Delta} [r^2 + a^2, \Delta, 0, a], \\ n^\mu &= \frac{1}{2\Sigma} [r^2 + a^2, -\Delta, 0, a], \\ m^\mu &= \frac{1}{\sqrt{2}(r + ia \cos \theta)} [ia \sin \theta, 0, 1, i \csc \theta]. \end{aligned} \quad (2.2.17)$$

The Kinnersley tetrad has the property that the vectors  $\ell^\mu$  and  $n^\mu$  are aligned with the *principal null vectors* of the spacetime. Such vectors are tangent to shear-free, null *geodesic congruences* (see for example [37] or [118]). The introduction of this null tetrad will be important when we come to discuss electromagnetic perturbations of rotating black hole spacetimes in chapter 4.

We now want to take the ideas of Killing and principal tensors developed in Sec. 2.1.6 and apply them specifically to the Kerr-Newman spacetime, as in [64]. In the Kinnersley tetrad, the principal tensor  $h_{\mu\nu}$  and the Killing tensor  $K_{\mu\nu}$  constructed from it according to (2.1.54) read

$$h_{\mu\nu} = 2r\ell_{[\mu}n_{\nu]} + (2ia \cos \theta) m_{[\mu}\bar{m}_{\nu]}, \quad (2.2.18)$$

$$K_{\mu\nu} = (2a^2 \cos^2 \theta) \ell_{(\mu}n_{\nu)} + 2r^2 m_{(\mu}\bar{m}_{\nu)} \quad (2.2.19)$$

and it can be shown that this  $h_{\mu\nu}$  satisfies the closed, conformal Killing-Yano equation (2.1.52). The Lorenz gauge vector potential (2.2.8) is

$$A^\mu = Qr \left( \frac{1}{2\Sigma} \ell^\mu + \frac{1}{\Delta} n^\mu \right) \quad (2.2.20)$$

and so the Faraday tensor  $F^{\mu\nu} = 2\nabla^{[\mu}A^{\nu]}$  is

$$F^{\mu\nu} = \frac{Q}{\Sigma^2} \left( -2(r^2 - a^2 \cos^2 \theta) \ell^{[\mu}n^{\nu]} + (4iar \cos \theta) m^{[\mu}\bar{m}^{\nu]} \right). \quad (2.2.21)$$

From this it can be shown that in the Kerr-Newman spacetime the symmetry condition (2.1.45) is satisfied via the vanishing inner products of the Kinnersley tetrad (2.2.15).

### 2.2.3 The Existence and Nature of Horizons

Here we summarise some properties of black hole spacetimes by discussing their Killing vectors, as well as the existence and nature of various important surfaces. All the black holes we study will be stationary and axisymmetric and so the metrics will possess the Killing vectors  $\xi_t^\mu = \partial_t^\mu$  and  $\xi_\phi^\mu = \partial_\phi^\mu$ .

There are three types of important surfaces we will discuss. An *event horizon* as defined by [37] is...

"...a 3D hypersurface in a 4D spacetime that separates those events that are connected to infinity by a timelike path from those that are not."

The cosmic censorship hypothesis [115] asserts that any realistic spacetime has any curvature singularities shrouded behind an event horizon.

A *stationary limit surface* is a hypersurface on which the time translation Killing vector  $\xi_t^\mu$  becomes null,  $g_{\mu\nu}\xi_t^\mu\xi_t^\nu = 0$ . This surface can be found by considering where the  $g_{tt}$  component of the metric vanishes. Immediately behind the stationary limit surface,  $\xi_t^\mu$  becomes spacelike.

Finally, a Killing vector field  $\xi^\mu$  can have a *Killing horizon*, which is a null hypersurface on which  $\xi^\mu$  becomes null. Note that a stationary limit surface is not necessarily a Killing horizon as that hypersurface is not necessarily null. As  $\xi^\mu$  is null everywhere on this surface it must also be normal to this surface (see [37, 118]) and so it satisfies the *null geodesic equation*,

$$\xi^\mu \nabla_\mu \xi^\nu = -\kappa \xi^\nu, \quad (2.2.22)$$

where  $\kappa$  is a constant called the *surface gravity* of the Killing horizon.

#### 2.2.3.1 Static, Spherically Symmetric Black Holes

In static spacetimes (such as the Schwarzschild and Reissner-Nordström spacetimes) each of these three surfaces coincide with one another [37], that is, the event horizon is both a stationary limit surface and a Killing horizon for the Killing vector  $\xi_t^\mu$  and we simply refer to this single surface as the event horizon. It is clear from the line elements (2.2.10) and (2.2.12) that the stationary limit surface where  $g_{tt} = 0$  is defined by  $f_{sch}(r) = 0$  or  $f_{rn}(r) = 0$ . Immediately behind this surface  $\xi_t^\mu$  will be spacelike. For the Schwarzschild spacetime this occurs only at  $r = 2M$ , but for the Reissner-Nordström spacetime this occurs at two radii,  $r_\pm = M \pm \sqrt{M^2 - Q^2}$ . The outer surface  $r = r_+$  is the event horizon, while  $r = r_-$  is referred to as the *Cauchy horizon*, beyond which  $\xi_t^\mu$  flips back to being a timelike vector. The locations of these horizons motivates the definition of the *extremal limit*  $Q \rightarrow M$ , in which these two horizons merge into one at  $r = M$ .

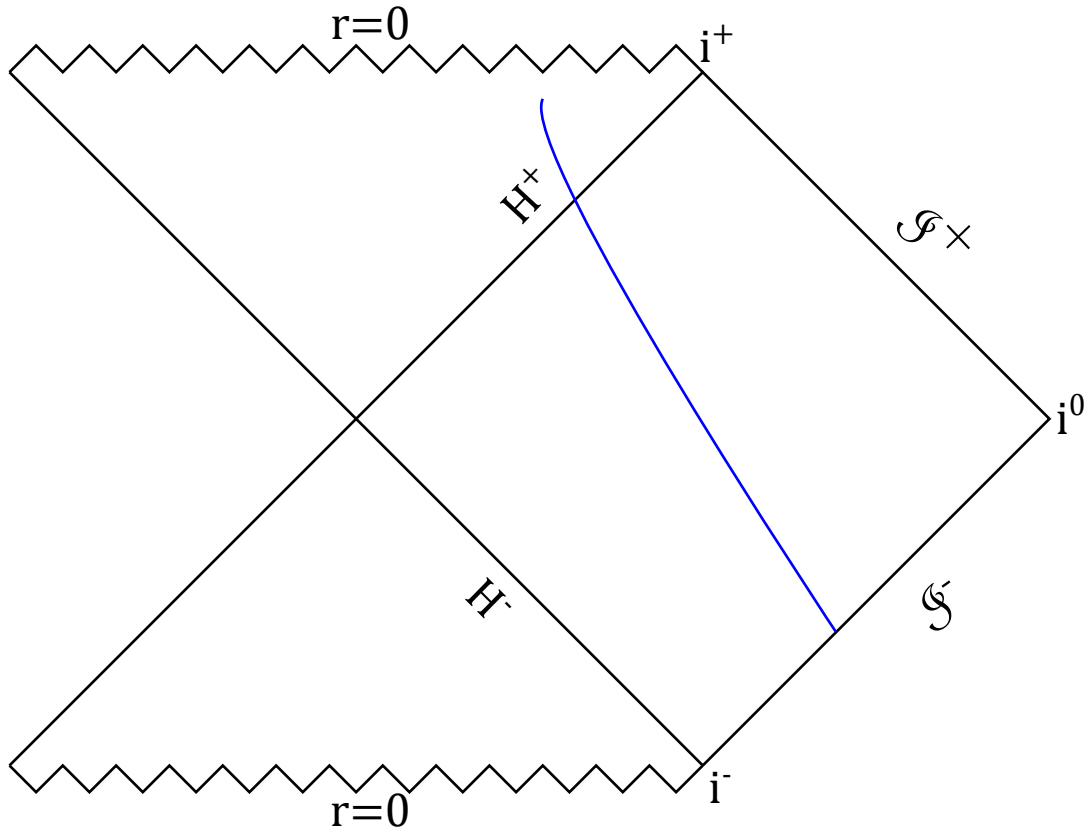


Figure 2.2.1: The Penrose-Carter diagram of the Schwarzschild spacetime.  $H^\pm$  indicates the past (-) and future (+) event horizons, while  $\mathcal{S}^\pm$  indicates past and future null infinity.  $i^\pm$  and  $i^0$  are the timelike and spacelike infinities. The past and future singularities at  $r = 0$  are indicated by zig-zag lines. The blue curve is a timelike trajectory that crosses the future event horizon and is doomed to hit the singularity.

In the Schwarzschild spacetime any timelike trajectory that crosses the event horizon is doomed to reach the spacelike curvature singularity at  $r = 0$  in a finite proper time, as shown in Fig. 2.2.1

The situation is different in the Reissner-Nordström spacetime. The event horizon at  $r = r_+$  still has the property that matter and information cannot return from the event horizon to the same asymptotically flat region of spacetime from which it entered. However, it is no longer true that timelike trajectories that pass through it are guaranteed to hit the, now timelike, curvature singularity. This is a by-product of the existence of the Cauchy horizon, past which the time-translation Killing vector  $\xi_t^\mu$  flips from being spacelike back to being timelike. There are, as Chandrasekhar puts it [43],

“...an infinite range of rich possibilities of experience, that are denied to one who crosses

the event horizon in the Schwarzschild geometry.”

Among these possibilities is for a trajectory to reach a new asymptotically flat region of the spacetime, distinct from the one from which it entered the event horizon, as shown in Fig. 2.2.2.

### 2.2.3.2 Stationary, Axisymmetric Black Holes

In stationary (but not static) spacetimes, it is no longer true that the stationary limit surface and the event horizon coincide, though the event horizon will still be a Killing horizon for some Killing vector  $\xi^\mu$ . In particular, there exists a constant  $\Omega_H$  such that the Killing vector, [37]

$$\xi^\mu = \partial_t^\mu + \Omega_H \partial_\phi^\mu, \quad (2.2.23)$$

is null on the event horizon. This constant is then called the *angular velocity* of the event horizon.

A coordinate singularity of the Kerr-Newman spacetime (2.2.4) in the Boyer-Lindquist coordinate system occurs whenever  $\Delta = 0$  (2.2.5), which is at the two radii  $r_\pm = M \pm \sqrt{M^2 - a^2 - Q^2}$ . It can be shown by considering the metric induced on the 3-surfaces of constant  $r$  (see for example, [143]) that null curves on these surfaces for  $r \leq r_+$  cannot escape to infinity, and so  $r = r_+$  is the event horizon. In analogy with the Reissner-Nordström spacetime, the surface  $r = r_-$  is called the Cauchy horizon. For  $Q = 0$  (Kerr spacetime), the merging of these two horizons (the extremal limit) occurs as  $a \rightarrow M$ . Otherwise, for a fixed  $a$ , this occurs when  $Q \rightarrow Q_{max}$ , where  $Q_{max} = \sqrt{M^2 - a^2}$ .

There are two radii that satisfy the condition of a stationary limit surface  $g_{tt} = 0$  given by  $r_{S\pm} = M \pm \sqrt{M^2 - a^2 \cos^2 \theta - Q^2}$ . The outer surface  $r_{S+}$  is what we will concern ourselves with, as  $r_{S-}$  lies within the event horizon. For a fixed  $t$ ,  $r = r_{S+}$  is a surface that meets the event horizon only at the poles  $\theta = 0$  and  $\theta = \pi$ , see Fig. 2.2.3. The region that lies in between  $r_+$  and  $r_{S+}$  is called the *ergoregion* [63] and will be especially important when we come to discuss superradiance in these spacetimes.

## 2.3 Geodesic Orbits

The timelike and null geodesic equations (2.1.30) and (2.2.22) arose when discussing the motion of uncharged particles and Killing horizons respectively. Here we discuss geodesics in more detail, in particular the circular geodesic orbits. These orbits have a connection to the quasinormal mode frequencies of perturbing fields in the eikonal limit, which will be explored in the coming chapters. The primary reference for this section is [63].

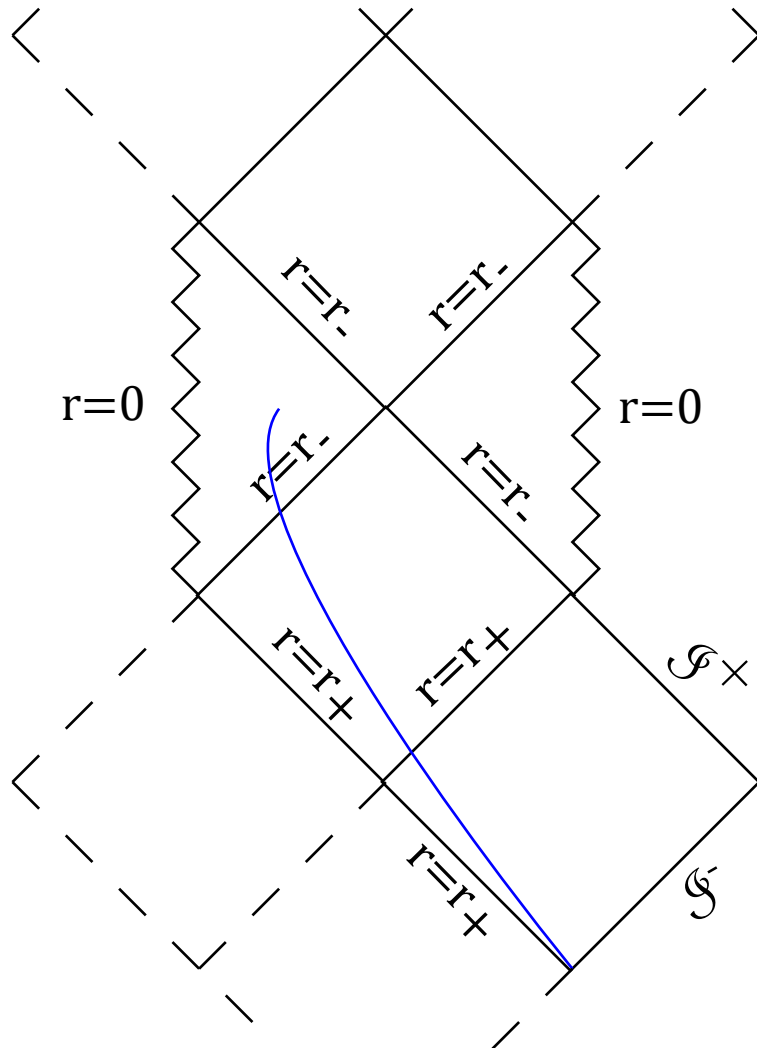


Figure 2.2.2: The Penrose-Carter diagram of the Reissner-Nordström spacetime, with the same conventions as Fig. 2.2.1 . The blue curve is a timelike trajectory that crosses both the outer and inner horizons, but does not hit the timelike singularity. The dashed lines indicate the diagram repeats indefinitely into the past and future.

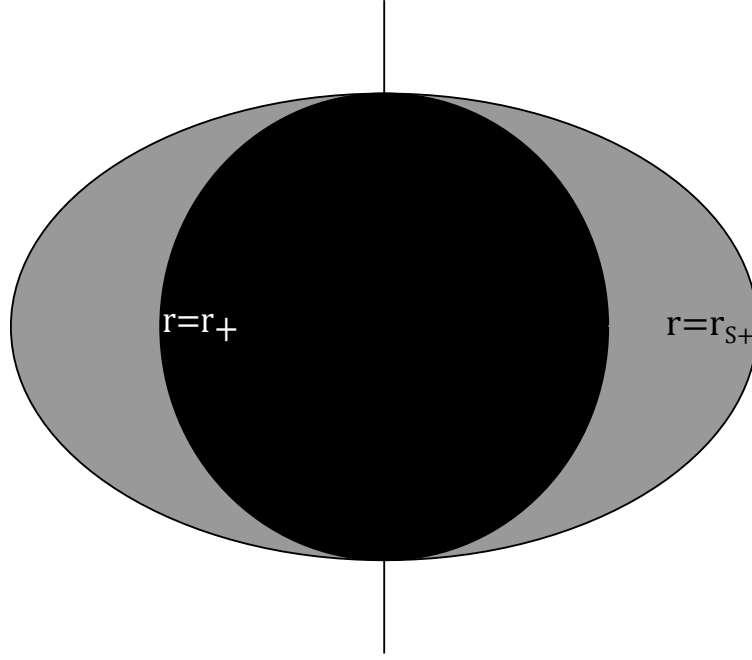


Figure 2.2.3: A Kerr or Kerr-Newman black hole. The event horizon and outer stationary limit surfaces are labeled. The black region is inside the event horizon, the grey region is the ergoregion.

### 2.3.1 Conserved Quantities and Equations of Motion on Kerr-Newman

The derivation of the equations of motion of a charged test particle in Boyer-Lindquist coordinates on the Kerr-Newman spacetime are summarised in [63]. Instrumental in the description of the trajectories of these particles are the conserved quantities of their motion. These quantities will come from the Killing vectors  $\xi_t^\mu$  and  $\xi_\phi^\mu$  as well as the Killing tensor  $K_{\mu\nu}$ .

The conserved quantities associated with the Killing vectors are  $I = \xi_t^\mu \pi_\mu$ . These are the energy and the axial component of the angular momentum of the particle [63],

$$E = -\xi_t^\mu \pi_\mu, \quad L_z = \xi_\phi^\mu \pi_\mu. \quad (2.3.1)$$

(We will omit the  $z$  subscript from  $L_z$  in subsequent equations).

The Killing tensor of the Kerr-Newman black hole (2.2.19) in Boyer-Lindquist coordinates is [63]

$$K_{\mu\nu} dx^\mu dx^\nu = a^2 \left[ 1 - \frac{(2Mr - Q^2) \cos^2 \theta}{\Sigma} \right] dt^2 + \frac{\sin^2 \theta}{\Sigma} \left[ \frac{1}{4} \Delta a^4 \sin^2 2\theta + r^2 (r^2 + a^2) \right] d\phi^2 \quad (2.3.2)$$

$$- \frac{a \sin^2 \theta}{\Sigma} [\Delta a^2 \cos^2 \theta + r^2 (r^2 + a^2)] dt d\phi - \frac{a^2 \cos^2 \theta}{\Delta} dr^2 + r^2 \Sigma d\theta^2,$$

from which another conserved quantity  $K = K_{\mu\nu} p^\mu p^\nu$  (Eqs. (2.1.43) and (2.1.44)) can be constructed

$$K = \left( Ea \sin \theta - \frac{L}{\sin \theta} \right)^2 + (p_\theta)^2 + \mu^2 a^2 \cos^2 \theta. \quad (2.3.3)$$

More commonly, one instead works with the *Carter constant*  $C$ , defined as  $C = K - (Ea - L)^2$ . Recall that the motion of a particle of mass  $\mu$  and charge  $e$  is governed by the equation (2.1.29)

$$\mu u^\nu \nabla_\nu u_\mu = e F_{\mu\nu} u^\nu, \quad (2.3.4)$$

where the 4-velocity  $u^\mu$  can now be written in terms of the conserved quantities  $E, L$  and  $C$ . With respect to the affine parameter  $s = \tau/\mu$  the equations of motion for each of the components of  $u^\mu$  are [63]

$$\Sigma \frac{dr}{ds} = \pm \left\{ [E(r^2 + a^2) - La - eQr]^2 - \Delta [\mu^2 r^2 + (L - aE)^2 + C] \right\}^{1/2}, \quad (2.3.5)$$

$$\Sigma \frac{d\theta}{ds} = \pm \left\{ C - \cos^2 \theta \left[ a^2 (\mu^2 - E^2) + \frac{L^2}{\sin^2 \theta} \right] \right\}^{1/2}, \quad (2.3.6)$$

$$\Sigma \frac{d\phi}{ds} = - \left( aE - \frac{L}{\sin^2 \theta} \right) + \frac{a}{\Delta} [E(r^2 + a^2) - La - eQr], \quad (2.3.7)$$

$$\Sigma \frac{dt}{ds} = -a(aE \sin^2 \theta - L) + \frac{(r^2 + a^2)}{\Delta} [E(r^2 + a^2) - La - eQr]. \quad (2.3.8)$$

These are the most general equations of motion we will consider. We will now find the circular geodesic orbits in various special cases by setting various parameters to zero in these equations.

## 2.3.2 Geodesic Orbits

### 2.3.2.1 Geodesic Effective Potential

All of the above expressions can be simplified to their Kerr counterparts simply by setting the black hole charge  $Q$  to zero. The quantity in the square-root on the right-hand-side of the radial differential equation (2.3.5) will be called  $\mathcal{R}$ . As a polynomial in  $r$  it is (where  $\dot{r} = dr/ds$ ) [63]

$$\begin{aligned} (\Sigma \dot{r})^2 = \mathcal{R} &= (E^2 - \mu^2) r^4 + 2M\mu^2 r^3 + [(E^2 - \mu^2) a^2 - L^2 - C] r^2 \\ &\quad + 2M [C + (Ea - L)^2] r - a^2 C. \end{aligned} \quad (2.3.9)$$

A bound orbit can only occur if  $\dot{r}$  cannot remain positive for arbitrarily large  $r$ . In the large  $r$  limit the  $r^4$  term clearly dominates and this will be negative for  $E^2 < \mu^2$ , hence this condition on the energy is *sufficient* for a bound orbit to exist (As we shall see later however, this condition is not *necessary*. There also exist *unstable* bound orbits for which  $E^2 > \mu^2$ ). A necessary condition for circular orbits is  $\mathcal{R} = 0$  and such a condition can be written as a quadratic in the energy

$$\mathcal{R} = \alpha E^2 - 2\beta E + \gamma = 0, \quad (2.3.10)$$

where

$$\alpha = r^4 + a^2 (r^2 + 2Mr),$$

$$\beta = 2aMLr,$$

$$\gamma = L^2 a^2 - (\mu^2 r^2 + L^2 + C) \Delta.$$

Thus, we can write the condition  $\mathcal{R} = 0$  in terms of an effective potential function  $V_{\pm}(r)$ ,

$$\dot{r}^2 = (E - V_+)(E - V_-), \quad (2.3.11)$$

$$V_{\pm}(r) = \frac{\beta \pm \sqrt{\beta^2 - \alpha\gamma}}{\alpha}. \quad (2.3.12)$$

Worth noting here is the  $a \rightarrow 0$  limit of this equation, where the effective potential reduces to what we will call  $V_g$ ,

$$\dot{r}^2 = E^2 - V_g(r), \quad (2.3.13)$$

$$V_g(r) = f \left( \mu^2 + \frac{L^2}{r^2} \right), \quad (2.3.14)$$

where  $f = f_{sch}$  defined in Sec. 2.2.1. Had we instead set  $a = 0$  but kept  $Q \neq 0$  we would arrive at the same geodesic potential except with  $f = f_{rn}$ .

### 2.3.2.2 Stable and Unstable Orbits, Photon Orbits and the ISCO

Using Kerr black holes as an example, we will now describe the various different kinds of circular geodesic orbits that can arise in a given spacetime. Each of these types of orbits have their own importance in relation to the quasinormal modes and quasibound states of perturbing fields, to be described in Sec. 3.2.

Although the Kerr spacetime is not spherically symmetric, we can still restrict our attention to the equatorial plane  $\theta = \pi/2$  without loss of generality, as all circular geodesic orbits (i.e., orbits of constant  $r$  and  $\theta$ ) will exist in this plane. This can be shown by looking at the  $\theta$  equation of motion (2.3.6). The quantity inside the square-root must be non-negative, hence if  $E^2 < \mu^2$  then  $C \geq 0$ . For  $\theta$  to be constant we need  $C = 0$ , which happens only for  $\theta = \pi/2$ .

Expressions for the energy and angular momentum of a particle on a circular orbit of radius  $r_c$  are then found from the condition  $\mathcal{R}(r_c) = \mathcal{R}'(r_c) = 0$  which gives

$$E/\mu = \frac{r_c^2 - 2Mr_c \pm a\sqrt{Mr_c}}{r_c (r_c^2 - 3Mr_c \pm 2a\sqrt{Mr_c})^{1/2}}, \quad (2.3.15)$$

$$L/\mu = \pm \frac{\sqrt{Mr_c} (r_c^2 \mp 2a\sqrt{Mr_c} + a^2)}{r_c (r_c^2 - 3Mr_c \pm 2a\sqrt{Mr_c})^{1/2}}, \quad (2.3.16)$$

where the upper and lower signs correspond to orbits moving with the black hole rotation or against the black hole rotation respectively. The denominator of these expressions is key to finding the radii of the circular orbits. To ensure  $E$  and  $L$  are real we must impose the inequality

$$r_c^2 - 3Mr_c \pm 2a\sqrt{Mr_c} \geq 0. \quad (2.3.17)$$

In the variable  $k = \sqrt{r}$ , this can be written (after pulling out a factor of  $k$ ) as a cubic in  $k$ , which has a standard solution in terms of trigonometric functions. Converting back to  $r$ , the smallest (i.e., innermost) solution for the circular orbit radius we will label  $r_p$  and this is attained only in the limit of massless particles  $\mu \rightarrow 0$ . It is given by

$$r_p = 2M \left\{ 1 + \cos \left[ \frac{2}{3} \arccos \left( \mp \frac{a}{M} \right) \right] \right\}. \quad (2.3.18)$$

We call such an orbit a *photon orbit*. For  $a = 0$  (i.e., the Schwarzschild limit) the co-rotating and counter-rotating photon orbits combine into a single unstable photon orbit at  $r_p = 3M$ . In the extremal limit  $a \rightarrow M$  the photon orbit either shrinks to  $r_p = M$  (co-rotating orbit) or grows to  $r_p = 4M$  (counter-rotating orbit).

We can determine whether or not a circular orbit is *stable* by considering the second derivative  $\mathcal{R}'' = V_{\pm}''$  at the circular orbit radius  $r_c$ . If  $V_{\pm}'' > 0$  then the potential function has a minimum at that radius and the circular orbit is *stable*. If  $V_{\pm}'' < 0$  then the potential function has a maximum at that radius and the circular orbit is *unstable*. The photon orbits found above are unstable.

Another important (unstable) circular orbit occurs when  $E = \mu$ , in which case the expression for the energy of a circular orbit (2.3.15) produces the radius

$$r_b = 2M \mp a + 2\sqrt{M(M \mp a)}. \quad (2.3.19)$$

This is the minimum radius a particle incoming on a parabolic trajectory can achieve.

As the sign of the second derivative  $\mathcal{R}'' = V_{\pm}''$  determines the stable/unstable nature of an orbit, it is worth considering the case  $\mathcal{R}(r_I) = \mathcal{R}'(r_I) = \mathcal{R}''(r_I) = 0$ . The orbit with radius  $r_I$  that satisfies this is called the *Innermost Stable Circular Orbit* (ISCO). The three simultaneous equations this gives have to be solved for  $E, L$  and the ISCO radius  $r_I$ . The result is presented in [63] as

$$\begin{aligned} r_I &= M \left\{ 3 + Z_2 \mp [(3 - Z_1)(3 + Z_1 + 2Z_2)]^{1/2} \right\}, \\ Z_1 &= 1 + \left( 1 - \frac{a^2}{M^2} \right)^{1/3} \left[ \left( 1 + \frac{a}{M} \right)^{1/3} + \left( 1 - \frac{a}{M} \right)^{1/3} \right], \\ Z_2 &= \left( \frac{3a^2}{M^2} + Z_1^2 \right)^{1/2}, \end{aligned} \quad (2.3.20)$$

where once again the upper sign is for co-rotating orbits and the lower sign is for counter-rotating. In the Schwarzschild limit  $a \rightarrow 0$  this becomes the Schwarzschild ISCO of  $r_I = 6M$  and in the extremal limit  $a \rightarrow M$  the orbit either shrinks to  $r_I = M$  in the co-rotating case (identically to the photon orbit) or grows to  $r_I = 9M$  in the counter-rotating case.

We can perform a similar analysis in the Reissner-Nordström spacetime starting from the radial equations (2.3.13) and (2.3.14) when  $f = f_{rn}$ . The equation to solve for  $r_c$  coming from  $V'_g = 0$  is now a cubic in  $r_c^{-1}$  [43]

$$-Q^2 r_c^{-3} + \frac{3}{2} M r_c^{-2} - \frac{1}{2} \left( 1 + \frac{Q^2 \mu^2}{L^2} \right) r_c^{-1} + \frac{M \mu^2}{2L^2} = 0. \quad (2.3.21)$$

We can extract information about the unstable photon orbit at radius  $r_p$  by setting  $\mu = 0$  and reducing the above equation to a quadratic with the solutions

$$r_p^{-1} = \frac{3M}{4Q^2} \left( 1 \pm \sqrt{1 - \frac{8Q^2}{9M^2}} \right) \Rightarrow r_p = \frac{3}{2} M \left( 1 \mp \sqrt{1 - \frac{8Q^2}{9M^2}} \right). \quad (2.3.22)$$

The lower sign is the one to choose, as this corresponds to a radius that is outside the event horizon. This is the unstable photon orbit in the Reissner-Nordström spacetime and the expression reduces to the Schwarzschild result of  $r_p = 3M$  when  $Q = 0$ .

For the ISCO, we must impose  $V'_g = 0$  and  $V''_g = 0$ . We can use this extra condition to eliminate  $L^2$  from Eq. (2.3.21) which reduces it to another cubic equation for the ISCO radius

$$4Q^4 r_I^{-3} - 9Q^2 M r_I^{-2} + 6M^2 r_I^{-1} - M = 0, \quad (2.3.23)$$

which allows the solution  $r_I = 6M$  when  $Q = 0$  (consistent with the  $a \rightarrow 0$  limit of Kerr) and  $r_I = 4M$  in the extremal limit  $Q = M$ . For general  $Q \neq 0$  this equation has only one real root which we will write as

$$\begin{aligned} r_I &= 2M + (4M^2 - 3Q^2) Z_1^{-1} + Z_1, \\ Z_1 &= (8M^3 - 9MQ^2 + 2Q^4/M + Z_2)^{1/3}, \\ Z_2 &= Q^2 (5M^4 - 9M^2Q^2 + 4Q^4)^{1/2}. \end{aligned} \quad (2.3.24)$$

Finally, we deal with the Schwarzschild spacetime  $f = f_{sch}$ . Setting  $Q = 0$  in Eq. (2.3.21) gives

$$3L^2 M r_c^{-2} - L^2 r_c^{-1} + M \mu^2 = 0, \quad (2.3.25)$$

and by checking the discriminant, we see that a circular orbit can only occur if  $L/M\mu \geq 2\sqrt{3}$ . For  $L/M\mu > 2\sqrt{3}$  there are two such orbits located at

$$r_c^{-1} = \frac{L \pm \sqrt{L^2 - 12M^2\mu^2}}{6LM}. \quad (2.3.26)$$

In particular, when  $L/M\mu$  approaches  $2\sqrt{3}$  from above, the two orbits coalesce into a single circular orbit at the ISCO radius  $r_I = 6M$ . We can consider the situation of a massless particle  $\mu = 0$  by allowing  $L/M\mu \rightarrow \infty$  which reproduces the photon orbit at  $r_p = 3M$ .

### 2.3.3 Relation to Energy Extraction

In the equatorial plane the radial differential equation in the Kerr-Newman spacetime (2.3.5) can be re-cast into the form [63]

$$r^3 \left( \frac{dr}{ds} \right)^2 = E^2 (r^3 + a^2 r + 2Ma^2) - 4aMEL - (r - 2M)L^2 - \mu^2 r \Delta, \quad (2.3.27)$$

which can then be solved for the energy  $E$

$$E = \frac{2aML \pm \left[ L^2 r^2 \Delta + (r^3 + a^2 r + 2Ma^2) \left( \mu^2 r \Delta + r^3 (dr/ds)^2 \right) \right]^{1/2}}{r^3 + a^2 r + 2Ma^2}. \quad (2.3.28)$$

The sign in front of the square-root can be determined by the condition that the particle 4-momentum be future directed, i.e., that  $dt/ds > 0$ . This can only occur for  $E > 2aML / (r^3 + a^2 r + 2Ma^2)$  which clearly requires us to take the positive root.

This expression for energy can clearly become negative under many physically relevant circumstances. A simple example is taking  $L < 0$  and setting  $\mu = 0$  (motion at the speed of light) and  $dr/ds = 0$  (motion in the azimuthal direction). The energy then becomes negative if  $2aM < r\sqrt{\Delta}$  which occurs exactly when  $r < r_{S+}$ , i.e., the particle is inside the ergoregion.

This conclusion is not exclusive to any of the conditions we have imposed, or indeed to motion in the equatorial plane. The possibility for the energy to be negative follows from the definition  $E = -p_\mu \xi_t^\mu$  and the fact that  $\xi_t^\mu$  is spacelike inside the ergoregion. Indeed, [63] explains that given a spacelike  $\xi_t^\mu$ , there will always exist some timelike or null  $p^\mu$  such that  $E < 0$ .

A particle having negative energy opens up the possibility of rotational energy being extracted from the black hole via a *Penrose process* [116]. Suppose a particle with energy  $E$  falls into the ergoregion of a black hole and breaks apart into two particles of energy  $E_- < 0$  and  $E_+ > E$ . The particle of energy  $E_-$  can fall into the black hole (thus reducing the black hole's energy) while the particle of energy  $E_+$  can escape to infinity and so this particle is the vehicle by which energy is extracted. The wave analogue of a Penrose process is called *superradiance* and will be discussed in the context of Reissner-Nordström black holes in Sec. 3.1 and for rotating black holes in chapter 4.

## 2.4 Solving Recurrence Relations

To find the quasinormal modes and quasibound states of the scalar and vector fields (to be defined in the following chapter) we will be employing Leaver's continued fraction method [96], in which a particular ansatz is used to transform the problem into solving a *recurrence relation*. The exact details of the ansatz used will be relegated to later (see Secs. 3.2.2, 3.2.3 and 4.2.4), as it depends not only on the equation but also the background spacetime. Here we will discuss general aspects of solving three-term recurrence relations.

### 2.4.1 Gaussian Elimination

The first step to solving a recurrence relation via Leaver's continued fraction method is to reduce the relation to a three-term one, if it has more than three terms. We can do this via Gaussian elimination. This is presented in [96] for the case of a four-term relation, like the one we use in Sec. 3.4, and we will apply the process twice to the five-term relation we find in Sec. 4.2.4. This two-step Gaussian elimination is also performed in [35], where the author arrived at a five-term recurrence relation in the context of more exotic spacetimes involving black branes and strings.

A general five-term recurrence relation of the form

$$\begin{aligned}
 \alpha_0 a_1 + \beta_0 a_0 &= 0, \\
 \alpha_1 a_2 + \beta_1 a_1 + \gamma_1 a_0 &= 0, \\
 \alpha_2 a_3 + \beta_2 a_2 + \gamma_2 a_1 + \delta_2 a_0 &= 0, \\
 \alpha_n a_{n+1} + \beta_n a_n + \gamma_n a_{n-1} + \delta_n a_{n-2} + \varepsilon_n a_{n-3} &= 0 \quad n > 2,
 \end{aligned} \tag{2.4.1}$$

for  $a_n(\omega)$  functions of some parameter  $\omega$  can be written in the form of a matrix equation

$$\begin{pmatrix}
 \beta_0 & \alpha_0 & 0 & 0 & 0 & 0 & \dots \\
 \gamma_1 & \beta_1 & \alpha_1 & 0 & 0 & 0 & \dots \\
 \delta_2 & \gamma_2 & \beta_2 & \alpha_2 & 0 & 0 & \dots \\
 \varepsilon_3 & \delta_3 & \gamma_3 & \beta_3 & \alpha_3 & 0 & \dots \\
 0 & \varepsilon_4 & \delta_4 & \gamma_4 & \beta_4 & \alpha_4 & \dots \\
 \vdots & \vdots & \vdots & \vdots & \vdots & \vdots & \ddots
 \end{pmatrix}
 \begin{pmatrix}
 a_0 \\
 a_1 \\
 a_2 \\
 a_3 \\
 a_4 \\
 \vdots
 \end{pmatrix}
 =
 \begin{pmatrix}
 0 \\
 0 \\
 0 \\
 0 \\
 0 \\
 \vdots
 \end{pmatrix}. \tag{2.4.2}$$

A solution to these equations occurs for a (possibly infinite) discrete set of  $\omega$  such that the determinant of this matrix is zero. The determinant is unchanged by row operations, allowing us to eliminate  $\varepsilon_n$  as follows

$$\varepsilon'_n = 0, \quad \delta'_n = \delta_n - \frac{\varepsilon_n \gamma'_{n-1}}{\delta'_{n-1}}, \quad \gamma'_n = \gamma_n - \frac{\varepsilon_n \beta'_{n-1}}{\delta'_{n-1}}, \quad \beta'_n = \beta_n - \frac{\varepsilon_n \alpha'_{n-1}}{\delta'_{n-1}}, \quad \alpha'_n = \alpha_n, \tag{2.4.3}$$

valid for  $n \geq 2$ . Gaussian elimination is then applied again to remove  $\delta'_n$

$$\varepsilon''_n = \delta''_n = 0, \quad \gamma''_n = \gamma'_n - \frac{\delta'_n \beta''_{n-1}}{\gamma''_{n-1}}, \quad \beta''_n = \beta'_n - \frac{\delta'_n \alpha''_{n-1}}{\gamma''_{n-1}}, \quad \alpha''_n = \alpha'_n, \quad (2.4.4)$$

valid for  $n \geq 1$ . This transforms the matrix in Eq. (2.4.2) into

$$\begin{pmatrix} \beta_0 & \alpha_0 & 0 & 0 & 0 & 0 & \dots \\ \gamma_1 & \beta_1 & \alpha_1 & 0 & 0 & 0 & \dots \\ 0 & \gamma''_2 & \beta''_2 & \alpha_2 & 0 & 0 & \dots \\ 0 & 0 & \gamma''_3 & \beta''_3 & \alpha_3 & 0 & \dots \\ 0 & 0 & 0 & \gamma''_4 & \beta''_4 & \alpha_4 & \dots \\ \vdots & \vdots & \vdots & \vdots & \vdots & \vdots & \ddots \end{pmatrix} \quad (2.4.5)$$

and this matrix now represents a three-term recurrence relation.

### 2.4.2 Continued Fractions

A standard method of acquiring solutions to a three-term recurrence relation is the continued fraction method. It has been applied to the equations of motion of perturbing fields on black hole spacetimes in many different contexts, see for example [96], [90], and [126].

We are searching for a *minimal solution* of the recurrence as  $n \rightarrow \infty$ . A set of coefficients  $\{a_n\}$  forming a solution is minimal if, for a linearly independent solution of the same recurrence  $\{b_n\}$  [120]

$$\lim_{n \rightarrow \infty} \frac{a_n}{b_n} = 0. \quad (2.4.6)$$

The solution  $\{b_n\}$  is called a *dominant solution* of the recurrence. The minimal solution is unique, but any multiple of the minimal solution can be added to a dominant solution and it will remain dominant. The minimal solution is the only one whose coefficient sum  $\sum_n a_n$  is guaranteed to converge. To find the minimal solution, we note that the ratio of successive radial coefficients  $a_n$  must die away in the large  $n$  limit. Such a ratio can be calculated in two different ways

$$\frac{a_{n+1}}{a_n} = \frac{\gamma_n}{\alpha_n} \frac{\alpha_{n-1}}{\beta_{n-1} - \frac{\alpha_{n-2}\gamma_{n-1}}{\beta_{n-2} - \alpha_{n-3}\gamma_{n-2}/\dots}} - \frac{\beta_n}{\alpha_n} = -\frac{\gamma_{n+1}}{\beta_{n+1} - \frac{\alpha_{n+1}\gamma_{n+2}}{\beta_{n+2} - \alpha_{n+2}\gamma_{n+3}/\dots}} \quad (2.4.7)$$

and these two expressions will be equal when the recurrence relation is solved, i.e., when  $\omega$  takes a value in the discrete solution set. Setting the first expression to zero, the equation we wish to solve is

$$\beta_0 - \frac{\alpha_0\gamma_1}{\beta_1} - \frac{\alpha_1\gamma_2}{\beta_2} - \frac{\alpha_2\gamma_3}{\beta_3} - \dots = 0. \quad (2.4.8)$$

The numerical method to evaluate a continued fraction of this form to a given order is called the modified Lentz algorithm and is detailed in [121]. The problem of then finding an  $\omega$  such that this vanishes is then solved by any standard numerical root-finding algorithm.

## Conclusion

In this chapter, we set the stage on which the following two chapters will take place: classical scalar and vector fields propagating on black hole spacetimes. We are now prepared to move on to the details of solving the equations of motion for these fields and an analysis of their quasinormal modes and quasibound states.

## Chapter 3

# Bosonic Fields on Static Black Hole Spacetimes

### Introduction and Overview

This chapter contains work pertaining to classical scalar and vector fields on the Schwarzschild and Reissner-Nordström spacetimes. It begins with background material available in the existing literature before leading into a piece of original work we will detail below.

We begin by returning to the equations of motion for scalar and vector perturbations of black holes presented in the previous chapter, Eqs. (2.1.14) and (2.1.17). We detail how these equations can be solved via the method of separation of variables on these spacetimes. By considering the boundary conditions one can impose on perturbations, we are led to discuss quasinormal modes (QNMs) and quasibound states (QBSs) of the perturbing fields. In the case of charged fields on the Reissner-Nordström metric, this also leads to a discussion of the phenomenon of superradiance, in which charge can be removed from the black hole by the field. We relate the circular geodesic orbits of the spacetimes to the QBSs and QNMs through the Eikonal approximation that is valid for large frequency or large angular momentum.

It is with the analytical and numerical calculation of QNMs and QBSs that we will be primarily concerned with over the course of this chapter and the next. We detail the method of asymptotic matching and how it can be used to analytically approximate the bound state frequencies, as well as the WKB approximation applied to study the behavior of QNMs and quasi-resonances. Most importantly, we consider the role recurrence relations play in finding QNMs and QBSs numerically and Leaver's continued fraction method [95] for evaluating these recurrences.

The chapter concludes with a piece of original work: we find a recurrence relation for the odd-

parity charged Proca field on Reissner-Nordström spacetime and so calculate the respective QNMs for the first time.

## 3.1 Solving the Perturbation Field Equations

### 3.1.1 Scalar Fields

Suppose a scalar field has a charge  $e$  and is propagating in a Reissner-Nordström spacetime of black hole charge  $Q$  [44]. The Klein-Gordon equation is Eq. (2.1.14) or, if we expand the covariant derivatives,

$$\left\{ (-g)^{-1/2} \partial_\mu \left[ (-g)^{1/2} g^{\mu\nu} (\partial_\nu - ieA_\nu) \right] - ieA_\mu [g^{\mu\nu} (\partial_\nu - ieA_\nu)] \right\} \Phi = \mu^2 \Phi, \quad (3.1.1)$$

where  $A_\mu$  is the electromagnetic 4-potential of the Reissner-Nordström black hole (2.2.11).

As the Reissner-Nordström spacetime is spherically symmetric we can perform a mode decomposition of the form

$$\Phi_{\ell m} = \frac{u_\ell(t, r)}{r} Y_{\ell m}(\theta, \phi), \quad (3.1.2)$$

where the functions  $Y_{\ell m}(\theta, \phi) = Y_{\ell m}(\theta) e^{im\phi}$  are the *spherical harmonics* and satisfy the equation

$$\frac{1}{\sin\theta} \frac{\partial}{\partial\theta} \left( \sin\theta \frac{\partial Y_{\ell m}}{\partial\theta} \right) + \frac{1}{\sin^2\theta} \frac{\partial^2 Y_{\ell m}}{\partial\phi^2} + \ell(\ell+1) Y_{\ell m} = 0. \quad (3.1.3)$$

Here,  $\ell(\ell+1)$  is a separation constant where  $\ell$  carries the physical interpretation of total angular momentum of the field. Similarly,  $m$  will have the physical interpretation of azimuthal angular momentum of the field and is an integer in the set  $m \in \{-\ell, \dots, \ell\}$ . The corresponding radial equation is

$$\left( f_{rn} \frac{\partial}{\partial r} f_{rn} \frac{\partial}{\partial r} - \frac{\partial^2}{\partial t^2} - V_\ell(r) \right) u_\ell(t, r) = 0, \quad (3.1.4)$$

where the effective potential  $V_\ell(r)$  is

$$V_\ell(r) = f_{rn} \left( \frac{\ell(\ell+1)}{r^2} + \frac{2M}{r^3} - \frac{2Q^2}{r^4} + \mu^2 \right) + \frac{2\omega e Q}{r} - \frac{e^2 Q^2}{r^2}. \quad (3.1.5)$$

For an uncharged particle  $e = 0$ , this potential can be related to the potential of a null ( $\mu = 0$ ) or timelike ( $\mu > 0$ ) geodesic  $V_g(r)$  from Eq. (2.3.12) if we take the eikonal limit  $\ell \gg 1$ . We do this by making the association  $L \leftrightarrow \ell + 1/2$  and then dropping ‘‘small’’ terms not proportional to  $\ell^2$  or  $\mu$ . We will use this to draw a link between the energies  $E$  of geodesic orbits and the frequencies  $\omega$  of quasinormal modes in Sec. 3.2.

One can now introduce the tortoise coordinate  $r_*$  defined by

$$\frac{d}{dr_*} = f_{rn} \frac{d}{dr}, \quad (3.1.6)$$

then the equation for the radial function  $u_\ell$  can be cast as a wave equation

$$\left( \frac{\partial^2}{\partial r_*^2} - \frac{\partial^2}{\partial t^2} - V_\ell(r) \right) u_\ell(t, r) = 0. \quad (3.1.7)$$

An expression for  $r_*$  can be found explicitly by integrating the definition in (3.1.6)

$$r_* = r + \frac{r_+^2}{r_+ - r_-} \log|r - r_+| - \frac{r_-^2}{r_+ - r_-} \log|r - r_-| \quad (3.1.8)$$

and the respective coordinate for the Schwarzschild spacetime can be obtained by setting  $r_+ = 2M$  and  $r_- = 0$ . The range of this coordinate is the entire real line, such that  $r_* \rightarrow -\infty$  as  $r$  approaches the event horizon of the spacetime and  $r_* \rightarrow +\infty$  as  $r \rightarrow +\infty$ .

If the time dependence of the perturbation is harmonic, i.e.  $u_\ell(t, r) = u_{\ell\omega}(r) e^{-i\omega t}$  for some (potentially complex) frequency  $\omega$ , the partial differential equation (PDE) in (3.1.7) reduces to an ordinary differential equation (ODE)

$$\left( \frac{d^2}{dr_*^2} + \omega^2 - V_\ell(r) \right) u_{\ell\omega}(r) = 0. \quad (3.1.9)$$

This equation is called the scalar *Regge-Wheeler equation*. It was first formulated in the context of gravitational perturbations [123] and we will comment on this equation for general fields in Sec. 3.1.2.

It is clear from (3.1.5) that  $\omega^2 - V_\ell(r)$  tends to  $\omega^2 - \mu^2$  as  $r_* \rightarrow \infty$  and tends to

$$\tilde{\omega}^2 \equiv \left( \omega - \frac{eQ}{r_+} \right)^2 \quad (3.1.10)$$

as  $r_* \rightarrow -\infty$  [13]. Hence, the linearly independent asymptotic behaviors of the solutions to the Regge-Wheeler equation in those limits are

$$u_{\ell\omega}(r) \sim \begin{cases} e^{\pm i\tilde{\omega}r_*} & r_* \rightarrow -\infty \\ e^{\pm ikr_*} & r_* \rightarrow +\infty \end{cases}, \quad (3.1.11)$$

where  $k = \sqrt{\omega^2 - \mu^2}$ .

This makes it straightforward to consider what kinds of boundary conditions should be placed on the solution. In a classical, physical scenario no waves should be emerging from the black hole event horizon, meaning there should be no  $e^{+i\tilde{\omega}r_*}$  contribution there. A mode that satisfies this condition is called an IN mode,

$$u_{\ell\omega}^{in}(r_*) \sim \begin{cases} e^{-i\tilde{\omega}r_*} & r_* \rightarrow -\infty \\ A_{out}(\omega) e^{ikr_*} + A_{in}(\omega) e^{-ikr_*} & r_* \rightarrow +\infty \end{cases}, \quad (3.1.12)$$

the complex conjugate of which is called an OUT mode. The coefficients  $A_{in/out}(\omega)$  are simply the amplitudes of the ingoing and outgoing waves at infinity. No normalisation is specified here but this

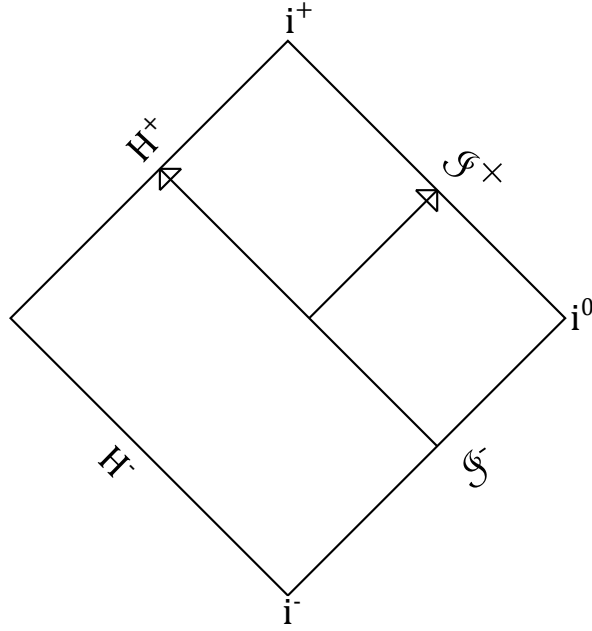


Figure 3.1.1: A Penrose diagram depicting the IN modes on the exterior of a black hole spacetime. Waves are incoming from  $\mathcal{I}^-$  before being partially reflected back to  $\mathcal{I}^+$  with the rest being transmitted through the event horizon  $H^+$ .

will be needed when discussing the propagation of quantised fields in chapter 5. The IN modes are shown on a Penrose diagram in Fig. 3.1.1. It is clear to see why this is the correct visualisation when we recall that  $r_* \rightarrow -\infty$  in the approach to the horizon,  $H^+ \cup H^-$  and  $r_* \rightarrow +\infty$  in the approach to infinity,  $\mathcal{I}^+ \cup \mathcal{I}^-$ .

Another typical solution to consider corresponds to waves that are purely outgoing at spatial infinity. These are called UP modes,

$$u_{\ell\omega}^{up}(r_*) \sim \begin{cases} B_{out}(\omega) e^{+i\tilde{\omega}r_*} + B_{in}(\omega) e^{-i\tilde{\omega}r_*} & r_* \rightarrow -\infty \\ e^{+ikr_*} & r_* \rightarrow +\infty \end{cases} \quad (3.1.13)$$

and these are shown on a Penrose diagram in Fig. 3.1.2. The complex conjugates of these modes are called DOWN modes.

Any two of these four linearly independent mode types can be taken as a basis of the space of all solutions.

Some standard results in scattering theory can now be derived. Any two functions  $u_1$  and  $u_2$  that satisfy the wave equation (3.1.9) must have a constant Wronskian  $W(u_1, u_2)$ , where

$$W(u_1, u_2) = u_1 \frac{du_2}{dr_*} - u_2 \frac{du_1}{dr_*}. \quad (3.1.14)$$

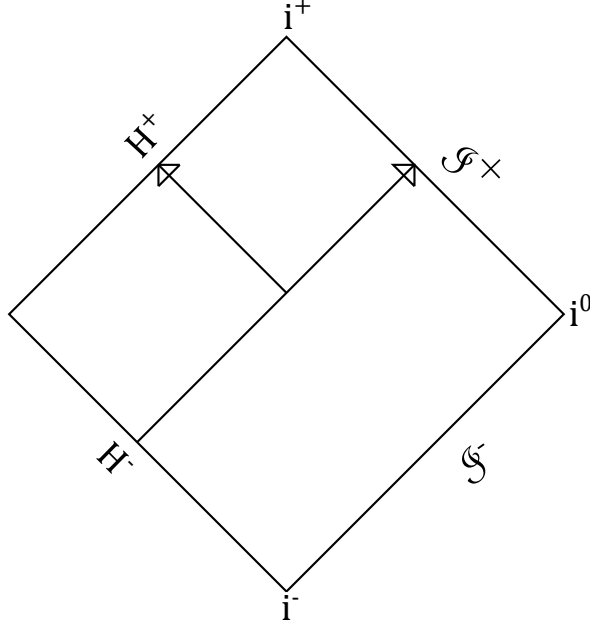


Figure 3.1.2: A Penrose diagram depicting the UP modes on the exterior of a black hole spacetime. Waves are outgoing from the past horizon  $H^-$  before being partially reflected back into the event horizon  $H^+$  with the rest escaping to  $\mathcal{S}^+$ .

Computing the Wronskian of the IN and OUT solutions at the two boundaries  $r_* \rightarrow \pm\infty$  and then equating these gives the condition

$$2i\tilde{\omega} = 2ik \left( |A_{in}|^2 - |A_{out}|^2 \right). \quad (3.1.15)$$

We could also, if we wish, select  $u_1$  and  $u_2$  to be any pair of IN,UP,OUT or DOWN to derive more relations between the various  $A$  and  $B$  coefficients.

Dividing (3.1.15) by  $|A_{in}|^2$ , rearranging, and defining the *transmission amplitude*  $\mathcal{T}$  and *reflection amplitude*  $\mathcal{R}$  leads to a form of conservation law

$$\mathcal{T} = \frac{1}{A_{in}}, \quad \mathcal{R} = \frac{A_{out}}{A_{in}}, \quad |\mathcal{R}|^2 = 1 - \frac{\tilde{\omega}}{k} |\mathcal{T}|^2, \quad (3.1.16)$$

where  $|\mathcal{T}|^2$  and  $|\mathcal{R}|^2$  will be referred to as the transmission and reflection coefficients. We will briefly consider the consequences of this relation more closely.

### 3.1.1.1 Superradiance

A recent and comprehensive review of the history and current developments in the field of superradiance is given in [28]. For a modern description based on quantum field theory, see [61].

Superradiance, in the context of black hole physics, is the phenomenon where waves incident on a rotating or charged black hole are reflected with a greater amplitude than they started with. In the language of reflection and transmission coefficients, (3.1.16) superradiance occurs when  $|\mathcal{R}|^2 > 1$  i.e., when  $\tilde{\omega}/k < 0$ . As the real part of  $k$  must be positive,  $\Re(k) > 0$ , to ensure the waves can escape to infinity, one can infer the superradiant condition on the frequency is  $\omega < eQ/r_+$ .

If superradiance occurs, it could lead to a *superradiant instability*. These were first formulated by Press and Teukolsky for massless field perturbations by introducing an artificial “mirror” around the black hole [119]. Such a reflective barrier would direct the field amplified by superradiance back onto the black hole allowing it to be amplified again repeatedly, causing the field’s amplitude to grow exponentially, an effect known as a “black hole bomb”. However, the same effect can be achieved without the mirror by simply endowing the field with a non-zero mass  $\mu$  and imposing the boundary condition that there is no outgoing radiation at infinity (i.e., we are looking at a *quasibound state*). We will discuss superradiance and superradiant instabilities more after we have introduced quasinormal modes and quasibound states in Sec. 3.2.

### 3.1.2 Vector Fields

#### 3.1.2.1 Electromagnetic Field

The equation of motion of a massless, neutral vector (electromagnetic) field in the absence of any external current is (2.2.2). The introduction of the Kinnersley tetrad (2.2.17) allows one to extract three complex scalar functions out of the Faraday tensor  $F_{\mu\nu}$  as follows

$$\begin{aligned}\Psi_1 &= F_{\mu\nu}\ell^\mu m^\nu, \\ \Psi_0 &= \frac{1}{2}F_{\mu\nu}(\ell^\mu n^\nu - m^\mu \bar{m}^\nu), \\ \Psi_{-1} &= F_{\mu\nu}\bar{m}^\mu n^\nu,\end{aligned}\tag{3.1.17}$$

referred to as the Maxwell scalars by Teukolsky in [138]. These carry the same information content as the original six real scalar functions for the three spatial components of the electric and magnetic fields. It should be noted that we are using different notation to Teukolsky, including labeling the scalars with different indices (Our  $\Psi_1, \Psi_0$  and  $\Psi_{-1}$  correspond to his  $\phi_0, \phi_1$  and  $\phi_2$  respectively). As in [15] the index on each of these scalars in our notation represents their *spin-weight*: under a transformation of the tetrad vector  $m^\mu \rightarrow e^{i\alpha}m^\mu$  for  $\alpha$  an arbitrary phase,  $\Psi_p$  transforms to  $e^{iap}\Psi_p$ .

On the Schwarzschild or Reissner-Nordström spacetime, the Maxwell scalars are amenable to a separation of variables in a similar manner to that of the scalar field, except one must use *spin-*

weighted spherical harmonics  $Y_p^{\ell m}$  [74] of spin weight  $p \in \{1, 0, -1\}$ ,

$$\Psi_p(t, r, \theta, \phi) = \sum_{\ell=|p|}^{\infty} \frac{u_p^{\ell m}(t, r)}{r} Y_p^{\ell m}(\theta, \phi), \quad (3.1.18)$$

which can be defined in terms of spin-raising and spin-lowering differential operators on the original  $Y^{\ell m}$  of Eq.(3.1.3), see [57]. It is then possible to find functions  $g_p(r)$  such that  $g_p(r) u_p^{\ell m}(t, r)$  satisfies the Regge-Wheeler equation (3.1.7) with a new effective potential that depends on the spin of the field (for an electromagnetic field,  $s = 1$  and so the second term vanishes),

$$V_{\ell s}(r) = f \left( \frac{\ell(\ell+1)}{r^2} + \frac{df}{dr} \frac{(1-s^2)}{r} \right). \quad (3.1.19)$$

Here, and for the remainder of this section, the function  $f$  can refer to either  $f_{sch}$  or  $f_{rn}$ . This is the *generalised Regge-Wheeler equation*. The cases  $p = \pm 1$  are covered in Table 1 of [138] while  $p = 0$  was covered by Price in [122]. Hence the  $p = 0$  equation, where  $g_0(r) = r^2$  such that  $r^2 \Psi_0$  satisfies the Regge-Wheeler equation, is sometimes referred to as the *Price equation*.

The reason for writing the potential (3.1.19) in a form that includes  $s$ , is that this general method also works to some extent when studying gravitational perturbations. Such perturbations can be decomposed into five scalar functions called the *Weyl scalars*  $\Theta_p$ , labeled by the index  $p \in \{0, \pm 1, \pm 2\}$ . There exist functions  $g_{\pm 2}(r)$  such that the two scalars  $g_{\pm 2}(r) \Theta_{\pm 2}$  satisfy the generalised Regge-Wheeler equation for  $s = 2$ . As such, the Regge-Wheeler equation is a *master* differential equation that has utility regardless of the spin of the perturbing field [15].

### 3.1.2.2 Uncharged Proca Field

The majority of our work will be focused on the massive vector field or *Proca field*, for which we refer primarily to [126]. Unlike in the case of the scalar field, adding a mass to the vector field is not just a simple matter of modifying the effective potential in (3.1.19) with a  $\mu^2$  term. We will see that this is at least partially to do with the multiple polarization states of the field, which isn't a consideration for the scalar field.

The equation of motion for a massive, uncharged vector field  $W^\nu$  of mass  $\mu$  is (see [66] and (2.1.17))

$$\nabla_\mu W^{\mu\nu} = \mu^2 W^\nu. \quad (3.1.20)$$

The Lorenz gauge condition  $\nabla_\mu W^\mu = 0$  is a direct consequence of (3.1.20), see (2.1.24)

The massive vector field can be decomposed into modes in the following manner [126]

$$W_\mu(t, r, \theta, \phi) = \sum_{i=1}^4 \sum_{\ell m} c_i \frac{u_{(i)}^{\ell m}(t, r)}{r} Z_\mu^{(i)\ell m}(\theta, \phi), \quad (3.1.21)$$

where  $c_1 = c_2 = 1$ ,  $c_3 = c_4 = (\ell(\ell + 1))^{-1/2}$  and the  $Z_\mu^{(i)}$  are *vector spherical harmonics* (not to be confused with the spin-weighted spherical harmonics used for separating the Maxwell scalars) constructed from the standard scalar spherical harmonics like so

$$Z_\mu^{(1)\ell m} = [1, 0, 0, 0] Y^{\ell m}, \quad (3.1.22)$$

$$Z_\mu^{(2)\ell m} = [0, f^{-1}, 0, 0] Y^{\ell m}, \quad (3.1.23)$$

$$Z_\mu^{(3)\ell m} = \frac{r}{\sqrt{\ell(\ell + 1)}} [0, 0, \partial_\theta, \partial_\phi] Y^{\ell m}, \quad (3.1.24)$$

$$Z_\mu^{(4)\ell m} = \frac{r}{\sqrt{\ell(\ell + 1)}} \left[ 0, 0, \frac{\partial_\phi}{\sin \theta}, -\sin \theta \partial_\theta \right] Y^{\ell m}. \quad (3.1.25)$$

The functions  $u_{(i)}$  now satisfy four coupled, second-order PDEs. The equations were derived in [126] in the Schwarzschild spacetime. Here, we will derive a more general set of equations that also applies to the Reissner-Nordström spacetime, by assuming a metric of the form (2.2.12) or (2.2.10), but with the function  $f$  unspecified.

In (3.1.20) we are free to add a term involving  $\nabla_\mu W^\mu$  as long as the Lorenz condition is satisfied, i.e. we will now work with the equation

$$P^\nu \equiv \nabla_\mu W^{\mu\nu} + \nabla^\nu (\nabla_\mu W^\mu) - \mu^2 W^\nu = 0. \quad (3.1.26)$$

As in [126] we will opt to expand the Lorenz condition using the ansatz (3.1.21) and include it as a supplementary condition to the four component equations of (3.1.26). The reason for these manipulations is so that the resulting equations are of a similar form to the Regge-Wheeler equation.

These equations are

$$\mathcal{D}_1 u_{(1)} + \frac{df}{dr} (\dot{u}_{(2)} - u'_{(1)}) = 0, \quad (3.1.27)$$

$$\mathcal{D}_1 u_{(2)} + \frac{df}{dr} (\dot{u}_{(1)} - u'_{(2)}) - \frac{2f^2}{r^2} (u_{(2)} - u_{(3)}) = 0, \quad (3.1.28)$$

$$\mathcal{D}_1 u_{(3)} + \frac{f}{r^2} 2\ell(\ell + 1) u_{(2)} = 0, \quad (3.1.29)$$

$$\mathcal{D}_1 u_{(4)} = 0, \quad (3.1.30)$$

where we have defined the second-order differential operator (cf. Eq. (3.1.7))

$$\mathcal{D}_s = \frac{\partial^2}{\partial r_*^2} - \frac{\partial^2}{\partial t^2} - f \left( \frac{\ell(\ell + 1)}{r^2} + \mu^2 + \frac{df}{dr} \frac{(1 - s^2)}{r} \right). \quad (3.1.31)$$

$\mathcal{D}_s$  is the Regge-Wheeler differential operator of spin  $s$  and mass  $\mu$ . In these equations a dot denotes differentiation with respect to  $t$  and a dash differentiation with respect to  $r_*$ . The first two equations (3.1.27) and (3.1.28), in the language of Eq. (3.1.26), arise from  $P_t = 0$  and  $P_r = 0$  while Eqs. (3.1.29) and (3.1.30) are  $\partial_\theta P_\phi - \partial_\phi P_\theta = 0$  and  $\partial_\theta (P_\theta \sin \theta) + \partial_\phi (P_\phi / \sin \theta) = 0$  respectively.

Of particular note is the equation for  $u_{(4)}$ , which is completely decoupled from the other modes. The remaining three equations for  $u_{(i)}$  when  $i \in \{1, 2, 3\}$  are all coupled together, but the system can be simplified with the use of the Lorenz condition. The Lorenz condition  $\nabla_\mu W^\mu = 0$  can be written

$$-\dot{u}_{(1)} + u'_{(2)} + \frac{f}{r} (u_{(2)} - u_{(3)}) = 0, \quad (3.1.32)$$

which can be used to eliminate  $\dot{u}_{(1)}$  from (3.1.28), giving

$$\mathcal{D}_1 u_{(2)} + \frac{f}{r} \left( \frac{df}{dr} - \frac{2f}{r} \right) (u_{(2)} - u_{(3)}) = 0. \quad (3.1.33)$$

This equation forms a coupled system with Eq. (3.1.29). Hence, the massive vector field has three degrees of freedom, encapsulated in the modes  $u_{(i)}$  for  $i \in \{2, 3, 4\}$ . The two coupled modes are referred to as *even-parity* modes and the remaining decoupled mode is referred to as the *odd-parity* mode. This naming convention comes from the behavior of the corresponding vector spherical harmonics  $Z_\mu^{(i)\ell m}$  under the parity inversion transformation  $\mathbf{x} \rightarrow -\mathbf{x}$ , where  $\mathbf{x}$  is the vector of spatial components of the spacetime point  $x$ . For a vector function, this doesn't just require the substitutions  $\theta \rightarrow \pi - \theta$  and  $\phi \rightarrow \phi + \pi$ , but we must also consider how the spatial components of the vector transform,  $[W_r, W_\theta, W_\phi] \rightarrow [-W_r, W_\theta, -W_\phi]$ . We conclude that, under parity inversion,  $Z_\mu^{(2)\ell m}$  and  $Z_\mu^{(3)\ell m}$  acquire a factor of  $(-1)^\ell$  (even parity) and  $Z_\mu^{(4)\ell m}$  acquires a factor of  $(-1)^{\ell+1}$  (odd-parity).

### 3.1.2.3 The Massless Limit

Some important information about the behavior of massive vector perturbations can be attained if we look at the massless limit and compare the results to what we know about electromagnetic perturbations. The decoupled equation for  $u_{(4)}$  (3.1.30) is nothing other than the Regge-Wheeler equation for  $s = 1$ . Taking the massless limit of this equation reduces it further to Price's equation,  $\mathcal{D}_1 (r^2 \Psi_0) = 0$  [126, 122].

The coupled system (3.1.29) and (3.1.33) has some satisfying properties. Combining the two coupled PDEs for  $u_{(2)}$  and  $u_{(3)}$  into a single fourth-order PDE and then taking the massless limit, the resulting equation can be written as one Regge-Wheeler equation "nested" inside another one,

$$\frac{1}{r} f^{-3} \mathcal{D}_1 [f^{-1} \mathcal{D}_0 (r u_{(3)})] = 0. \quad (3.1.34)$$

The mode  $u_{(2)}$  has been eliminated and we can now think of our two even-parity modes as being  $u_{(3)}$  and the new mode  $\psi$ :

$$\psi \equiv f^{-1} \mathcal{D}_0 (r u_{(3)}). \quad (3.1.35)$$

The form of this “nested” equation allows us, as is done in [126], to infer information about the different degrees of freedom of the field. If the “inner” wave equation is satisfied, (i.e.  $\psi = 0$ ) it follows that our vector field  $W_\mu$  can be written as the gradient of a scalar field  $\chi$

$$W_\mu = \partial_\mu \chi, \quad \chi = \frac{u_{(3)}}{\ell(\ell+1)} Y_{\ell m}(\theta, \phi), \quad (3.1.36)$$

meaning that the field is *pure gauge*. In other words, the solution  $\psi = 0$  to the “inner” Regge-Wheeler equation has no physical significance as it can be removed by a gauge transformation.

Notice also that the “outer” differential equation this mode satisfies,  $\mathcal{D}_1 \psi = 0$  is identical to the one  $u_{(4)}$  satisfies. In other words, the massless limit introduces a *degeneracy* in the degrees of freedom of the vector field. This was to be expected, as the polarization states of the massless limit of this field must agree with those of the electromagnetic field, which we know has only two independent polarization states.

This analysis motivates the following classification. One of the two coupled modes, in this case  $u_{(3)}$ , will be referred to as a mode of *scalar-type*, for two main reasons: firstly, the differential equation satisfied by  $ru_{(3)}$  is simply the Regge-Wheeler equation for  $s = 0$  and secondly, when this differential equation is satisfied the vector field  $W_\mu$  can be written as the gradient of a scalar field. Hence, the scalar mode is a gauge mode in the electromagnetic case ( $\mu = 0$ ). In contrast, the modes  $\psi$  and  $u_{(4)}$  will be referred to as modes of *vector-type* as they solve the Regge-Wheeler equation for  $s = 1$ .

### 3.1.2.4 Charged Proca Field

The separation of the Proca equation of a massive, charged vector field of charge  $e$  is discussed in [80]. The separation is performed on a spacetime that can be locally written as the product of a  $m$ -dimensional spacetime with metric  $h_{ab}$  (spanned by the coordinates  $\{y^a\}$ ) and an  $n$ -dimensional spacetime with a metric of constant curvature  $K$  and line element  $d\sigma^2$ . The metric of the full spacetime has a line element that can be written in the form [88]

$$ds^2 = h_{ab}(y) dy^a dy^b + r^2(y) d\sigma^2 \quad (3.1.37)$$

and this includes spherically symmetric spacetimes as a special case.

The equation of motion of the charged Proca field is (2.1.17). The calculations performed in the previous subsection for an uncharged field don’t easily carry over to a charged field as  $\nabla_\mu W^\mu$  doesn’t vanish as it does for a uncharged field. In fact,  $\nabla_\mu W^\mu$  in terms of the  $u_{(i)}$  modes takes the form (cf. Eq. (3.1.32))

$$-\dot{u}_{(1)} + u'_{(2)} + \frac{f}{r}(u_{(2)} - u_{(3)}) = -\frac{2ieQ}{r^2\mu} \left( \dot{u}_{(2)} - u'_{(1)} + \frac{f}{r}u_{(1)} \right). \quad (3.1.38)$$

Adding the gradient of the above quantity to (2.1.17) doesn't reduce the equation to a wavelike equation like adding the gradient of the Lorenz condition did for (3.1.26).

Instead, we turn to the work of [127] where charged, massive vector fields around Reissner-Nordström black holes are discussed. The equation for the single decoupled mode (which they call the *transverse mode*) can be cast into a Schrödinger-like form (3.1.9) just like the charged and uncharged scalar fields

$$\left(\frac{d^2}{dr_*^2} + \omega^2 - V_\ell(r)\right) u_{(4)} = 0, \quad V_\ell(r) = f_{rn} \left(\frac{\ell(\ell+1)}{r^2} + \mu^2\right) + \frac{2\omega eQ}{r} - \frac{e^2 Q^2}{r^2}. \quad (3.1.39)$$

This is exactly the potential function that one might naively expect, considering the potentials of the charged scalar field (3.1.5) and the uncharged vector field (3.1.19). If we assume a harmonic time dependence  $u(r, t) = u(r) e^{-i\omega t}$ , this reduces to  $\mathcal{D}_1 u_{(4)} = 0$  in the limit  $e \rightarrow 0$ . In particular, the form of the potential motivates us to define the charged wave operator

$$\tilde{\mathcal{D}}_1 = \frac{\partial^2}{\partial r_*^2} - \frac{\partial^2}{\partial t^2} - f \left(\frac{\ell(\ell+1)}{r^2} + \mu^2\right) - \frac{2ieQ}{r} \frac{\partial}{\partial t} + \frac{e^2 Q^2}{r^2}, \quad (3.1.40)$$

such that the equation for the charged transverse mode is  $\tilde{\mathcal{D}}_1 u_{(4)} = 0$ . In Sec. 3.4 we will numerically investigate this decoupled, odd-parity mode of the charged Proca field.

As a brief aside, we will complete this discussion for the two coupled modes also. [127] denotes these modes as  $\psi$  and  $\chi$  and report the following pair of coupled equations for these modes of a charged field around a charged black hole

$$\left[ f_{rn}^2 r^2 \frac{d^2}{dr^2} + (\omega r - eQ)^2 - f_{rn} (\ell(\ell+1) + \mu^2 r^2) \right] \chi + \left[ 2ieQ f_{rn} - ir(\omega r - eQ) \frac{df_{rn}}{dr} \right] \psi = 0, \quad (3.1.41)$$

$$\left[ f_{rn}^2 \frac{d}{dr} \left( r^2 \frac{d}{dr} \right) + (\omega r - eQ)^2 - f_{rn} (\ell(\ell+1) + \mu^2 r^2) \right] \psi + \left[ 2i\omega r f_{rn} - ir(\omega r - eQ) \frac{df_{rn}}{dr} \right] \chi = 0. \quad (3.1.42)$$

Like the decoupled equation, we can also write these equations in a similar manner to [126]. Under the identification  $\chi = u_{(1)}$  and  $\psi = u_{(2)}$  (3.1.41) reduces to (3.1.27) in the uncharged limit and (3.1.42) reduces to

$$\mathcal{D}_1 u_{(2)} + \left( \frac{df}{dr} - \frac{2f}{r} \right) (\dot{u}_{(1)} - u'_{(2)}) = 0, \quad (3.1.43)$$

which is also the equation we obtain if we use (3.1.32) to eliminate  $u_{(3)}$  in Eq. (3.1.28). In particular, (3.1.41) and (3.1.42) can be written in the wave equation formalism of [126] using the charged wave operator, as follows

$$\tilde{\mathcal{D}}_1 u_{(1)} + \frac{df}{dr} (\dot{u}_{(2)} - u'_{(1)}) + \frac{2ieQ}{r^2} f u_{(2)} = 0, \quad (3.1.44)$$

$$\tilde{\mathcal{D}}_1 u_{(2)} + \left( \frac{df}{dr} - \frac{2f}{r} \right) (\dot{u}_{(1)} - u'_{(2)}) - \frac{ieQ}{r} f u_{(1)} = 0. \quad (3.1.45)$$

## 3.2 Quasinormal Modes and Quasibound States

### 3.2.1 Introduction and Motivation

#### 3.2.1.1 Massless Quasinormal Modes

As was described in chapter 1, when a black hole is perturbed by an external field it will attempt to revert to a latent state by emitting radiation at certain characteristic frequencies, which we call *quasinormal modes* (QNMs) [63]. Similarly, when two black holes merge into one, the final black hole undergoes a “ringdown phase” where it emits gravitational waves at QNM frequencies. These frequencies depend only on the mass and spin parameters of the black hole itself [89]. Hence, if QNMs can be observed in gravitational wave data, one can infer the properties of the black hole that produced the signal. A review of other phenomenological consequences of QNMs, including their relevance to string theory, can be found in [93].

The complex QNM frequencies  $\omega_{\ell mn}$  form an infinite discrete set, the elements of which are labeled by the parameters  $\ell$ ,  $m$ , and  $n$  [95]. Here,  $\ell$  is the total angular momentum of the perturbing field (3.1.3),  $m$  is the azimuthal angular momentum and integer  $n \geq 0$  is the *overtone number*. For the massive vector (Proca) field, we may also add a label  $S$  to  $\omega$  to indicate which of three polarization states we are in. For the Proca field, the odd-parity vector mode is labeled  $S = 0$ , the even-parity scalar mode with  $S = -1$  and the even-parity vector mode with  $S = +1$ . The QNMs experimentally observed from the ringdown of black hole mergers correspond to the  $\ell = m = 2, n = 0$  QNM of the gravitational field [3]. The real part of the frequency  $\Re(\omega)$  corresponds to the characteristic frequency of the oscillation while the imaginary part  $\Im(\omega) < 0$  corresponds to the *decay rate*.

An analogy can be drawn to the electron energy levels in a hydrogen atom which are found by the solution of the Schrödinger equation with regular boundary conditions at the origin and a decaying probability amplitude at infinity. These boundary conditions quantise the allowed energies of the electron into discrete, real values. The corresponding black hole problem has the boundary condition of purely ingoing waves at the event horizon and it is this draining of the field into the horizon that leads to complex frequencies with a non-zero decay rate.

We consider first the QNMs of massless fields, such as a massless scalar field, the electromagnetic field or the gravitational field. QNM frequencies will occur near the square root of the maximum of the potential function  $V_\ell(r)$  in the radial differential equation (3.1.7) as described in [131]. The maximum is assumed to occur at a radial value  $r = r_{QNM}$ , hence we have  $\omega_{QNM}^2 \approx V_\ell(r_{QNM})$ . This comes from the lowest order WKB approximation in the eikonal limit,

$$\omega_{QNM}^2 \approx V_g(r_{QNM}) - i(n + 1/2) \sqrt{-2V_g''(r_{QNM})}, \quad (3.2.1)$$

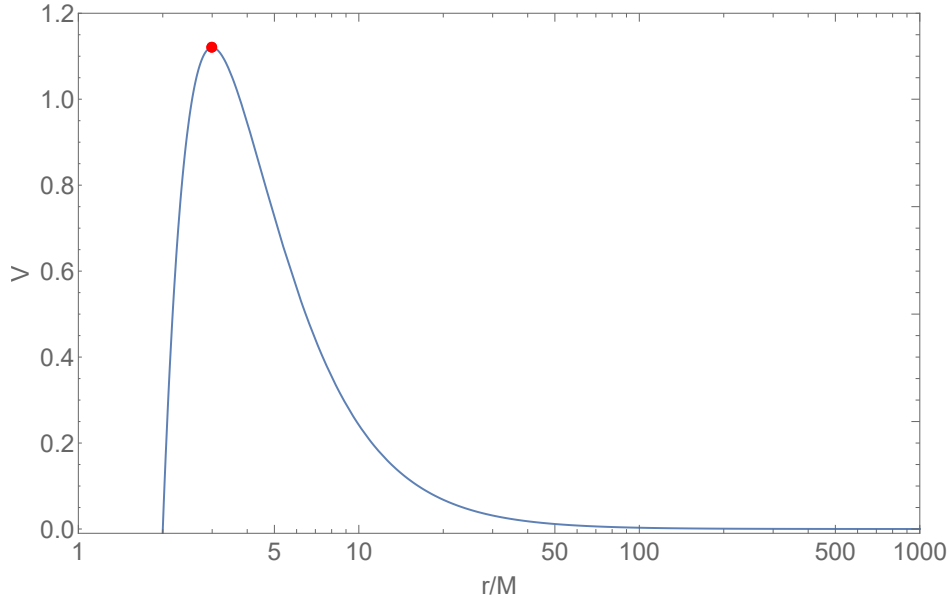


Figure 3.2.1: The massless limit of the geodesic potential  $V_g(r)$  in Eq. (2.3.12). The red point marks the potential peak (the energy of an unstable geodesic orbit, or the frequency of a QNM in the eikonal limit).

where it is because of the eikonal approximation that we can instead use the geodesic potential  $V_g(r)$  (2.3.12) in the above equation. A typical such potential is shown in Fig. 3.2.1. Hence, there is a clear connection between QNM frequencies and the energies of unstable circular geodesic orbits. Links of this kind have been studied for a long while, see for example [73]. After we have covered the case of massive QNMs later in this section we will expand on this concept further.

As  $r_{QNM}$  is the location of a local maximum of  $V_g$  we must have  $V_g'(r_{QNM}) = 0$  and  $V_g''(r_{QNM}) < 0$ . In the limit that  $V_g''(r_{QNM}) \rightarrow 0$  the imaginary part (the damping rate) of the QNM frequency vanishes and so the QNM is arbitrarily long-lived [111]. Such a mode is called a *quasiresonance*.

### 3.2.1.2 Quasibound States

Now let's introduce a mass to the field,  $\mu \neq 0$ . This shifts the typical potential to one shown in Fig. 3.2.2. The important additional feature is the presence of a local minimum. As QNMs are linked to the local maximum of the potential, another type of frequency is linked to the local minimum: the *quasibound state* (QBS) frequencies [126]. In the eikonal limit, these are linked to the energies of the stable circular geodesic orbits. Classically, these states would be confined to the potential well near the local minimum, but as fields they can tunnel through the potential barrier and into the event horizon, thus leading to the field decaying over time. Unlike a QNM, a field in a quasibound state

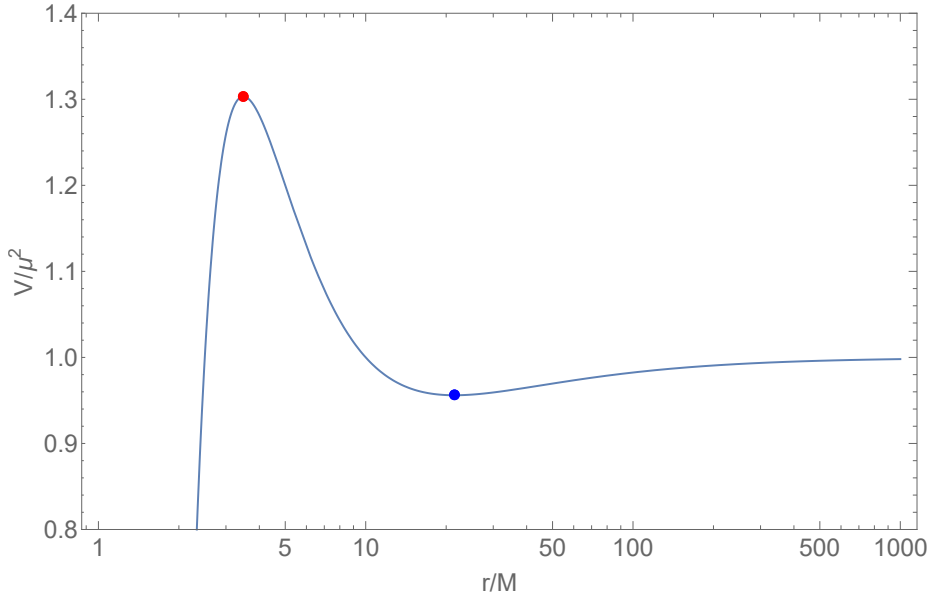


Figure 3.2.2: The geodesic potential in Eq. (2.3.12) plotted for  $L/M\mu = 5$ . The red point marks the potential peak (the energy of an unstable geodesic orbit, or the frequency of a QNM for large  $\ell$ ) and the blue point marks the local minimum (the energy of a stable geodesic orbit, or the frequency of a QBS in the eikonal limit).

cannot propagate to infinity, as the local minimum of the potential will be at a value  $\omega_{QBS}^2 < \mu^2$ .

If a bound state frequency  $\omega_{QBS}$  also happens to satisfy the superradiance condition, which in the Reissner-Nordström spacetime reads  $\omega < eQ/r_+$  (see Sec. 3.1.1.1), then the positive energy extraction from the black hole can lead to  $\Im(\omega_{QBS}) > 0$ , i.e., the bound state is not decaying, but growing. This can lead to the superradiant instabilities mentioned at the end of Sec. 3.1. We will find in Sec. 3.3 that superradiant instabilities actually cannot occur in the Reissner-Nordström spacetime, but in chapter 4 we will see that they can occur in rotating black hole spacetimes.

The existence of quasibound states has interesting phenomenological consequences, as was discussed in chapter 1. It has been hypothesised that ultra-light vector bosonic particles could be potential dark matter candidates [58, 11, 86]. If these beyond Standard Model particles exist, they would potentially collect in “clouds” around black holes at specific bound state frequencies [27, 82, 127, 129]. These clouds can then extract mass or charge (and for rotating black holes, angular momentum) from the black hole through superradiance, leading to superradiant instabilities [16, 17, 148]. The existence of these clouds would constrain the mass of these hypothetical particles [33, 112].

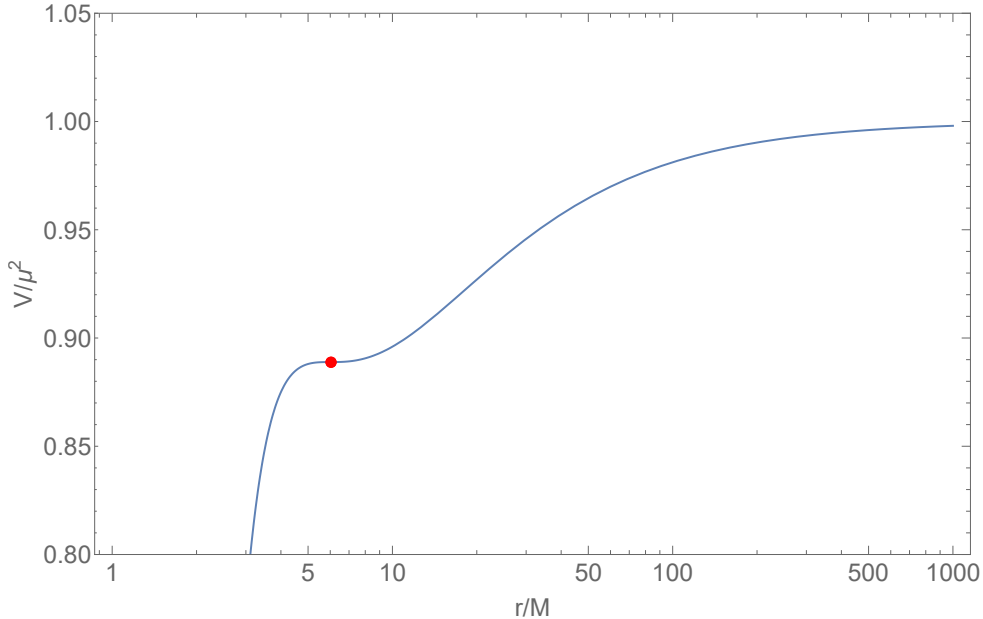


Figure 3.2.3: The geodesic potential in Eq. (2.3.12) plotted for  $L/M\mu = 2\sqrt{3}$ . The red point marks the stationary point (the energy of the ISCO geodesic, or the frequency of an evanescent QNM in the eikonal limit).

### 3.2.1.3 Massive Quasinormal Modes

While including a non-zero mass allows for the possibility of QBSs, it also enriches the spectrum of QNMs. Equation (3.2.1) motivates the definition of two distinct types of QNM: the *propagative* modes and the *evanescent* modes, for which  $V_g(r_{QNM}) > \mu^2$  or  $V_g(r_{QNM}) < \mu^2$  respectively. As noted in [49], evanescent modes are potentially less physically relevant than their propagative counterparts as they are harder to pick out of gravitational wave signals. This is made clear in Fig. 3.2.3 where the maximum that indicates the QNM has become an inflection point and it can be seen that the potential barrier will impede the motion of the field perturbation towards infinity, in a similar manner to that of a QBS. The merging of the maximum and the minimum into a single stationary point is analogous to the merging of the unstable and stable circular geodesic orbits into a single innermost stable circular orbit (ISCO).

The authors of [134] make a comment about the maximum mass  $\mu$  for which we would expect propagative quasinormal mode solutions to exist (i.e., the mass at which we would expect quasinormal resonance to occur), based on the WKB approximation (3.2.1). That the QNM is propagative means  $\omega^2 > \mu^2$ . Combining this with  $\omega_{QNM}^2 \approx V_g(r_{QNM})$ , it follows that we would expect  $\mu^2 < V_g(r_{QNM})$ . It is straightforward in the Schwarzschild spacetime to find  $r_{QNM}$  by considering the derivative of

the potential function, leading to an estimate for the maximum mass

$$\mu_{max}^2 = \frac{1}{54} \left[ 1 + \frac{3}{2}l - \frac{3}{2}l^2 - l^3 + (1 + l + l^2)^{3/2} \right], \quad (3.2.2)$$

where  $l = \ell(\ell + 1)$ . This general method works for spacetimes other than the Schwarzschild spacetime and fields other than the scalar field, but it becomes much more difficult, if not impossible, to procure an analytical expression for  $\mu_{max}$ .

### 3.2.1.4 QNMs and Geodesics

The link between QNMs and geodesic orbits can be made more explicit than Eq. (3.2.1) shows. A more detailed relationship between the two was derived for scalar fields in [34]. They perform the derivation for any static, spherically symmetric, asymptotically flat spacetime but we will describe the method specifically for Reissner-Nordström spacetime for simplicity.

First, one can define the *orbital angular velocity* of a timelike, circular geodesic orbit and then express it in terms of the  $g_{tt}$  metric function  $f_{rn}$ ,

$$\Omega \equiv \frac{\dot{\phi}}{\dot{t}} = \sqrt{\frac{f'_{rn}}{2r}} \Big|_{r=r_c}, \quad (3.2.3)$$

where  $r_c$  is the radius of the orbit. Here we have used expressions for  $E$  and  $L$  in the Reissner-Nordström spacetime

$$E = -\xi_t^\mu p_\mu = f_{rn} \dot{t}, \quad (3.2.4)$$

$$L = \xi_\phi^\mu p_\mu = r^2 \dot{\phi} \quad (3.2.5)$$

and then written  $E^2$  and  $L^2$  in terms of  $f_{rn}$  by setting  $V_g = V'_g = 0$ ,

$$E^2 = \frac{2f_{rn}^2}{2f_{rn} - rf'_{rn}}, \quad L^2 = \frac{r^3 f'_{rn}}{2f_{rn} - rf'_{rn}}. \quad (3.2.6)$$

Equation (3.2.3) also happens to be valid for a null geodesic orbit, which can be seen as the innermost possible timelike geodesic orbit [34].

Next we define the *Lyapunov exponent* of a geodesic orbit. In a spacetime, one can consider trajectories that are “close” to each other through a small change in initial conditions. The Lyapunov exponent  $\lambda$  then measures how quickly these neighboring trajectories converge to ( $\lambda < 0$ ), or diverge from ( $\lambda > 0$ ), the original trajectory. For circular timelike geodesics an expression for  $\lambda$  is [34]

$$\lambda \equiv \sqrt{\frac{V_g''}{2\dot{t}^2}} = \frac{1}{2} \sqrt{(2f_{rn} - rf'_{rn}) V_g''} \Big|_{r=r_c} \quad (3.2.7)$$

and for null orbits it is

$$\lambda = \frac{1}{\sqrt{2}} \sqrt{-\frac{r^2}{f_{rn}} \left( \frac{d^2 f_{rn}}{dr_*^2} \frac{1}{r^2} \right)} \Big|_{r=r_c}. \quad (3.2.8)$$

The lowest order WKB approximation for the QNMs of a scalar field (3.2.1) can then be written in terms of these quantities. In any static, spherically symmetric, asymptotically flat spacetime

$$\lim_{\ell \rightarrow \infty} \Re(\omega) = \Omega \ell, \quad \lim_{\ell \rightarrow \infty} \Im(\omega) = - \left( n + \frac{1}{2} \right) |\lambda|. \quad (3.2.9)$$

This is put to use in [56], where an expansion in powers of  $(\ell + 1/2)^{-1}$  is found for the scalar field QNMs in the Schwarzschild spacetime, valid in the eikonal limit. We compare this large  $\ell$  result to numerical data for the QNMs of the odd-parity Proca field in Sec. 3.4.

### 3.2.1.5 Unifying QNMs and QBSs

Although QNMs and QBSs have very different physical properties, mathematically they are intrinsically linked through the boundary conditions imposed on the radial differential equation (Eq. (3.1.9) for the scalar field, for example). QNMs can be defined by the condition that the Wronskian of the IN and UP solutions  $W(u^{in}, u^{up})$  (see Sec. 3.1), vanishes. (This definition of QNM comes from a consideration of the Green's function of the radial differential equation, see for example [39] where this is explained in the context of self-force calculations. The QNM frequencies are then the poles of the Green's function in the complex plane.) Hence,  $u^{in}$  and  $u^{up}$  must be linearly proportional. As  $r_* \rightarrow +\infty$  this implies that  $A_{in} = 0$ , while as  $r_* \rightarrow -\infty$  this implies that  $B_{out} = 0$ , leading to the boundary conditions that must be satisfied by QNMs

$$u_{\ell\omega}^{QNM}(r_*) \sim \begin{cases} C_-^{QNM} e^{-i\tilde{\omega}r_*} & r_* \rightarrow -\infty \\ C_+^{QNM} e^{+ikr_*} & r_* \rightarrow +\infty \end{cases}, \quad (3.2.10)$$

where  $C_{\pm}^{QNM}$  are constants,  $\tilde{\omega}$  was defined in (3.1.10) and  $k$  was defined below Eq. (3.1.11). The corresponding boundary conditions for a QBS are, similarly to the condition for an electron bound state in a hydrogen atom, that the field must decay away exponentially quickly as  $r_* \rightarrow +\infty$

$$u_{\ell\omega}^{QBS}(r_*) \sim \begin{cases} C_-^{QBS} e^{-i\tilde{\omega}r_*} & r_* \rightarrow -\infty \\ C_+^{QBS} e^{-qr_*} & r_* \rightarrow +\infty \end{cases}, \quad (3.2.11)$$

where  $q \equiv ik = \sqrt{\mu^2 - \omega^2}$ . The connection between QNMs and QBSs then follows from the fact that these two boundary conditions can be combined into

$$u_{\ell\omega}(r_*) \sim \begin{cases} C_- e^{-i\tilde{\omega}r_*} & r_* \rightarrow -\infty \\ C_+ e^{\pm qr_*} & r_* \rightarrow +\infty \end{cases}, \quad (3.2.12)$$

where taking the + sign on the second condition specifies QNMs and taking the – sign specifies QBSs. The fact that these two sets of frequencies are related by a simple sign change in the boundary condition is why our recurrence relation results presented at the end of this chapter and the next can be applied to find both of the spectra.

### 3.2.2 QNMs and QBSs of a Scalar Field

In this subsection we will briefly look at some prior work done on searching for the QNM and QBS frequencies of the scalar field on static black hole spacetimes. The QNMs of the massive scalar field on the Schwarzschild spacetime, with particular attention paid to the imaginary part (the decay rate) were studied in [90], and on the Reissner-Nordström spacetime in [91]. The QBSs of the massive, charged, scalar field on the spacetime of a charged, rotating black hole were discussed in [85] using Leaver’s method, but the non-rotating limit can be taken to observe how the situation would be handled on the Reissner-Nordström spacetime. We will summarise the methods used to find these frequencies.

The boundary conditions on the radial function  $u(r_*)$  take the general form of Eq.(3.2.12). The steps to obtain a recurrence relation to apply Leaver’s method on are as follows: one forms a Frobenius series style ansatz for  $u(r_*)$  that takes into account the irregular singular point of the radial equation (3.1.9) at infinity. This ansatz will contain a series of coefficients  $a_n$  that can be found by substituting the ansatz back into the equation. The result will be a recurrence relation of at least three terms of which we must seek a minimal solution, i.e., a solution for which the coefficients  $a_n$  decay as  $n \rightarrow \infty$ , see Sec.2.4. Such a solution will exist only for QNM or QBS frequencies, depending on the boundary condition chosen. For the rest of this subsection we will work with the boundary condition for QNMs, with the understanding that the substitution  $q \rightarrow -q$  will adapt the results to be suitable for finding QBSs.

To account for the irregular singular point, the boundary condition at infinity must be modified with the sub-leading in  $r$  behavior as follows,

$$u(r_*) \sim C_+ e^{qr_*} r^{-M\mu^2/q}. \quad (3.2.13)$$

An appropriate ansatz for the radial function now takes the form of the Frobenius series,

$$u(r) = e^{qr} (r - r_-)^{\chi-1} \sum_{n=0}^{\infty} a_n \left( \frac{r - r_+}{r - r_-} \right)^{n-i\rho}, \quad (3.2.14)$$

with

$$\chi = \frac{M(\mu^2 - 2\omega^2) + eQ\omega}{q}, \quad \rho = \frac{r_+(r_+\omega - eQ)}{r_+ - r_-}. \quad (3.2.15)$$

When this is substituted back into the radial equation (3.1.9), it can be solved term by term for each individual power of  $(r - r_+) / (r - r_-)$  and so one can arrive at a three-term recurrence relation for the radial coefficients  $a_n$

$$\begin{aligned} \alpha_0 a_1 + \beta_0 a_0 &= 0, \\ \alpha_n a_{n+1} + \beta_n a_n + \gamma_n a_{n-1} &= 0 \quad n > 0, \end{aligned} \quad (3.2.16)$$

where  $\alpha_n$ ,  $\beta_n$  and  $\gamma_n$  are given by [90],

$$\begin{aligned} \alpha_n &= (n+1)(n+1 - 4iM\omega), \\ \beta_n &= iMq^{-1}(\omega - iq) \left( 4M(\omega - iq)^2 + i(2n+1)(\omega - 3iq) \right) - 2n(n+1) - 1 - \ell(\ell+1), \\ \gamma_n &= \left( n + \frac{M(\omega - iq)^2}{q} \right)^2. \end{aligned} \quad (3.2.17)$$

This recurrence relation can then be solved with the continued fraction method detailed in Sec. 2.4.

### 3.2.3 QNMs and QBSs of a Vector Field

The QNMs and QBSs of a vector field on the Schwarzschild spacetime were studied using an extended version of Leaver's method in [126] following prior work by Konoplya [92]. An ansatz similar to the non-rotating, uncharged limit of the scalar field ansatz (3.2.14) is used,

$$u_{(i)}(r) = e^{-qr} r^\chi \left( 1 - \frac{2M}{r} \right)^{-2iM\omega} \sum_{n=0}^{\infty} a_n^{(i)} \left( 1 - \frac{2M}{r} \right)^n, \quad (3.2.18)$$

for each of the radial functions  $u_{(i)}(r)$  defined in (3.1.21), each with different radial coefficients, labeled  $a_n^{(i)}$ . Recurrence relations must then be found for each  $i$ .

For the odd-parity decoupled mode the coefficients  $a_n^{(4)}$  satisfy a three-term recurrence relation somewhat similar to Eq. (3.2.17) (see equations (34-38) of [126]). For the coupled even-parity modes, the recurrence relations for  $a_n^{(2)}$  and  $a_n^{(3)}$  also become coupled together. This is best represented as a *matrix valued* recurrence relation of the form

$$\begin{aligned} \alpha_0 \mathbf{U}_1 + \beta_0 \mathbf{U}_0 &= 0, \\ \alpha_n \mathbf{U}_{n+1} + \beta_n \mathbf{U}_n + \gamma_n \mathbf{U}_{n-1} &= 0 \quad n > 0, \end{aligned} \quad (3.2.19)$$

where  $\mathbf{U}_n$  is a vector coefficient

$$\mathbf{U}_n = \begin{pmatrix} a_n^{(2)} \\ a_n^{(3)} \end{pmatrix}$$

and  $\alpha_n, \beta_n$  and  $\gamma_n$  are  $2 \times 2$  matrices (see equation 41 of [126]). In particular the matrix  $\beta_n$  is non-diagonal, which is how the coupling between the recurrence relations manifests. An extension of Leaver's method using matrix-valued continued fractions is then needed to solve this [133].

To our knowledge, there is no work on recurrence relations for a charged vector field on a charged black hole spacetime. We perform this work at the end of this chapter in Sec. 3.4.2.2. This crosses over with our original work in chapter 4, where we find a five-term recurrence relation to solve the radial differential equation of the massive vector field on the Kerr spacetime (Eqs. (4.2.75)-(4.2.79)). In the non-rotating limit and for odd-parity modes, this reduces to a three-term recurrence relation (as expected, as  $a_n^{(4)}$  satisfies a three-term relation) and produces the same QNM spectrum as that found in [126].

### 3.3 Analytical Approximations for Quasibound States

In this section, in anticipation of finding QBSs numerically via Leaver's method, we discuss analytical approximations to these quantities. These approximations are found by the method of *asymptotic matching*, where two solutions to the radial differential equation valid in two different regions of the spacetime have their leading-order behaviours matched together where the two regions overlap. In the case of the scalar field we present some of the results of [69], while a more detailed explanation of the derivation of these results is given in the appendix. For the vector field, we present elements of the asymptotic matching calculation for the odd-parity, uncharged field on an uncharged black hole spacetime, while directing to reader to [126] for the full details. We briefly comment on progress made for the charged vector field in [127].

#### 3.3.1 Scalar Field

The primary results we are interested in from [69] are the approximate results for the real and imaginary parts of the QBS frequencies of a charged scalar field in the Reissner-Nordström spacetime. These are derived in more detail in appendix A. In particular we refer to Eq. (A.1.8) for the real part

$$\Re(\omega) \approx \mu \left[ 1 - \frac{1}{2} \left( \frac{M\mu - eQ}{\ell + n + 1} \right)^2 \right] \quad (3.3.1)$$

and Eq. (A.1.9) for the imaginary part

$$\Im(\omega) = \mu \delta \nu \frac{(M\mu - eQ)^2}{(\ell + 1 + n)^3}, \quad (3.3.2)$$

where  $\delta\nu$  is defined in Eq.(A.1.10). The important feature of (3.3.1) are that the real part is *hydrogenic*, in that it has a similar structure to the allowed energy levels of an electron in a hydrogen atom.

The imaginary part of the frequency is often written as a power of  $\mu$ . This allows us to more easily compare the relative magnitude of  $\Im(\omega)$  with that of other fields and so compare their decay rates (when  $\Im(\omega) < 0$ ) or rate of superradiant growth (when  $\Im(\omega) > 0$ ). In general, because  $\mu$  is small, a smaller power implies a faster rate of decay or growth. Equations (A.1.9) and (A.1.10) show that the imaginary part of the scalar field scales like  $\mu^{4\ell+6}$ . It is a closer inspection of the structure of the imaginary part (3.3.2) that leads one to the conclusion that the superradiant instability condition  $\Im(\omega) > 0$  is incompatible with the superradiance condition  $\omega < eQ/r_+$  and so superradiant instabilities cannot occur for a charged scalar field on the Reissner-Nordström spacetime.

### 3.3.2 Vector Field

The work of [126] performs a similar asymptotic matching calculation to approximate the bound state frequencies of the massive, uncharged vector field in the Schwarzschild spacetime. Here, they consider separately the single, decoupled odd-parity mode  $u_{(4)}$  and the two coupled even-parity modes  $u_{(2,3)}$ . As our numerical work in Sec.3.4 will focus on the odd-parity mode, we will detail the asymptotic matching calculation for that mode here. The asymptotic matching for the even parity modes is also attempted in [126], but it is much harder to perform and gives relatively limited results.

On the Schwarzschild spacetime the radial variable  $x = r/2M - 1$  is a natural choice, such that  $x = 0$  at the event horizon. The equation for the odd-parity mode is written in this variable as follows [126],

$$\left[ x^2(x+1)^2 \frac{d^2}{dx^2} + x(x+1) \frac{d}{dx} + V(x) \right] u_{(4)} = 0, \quad (3.3.3)$$

with the potential function

$$V(x) = 4M^2\omega^2(x+1)^4 - 4M^2\mu^2x(x+1)^3 - \ell(\ell+1)x(x+1). \quad (3.3.4)$$

The asymptotic matching of the odd-parity equation is very similar to that of the scalar field equation, shown in appendix A. The solution to Eq. (3.3.3) far from the black hole obeying the QBS boundary condition is (cf. Eq. (A.1.4))

$$u_{(4)}^{far} \sim e^{-z/2} z^{\ell+1} U(\ell+1-\chi, 2\ell+2, z), \quad (3.3.5)$$

where  $z = 4Mqx$  and  $U$  is a confluent hypergeometric function. The solution close to the event

horizon obeying the boundary condition of being purely ingoing is (cf. Eq. (A.1.7)),

$$u_{(4)}^{near} = x^{-2iM\omega} (x+1)^{1+\delta/M} {}_2F_1(-\ell - 2i\omega + \delta/M, \ell + 1 - 2iM\omega + \delta/M, 1 - 4iM\omega, -x), \quad (3.3.6)$$

where  $\delta = \sqrt{1 - 4\omega^2}$  and  ${}_2F_1$  is a Gauss hypergeometric function. Asymptotically matching these two functions in the overlap between the near and far regions leads to an expression for  $\Re(\omega)$  for the odd-parity mode of the massive vector field that is hydrogenic, in the same manner to that of the scalar field (3.3.1).

The imaginary part  $\Im(\omega)$  is calculated by continuing this matching process to the next-to-leading order, in the same manner as in [69], see equation (64) of [126]. This has the same scaling as for the scalar field ( $\mu^{4\ell+6}$ ), but the odd-parity vector field still decays faster due to a larger coefficient, twice as fast for the most unstable mode  $\ell = 1, n = 0$ .

Analytical approximations for the quasibound states of charged vector fields on the Reissner-Nordström spacetime have only been obtained under certain circumstances. In the case of a *marginally bound* vector field (where the bound state condition is only just satisfied,  $M\mu = eQ$ ) the authors of [127] (see equation (40)) produce an exact result in the double-extremal limit,  $Q = M$  and  $e = \mu$ . The most that can be shown away from this limit is that non-trivial solutions exist.

We will return to asymptotic matching arguments in the next chapter (Sec. 4.2.3) to obtain information about the quasibound states of these fields around rotating black holes. See also, Sec. A.2 in the appendix.

## 3.4 Numerical Methods and Results

Having discussed the various analytical methods that can be used to obtain approximations to the QBS frequencies, as well as having discussed the eikonal approximation and its relevance to QNM frequencies (see Eq. (3.2.1)), we now describe some of the methods used to find the frequencies numerically. We begin by detailing the method of direct integration of the radial equation used in prior works. This allowed the authors of [127] to arrive at a hydrogenic spectrum of frequencies for the even-parity polarizations of the Proca field. Then, we move on to presenting our original results from a direct application of Leaver's method to the case of the odd-parity, massive, charged vector field in Reissner-Nordström spacetime.

### 3.4.1 Direct Integration

The authors of [127] do not produce a recurrence relation while searching for QBSs of scalar and vector fields on the Reissner-Nordström spacetime. Instead they rely on direct numerical integration

of the radial differential equation starting from the event horizon and heading outwards to large  $r$ . They use as their starting value for the integration the value of the radial Frobenius series ansatz (3.2.14) just outside the event horizon.

They perform this integration for a grid of values of  $\omega$  in the complex plane and evaluate the solutions  $u_{(i)}$  at large values of  $r = r_{max}$ . These  $u_{(i)}(r_{max})$  form a merit function that will be large for  $\omega$  not close to a bound state frequency, but very small for  $\omega$  in the vicinity of a bound state frequency. They find numerically a good approximation for the real part of these frequencies for small  $\mu$  for the three polarizations of the vector field

$$\Re(\omega) \approx \mu \left[ 1 - \frac{1}{2} \left( \frac{M\mu - eQ}{\ell + S + n + 1} \right)^2 \right], \quad (3.4.1)$$

where the integer  $n \geq 0$  is the overtone number and  $S \in \{-1, 0, +1\}$  is the label used to designate the polarization state defined in Sec. 3.2.1. This agrees with the form of the analytical approximation found by [69], Eq. (3.3.1), if we designate that  $S = 0$  for the scalar field.

Details about the scaling of the imaginary part of the QBS frequencies of the Proca field are found numerically in [126] using both direct integration and a recurrence relation. The scaling is  $\Im(\omega) \sim \mu^{4\ell+2S+6}$  which also matches with the scalar field when  $S = 0$ . This shows a clear link between the QBSs of the odd-parity Proca field and the QBSs of the scalar field, but tells us nothing of the QNMs. We will study the relationship between the QNMs of the various polarizations of the Proca field and the QNMs of the scalar field numerically towards the end of chapter 4.

As the results of [127] and [126] show, direct integration of the radial equation is a suitable method for finding QBSs. However, it is much less useful when trying to find QNMs. This is because of the exponential growth of the QNM solution in the limit of large  $r$  on account of the boundary condition Eq. (3.2.12). This exponential growth is not a problem when finding QNMs through a recurrence relation, which we will now detail.

### 3.4.2 Recurrence Relations and Leaver's Method

#### 3.4.2.1 How many terms?

In [96] it is hypothesised that when solving a differential equation subject to QNM or QBS boundary conditions via a recurrence relation, the minimum number of terms in the relation is equal to the number of singular points the equation has. This is why all the recurrence relations in Schwarzschild spacetime we have described were three-term relations: the radial differential equation (for the scalar field, Eq. (3.1.9) with  $e = Q = 0$  in the potential) has two regular singular points situated at the origin and at the event horizon and a confluent singular point at radial infinity.

Leaver in [96] finds a four-term recurrence relation when considering the odd-parity gravitational perturbations of the Reissner-Nordström spacetime. This is consistent with four singular points located at  $0, r_+, r_-$  and infinity. Following this, one would also expect four-term recurrence relations for the scalar field and the odd-parity vector field on this spacetime.

We briefly note here that our five term recurrence relation for the vector field on the Kerr spacetime (Eqs. (4.2.75)-(4.2.79)), when applied to the two even-parity polarizations, retains all five terms even in the non-rotating limit  $a \rightarrow 0$ . This is because the radial differential equation for the even-parity vector field (see Eq. (4.2.51)) has singular points in such a limit at  $0, 2M$ , infinity and an additional pair of conjugate singularities in the complex plane.

### 3.4.2.2 A Recurrence Relation for Odd-Parity, Charged, Massive Vector Fields in Reissner-Nordström

In this section we will produce a recurrence relation and apply Leaver's method to find the QNMs and QBSs of an odd-parity charged, massive vector field on the Reissner-Nordström spacetime. To our knowledge, these QNMs have not been calculated previously.

We begin with equation (6) of [127], which is equivalent to Eq. (3.1.39)

$$\left[ r^2 f_{rn} \frac{d}{dr} \left( f_{rn} \frac{d}{dr} \right) + (\omega r - eQ)^2 - (\ell(\ell + 1) + \mu^2 r^2) \right] \Upsilon = 0, \quad (3.4.2)$$

where  $\Upsilon$  is the decoupled odd-parity mode, that can be expanded according to the ansatz (3.2.14). The number of terms in the recurrence relation for the radial coefficients  $a_n$  is sensitive to multiplying the radial differential equation (3.4.2) by an overall factor. We hypothesise the minimum number of terms for the recurrence relation is four, as mentioned at the beginning of this section. This can be achieved by imposing that the coefficient of the second derivative term in (3.4.2) is the horizon function  $r^2 f_{rn}$ . The coefficients of the resulting recurrence relation can be written in the form

$$\alpha_n = -8(n+2)q^2r_+(b(n+2) + ir_+(eQ - r_+\omega)), \quad (3.4.3)$$

$$\begin{aligned} \beta_n = 2q & \left\{ 2q^3r_+^2(r_+^2 - Q^2) + 2\omega(eQ - M\omega)(-(2n+3)Q^2 + r_+^2(3 + 2ieQ + 2n - 2ir_+\omega)) \right. \\ & - 2q \left[ (n^2 - 1)r_-^2 + Q^2(5 + \ell(\ell+1) + n(6 - 2ieQ + n) + 2inr_+\omega + r_+^2\omega^2) \right. \\ & \left. \left. + r_+^2(2e^2Q^2 - \ell(\ell+1) - 2(n+1)(n+2) + 2i(2n+3)r_+\omega + 3r_+^2\omega^2 - 2ieQ(2n+3 - 3ir_+\omega)) \right] \right. \\ & \left. + q^2[3r_+^3(3 + 2ieQ + 2n - 2ir_+\omega) + Q^2((2n+3)r_- + 2ir_+(6i - eQ + 4in + r_+\omega))] \right\}, \end{aligned} \quad (3.4.4)$$

$$\begin{aligned} \gamma_n = -q^2 & \left[ 8b\ell(\ell+1)r_- + 8bn^2(r_+ + 2r_-) + 4n(2r_-^2 + qr_-^3 + r_+^2(qr_+ + 2) + Q^2(-4 - 5qr_- + 3qr_+)) \right. \\ & \left. + q(-2r_-^3 + Q^2(4r_- - 6r_+) + 4r_+^3 + q(-5Q^4 - Q^2r_-^2 + 5Q^2r_+^2 + r_+^4)) \right] + 4i\omega q^3 r_+^4 \\ & - 2iq^2\omega(6MQ^2 + 2qQ^4 - 2Q^2r_- - 2Mr_-^2 + r_-^3 + (3 - 8n)Q^2r_+ - 4r_+^2(M + 2qQ^2) - 2(2n+1)r_+^3) \\ & + q\omega^2(32bM^2n + q(Q^4 + Q^2r_-^2 + 11Q^2r_+^2 + 3r_+^4) + 2M(2r_-^2 + r_+^2(4 + 3qr_+) + Q^2(-6 + qr_- + 4qr_+))) \\ & - 2iMq\omega^3(4bMr_+ + 3r_+^3 + Q^2(r_- + 4r_+)) - 8bM^2r_+\omega^4 + 4e^2Q^2(q - i\omega)(q(3Q^2 + r_+^2) - 2ibr_+\omega) \\ & + 4eQ \left[ -iq^2(r_+^2(2 + 2n + qr_+) + Q^2(-2 + 4n - qr_- + 4qr_+)) + iq\omega^2(3r_+^3 + Q^2(r_- + 4r_+)) \right. \\ & \left. - 2M\omega^3(Q - r_+)(Q + r_+) - q\omega(8bMn + r_-^2 + r_+^2(2 + 3qr_+) + Q^2(-3 + qr_- + 8qr_+)) \right], \end{aligned} \quad (3.4.5)$$

$$\begin{aligned} \delta_n = 4r_- & \left\{ -2ib^2Mq\omega(q - i\omega)^2 + q \left[ -2eQ^2M(q - i\omega) - 2i\omega((n-1)qr_+^2 + M^3(q - i\omega)^2) \right. \right. \\ & \left. \left. + eQ(2iqr_+(n-1 + Mq) + q\omega(Q^2 + r_-^2 + 2r_+(M + r_+)) - i\omega^2(Q^2 + r_-^2 + 2r_+^2)) \right] \right. \\ & + 2b \left[ M^2Q^4 + \omega^2(eQ - M\omega)^2 + 2Mq^3(n-1 - iM\omega) + q^2((n-1)^2 - 2M^2\omega^2) \right. \\ & \left. \left. + q\omega(i e^2Q^2 + 2eQ(n-1 - iM\omega) + 2M\omega(1 - n + iM\omega)) \right] \right\}. \end{aligned} \quad (3.4.6)$$

We then apply one use of Gaussian elimination, see Eq. (2.4.4), before numerically solving the resulting continued fraction equation (2.4.8). In the recurrence,  $q$  can be set to either  $\pm\sqrt{\mu^2 - \omega^2}$ , where we select  $\Re(q) > 0$  for QBSs and  $\Re(q) < 0$  for QNMs. Hence, the recurrence relation is

suitable for calculating both sets of frequencies. To verify our result, we used the recurrence to calculate some QBSs to compare with the data presented in [127] Table I and we find agreement to seven significant figures in the real part and three significant figures in the imaginary part (this discrepancy in the level of accuracy between the real and imaginary parts is also present in the case of the rotating black hole, and is discussed in more detail in Sec. 4.2.5). We used the hydrogenic approximation (3.4.1) (with  $S = 0$  according to [127]) to form the initial guess for the root-finding algorithm for a small value of the mass  $\mu_{start} = 0.1$  and then used the previous QBS frequency as the initial guess to find the next as we increment  $\mu$ . Some example data for the real part is presented in Fig. 3.4.1, where we have plotted

$$f(\Re(\omega)) = 2(\ell + n + 1) \frac{1 - \Re(\omega)/\mu}{(M\mu)^2} \quad (3.4.7)$$

to show agreement with the hydrogenic approximation in the small  $\mu$  limit. The corresponding imaginary part is shown in Fig. 3.4.2 and the results are also consistent with the mass scaling of the analytical approximation presented in Sec. 3.3.2.

For the QNMs, we fixed the mass  $\mu$  of the field and used the known QNM of the uncharged field in Schwarzschild spacetime (see [126, 54]) as the initial guess for the root-finding. We then varied the black hole charge  $Q$  from  $Q/M = 0$  up to  $Q/M = 1$ , the extremal value, in small increments, using the previously found QNM as the initial guess for the root-finding each time. Finally, we fix  $Q$  and vary the charge coupling  $eQ$  in small increments in the same manner as we did with  $Q$ . This produces the data in Figs. 3.4.3 and 3.4.4 for  $\ell = 1$  and  $\ell = 2$  respectively.

We now discuss some of the qualitative features of the QNM data. For the uncharged field we see that the oscillation frequency  $\Re(\omega)$  increases with  $Q$  all the way up to the extremal value. The decay rate  $-\Im(\omega)$  increases until a critical value of  $Q$ , after which the QNMs curve upwards towards the real axis. We can compare this data for the uncharged field with the eikonal approximation in Eq. (3.2.1). This is done in Fig. 3.4.5. We see that the eikonal approximation has the same qualitative behaviour as the data obtained from the recurrence relation, even for low  $\ell$  modes.

In the case of the charged field, both the oscillation frequency and the decay rate consistently increases as the particle charge  $e$  increases.

## Conclusion

In this chapter we have summarised results throughout the literature concerning uncharged and charged, massive scalar and vector fields propagating on the Schwarzschild and Reissner-Nordström spacetimes. These included analytical approximations to their quasinormal modes and quasibound

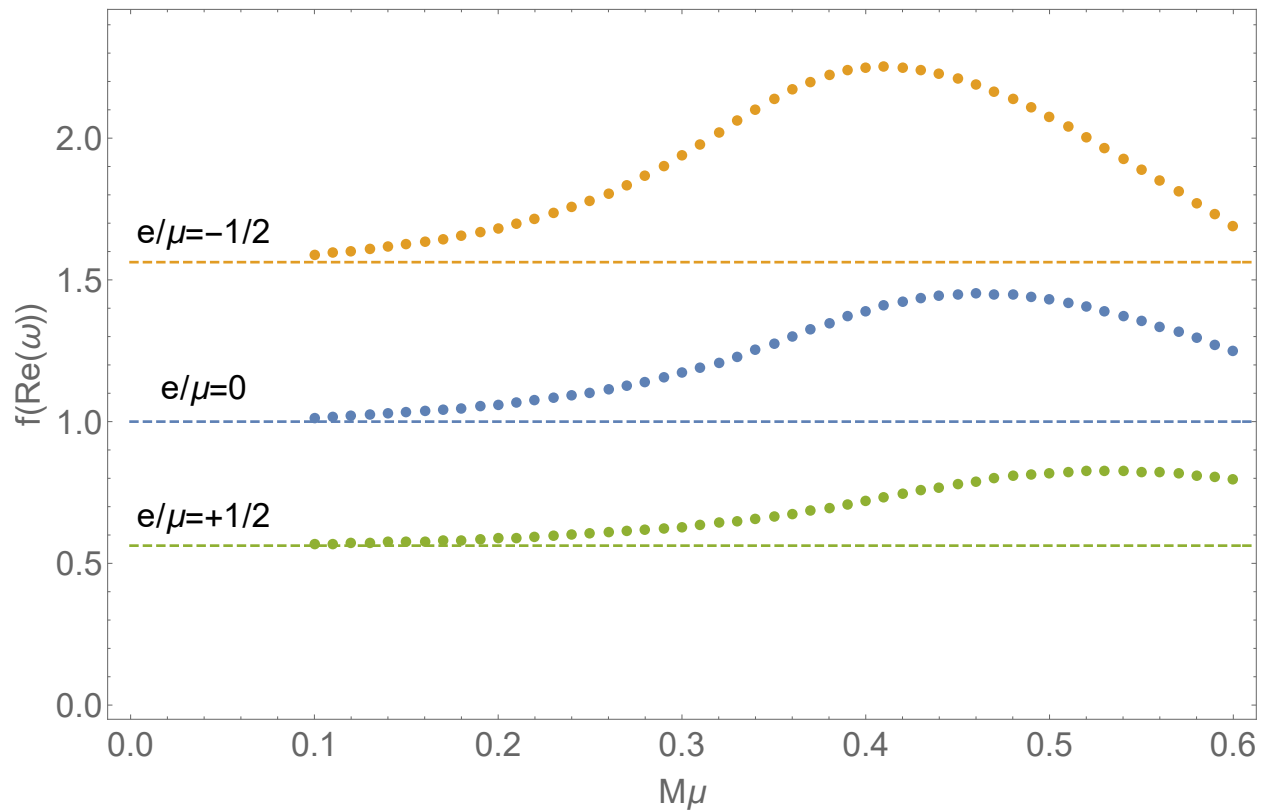


Figure 3.4.1: A function  $f(\Re(\omega))$  of the real part of the QBS frequencies of the odd-parity  $\ell = 1, n = 0$  Proca field on the Reissner-Nordström spacetime of charge to mass ratio  $Q/M = 1/2$ . The dashed lines show  $(1 - eQ/M\mu)^2$ , the expected behaviour of  $f(\Re(\omega))$  from the hydrogenic approximation in the small  $\mu$  limit.

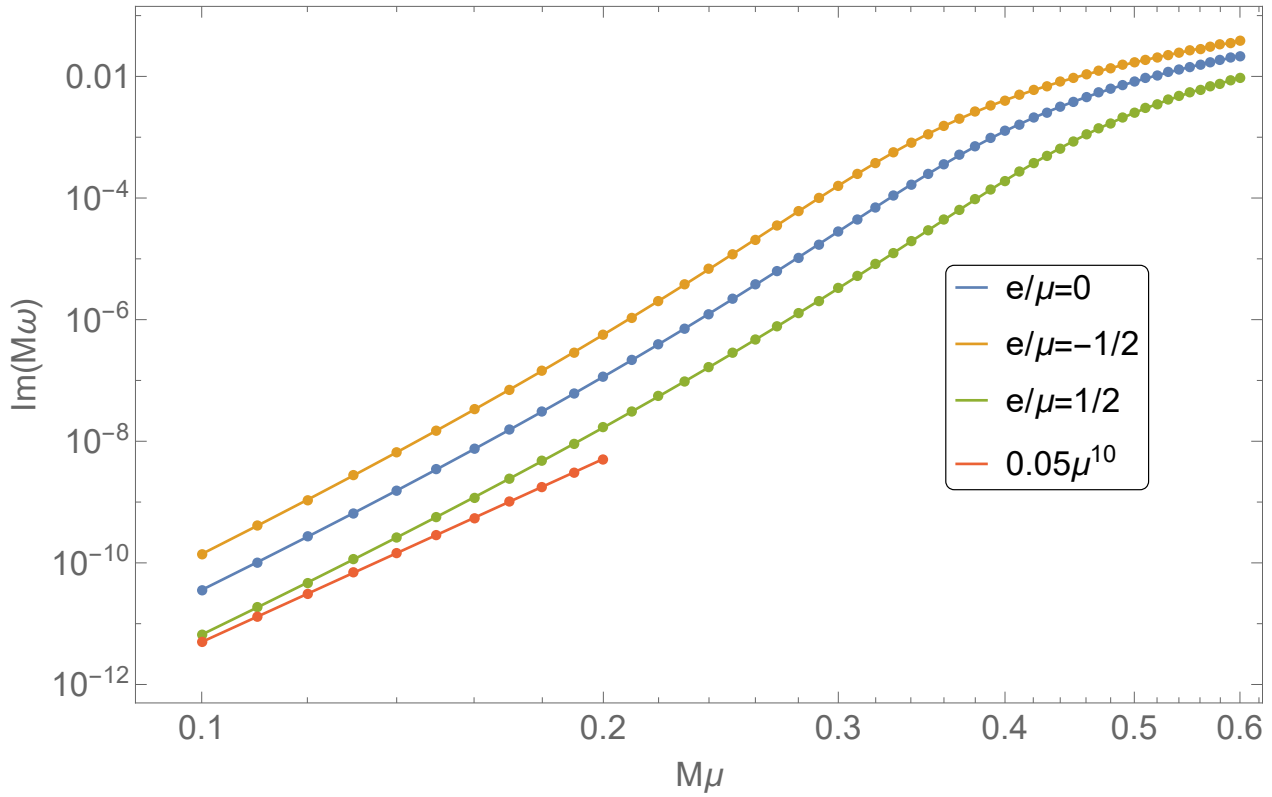


Figure 3.4.2: The decay rate  $-\Im(\omega)$  of the QBS frequencies of the odd-parity  $\ell = 1, n = 0$  Proca field on the Reissner-Nordström spacetime of charge to mass ratio  $Q/M = 1/2$ . The red points show a guide line proportional to  $\mu^{10}$ , the expected scaling of  $\Im(\omega)$  in the small  $\mu$  limit for the odd-parity vector polarization.

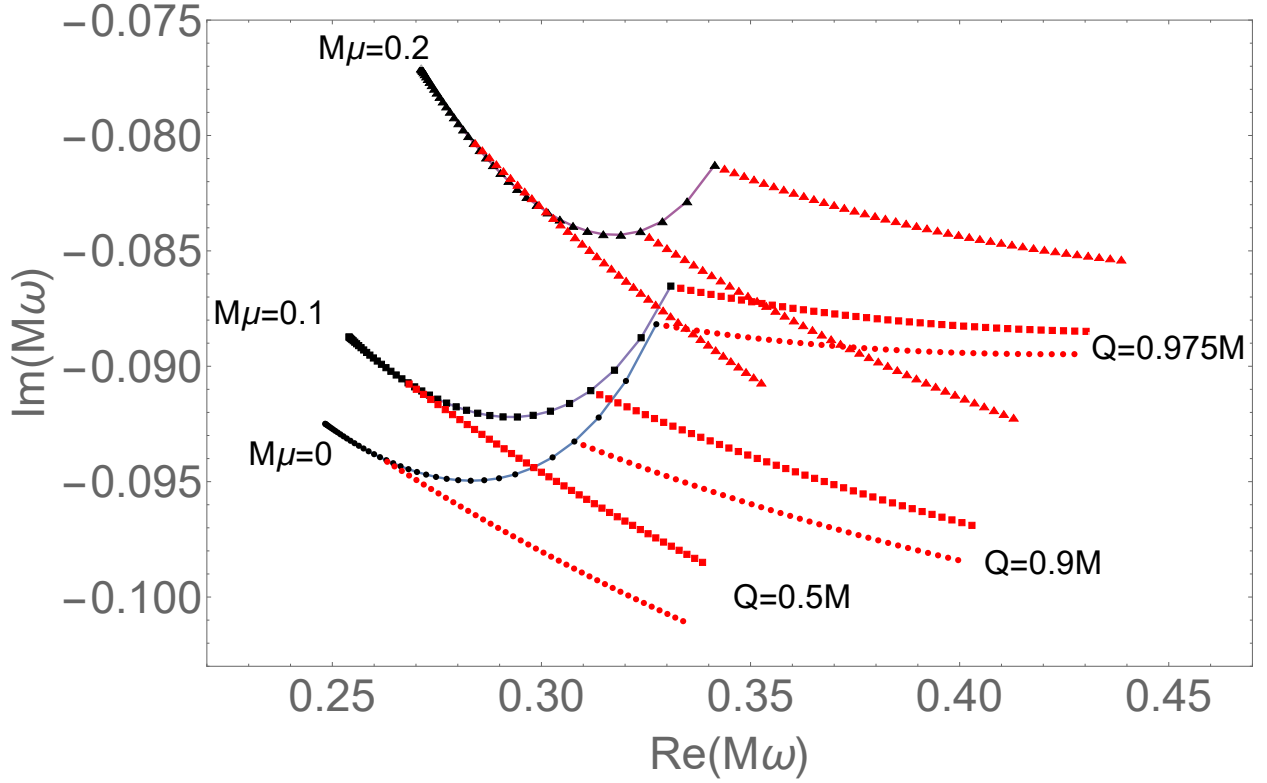


Figure 3.4.3: The QNMs of the odd-parity,  $\ell = 1, n = 0$  Proca field of charge  $e$  in the Reissner-Nordström spacetime of charge to mass ratio  $Q/M$ , in the complex frequency plane. Black points are for no charge coupling  $e = 0$  and  $Q/M$  increasing in increments of 0.025. The red points are for non-zero  $eQ$  increasing in increments of 0.005 to a maximum of 0.2, with  $Q/M$  fixed at 0.5, 0.9 or 0.975. Circles, squares and triangles are for mass couplings of  $M\mu = 0, 0.1, 0.2$  respectively.

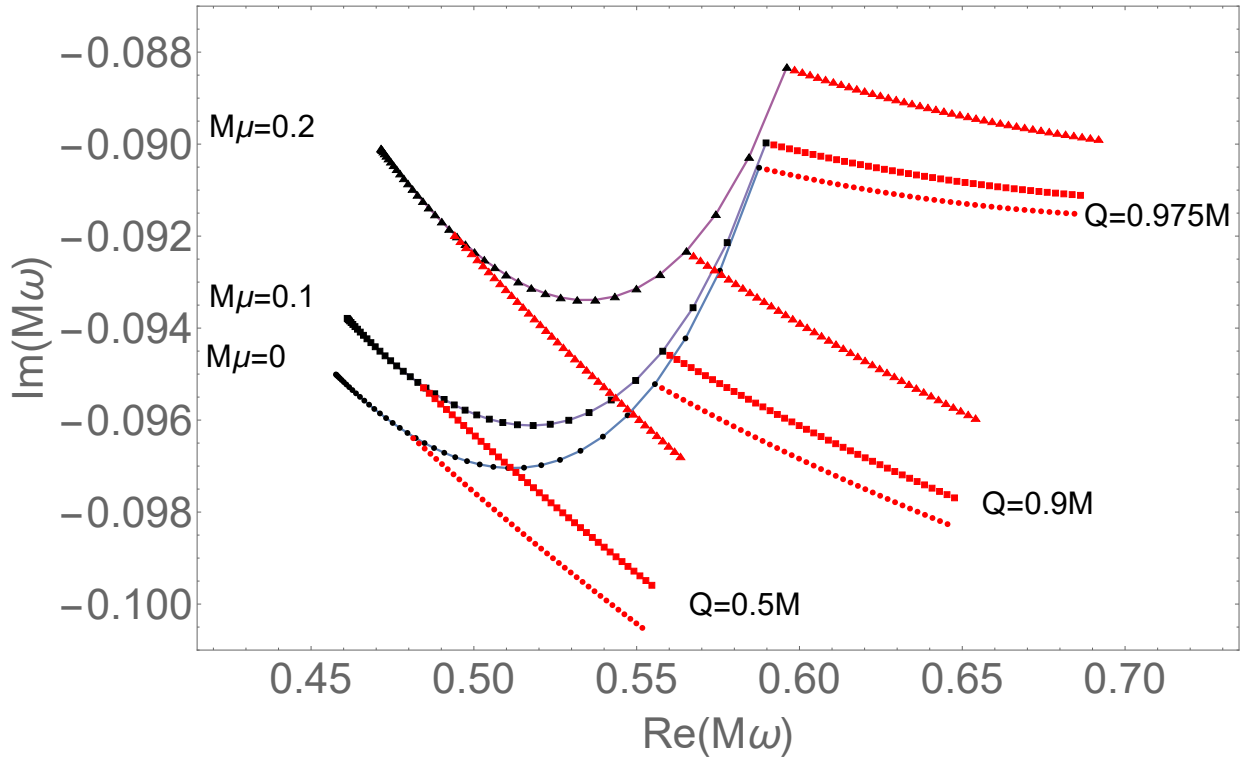


Figure 3.4.4: The QNMs of the odd-parity,  $\ell = 2, n = 0$  Proca field of charge  $e$  in the Reissner-Nordström spacetime of charge  $Q/M$ , in the complex frequency plane with the same  $Q$  and  $e$  increments as the previous figure.

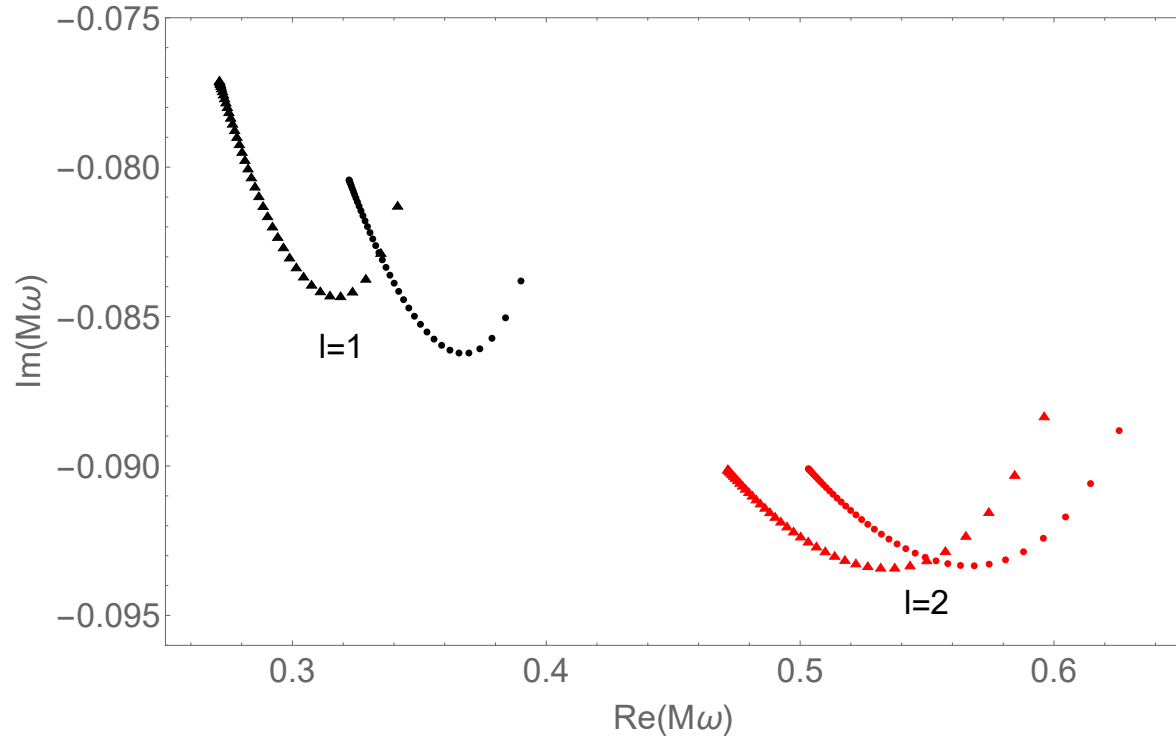


Figure 3.4.5: The QNMs of the odd-parity, uncharged, massive vector field in the Reissner-Nordström spacetime of charge  $Q$ , plotted in the complex plane. The  $\ell = 1, n = 0$  QNMs are plotted in black and the  $\ell = 2, n = 0$  QNMs are plotted in red. The circle points are the results of the eikonal approximation, Eq. (3.2.1) with the geodesic potential of (2.3.12), the triangle points are the results of using the recurrence relation, Eqs. (3.4.3)-(3.4.6).

state frequencies. We concluded with an original numerical calculation of the QNMs of the odd-parity charged, massive vector field around a static, charged black hole, the results of which are presented in Figs. 3.4.3, 3.4.4 and 3.4.5.

## Chapter 4

# Bosonic Fields on Rotating Black Hole Spacetimes

### Introduction and Overview

In this chapter we discuss QBSs and QNMs of scalar and vector fields on rotating black hole spacetimes. As we did in the static case in the previous chapter, we begin with the solution of the equations of motion via separation of variables. We then discuss the asymptotic matching method to analytically approximate the quasibound state frequencies and the numerical methods used to calculate them and the QNMs [18, 45]. We conclude with an original calculation of the QNMs of the Proca field on the Kerr spacetime via Leaver's method, as per our own work with Dolan in [117] and then an extension of that work to the calculation of the same QNMs on the Kerr-Newman spacetime.

### 4.1 Massless Fields on the Kerr Spacetime

Before we discuss massive vector perturbations on rotating black hole spacetimes, we describe the derivation of the corresponding equation for massless perturbations. This will be used in Sec. 4.2 when we consider the propagation of the electromagnetic field on the Kerr spacetime.

The motion of the massless scalar field and of two of the the Maxwell scalars of the electromagnetic field on the Kerr spacetime are governed by the same differential equation, called the Teukolsky

equation, [138, 137]. Written fully, it takes the form

$$\begin{aligned}
& \left[ \frac{(r^2 + a^2)^2}{\Delta} - a^2 \sin^2 \theta \right] \frac{\partial^2 \Phi}{\partial t^2} + \frac{4Mar}{\Delta} \frac{\partial^2 \Phi}{\partial t \partial \phi} + \left[ \frac{a^2}{\Delta} - \frac{1}{\sin^2 \theta} \right] \frac{\partial^2 \Phi}{\partial \phi^2} \\
& - \Delta^{-s} \frac{\partial}{\partial r} \left( \Delta^{s+1} \frac{\partial \Phi}{\partial r} \right) - \frac{1}{\sin \theta} \frac{\partial}{\partial \theta} \left( \sin \theta \frac{\partial \Phi}{\partial \theta} \right) - 2s \left[ \frac{a(r-M)}{\Delta} + \frac{i \cos \theta}{\sin^2 \theta} \right] \frac{\partial \Phi}{\partial \phi} \\
& - 2s \left[ \frac{M(r^2 - a^2)}{\Delta} - r - ia \cos \theta \right] \frac{\partial \Phi}{\partial t} + (s^2 \cot^2 \theta - s) \Phi = 0.
\end{aligned} \tag{4.1.1}$$

The three quantities we are interested in that will satisfy this equation are the massless scalar field (when  $s = 0$ ), the Maxwell scalar  $\Psi_1$  (when  $s = 1$ ) and  $(r - ia \cos \theta)^2 \Psi_{-1}$  (when  $s = -1$ ), see Eq. (3.1.17). Note that the remaining Maxwell scalar  $\Psi_0$  does not satisfy the Teukolsky equation.

We now discuss the derivation of this equation. We will focus primarily on the derivation when  $s = \pm 1$ , as for  $s = 0$  Eq. (4.1.1) is exactly the massless Klein-Gordon equation ((2.1.14) with  $\mu = 0$ ) in the Kerr spacetime in Boyer-Lindquist coordinates.

The Maxwell equations on the tensor  $F_{\mu\nu}$  ((2.1.9) and (2.2.2)) can be written as a set of four differential equations between the Maxwell scalars. The form of these equations depends on the null tetrad chosen. In a general null tetrad  $\{\ell^\mu, n^\mu, m^\mu, \bar{m}^\mu\}$  with spin coefficients  $\alpha, \beta, \gamma, \varepsilon, \rho, \tau, \pi, \mu$  defined in [108] these four equations are

$$(D - 2\rho) \Psi_0 = (\delta^* + \pi - 2\alpha) \Psi_1, \tag{4.1.2}$$

$$(\delta - 2\tau) \Psi_0 = (\bar{\Delta} + \mu - 2\gamma) \Psi_1, \tag{4.1.3}$$

$$(D - \rho + 2\varepsilon) \Psi_{-1} = (\delta^* + 2\pi) \Psi_0, \tag{4.1.4}$$

$$(\delta - \tau + 2\beta) \Psi_{-1} = (\bar{\Delta} + 2\mu) \Psi_0, \tag{4.1.5}$$

with the three differential operators  $D = \ell^\mu \partial_\mu$ ,  $\bar{\Delta} = n^\mu \partial_\mu$ ,  $\delta = m^\mu \partial_\mu$ . Following [138], Eqs. (4.1.2) and (4.1.3) can be combined into a single second order equation for  $\Psi_1$  and (4.1.4) and (4.1.5) can be combined into an equation for  $\Psi_{-1}$

$$[(D - \varepsilon + \varepsilon^* - 2\rho - \rho^*)(\bar{\Delta} + \mu - 2\gamma) - (\delta - \beta - \alpha^* - 2\tau + \pi^*)(\delta^* + \pi - 2\alpha)] \Psi_1 = 0, \tag{4.1.6}$$

$$[(\bar{\Delta} + \gamma - \gamma^* + 2\mu + \mu^*)(D - \rho + 2\varepsilon) - (\delta^* + \alpha + \beta^* + 2\pi - \tau^*)(\delta - \tau + 2\beta)] \Psi_{-1} = 0. \tag{4.1.7}$$

When we specify the Kinnersley tetrad (2.2.17) the spin coefficients are

$$\rho = -1/(r - ia \cos \theta), \quad \beta = -\rho^* \cot \theta / (2\sqrt{2}), \quad \pi = ia\rho^2 \sin \theta / \sqrt{2}, \quad \alpha = \pi - \beta^*, \tag{4.1.8}$$

$$\tau = -ia\rho\rho^* \sin \theta / \sqrt{2}, \quad \mu = \rho^2 \rho^* \Delta / 2, \quad \gamma = \mu + \rho\rho^* (r - M) / 2, \quad \varepsilon = 0$$

and this reduces Eq. (4.1.6) to the Teukolsky equation (4.1.1) for  $s = 1$  satisfied by  $\Psi_1$  and (4.1.7) to the Teukolsky equation for  $s = -1$  satisfied by  $(r - ia \cos \theta)^2 \Psi_{-1}$ . In a similar manner to the

generalised Regge-Wheeler equation (Eq. (3.1.7) with potential given by (3.1.19)), the Teukolsky equation can also be applied in the context of gravitational perturbations: in terms of the Weyl scalars,  $\Theta_2$  and  $(r - ia \cos \theta)^4 \Theta_{-2}$  satisfy (4.1.1) with  $s = 2$  and  $s = -2$  respectively.

The Teukolsky equation, like the Regge-Wheeler equation, is amenable to a decomposition into modes

$$\Phi = \int d\omega \sum_{\ell m} R_{\ell m}(r) S_{\ell m}(\theta) e^{-i\omega t + im\phi}. \quad (4.1.9)$$

The angular functions are called *spin-weighted spheroidal harmonics* of spin weight  $s$  and they satisfy the equation

$$\left[ \frac{1}{\sin \theta} \frac{d}{d\theta} \left( \sin \theta \frac{d}{d\theta} \right) + a^2 \omega^2 \cos^2 \theta - \frac{(m + s \cos \theta)^2}{\sin^2 \theta} - 2a\omega s \cos \theta + s + 2ma\omega - a^2 \omega^2 + \tilde{\lambda} \right] S_{\ell m} = 0, \quad (4.1.10)$$

where  $\tilde{\lambda}$  is a separation constant called the *spin-weighted spheroidal eigenvalue*. This separation also leads to a second order ODE for the radial function

$$\Delta^{-s} \frac{d}{dr} \left[ \Delta^{s+1} \frac{dR}{dr} \right] + \left[ \frac{K_r^2 - 2is(r - M)K_r}{\Delta} + 4is\omega r - \tilde{\lambda} \right] R = 0, \quad (4.1.11)$$

where

$$K_r = (r^2 + a^2)\omega - am. \quad (4.1.12)$$

## 4.2 Vector Fields on Kerr Spacetime

### 4.2.1 The Electromagnetic Field

The discussion of the electromagnetic field on the Kerr spacetime begins with the same separation of  $F_{\mu\nu}$  into complex scalar functions (the Maxwell scalars, see Eq. (3.1.17)) as was done in the non-rotating case, with the Kinnersley tetrad  $\{\ell^\mu, n^\mu, m^\mu, \bar{m}^\mu\}$  as in (2.2.17). Then, Maxwell's equations (2.1.9) and (2.2.2) become four equations relating the Maxwell scalars. From these equations,  $\Psi_0$  can be eliminated and the remaining two scalars  $\Psi_{\pm 1}$  satisfy Teukolsky's equation (4.1.1). Thus, a separation of variables can be applied to both of them

$$\Psi_{+1} = R_{+1} S_{+1} e^{-i\omega t + im\phi}, \quad 2(r - ia \cos \theta)^2 \Psi_{-1} = R_{-1} S_{-1} e^{-i\omega t + im\phi}. \quad (4.2.1)$$

The equations for the functions  $R_{\pm 1}$  and  $S_{\pm 1}$  can be written succinctly as (see for example [54])

$$\left(\Delta \mathcal{D}_0^\dagger \mathcal{D}_0 - 2i\omega r\right) R_{-1} = \lambda R_{-1}, \quad (4.2.2)$$

$$\left(\Delta \mathcal{D}_0 \mathcal{D}_0^\dagger + 2i\omega r\right) \Delta R_{+1} = \lambda \Delta R_{+1}, \quad (4.2.3)$$

$$\left(\mathcal{L}_0 \mathcal{L}_1^\dagger + 2a\omega \cos \theta\right) S_{-1} = -\lambda S_{-1}, \quad (4.2.4)$$

$$\left(\mathcal{L}_0^\dagger \mathcal{L}_1 - 2a\omega \cos \theta\right) S_{+1} = -\lambda S_{+1}, \quad (4.2.5)$$

where  $\lambda$  is defined

$$\lambda \equiv \tilde{\lambda} + 2ma\omega - a^2\omega^2 \quad (4.2.6)$$

and  $\tilde{\lambda}$  is the spin-weighted spheroidal eigenvalue for  $s = -1$ . The radial differential operators  $\mathcal{D}$  and angular differential operators  $\mathcal{L}$  are (see [43])

$$\mathcal{L}_n = \partial_\theta + m \csc \theta - a\omega \sin \theta + n \cot \theta, \quad (4.2.7)$$

$$\mathcal{L}_n^\dagger = \partial_\theta - m \csc \theta + a\omega \sin \theta + n \cot \theta, \quad (4.2.8)$$

$$\mathcal{D}_n = \partial_r - i\Delta^{-1}K_r + n\Delta^{-1}\partial_r\Delta, \quad (4.2.9)$$

$$\mathcal{D}_n^\dagger = \partial_r + i\Delta^{-1}K_r + n\Delta^{-1}\partial_r\Delta. \quad (4.2.10)$$

This clearly shows that the functions with index  $+1$  and those with index  $-1$  are not independent of one another:  $R_{-1}$  and  $\Delta R_{+1}$  satisfy complex-conjugate equations and the equations for  $S_{\pm 1}$  satisfy a symmetry between each other under the transformation  $\theta \rightarrow \pi - \theta$ .

In this formalism the remaining Maxwell scalar  $\Psi_0$  isn't separable and doesn't satisfy Teukolsky's equation. As is explained by Lunin in [101], this remaining scalar carries the required information to be able to discuss both polarization states of the electromagnetic field, without it we can only describe a single polarization. Lunin attempts to address this problem by forming a different ansatz. This will be the precursor to the Lunin-Frolov-Krtouš-Kubizňák (LFKK) ansatz that will allow the differential equation for the massive vector field in Kerr spacetime to be separated.

The ansatz specifies the form of the inner product of the vector potential with each of the four basis null vectors

$$\begin{aligned} \ell^\mu A_\mu &= G_+(r) \ell^\mu \partial_\mu Z, & n^\mu A_\mu &= G_-(r) n^\mu \partial_\mu Z, \\ m^\mu A_\mu &= F_+(\theta) m^\mu \partial_\mu Z, & \bar{m}^\mu A_\mu &= F_-(\theta) \bar{m}^\mu \partial_\mu Z, \end{aligned} \quad (4.2.11)$$

$$Z = e^{i\omega t + im\phi} R(r) S(\theta).$$

To show that this ansatz covers both polarizations, Lunin remarks that to maintain consistency with Maxwell's equations the only way to get physically relevant solutions is to choose either  $G_+ \neq 0$  or  $F_+ \neq 0$ . These choices are mutually exclusive, leading to two distinct "branches" of solution,

representing the two polarization states. Maxwell's equations can also be satisfied by setting each of the functions  $G_{\pm}, F_{\pm}$  to unity, but this corresponds to a solution that is pure gauge. This third “gauge polarization” state will become physically relevant when we discuss massive vector fields.

It is possible to derive a direct relationship between Lunin's ansatz (with the two functions  $R, S$ ) and the original ansatz used by Teukolsky (with the four functions  $R_{\pm}, S_{\pm}$ ), but the explanation is best left until the analysis is performed in the massive case, see Eqs. (4.2.41) and (4.2.42).

## 4.2.2 The Separability of the Proca Equation on Kerr Spacetime

### 4.2.2.1 The LFKK Ansatz

Frolov, Krtouš, Kubizňák and Santos showed in [66], contrary to the consensus at the time, that the Proca equation in a Kerr-NUT-(A)dS spacetime is separable through the use of the principal tensor  $h_{\mu\nu}$ , defined in Sec. 2.1.6. This remarkable result has since been utilised to study the QBSs and superradiant instabilities of the Proca field on the Kerr [54] and Kerr-Newman spacetimes [41], building on work done prior in [59, 60]. Such work was often restricted to slowly-rotating black holes [113], a restriction that is not required with the LFKK method. This separability of the Proca equation has also been used to study the possibility of the existence of black holes with Proca hair, see [128].

Explicitly, Frolov *et al.*, showed the equation of motion of a massive, uncharged vector perturbation (cf. Eq. (2.1.17)),

$$\nabla_{\nu} W^{\mu\nu} + \mu^2 W^{\mu} = 0, \quad (4.2.12)$$

is amenable to a separation of variables if one applies the LFKK ansatz

$$W^{\mu} = B^{\mu\nu} \nabla_{\nu} Z, \quad (4.2.13)$$

where  $Z$  is a scalar function. Here,  $B^{\mu\nu}$  is called the *polarization tensor* and is defined in terms of the principal tensor  $h_{\mu\nu}$  via

$$B^{\mu\nu} (g_{\nu\rho} + i\nu h_{\nu\rho}) = \delta_{\rho}^{\mu}, \quad (4.2.14)$$

where  $\nu$  is a separation constant, called the angular eigenvalue. The polarization tensor can be written in Boyer-Lindquist coordinates as (with  $\Delta$  and  $\Sigma$  as in (2.2.5) and (2.2.6) respectively, with  $Q = 0$ )

$$B^{\mu\nu} = \frac{\Delta}{2\Sigma} \left( \frac{\ell_{+}^{\mu} \ell_{-}^{\nu}}{1 - i\nu r} + \frac{\ell_{-}^{\mu} \ell_{+}^{\nu}}{1 + i\nu r} \right) + \frac{1}{2\Sigma} \left( \frac{m_{+}^{\mu} m_{-}^{\nu}}{1 - a\nu \cos \theta} + \frac{m_{-}^{\mu} m_{+}^{\nu}}{1 + a\nu \cos \theta} \right), \quad (4.2.15)$$

using the basis null vectors

$$\ell_{\pm}^{\mu} = \left[ \pm \frac{r^2 + a^2}{\Delta}, 1, 0, \pm \frac{a}{\Delta} \right], \quad (4.2.16)$$

$$m_{\pm}^{\mu} = [\pm ia \sin \theta, 0, 1, \pm i \csc \theta]. \quad (4.2.17)$$

The separation splits the Proca equation into two second-order ODEs. To show this, we follow the explanation of [55]. The LFKK ansatz allows us to write  $W^{\mu}$  in the form

$$W^{\mu} = \frac{1}{2\Sigma} \left[ \frac{\Delta \mathcal{D}_0^{\dagger} Z}{1 - i\nu r} \ell_{+}^{\mu} + \frac{\Delta \mathcal{D}_0 Z}{1 + i\nu r} \ell_{-}^{\mu} + \frac{\mathcal{L}_0 Z}{1 - a\nu \cos \theta} m_{+}^{\mu} + \frac{\mathcal{L}_0^{\dagger} Z}{1 + a\nu \cos \theta} m_{-}^{\mu} \right], \quad (4.2.18)$$

with the radial  $\mathcal{D}$  and angular  $\mathcal{L}$  operators defined in Eqs. (4.2.7)-(4.2.10). We know that the Proca equation necessarily implies the Lorenz condition (see Sec. 2.1.3) and so we need to write both the Proca equation and the Lorenz condition in this ansatz. We start with the Lorenz condition, like so,

$$\nabla_{\mu} W^{\mu} = \mathcal{D}_0 \left( \frac{\Delta \mathcal{D}_0^{\dagger} Z}{1 - i\nu r} \right) + \mathcal{D}_0^{\dagger} \left( \frac{\Delta \mathcal{D}_0 Z}{1 + i\nu r} \right) + \mathcal{L}_1^{\dagger} \left( \frac{\mathcal{L}_0 Z}{1 - a\nu \cos \theta} \right) + \mathcal{L}_1 \left( \frac{\mathcal{L}_0^{\dagger} Z}{1 + a\nu \cos \theta} \right) = 0. \quad (4.2.19)$$

This PDE for the scalar function  $Z$  is clearly separable in the usual manner

$$Z = R(r) S(\theta) e^{-i\omega t} e^{im\phi} \quad (4.2.20)$$

and so Eq. (4.2.19) splits into two ODEs like so,

$$\mathcal{D}_0 \left( \frac{\Delta \mathcal{D}_0^{\dagger} R}{1 - i\nu r} \right) + \mathcal{D}_0^{\dagger} \left( \frac{\Delta \mathcal{D}_0 R}{1 + i\nu r} \right) + \kappa_1 R = 0, \quad (4.2.21)$$

$$\mathcal{L}_1^{\dagger} \left( \frac{\mathcal{L}_0 S}{1 - a\nu \cos \theta} \right) + \mathcal{L}_1 \left( \frac{\mathcal{L}_0^{\dagger} S}{1 + a\nu \cos \theta} \right) - \kappa_1 S = 0, \quad (4.2.22)$$

where  $\kappa_1$  is a separation constant.

Moving on to the Proca equation, the left-hand-side of (4.2.12) reads [65]

$$\nabla_{\nu} W^{\mu\nu} + \mu^2 W^{\mu} = -B^{\mu\nu} \nabla_{\nu} J, \quad (4.2.23)$$

where

$$J = \square Z - 2i\xi_t^{\mu} W_{\mu} - \mu^2 Z \quad (4.2.24)$$

and  $\xi_t^{\mu}$  is the Killing vector of time-translation, which is  $\partial_t^{\mu}$  in Boyer-Lindquist coordinates, see Sec. 2.2.1. If we assume harmonic dependence on  $t$  and  $\phi$  (in accordance with the separation (4.2.20)) the equation  $J = 0$  becomes the following PDE for  $Z$ ,

$$\begin{aligned} 2\mu^2 \Sigma Z &= i\nu r \left( \mathcal{D}_0^{\dagger} \left( \frac{\Delta \mathcal{D}_0 Z}{1 + i\nu r} \right) - \mathcal{D}_0 \left( \frac{\Delta \mathcal{D}_0^{\dagger} Z}{1 - i\nu r} \right) \right) + a\nu \cos \theta \left( \mathcal{L}_1 \left( \frac{\mathcal{L}_0^{\dagger} Z}{1 + a\nu \cos \theta} \right) - \mathcal{L}_1^{\dagger} \left( \frac{\mathcal{L}_0 Z}{1 - a\nu \cos \theta} \right) \right) \\ &- i\nu \left( \frac{\Delta \mathcal{D}_0 Z}{1 + i\nu r} - \frac{\Delta \mathcal{D}_0^{\dagger} Z}{1 - i\nu r} \right) + a\nu \sin \theta \left( \frac{\mathcal{L}_0^{\dagger} Z}{1 + a\nu \cos \theta} - \frac{\mathcal{L}_0 Z}{1 - a\nu \cos \theta} \right) = 0. \end{aligned} \quad (4.2.25)$$

This also clearly separates in the variables  $r$  and  $\theta$ , splitting this into two ODEs with a new separation constant  $\kappa_2$ ,

$$(2\mu^2 r^2 + \kappa_2) R = i\nu \left( (r\mathcal{D}_0^\dagger - 1) \frac{\Delta \mathcal{D}_0 R}{1 + i\nu r} - (r\mathcal{D}_0 - 1) \frac{\Delta \mathcal{D}_0^\dagger R}{1 - i\nu r} \right), \quad (4.2.26)$$

$$(2\mu^2 a^2 \cos^2 \theta - \kappa_2) S = a\nu \left( (\cos \theta \mathcal{L}_1 + \sin \theta) \frac{\mathcal{L}_0^\dagger S}{1 + a\nu \cos \theta} - (\cos \theta \mathcal{L}_1^\dagger + \sin \theta) \frac{\mathcal{L}_0 S}{1 - a\nu \cos \theta} \right). \quad (4.2.27)$$

Information about the separation constants can be obtained by comparing this pair of ODEs with the pair (4.2.21) and (4.2.22). Multiplying (4.2.21) by  $\nu^2 r^2$  and subtracting (4.2.26) produces the following,

$$(\kappa_2 - 2a\nu(m - a\omega)) + \left( \kappa_1 - 2 \left( \frac{\omega}{\nu} - \frac{\mu^2}{\nu^2} \right) \right) \nu^2 r^2 = 0, \quad (4.2.28)$$

which clearly indicates the forms of  $\kappa_1$  and  $\kappa_2$ . Finally, substituting  $\kappa_1$  into the pair of ODEs (4.2.21) and (4.2.22) completes the separation of the Proca equation. The result is,

$$q_r \frac{d}{dr} \left[ \frac{\Delta}{q_r} \frac{dR}{dr} \right] + \left[ \frac{K_r^2}{\Delta} + \frac{2 - q_r \sigma}{q_r \nu} - \frac{q_r \mu^2}{\nu^2} \right] R = 0, \quad (4.2.29)$$

$$\frac{q_\theta}{\sin \theta} \frac{d}{d\theta} \left[ \frac{\sin \theta}{q_\theta} \frac{dS}{d\theta} \right] - \left[ \frac{K_\theta^2}{\sin^2 \theta} + \frac{2 - q_\theta \sigma}{q_\theta \nu} - \frac{q_\theta \mu^2}{\nu^2} \right] S = 0, \quad (4.2.30)$$

where  $K_r$  was defined previously in Eq. (4.1.12) and

$$K_\theta = m - a\omega \sin^2 \theta, \quad (4.2.31)$$

$$q_r = 1 + \nu^2 r^2, \quad (4.2.32)$$

$$q_\theta = 1 - \nu^2 a^2 \cos^2 \theta, \quad (4.2.33)$$

$$\sigma = \omega + a\nu^2 (m - a\omega). \quad (4.2.34)$$

Both of these ODE's can be rearranged into a form such that all the terms that were present in the equations for a massive scalar field are on the left-hand-side (such scalar equations are presented in the appendix, Eqs. (A.2.2) and (A.2.1)),

$$\frac{d}{dr} \left( \Delta \frac{dR}{dr} \right) + \left( \frac{K_r^2}{\Delta} - \Lambda + 2a\omega m - a^2 \omega^2 - \mu^2 r^2 \right) R = \frac{2r\nu^2}{q_r} \left( \Delta \frac{d}{dr} + r \frac{\sigma}{\nu} \right), \quad (4.2.35)$$

$$\frac{1}{\sin \theta} \frac{d}{d\theta} \left( \sin \theta \frac{dS}{d\theta} \right) + \left( \Lambda - \frac{m^2}{\sin^2 \theta} + a^2 (\omega^2 - \mu^2) \cos^2 \theta \right) S = \frac{2a^2 \nu^2 \cos \theta}{q_\theta} \left( \sin \theta \frac{d}{d\theta} + \frac{\sigma}{\nu} \cos \theta \right) S, \quad (4.2.36)$$

where

$$\Lambda = \frac{\mu^2}{\nu^2} - \frac{\sigma}{\nu} + 2a\omega m - a^2 \omega^2. \quad (4.2.37)$$

To retain consistency with the known radial and angular equations in the non-rotating limit (consider for example Eq. (3.1.3) with  $m = 0$ ),  $\Lambda$  must reduce to  $\ell(\ell + 1)$  as  $a \rightarrow 0$ , which produces a quadratic equation to solve for  $\nu$

$$\nu_{static} = \begin{cases} \mu^2/\omega & \ell = 0 \\ -\frac{\omega}{\ell(\ell+1)} \frac{1 \pm \sqrt{1+4\ell(\ell+1)\mu^2/\omega^2}}{2} & \ell > 0 \end{cases}. \quad (4.2.38)$$

We will denote as  $\nu_0$  the angular eigenvalue when both the non-rotating and massless limits are taken. Taking the massless limit of Eq. (4.2.38), the eigenvalue reduces to  $\nu_0 = 0$  or  $\nu_0 = -\omega/\ell(\ell + 1)$ .

#### 4.2.2.2 The Maxwell Scalars

Just like in the Teukolsky formalism for the separation of variables described in Eq. (4.2.1), the Maxwell scalars can also be separated using the LFKK ansatz

$$\Psi_{-1} = \frac{i\nu}{\sqrt{2}} \frac{\mathcal{D}_0 R}{1 + i\nu r} \frac{\mathcal{L}_0^\dagger S}{1 + a\nu \cos \theta}, \quad (4.2.39)$$

$$2(r - ia \cos \theta)^2 \Psi_{+1} = -\frac{i\nu}{\sqrt{2}} \frac{\Delta \mathcal{D}_0^\dagger R}{1 - i\nu r} \frac{\mathcal{L}_0 S}{1 - a\nu \cos \theta}. \quad (4.2.40)$$

As mentioned at the end of the previous section, we can directly compare this form of  $\Psi_{\pm 1}$  to that of Teukolsky to get a relationship between  $(R, S)$ , and  $(R_\pm, S_\pm)$

$$R_{+1} = \frac{i\nu}{\sqrt{2}C_+} \frac{\mathcal{D}_0 R}{1 + i\nu r}, \quad R_{-1} = -\frac{i\nu}{\sqrt{2}C_-} \frac{\Delta \mathcal{D}_0^\dagger R}{1 - i\nu r}, \quad (4.2.41)$$

$$S_{+1} = \frac{C_+ \mathcal{L}_0^\dagger S}{1 + a\nu \cos \theta}, \quad S_{-1} = \frac{C_- \mathcal{L}_0 S}{1 - a\nu \cos \theta}, \quad (4.2.42)$$

for  $C_\pm$  normalisation constants. These can be substituted back into Teukolsky's equations in the massless limit, to get a relationship between  $\nu$  and  $\lambda$  in this limit

$$\nu_{massless} = \frac{\lambda \pm \mathcal{B}}{2a(m - a\omega)}, \quad \mathcal{B} = \sqrt{\lambda^2 + 4m\omega - 4a^2\omega^2}, \quad (4.2.43)$$

where  $\mathcal{B}$  is referred to as the Teukolsky-Starobinsky constant. In the non-rotating limit, this either reduces to  $\nu_0 = 0$  or diverges like  $a^{-1}$  to  $\nu_0 = \infty$ .

As such, we have found that  $\nu_0$  has three possible values that will correspond to the three polarization states of the Proca field, as we detail in the next subsection.

#### 4.2.2.3 The Three Polarization States

Teukolsky's original separation of variables only covered a single polarization state. This was improved by Lunin's ansatz that covered both non-gauge polarizations of the electromagnetic field. How does the LFKK ansatz handle the three polarization states of the Proca field?

We know from the discussion in Sec. 3.1.2 of the Proca field on static spacetimes that the field consists of two coupled modes (the even-parity modes, one of scalar-type and one of vector-type) and a third decoupled mode (the odd-parity mode which is of vector-type). It was just demonstrated that in the  $a \rightarrow 0$  and  $\mu \rightarrow 0$  limit, there are three choices for the angular eigenvalue  $\nu_0$ . Which polarization the LFKK solution describes depends on the choice taken for  $\nu_0$ .

Consider first the polarization of scalar-type. We would expect the LFKK ansatz to reduce in the massless limit to  $W_\mu = \nabla_\mu Z$  in this case, hence Eq. (4.2.13) implies that  $B^{\mu\nu} = g^{\mu\nu}$  and from the definition of the polarization tensor in Eq. (4.2.14) we see that  $\nu_0 = 0$ , so this is the correct non-rotating, massless eigenvalue for the polarization.

Next, we consider the circumstance in which  $\nu$  diverges in the non-rotating limit,  $\nu_0 = \infty$ . We will begin by relating the radial function  $R$  from the LFKK ansatz in the non-rotating limit to the  $u_{(i)}$  functions of Ref. [126], see Eq. (3.1.21). This is done by substituting the vector spherical harmonic expansion of  $W_\mu$  that was used in Eqs. (3.1.22)-(3.1.25) into the LFKK ansatz. For an even-parity mode this is (see Appendix B of [117])

$$\begin{aligned} u_1(r) &= -\frac{ir}{q_r} f_{sch} \left( \nu r \frac{d}{dr} + \frac{\omega}{f_{sch}} \right) R, \\ u_2(r) &= \frac{r}{q_r} f_{sch} \left( \frac{d}{dr} - \frac{\omega \nu r}{f_{sch}} \right) R, \\ u_3(r) &= \Lambda R \end{aligned} \tag{4.2.44}$$

and  $u_4(r) = 0$ , with an angular function  $S(\theta) = Y_{\ell m}$ . For an odd-parity mode one simply has  $u_1 = u_2 = u_3 = 0$ ,  $u_4 = R$ , but the angular function satisfies a pair of ODE's

$$(\sin \theta \partial_\theta + m a \nu \cos \theta) S = \frac{i m q_\theta}{\ell(\ell+1)} Y_{\ell m}, \tag{4.2.45}$$

$$(m + a \nu \sin \theta \cos \theta \partial_\theta) S = \frac{i \sin \theta q_\theta}{\ell(\ell+1)} \partial_\theta Y_{\ell m}. \tag{4.2.46}$$

These need to have the same non-rotating limit as Eq. (4.2.36), implying the following,

$$\lim_{a \rightarrow 0} a \nu = \frac{\ell(\ell+1)}{m}, \tag{4.2.47}$$

which is only possible if  $\nu$  diverges in the non-rotating limit,  $\nu_0 = \infty$ .

We can now confirm that this refers to the odd-parity polarization by taking the non-rotating limit of the radial and angular equations (4.2.35) and (4.2.36), using Eq. (4.2.47) as well as

$$-\lim_{a \rightarrow 0} \Lambda = \lim_{a \rightarrow 0} \frac{\sigma}{\nu} = \ell(\ell+1) \tag{4.2.48}$$

and so the radial differential equation (4.2.35) as a whole is finite in the non-rotating limit. In fact, the radial equation reduces exactly to the Regge-Wheeler equation for  $s = 1$  (3.1.31), establishing

that this mode is of vector-type. To determine whether this is the even-parity or odd-parity vector mode, Eqs. (4.2.45) and (4.2.46) can be solved simultaneously to get

$$S(\theta) = \frac{i}{\ell(\ell+1)m} (\sin\theta\partial_\theta - \ell(\ell+1)\cos\theta) Y_{\ell m}. \quad (4.2.49)$$

This can be written in terms of associated Legendre polynomials. Up to an overall constant we have

$$S(\theta) \propto \ell^2(\ell+1-m) P_{\ell+1}^m(\cos\theta) + (\ell+1)^2(\ell+m) P_{\ell-1}^m(\cos\theta), \quad (4.2.50)$$

which demonstrates that this is an odd-parity solution.

This leaves the remaining  $\nu_0 = -\omega/\ell(\ell+1)$  to refer to the even-parity vector mode.

### 4.2.3 Analytical Approximations for QBSs

As was discussed in Sec. 3.3.2, the asymptotic matching method when applied to a vector field is potentially fraught with problems. However, using the LFKK ansatz, Baumann *et.al* in [18] managed to successfully procure an analytical approximation for the bound state frequencies of a massive vector field on the Kerr spacetime by performing the matching in a two-step process. For this they introduce, as well as a near-horizon region and a far-field region, an *intermediate region* between the two.

To begin, they write the radial equation in a form that will be very useful to us in Sec. 4.2.4, as it highlights very clearly the five singular points the equation has

$$\begin{aligned} & \frac{d^2 R}{dr^2} + \left( \frac{1}{r-r_+} + \frac{1}{r-r_-} - \frac{1}{r-i/\nu} - \frac{1}{r+i/\nu} \right) \frac{dR}{dr} \\ & + \left[ -\frac{\tilde{\Lambda}}{\Delta} - q^2 + \frac{\rho_+^2}{(r-r_+)^2} + \frac{\rho_-^2}{(r-r_-)^2} - \frac{A_+}{(r_+ - r_-)(r-r_+)} \right. \\ & \left. + \frac{A_-}{(r_+ - r_-)(r-r_-)} - \frac{\sigma}{\nu} \frac{r}{\Delta(r-i/\nu)} - \frac{\sigma}{\nu} \frac{r}{\Delta(r+i/\nu)} \right] R = 0, \end{aligned} \quad (4.2.51)$$

where

$$A_\pm = \rho_+^2 + \rho_-^2 + \frac{1}{4}(r_+ - r_-)^2 q^2 + [M^2(q^2 - 6\omega^2) \pm M(r_+ - r_-)(q^2 - \omega^2)], \quad (4.2.52)$$

$$\rho_\pm = \frac{(r_\pm^2 + a^2)\omega - am}{r_+ - r_-} \quad (4.2.53)$$

and in the Kerr spacetime,  $\tilde{\Lambda}$  is equal to the  $\Lambda$  defined in (4.2.37). When we discuss the QNMs of the Kerr-Newman spacetime in Sec. 4.3  $\tilde{\Lambda}$  will have to be modified.

The singular points of (4.2.51) are located at the radial values  $r_+, r_-, \infty$ , and  $r = \pm i/\nu$ . Ref. [18] cites the existence of the singularities in the complex plane as the reason the near and far regions no longer overlap. Said regions are treated similarly to the Schwarzschild case, by defining suitable

radial coordinates labeled  $z$  and  $x$  respectively, but they also introduce a coordinate  $y$  to be used in the intermediate region

$$x = 2q(r - r_+), \quad (4.2.54)$$

$$y = r - r_+, \quad (4.2.55)$$

$$z = \frac{r - r_+}{r_+ - r_-}. \quad (4.2.56)$$

(Note that each of these are proportional to  $r$ ).

For the rest of this section, it is important to note that we will be denoting the *total angular momentum* by  $\ell$  and the *orbital angular momentum* by  $\hat{\ell}$ . The relationship between the two is  $\ell = \hat{\ell} - S$ , where  $S = -1$  for the even scalar-type mode,  $S = +1$  for the even vector-type mode and  $S = 0$  for the odd vector-type mode. This labeling convention is different to [18], where the total angular momentum is labeled  $j$  and the orbital angular momentum is labeled  $\ell$ .

The near-horizon solution of (4.2.51) is written in terms of a Gauss hypergeometric function, the far-field solution in terms of a confluent hypergeometric function and the intermediate solution is

$$R^{int}(y) = C^{int}y^{-\lambda_0} + D^{int}y^{\lambda_0-1} (\lambda_0^2(2\lambda_0+1) + (2\lambda_0+1)y^2), \quad (4.2.57)$$

where  $C^{int}$  and  $D^{int}$  are integration constants. The quantity  $\lambda_0$  is  $\hat{\ell} + 1$  or  $-\hat{\ell}$  for the scalar-type and vector-type even-parity modes respectively and  $\lambda_0$  is either  $\hat{\ell}$  or  $-\hat{\ell} - 1$  for the odd-parity mode (in particular, the substitution  $\hat{\ell} \rightarrow -\hat{\ell} - 1$  swaps the even-parity modes and leaves the odd-parity mode invariant).

There are now *two* overlap regions, one between the far region and the intermediate region and one between the intermediate region and the near region. Here it can be seen that there are three distinct ‘‘branches’’ in the intermediate solution (4.2.57) proportional to  $r^{-\lambda_0}$ ,  $r^{\lambda_0-1}$  and  $r^{\lambda_0+1}$ . For example, if we choose the polarization  $\ell = \hat{\ell} - 1$  such that  $\lambda_0 = -\ell$ , the three branches become proportional to  $r^\ell$ ,  $r^{-\ell-1}$  and  $r^{-\ell+1}$ , see equation (3.44) of [18]. For comparison, the far region and near region solutions contain two branches each, proportional to  $r^{-\ell+1}$ ,  $r^\ell$  and  $r^\ell$ ,  $r^{-\ell-1}$  respectively. Hence, in each overlap region, two branches of each solution have the same behavior and can be matched up.

The matching conditions provide information about the bound-state frequencies  $\omega$ , that depend on the parameters  $\{N, \ell, \hat{\ell}, m\}$  (where  $N = \hat{\ell} + n + 1 = \ell + S + n + 1$  for an overtone number  $n$ ). The real part of the frequency takes the same form as Eq. (A.2.12) for the scalar field, which we repeat here,

$$\Re(\omega) = \mu \left( 1 - \frac{\alpha^2}{2N^2} - \frac{\alpha^4}{8N^4} + \frac{f_{N\hat{\ell}\ell}}{N^3} \alpha^4 + \frac{h_{\hat{\ell}\ell}}{N^3} m \alpha^5 + \dots \right), \quad (4.2.58)$$

where  $\alpha = M\mu$ , with modified fine and hyper-fine structure coefficients

$$f_{N\hat{\ell}\ell} = -\frac{4(6\hat{\ell}\ell + 3\hat{\ell} + 3\ell + 2)}{(\hat{\ell} + \ell)(\hat{\ell} + \ell + 1)(\hat{\ell} + \ell + 2)} + \frac{2}{N}, \quad (4.2.59)$$

$$h_{\hat{\ell}\ell} = \frac{16}{(\hat{\ell} + \ell)(\hat{\ell} + \ell + 1)(\hat{\ell} + \ell + 2)}. \quad (4.2.60)$$

The imaginary part of the frequency is given by equations (2.34)-(2.36) of [18], as follows,

$$\Im(\omega) = 2r_+ C_{n\hat{\ell}\ell} g_{\hat{\ell}m}(a, \alpha, \omega) (m\Omega_H - \omega) \alpha^{2\hat{\ell}+2\ell+5}, \quad (4.2.61)$$

$$C_{n\hat{\ell}\ell} = \frac{2^{2\hat{\ell}+2\ell+1} (n + \hat{\ell})!}{n^{2\hat{\ell}+4} (n - \hat{\ell} - 1)!} \left[ \frac{\hat{\ell}!}{(\hat{\ell} + \ell)! (\hat{\ell} + \ell + 1)!} \right]^2 \left[ 1 + \frac{2(1 + \hat{\ell} - \ell)(1 - \hat{\ell} + \ell)}{\hat{\ell} + \ell} \right]^2, \quad (4.2.62)$$

$$g_{\ell m}(a, \alpha, \omega) = \prod_{k=1}^{\ell} \left( k^2 (1 - a^2) + (ma - 2r_+ \omega)^2 \right) \quad (4.2.63)$$

and  $\Omega_H$  is the angular velocity of the black hole event horizon, see (A.2.6). This scales like  $\alpha^{2\hat{\ell}+2\ell+5} \sim \mu^{4\hat{\ell}-2S+5}$ . The least suppressed vector mode at small  $\mu$  (and hence the fastest growing mode), occurs when  $|N\hat{\ell}\ell m\rangle = |1011\rangle$  and so  $\Im(\omega) \sim \mu^7$ , which is faster than the fastest growing mode of the scalar field in the Kerr spacetime, which scales like  $\mu^9$ , see Eq. (A.2.8). This scalar field scaling is consistent with setting  $S = 0$  and  $\ell = \hat{\ell} = 1$  in the general formula. We will compare our numerical data found via a recurrence relation to some of these analytical approximations in Sec. 4.2.5.

## 4.2.4 Solving the Proca Equation

Now that the Proca equation has been separated through the LFKK ansatz and we have covered analytical results obtained through asymptotic matching, we will now detail the numerical methods we will use to solve the Proca equation.

### 4.2.4.1 The Angular Eigenvalue: Spectral Decomposition

The known massless and non-rotating limits of  $\nu$ , which we labeled  $\nu_0$  in Sec. 4.2.2, can be used as initial guesses for a numerical scheme to find  $\nu$  for general  $a$  and  $\mu$ . This will be done through the *spectral decomposition* method, which was first applied to the calculation of QNMs in [48]. The scheme is detailed in [54] and is constructed using a spectral ansatz for the angular function  $S(\theta)$  satisfying (4.2.36)

$$S(\theta) = \sum_{k'=0}^{\infty} b_{k'} Y_{\ell'}^m(\theta) \quad \ell' = |m| + 2k' + \eta. \quad (4.2.64)$$

This expansion will be entirely in terms of even-parity or odd-parity  $\ell$  modes, because of the fixed and definite parity of Eq. (4.2.36). Here, “even-parity” refers to the function  $S(\theta)$  acquiring a factor of  $(-1)^{\ell+m}$  under parity inversion  $\theta \rightarrow \pi - \theta$ , while “odd-parity” refers to  $S(\theta)$  acquiring a factor of  $(-1)^{\ell+m+1}$ . The parameter  $\eta$  takes either the value 0 or 1 depending on the parity being considered and the values of  $\ell$  and  $m$ ,

$$\eta = \frac{1}{2} \left( 1 - (-1)^{\ell+m+P} \right), \quad (4.2.65)$$

where  $P = 0$  for an even-parity mode and  $P = 1$  for the odd-parity mode.

This spherical mode decomposition is substituted into the angular equation (4.2.36) and then integrated against  $2\pi \int_0^\pi Y_\ell^{*m}(\theta) \sin\theta$ . The orthogonality of the spherical harmonics allows the coefficients  $b_{k'}$  to be isolated in the form of a matrix equation

$$\sum_{k'=0}^{\infty} \mathcal{M}_{kk'} b_{k'} = 0, \quad (4.2.66)$$

with matrix elements

$$\mathcal{M}_{kk'} = [\Lambda - \ell'(\ell' + 1)] \delta_{\ell\ell'} + a^2 [\nu^2 \ell'(\ell' + 1) - \nu^2 \Lambda - 2\sigma\nu - q^2] c_{\ell\ell'}^{(2)} - 2a^2 \nu^2 d_{\ell\ell'}^{(2)} + q^2 \nu^2 a^4 c_{\ell\ell'}^{(4)}, \quad (4.2.67)$$

where  $\ell = |m| + 2k + \eta$ . The coefficients  $c_{\ell\ell'}^{(2)}$ ,  $c_{\ell\ell'}^{(4)}$  and  $d_{\ell\ell'}^{(2)}$  are defined in equation (32) of [54]. The important properties of these coefficients are that  $c_{\ell\ell'}^{(2)}$  and  $d_{\ell\ell'}^{(2)}$  vanish for  $|k - k'| > 1$  and  $c_{\ell\ell'}^{(4)}$  vanishes for  $|k - k'| > 2$ , hence the matrix  $\mathcal{M}_{kk'}$  is penta-diagonal in general, tri-diagonal when  $q = 0$  (i.e. when  $\omega^2 = \mu^2$ ) and diagonal when  $a = 0$ . The matrix equation for the coefficients  $b_{k'}$  has solutions when  $\det \mathcal{M} = 0$ , hence [54] and ourselves in [117] search numerically for a root of the determinant of  $\mathcal{M}$  over the complex  $\nu$  plane.

This method works well for the two vector-type polarization states where, for  $a \neq 0$ ,  $\nu$  takes a non-zero, finite value in the massless limit given by Eq. (4.2.43), which forms a suitable starting guess for the numerical solver. For the remaining, scalar-type polarization,  $\nu \rightarrow 0$  in the massless limit for all values of  $\ell$  causing these eigenvalues for different values of  $\ell$  to “pile-up” together and so a numerical solver struggles to pick out the correct massive  $\nu$ . We can infer the behavior of  $\nu$  in the small mass regime by noting that in the massless limit the angular differential equation (4.2.36) must reduce to the  $s = 0$  spheroidal harmonic equation (Eq. (4.1.10) with  $s = 0$ ). This motivates us to introduce the change of variables

$$\nu = \frac{\mu^2}{\omega} (1 + \tau\mu^2), \quad (4.2.68)$$

where as  $\mu \rightarrow 0$  the parameter  $\tau$  must reduce to  $\tau_0 = -\lambda_0/\omega^2$  where  $\lambda_0$  is the eigenvalue of the  $s = 0$  Teukolsky equation. After this change,  $\tau$  can be found by the same numerical scheme used to find  $\nu$  with  $\tau_0$  as the starting guess.

This method works well for QNMs. For QBSs, we cannot start the angular eigenvalue finder from the massless eigenvalue, as QBSs don't exist for massless fields. We instead use the scheme described in [54] where the eigenvalue finder begins from the marginally bound case  $\omega^2 = \mu^2$ . The form of the marginally bound eigenvalue depends on the chosen polarization of the Proca field. For  $S = -1$  and  $m = \pm\ell$  it is

$$\nu = \frac{\mp\omega}{m - a\omega}, \quad (4.2.69)$$

for  $S = 0$  it is

$$\nu = \frac{1}{2a} \left( \pm\ell - a\omega \pm \sqrt{(\mp\ell + a\omega)^2 + 4a\omega} \right) \quad (4.2.70)$$

and for  $S = +1$  one must take the middle root of the cubic equation

$$a\nu^3 (1 - a\omega) - (6 - a\omega(2 - a\omega))\nu^2 + \omega\nu + \omega^2 = 0. \quad (4.2.71)$$

#### 4.2.4.2 The Radial Equation via Direct Integration

As in the non-rotating case, there are multiple methods that can be employed to solve the radial differential equation (4.2.35). In [54], a numerical integration scheme was employed to find the bound state frequencies of the Proca field. A Frobenius series initial condition is imposed near the black hole horizon of the form

$$R(z) = z^{-i\rho_+} (1 + c_1 z + c_2 z^2 + \dots), \quad (4.2.72)$$

where the radial variable  $z$  is the same as in Eq.(4.2.56) and the index  $\rho_+$  is the same as in Eq.(4.2.53). The differential equation is then integrated from the horizon to a large value of  $r = r_{max}$ . To satisfy the boundary condition of a bound state, one would expect this radial function to die away as  $r \rightarrow \infty$ . In practice, if  $r$  is taken to be too large, the radial function will begin to grow again even if  $\omega$  is chosen to be a bound state frequency due to the accumulation of numerical error, but this doesn't pose much of an issue in practice. A merit function is constructed by attempting to minimise  $\log |R(r_{max})|^2$  over the complex frequency plane, using the hydrogenic approximation (4.2.58) as an initial guess. The results obtained by Dolan in [54] are consistent with the analytical approximations of [18] detailed in Sec.4.2.3. In particular, Dolan concludes that the even-parity scalar-type mode, corresponding to  $S = -1$ , has the largest imaginary part and so has the largest growth rate.

#### 4.2.4.3 The Radial Equation via Leaver's Method

In our work with Dolan in [117], we instead apply Leaver's method to solve a recurrence relation derived from Eq.(4.2.51). As the equation has five singular points, following the discussion in

Sec.3.4.2 this leads us to hypothesise that the minimum number of terms our recurrence relation can have is five,

$$\alpha_n a_{n+2} + \beta_n a_{n+1} + \gamma_n a_n + \delta_n a_{n-1} + \varepsilon_n a_{n-2} = 0 \quad n \geq 2. \quad (4.2.73)$$

The coefficients  $a_n$  are those in the radial ansatz that we impose to solve the equation with the correct boundary conditions

$$R(r) = \left( \frac{r - r_+}{r - r_-} \right)^{-i\rho} (r - r_-)^\chi e^{-qr} \sum_{k=0}^{\infty} a_k \left( \frac{r - r_+}{r - r_-} \right)^k, \quad (4.2.74)$$

where  $\chi$  and  $q$  carry the same definitions as they did in the Schwarzschild case

$$q = \pm \sqrt{\mu^2 - \omega^2}, \quad \chi = \frac{M(\mu^2 - 2\omega^2)}{q}.$$

Here we have absorbed the  $\pm$  sign from the QNM and QBS boundary conditions (3.2.12) into the definition of  $q$ , so  $\Re(q) < 0$  for QNMs and  $\Re(q) > 0$  for QBSs. If this ansatz is substituted into the radial equation (4.2.51) and then the equation is expanded around  $r = r_+$ , setting the leading order term to zero imposes the condition  $\rho = \pm\rho_+$ . Imposing regularity of the solution at the future horizon (in any coordinate system that is also regular on the future horizon) requires that we choose  $\rho = \rho_+$ , which is also consistent with the Schwarzschild case.

Setting every other power of the expansion around  $r = r_+$  to zero gives a series of equations that can be solved term by term for the coefficients  $a_n$ . The manipulations are very involved and so are best performed in a symbolic algebra package such as Mathematica. We have defined the following quantities so that the recurrence can be presented more succinctly:  $u_\pm = 1 + \nu^2 r_\pm^2$ ,  $t_\pm = 1 \pm \nu^2 r_+ r_-$ ,  $c_\pm = 1 + r_\pm M \nu^2$ ,  $b = \frac{1}{2}(r_+ - r_-)$ ,

$$\alpha_n = 16b^2 (n+2) q^2 u_+ (n+2 - 2i\rho_+), \quad (4.2.75)$$

$$\beta_n = -4bq \left\{ 16b(n+1)^2 q c_+ + (A_- - A_+) u_+ (1 - 2i\rho_+) + 4bq A_+ u_+ \right. \\ \left. - 2(n+1) [u_+ (A_+ - A_-) + 8bq (b(q + r_+ (qr_+ - 1)\nu^2) + 2ic_+ \rho_+)] \right. \\ \left. - 4bq [-\Lambda + 2bqu_+ (1 - 2i\rho_+) - 2ir_- r_+ \nu^2 \rho_+ + 2\rho_+^2 + r_+^2 \nu (-\Lambda \nu + 2\nu \rho_+ (i + \rho_+) - 2\sigma)] \right\}, \quad (4.2.76)$$

$$\begin{aligned}
\gamma_n = & u_+ (A_- - A_+)^2 + 8A_- bq (1 + n (3 + r_+ (2M + r_-) \nu^2) - 3i\rho_+ + r_+ \nu^2 (r_+ - i (2M + r_-) \rho_+)) \\
& + 8A_+ bq (-1 + 4bqt_+ + n (-3 - r_+ (2M + r_-) \nu^2) + 3i\rho_+ + ir_+ \nu^2 (2r_- \rho_+ + r_+ (i + \rho_+))) \\
& - 16b^2 q^2 \left[ -2t_+ \Lambda + n^2 (-6 - (4M^2 + 2r_+ r_-) \nu^2) + 8bn (-M\nu^2 + qt_+) - u_+ \rho_-^2 \right. \\
& \left. + 2in (6 + (4M^2 + 2r_+ r_-) \nu^2) \rho_+ + \rho_+ (8ibM\nu^2 - 8ibqt_+ + 5\rho_+ + r_+ (2M + 3r_-) \nu^2 \rho_+) - 4r_- r_+ \nu \sigma \right],
\end{aligned} \tag{4.2.77}$$

$$\begin{aligned}
\delta_n = & -2 \left\{ t_+ (A_- - A_+)^2 + 32b^2 (n-1)^2 q^2 c_- - 2A_- bq (-1 + 6i\rho_+ + r_- \nu^2 (-2b - r_+ + 2i (2M + r_+) \rho_+)) \right. \\
& + 2A_+ bq (-1 + 4bqu_- + 6i\rho_+ + r_- \nu^2 (-2b - r_+ + 2i (2M + r_+) \rho_+)) - 64ib^2 (n-1) q^2 c_- \rho_+ + 8b^2 q^2 \Lambda u_- \\
& - 4b (n-1) q [A_- (-3 - r_- (2M + r_+) \nu^2) + A_+ (3 + r_- (2M + r_+) \nu^2) + 8bq (b (q + r_- (qr_- - 1) \nu^2))] \\
& \left. - 8b^2 q^2 [-2\rho_-^2 - 2bqu_- (1 + 2i\rho_+) + 4\rho_+^2 + 2r_- r_+ \nu^2 (-\rho_-^2 + \rho_+ (i + \rho_+)) - r_-^2 \nu (-2\nu\rho_+ (\rho_+ - i) + 2\sigma)] \right\},
\end{aligned} \tag{4.2.78}$$

$$\varepsilon_n = u_- (A_- - A_+ + 4bq (n - 2 + i\rho_- - i\rho_+)) (A_- - A_+ + 4bq (n - i (-2i + \rho_- + \rho_+))), \tag{4.2.79}$$

where  $A_{\pm}$  are as in (4.2.52).

This recurrence relation was used to find the  $a_n$  by the methods presented in Sec. 2.4, beginning with two applications of Gaussian elimination to reduce it to a three term relation. Then, the continued fraction method was used to find a minimal solution to this recurrence, which occurs when  $\omega$  is either a QNM or a QBS frequency, depending on the boundary conditions chosen.

## 4.2.5 Numerical Results

### 4.2.5.1 Consistency Checks and QBSs

First, to test the recurrence relation we followed a direct approach and calculated the radial coefficients  $a_n$  by a standard forward recurrence on Eqs. (4.2.75)-(4.2.79) for some large number of iterations  $n_{max}$ . Then  $|a_{nmax}|$  forms a suitable merit function to minimise with respect to  $\omega$ . In a similar manner to the  $\log |R(r_{max})|^2$  merit function constructed by Dolan in [54], the magnitude of the merit function decreases with  $n$  initially ( $|a_{n+1}| < |a_n|$ ) but taking  $n_{max}$  large enough causes the merit function to grow without bound, even if it is evaluated at a QNM or QBS frequency  $\omega$ . This is due to the accumulation of numerical error. An example merit function is plotted in Fig. 4.2.1. There are two clear minima located at the fundamental mode ( $n = 0$ ) and first overtone ( $n = 1$ ) QNMs for the shown parameter set. As a second test, we set  $a = 0$  in the recurrence relation and

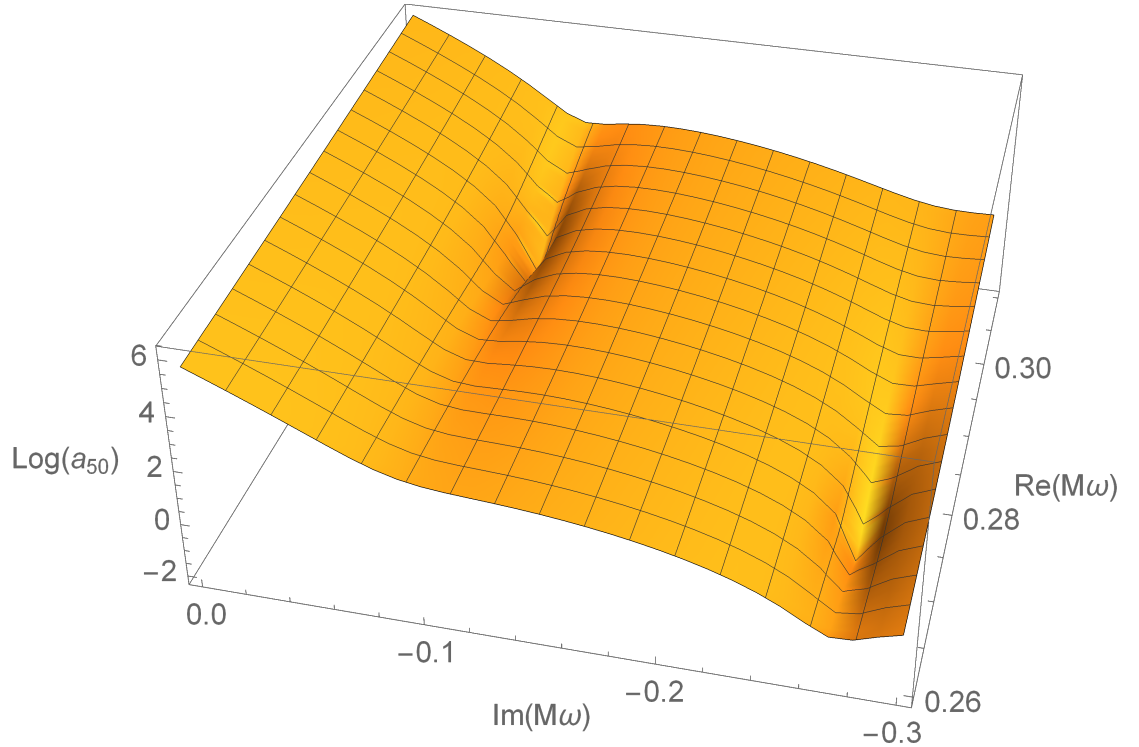


Figure 4.2.1: An example merit function plotted over the complex plane, for the parameters  $a = 0.5$ ,  $\ell = m = 1$ ,  $\mu = 0$ .

calculated QNMs for the Schwarzschild spacetime, which agreed with the data presented in [126] to 9 significant figures.

The recurrence relation can also be validated by using it to calculate QBSs and comparing the results to the data in [54]. All that is required to substitute  $q \rightarrow -q$  and change the initial guess for the angular eigenvalue, according to the scheme laid out in [54], see Eqs. (4.2.69)-(4.2.71). The imaginary part of these bound state frequencies are plotted in Fig. 4.2.2 for the two polarizations labeled by  $S = -1$  and  $S = 0$ . Note that in the mass range considered,  $\Im(\omega) > 0$ , i.e., the modes are unstable. The frequencies found agree with the known data to at least six significant figures in the real part and at least three significant figures in the imaginary part, with better agreement (up to six significant figures for  $S = -1$  and up to five significant figures for  $S = 0$ ) as the mass increases towards the peak of the superradiant instability. For the remaining  $S = +1$  polarization, the recurrence relation as we have implemented it fails to converge to a smooth curve of QBS frequencies. We discuss the possible reasons for this in the conclusion to this chapter. This will not be a problem when we come to discuss QNMs.

We can also compare this numerical bound state data to the analytical approximations described

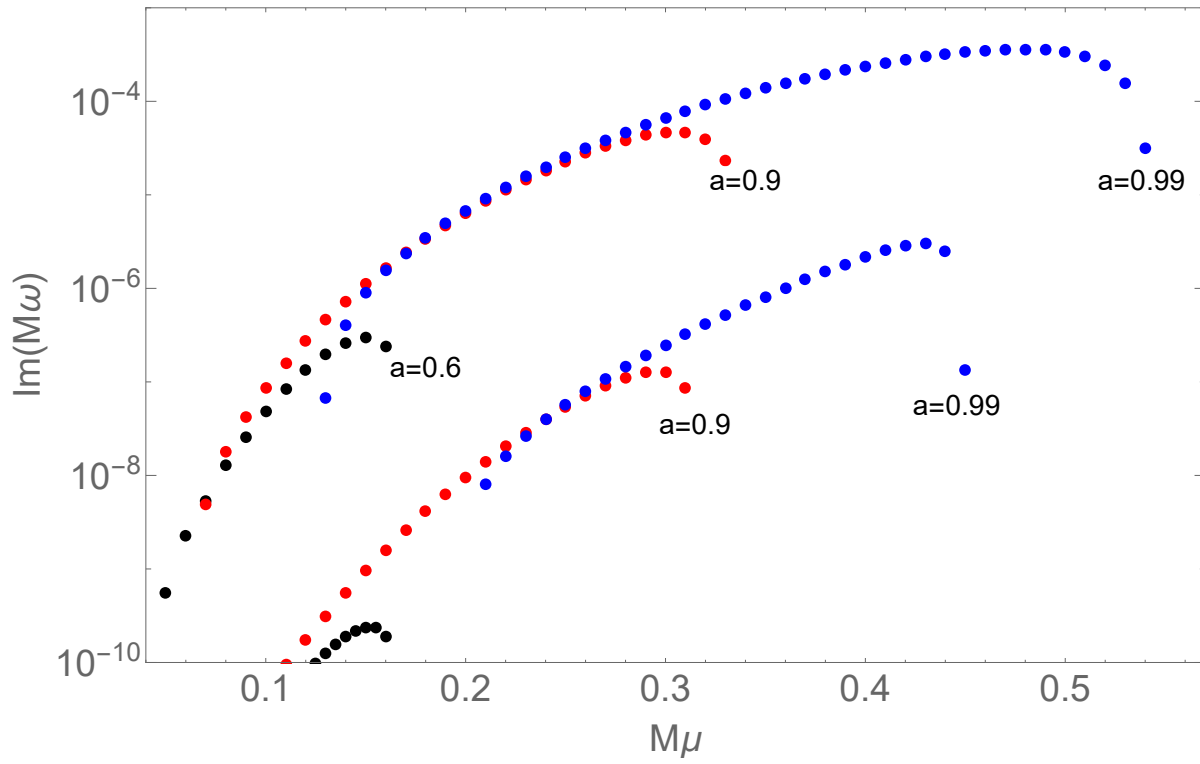


Figure 4.2.2: The imaginary part of the bound state frequencies of the Proca field in the Kerr spacetime for  $\ell = m = 1$ ,  $n = 0$  and various  $a$ . The upper curves are for the polarization  $S = -1$  and the lower curves are for  $S = 0$ .

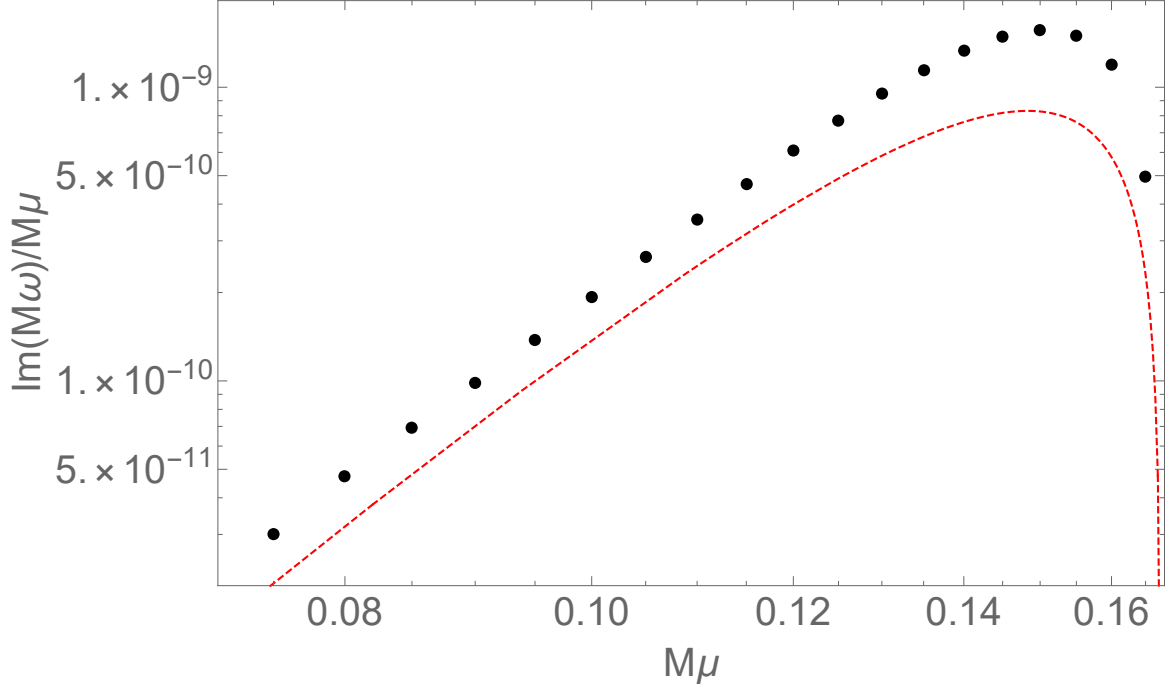


Figure 4.2.3: The imaginary part of the bound state frequencies of the Proca field in the Kerr spacetime for  $\ell = m = 1$ ,  $n = 0$ ,  $a = 0.6$  and polarization  $S = 0$ . The red dashed line is the analytical approximation of Eq. (4.2.61).

previously, Eqs. (4.2.58) and (4.2.59)-(4.2.60) for the real part and Eqs. (4.2.61)-(4.2.63) for the imaginary part. The imaginary part is compared with its approximation in Fig. 4.2.3. We can see that although the approximation matches the qualitative shape of the data, at the peak of the superradiant instability at  $M\mu \approx 0.15$  the approximation underestimates  $\Im(\omega)$  by a factor of about 2. This is consistent with Figure 8 of [18], where the analytical approximation is shown to perform worse as  $\mu$  and  $a$  grow. The fine structure of the real part of the bound state frequency is compared with the analytical approximation in Fig. 4.2.4.

#### 4.2.5.2 QNM Data

We now present our original data for the QNMs of all three polarizations of the Proca field in the Kerr spacetime. We begin by presenting the found QNM data for the  $\ell = m = 1$ , fundamental mode, shown in Fig. 4.2.5. The two vector-type polarizations agree, in the massless limit, with the QNMs of the electromagnetic field, represented by the upper blue curve. The scalar-type polarization agrees, in the massless limit, with the QNMs of the massless scalar field, represented by the lower blue curve. This is in contrast to QBSs, where it was the odd-parity vector polarization  $S = 0$  of the

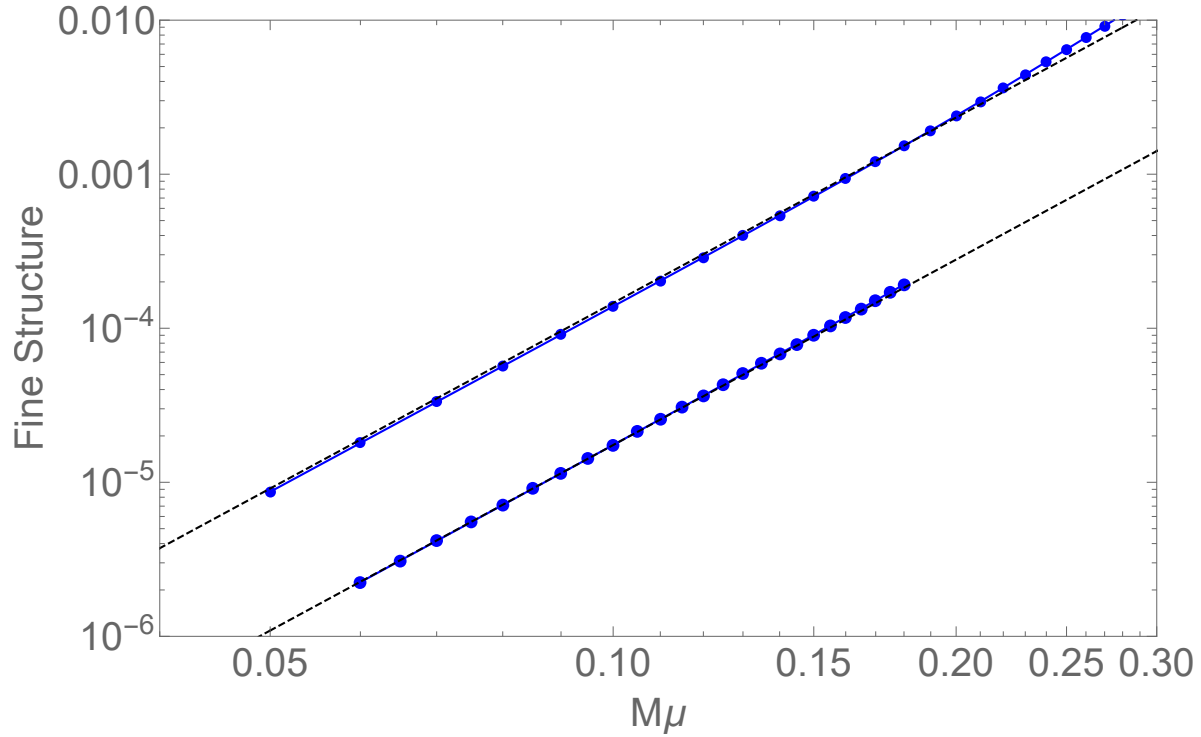


Figure 4.2.4: The fine structure of the real part of the bound state frequencies of the Proca field in the Kerr spacetime, for the small mass regime where the analytical approximations are most applicable,  $\ell = m = 1$ ,  $n = 0$  and  $a = 0.6$ . The upper points are for polarization  $S = -1$ , the lower points for  $S = 0$ . The data points were found by subtracting  $1 - \frac{\alpha^2}{2N^2}$  (see (4.2.58)) from  $\Re(\omega)/\mu$  to obtain an estimate of the fine structure coefficient  $f_{N\hat{\ell}\ell}$ . The black dashed lines are the analytical approximation to the fine structure coefficient from Eq. (4.2.59).

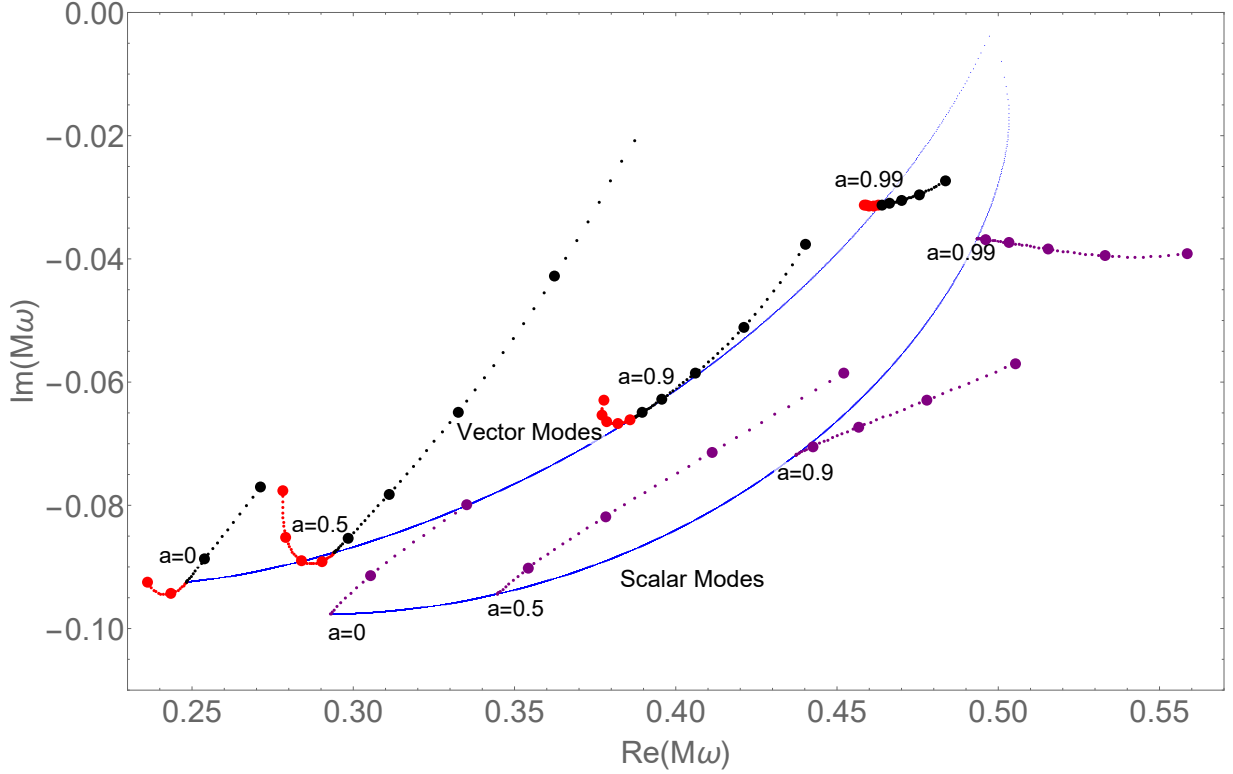


Figure 4.2.5: Fundamental QNMs of massless and massive vector fields in the complex plane,  $\ell = m = 1; n = 0$ . The blue curves show the QNMs of the massless vector (electromagnetic) and scalar fields for varying  $a$ . On the upper curve, the black points show the odd-parity Proca QNMs, and the red points show the even-parity Proca QNMs of vector type. On the lower curve, the purple points show QNMs of even-parity scalar type. The mass spacing between large (small) points is  $M\mu = 0.1(0.01)$ .

Proca field that was best compared to the scalar field.

For the odd-parity vector-type and even-parity scalar-type modes, as  $\mu$  increases the oscillation frequency  $\Re(\omega)$  increases and the decay rate  $-\Im(\omega)$  decreases, so the modes become more long-lived. The one exception to this is for the scalar-type polarization for a large black hole spin  $a$ , for which the decay rate increases for small  $\mu$ , before beginning to decrease again when  $\mu$  passes a certain value (about  $M\mu = 0.4$  for  $a = 0.99$ ). The even-parity vector-type modes behave differently: the oscillation frequency decreases as  $\mu$  increases and the decay rate increases for small  $\mu$  for all  $a$ . In all cases, as  $\mu$  grows large, the QNMs approach the real axis and hence approach quasinormality, see Sec. 3.2.

These same general trends also hold in the case of the first overtone  $n = 1$  presented in Fig. 4.2.6.

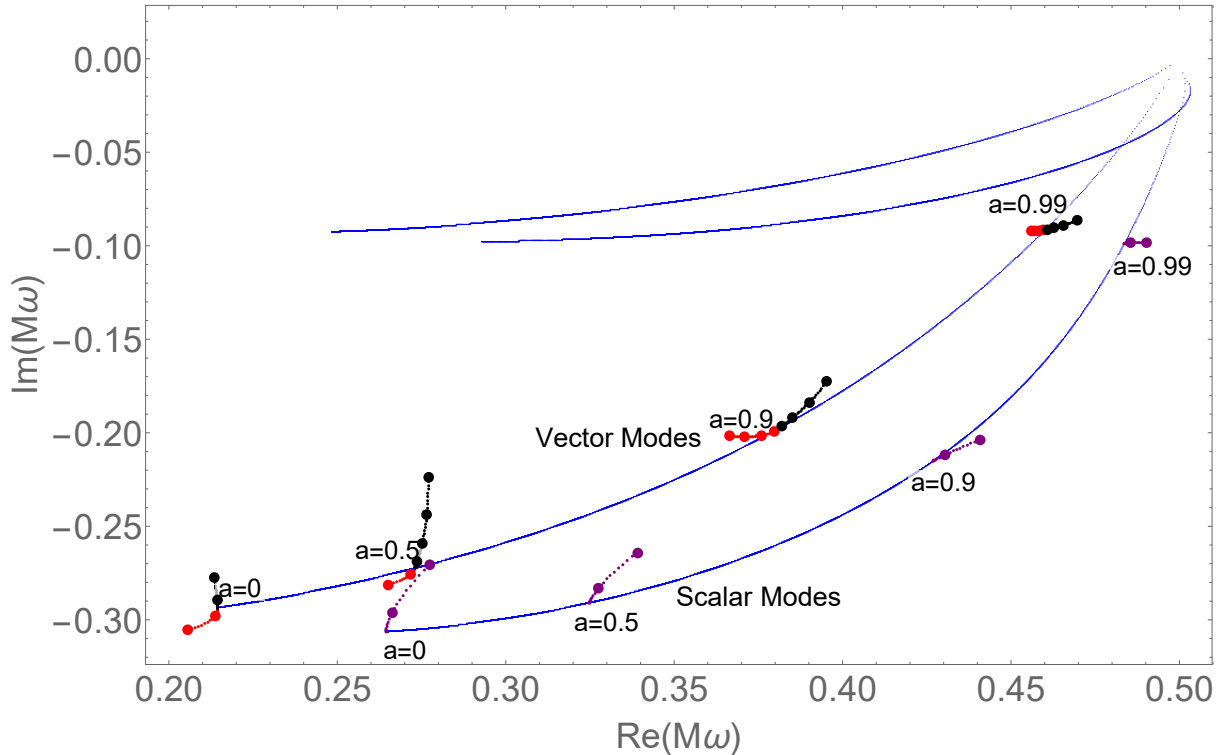


Figure 4.2.6: QNMs of massless and massive vector fields in the complex plane,  $\ell = m = 1; n = 1$ , with the same conventions as in Fig. 4.2.5. The upper blue curves are the massless QNMs for the electromagnetic and scalar fields from Fig. 4.2.5.

The main differences from the fundamental mode are that the decay rates are much larger and the QNMs approach the real axis much slower with increasing  $\mu$ .

Figs. 4.2.7 and 4.2.8 display the vector-type and scalar-type QNMs respectively for  $\ell = 1$  and all three possible values of  $m \in \{-1, 0, 1\}$ . It can be seen that the QNMs that would be characterised by counter-rotating geodesic orbits in the eikonal approximation (i.e.,  $m < 0$ ) have smaller oscillation frequencies than their co-rotating counterparts ( $m > 0$ ). The QNMs of the odd-parity vector polarization of the Proca field are not presented when  $m = 0$ . This was the one circumstance where our recurrence relation failed to produce a smooth curve of QNM frequencies. Like the QBS frequencies we were unable to find in Sec. 4.2.5.1, we will briefly consider why this might be in the conclusion to this chapter.

In Fig. 4.2.9 we show a direct comparison of the QNMs of the scalar-type polarization of the Proca field and those of the scalar field. It can be seen that, in the small mass limit, the two are close together, even more so the larger the black hole rotation. As the mass increases, the spectrum of the two fields become more and more different. In all cases the Proca field has a larger damping

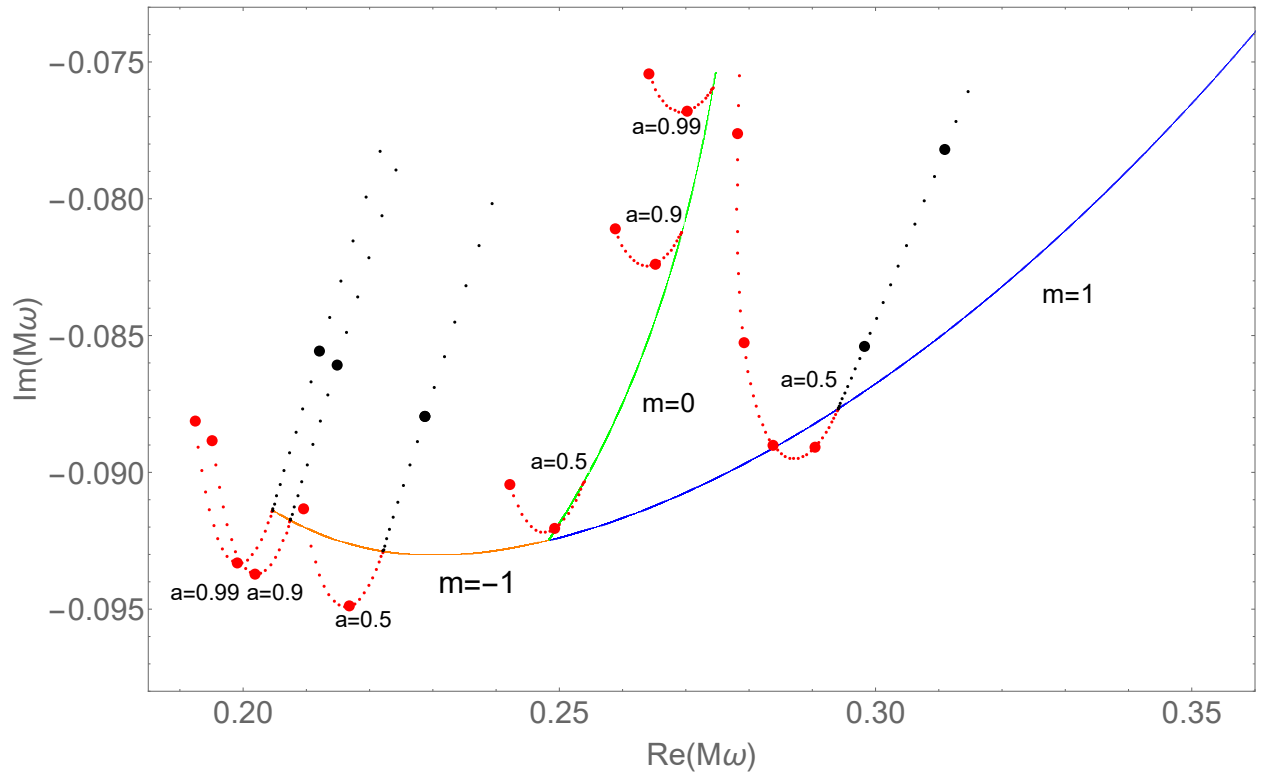


Figure 4.2.7: Vector-type QNM frequencies for  $m = -1$  ( left, orange),  $m = 0$  (centre, green) and  $m = 1$  (right, blue) modes, for  $\ell = 1$ , with a mass spacing  $\Delta(M\mu) = 0.01$ . The plot shows the detail of the  $m = -1$  and  $m = 0$  cases; the  $m = 1$  cases for higher  $a$  are shown in Fig. 4.2.5.

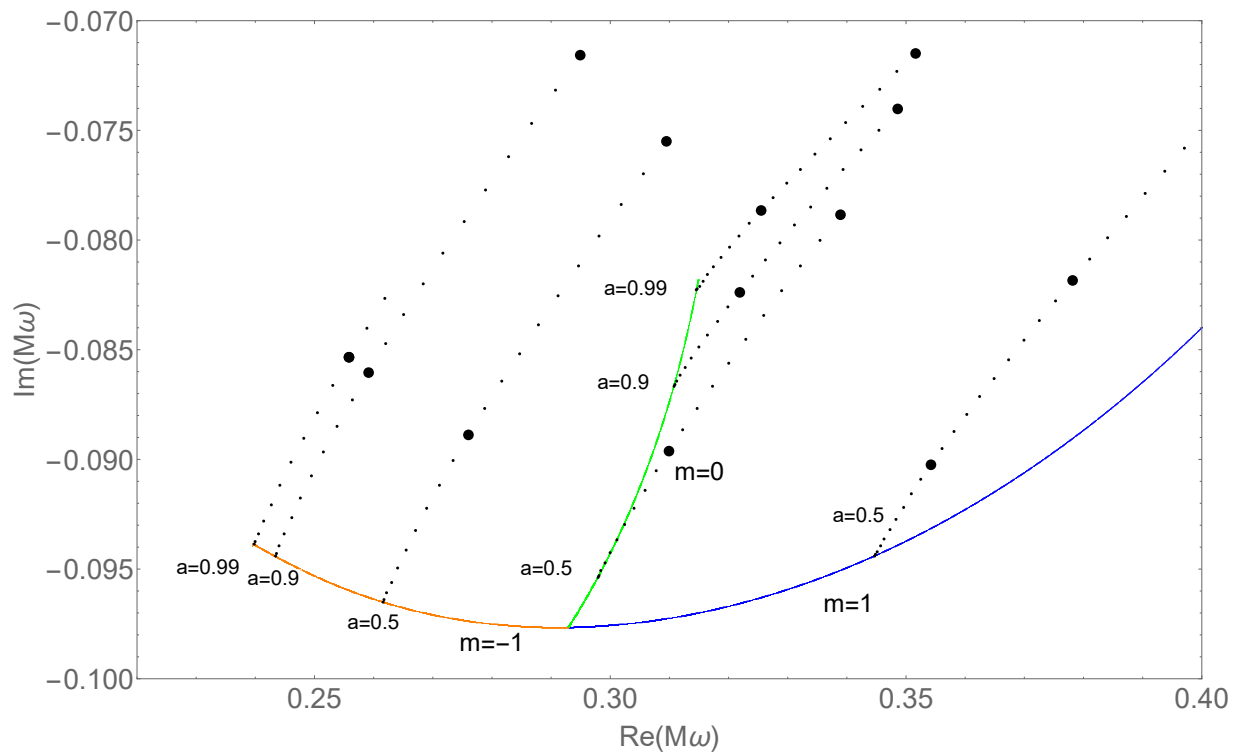


Figure 4.2.8: The scalar-type Proca QNMs for the  $m = -1$ ,  $m = 0$  and  $m = 1$  branches of the  $\ell = 1, n = 0$  spectrum. As in Fig.4.2.5, the mass spacing between large (small) points is  $M\mu = 0.1(0.01)$ .

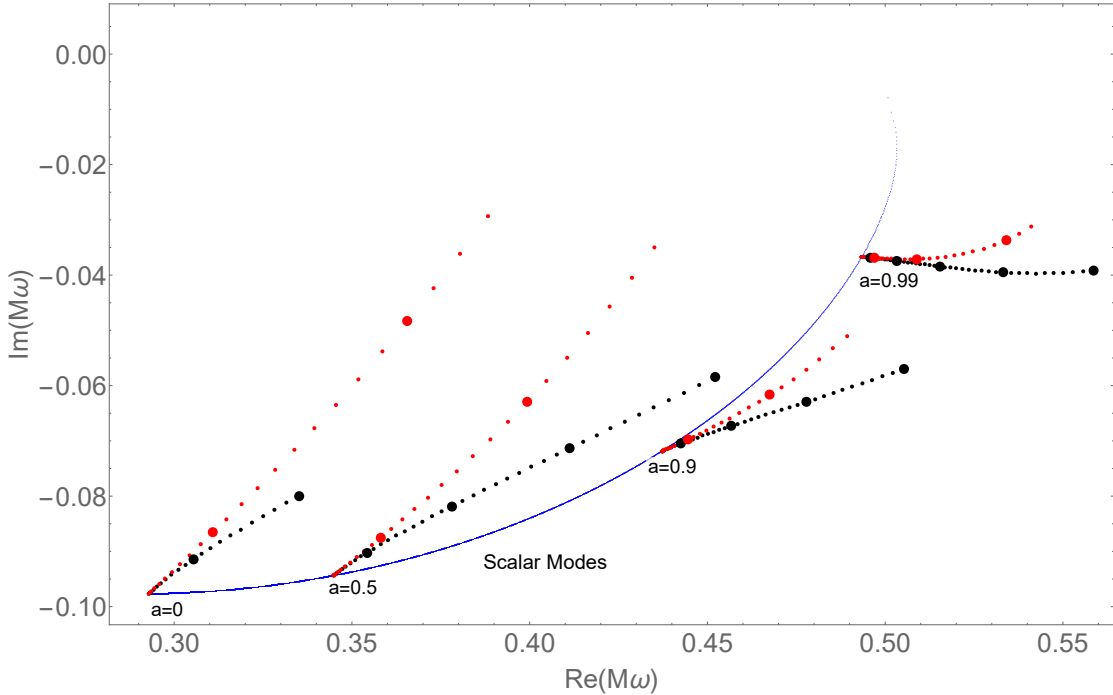


Figure 4.2.9: Comparing the QNM spectrum of the scalar-type polarization of the Proca field (black) with the QNM spectrum of the massive scalar field (red). As in Fig 4.2.5, the mass spacing between large (small) points is  $M\mu = 0.1(0.01)$ .

rate and a smaller oscillation frequency than the scalar field for the same mass value.

The higher multipoles (higher values of  $\ell$ ) of the fundamental mode of the even-parity vector-type Proca field are presented in Fig. 4.2.10. We see that the behavior that was present for  $\ell = 1$  persists into these high multipoles, the damping rate increases for small  $\mu$ , before all the modes trend upwards towards the real axis as  $\mu$  grows larger.

### 4.3 QNMs in the Kerr-Newman Spacetime

In this section, we calculate the QNMs of the (uncharged) massive scalar field and all three polarizations of the Proca field on the Kerr-Newman spacetime using a recurrence relation and the continued fraction method. The scalar field is studied to compare the results to the scalar polarization of the Proca field in Fig. 4.3.3. Like the Kerr case, to our knowledge the data for the Proca field is entirely new.

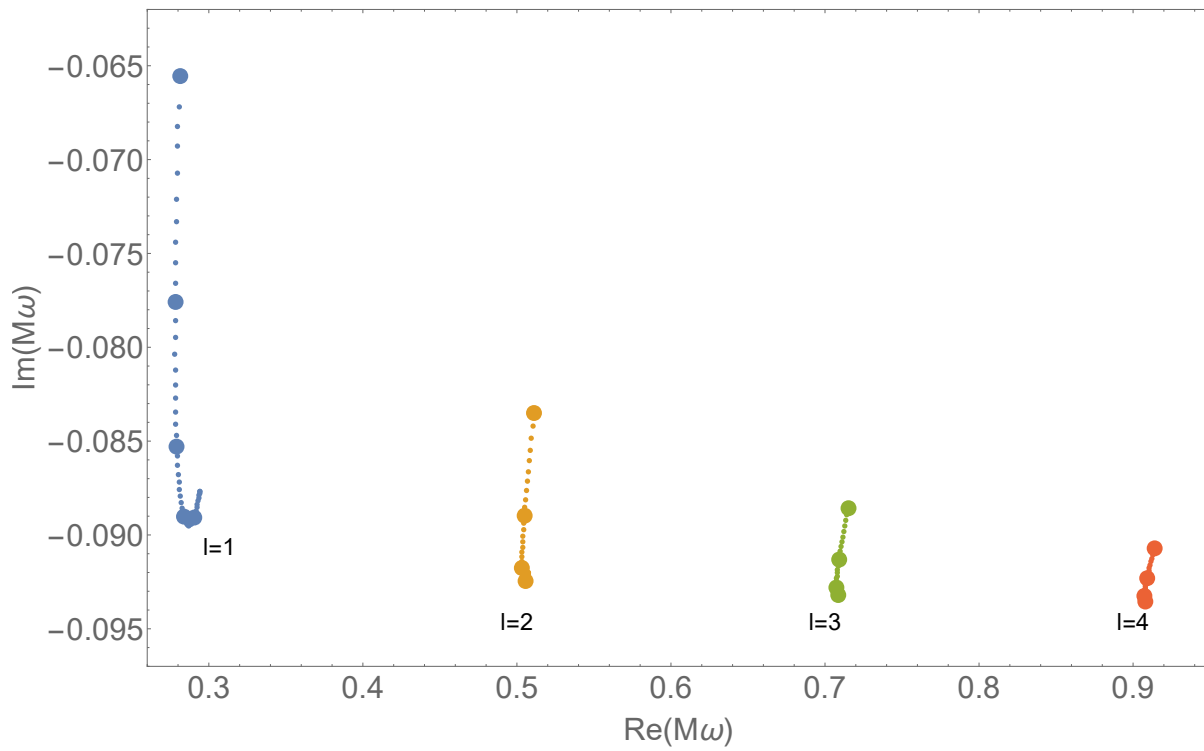


Figure 4.2.10: The higher multipoles of the even-parity vector QNMs on the Kerr spacetime for  $a = 0.5$  and  $m = 1$ . As in Fig. 4.2.5, the mass spacing between large (small) points is  $M\mu = 0.1(0.01)$  with the largest mass values being closest to the real axis.

### 4.3.1 Scalar Field

The radial equation for a scalar field in a rotating black hole spacetime can be written in the following form,

$$\frac{d}{dr} \left( \Delta \frac{dR}{dr} \right) + \left( \frac{K_r^2}{\Delta} - \Lambda + 2a\omega m - a^2\omega^2 - \mu^2 r^2 \right) R = 0. \quad (4.3.1)$$

The form of this equation is obtained by setting the right-hand-side of (4.2.35) to zero and is valid in the Kerr and Kerr-Newman spacetimes. The QBSs of the scalar field on the Kerr spacetime were studied in [52] by applying Leaver's method to a three term recurrence relation and the same was done for a charged scalar field in the Kerr-Newman spacetime in [85]. Neither of these papers covered the QNMs and so we opt to find the scalar field QNMs ourselves by deriving a recurrence relation from (4.3.1).

Substituting into this equation the same ansatz used in [52], which is very similar to that in (4.2.74),

$$R(r) = \left( \frac{r-r_+}{r-r_-} \right)^{-i\rho} (r-r_-)^{\chi-1} e^{-qr} \sum_{k=0}^{\infty} a_k \left( \frac{r-r_+}{r-r_-} \right)^k, \quad (4.3.2)$$

(note the  $\chi - 1$ ), the indices  $\rho$  and  $\chi$  take their usual values

$$\rho = \frac{(r_+^2 + a^2)\omega - am}{r_+ - r_-}, \quad \chi = \frac{M(\mu^2 - 2\omega^2)}{q}.$$

Setting the coefficient of each power of the radial variable to zero in the usual way gives the three term relation,

$$\alpha_n a_{n+2} + \beta_n a_{n+1} + \gamma_n a_n = 0 \quad n > -1,$$

$$\alpha_n = 8bq^2 (n+2) (2i\rho - n - 2), \quad (4.3.3)$$

$$\beta_n = 2q \left\{ 4q^3 r_+^2 b + 4qb(5 + 2n(n+3) + \Lambda) - 4i(3+2n)qr_+^2\omega - 4qr_+^2(M+r_+)\omega^2 \right. \quad (4.3.4)$$

$$\left. + 4(M\omega^2 - q^2(b+r_+))(ir_+^2\omega - (3+2n)b) \right.$$

$$\left. 4ia(a\omega - m)(q(-3-2n-q(b+r_+)) + M\omega^2) - 4a^2\omega^2q(M+r_+) + 8amqM\omega \right\},$$

$$\gamma_n = 4 \left( M(q^2 - \omega^2) + q(1+n-2iM\omega) \right) \quad (4.3.5)$$

$$\times \left( iq(2a^2 + r_-^2 + r_+^2)\omega + \frac{1}{2}(r_+^2 - r_-^2)\omega^2 - 2iamq - 2qb(1+n+qM) \right).$$

The angular eigenvalue  $\Lambda$  is found using the Black Hole Perturbation Toolkit for Mathematica [1]. We first test this recurrence relation by using it to calculate the well known QNMs of the

massless scalar field on the Kerr spacetime for a range of  $a$ . We find agreement with the data in [21] to at least six significant figures.

We now present the QNMs of the scalar field in the Kerr-Newman spacetime in Fig. 4.3.1. The blue points are the QNMs of the massless scalar field for  $\ell = m = 1$ ,  $n = 0$  and the given values of  $a$ . These were found by using the known massless QNMs in the Kerr spacetime from [21] as an initial guess to minimise the continued fraction (2.4.8). The charge  $Q$  on the hole is then increased in increments, with the previously found QNM forming the initial guess for the next one in the sequence. As can be seen from the figures, the QNMs vary more rapidly as we approach the extreme value of charge  $Q_{max} = \sqrt{M^2 - a^2}$  and so we clustered the sampled values of  $Q$  closer to this extreme. We then selected three values of charge and increased  $\mu$  in increments of 0.01, producing the purple points.

For values of  $Q$  and  $a$  not close to the extremal limits, as  $\mu$  increases the oscillation frequency  $\Re(\omega)$  increases and the decay rate  $-\Im(\omega)$  decreases. This pattern no longer holds as  $a$  approaches  $M$  or  $Q$  approaches  $Q_{max}$ , where we see an initial increase in the decay rate ( $\Im(\omega)$  becomes more negative) until the mass reaches a specific value, before the QNMs trend once more towards the real axis. When both the spin and charge are near the extremal values, we see that the oscillation frequency of the QNM decreases and the decay rate increases as the mass increases.

### 4.3.2 Proca Field Numerical Results

We will now move on to discussing the Proca field. Equations (4.2.75) to (4.2.79) can be easily generalised to apply to the Kerr-Newman spacetime. Let's consider two forms of the radial differential equation for the Proca field on a rotating black hole spacetime, Eqs. (4.2.51) and (4.2.29). When we subtract Eq. (4.2.51) (multiplied by  $\Delta^{-1}$ ) from (4.2.29), rather than getting zero, we are left with a difference in the form of a term

$$\left[ \frac{\omega^2}{\Delta} (a^2 - r_+ r_-) \right] R(r). \quad (4.3.6)$$

This reflects the fact that Eq. (4.2.51) is valid only in the Kerr spacetime, while Eq. (4.2.29) is valid in the Kerr and Kerr-Newman spacetimes. Indeed, this difference term (4.3.6) vanishes if the black hole charge  $Q = 0$ , as in that case  $a^2 = r_+ r_-$ . To generalise the Kerr specific differential equation (4.2.51) to the Kerr-Newman spacetime, we see that this term (4.3.6) can be canceled through a re-definition of  $\tilde{\Lambda}$

$$\tilde{\Lambda} = \Lambda - \omega^2 Q^2, \quad (4.3.7)$$

with  $\Lambda$  defined in (4.2.37).

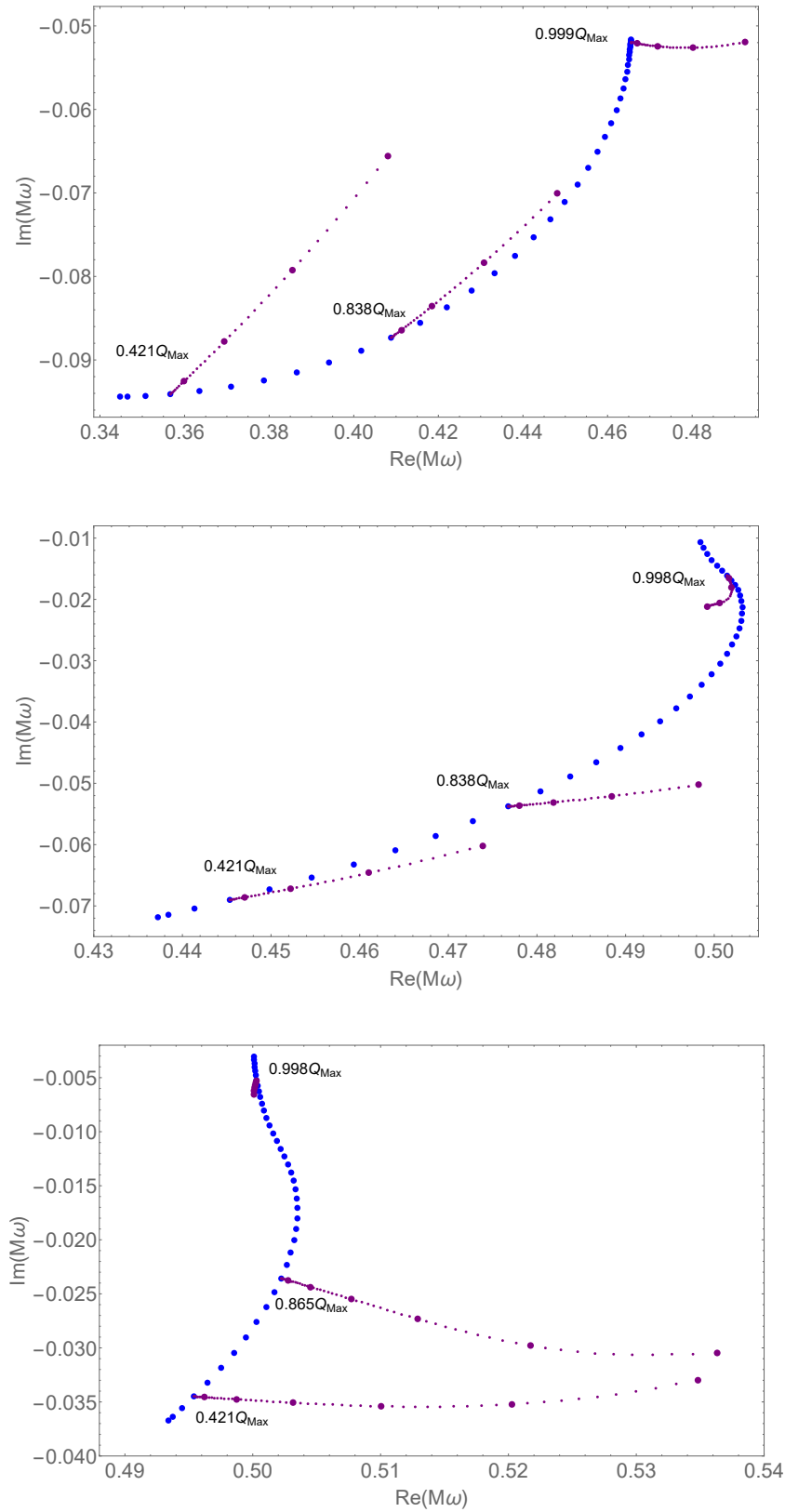


Figure 4.3.1: The QNMs of the scalar field in the Kerr-Newman spacetime found from the recurrence in Eqs. (4.3.3)-(4.3.5), for  $a = 0.5$  (top)  $0.9$  (middle) and  $0.99$  (bottom). The blue points are the QNMs of the massless field for various  $Q$  and the purple points are for fixed  $Q$  and increasing mass. The small (large) purple points are in mass increments of  $0.01$  ( $0.1$ ).

This re-definition must be performed in the radial differential equation (and hence in the recurrence relation Eqs. (4.2.75)-(4.2.79)). It is not required in Eq. (4.2.67) when finding the angular eigenvalue, as the angular differential equation (4.2.36) does not change when adding a black hole charge.

This is all that is required to calculate the QNMs of all three polarizations of the Proca field in the Kerr-Newman spacetime using the same scheme explained for the scalar field in the previous subsection, which are presented for  $\ell = m = 1, n = 0$  in Fig. 4.3.2. As the mass increases they behave qualitatively similar to the QNMs presented in Fig. 4.2.5 for the Kerr spacetime, with  $\Re(\omega)$  and  $\Im(\omega)$  initially decreasing as  $\mu$  increases for the even-parity vector polarization and both increasing for the odd-parity vector and scalar polarizations. This trend changes when either  $a$  or  $Q$  approaches their extremal values, with  $\Im(\omega)$  initially decreasing with  $\mu$  for the odd-parity vector and scalar polarizations. As we approach the double extremal limit,  $\Re(\omega)$  and  $\Im(\omega)$  for the QNMs of the scalar polarization both decrease with mass, as for the scalar field.

A point needs to be made here about the interpretation of the blue points in Fig. 4.3.2. It is tempting to say that they are the QNMs of the electromagnetic field in the Kerr-Newman spacetime, but the truth is more complicated. In Ref. [75] it is shown that incident electromagnetic waves can, at least partially, be reflected from the potential of a charged black hole as gravitational waves (and vice versa). Hence, the most we can say is that the blue points are the massless QNMs of some combination of electromagnetic and gravitational waves.

As for the Kerr spacetime, we can directly compare the QNMs of the scalar field and the scalar polarization of the Proca field, shown in Fig. 4.3.3 and observe that they have qualitatively similar behavior. Unlike in the Kerr case however, for non-extremal black hole charge and spin, the Proca QNMs have a larger oscillation frequency and a smaller decay rate than their scalar counterparts. When either the spin or the charge approaches the extremal limit, the Proca QNMs still have a larger oscillation frequency, but now also have a larger decay rate.

## Conclusion and Further Study

In this chapter we have primarily focused on the analytical approximation and numerical calculation of QNMs and quasibound state frequencies of scalar and vector fields in the Kerr and Kerr-Newman spacetimes. As far as we are aware, the QNM results for the massive scalar field in Kerr-Newman spacetime and for the massive vector field in both the Kerr and Kerr-Newman spacetimes are entirely new. We also discussed the similarities and differences between the QNMs of the scalar field and the QNMs of the scalar polarization of the Proca field.

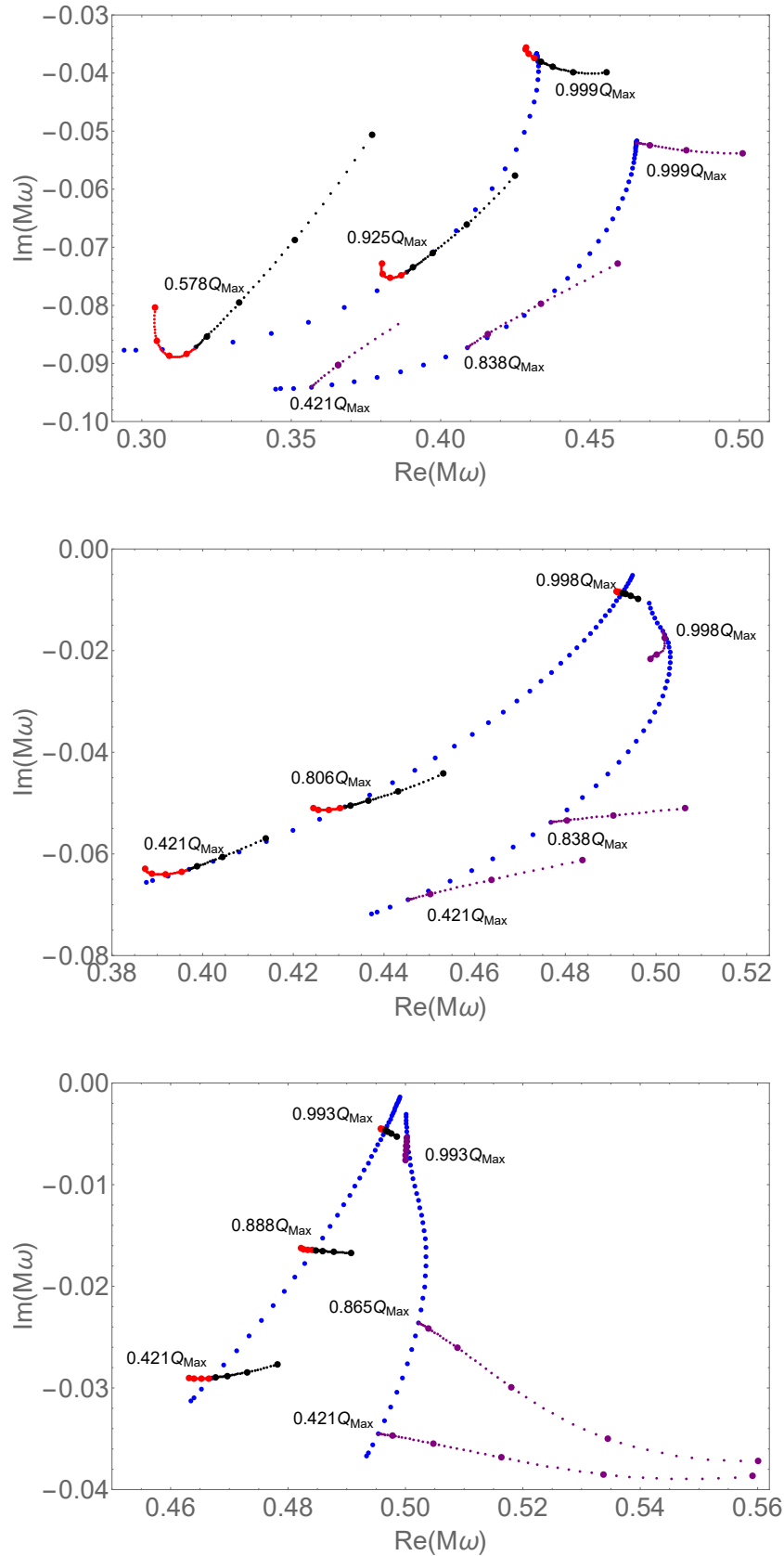


Figure 4.3.2: The QNMs of the Proca field in the Kerr-Newman spacetime, for  $a = 0.5$  (top) 0.9 (middle) and 0.99 (bottom). The upper (lower) blue points are the QNMs of the massless vector (scalar) field for various  $Q$  and the red, black and purple points are for fixed  $Q$  and increasing mass in the even-parity vector, odd-parity vector and scalar polarizations respectively.

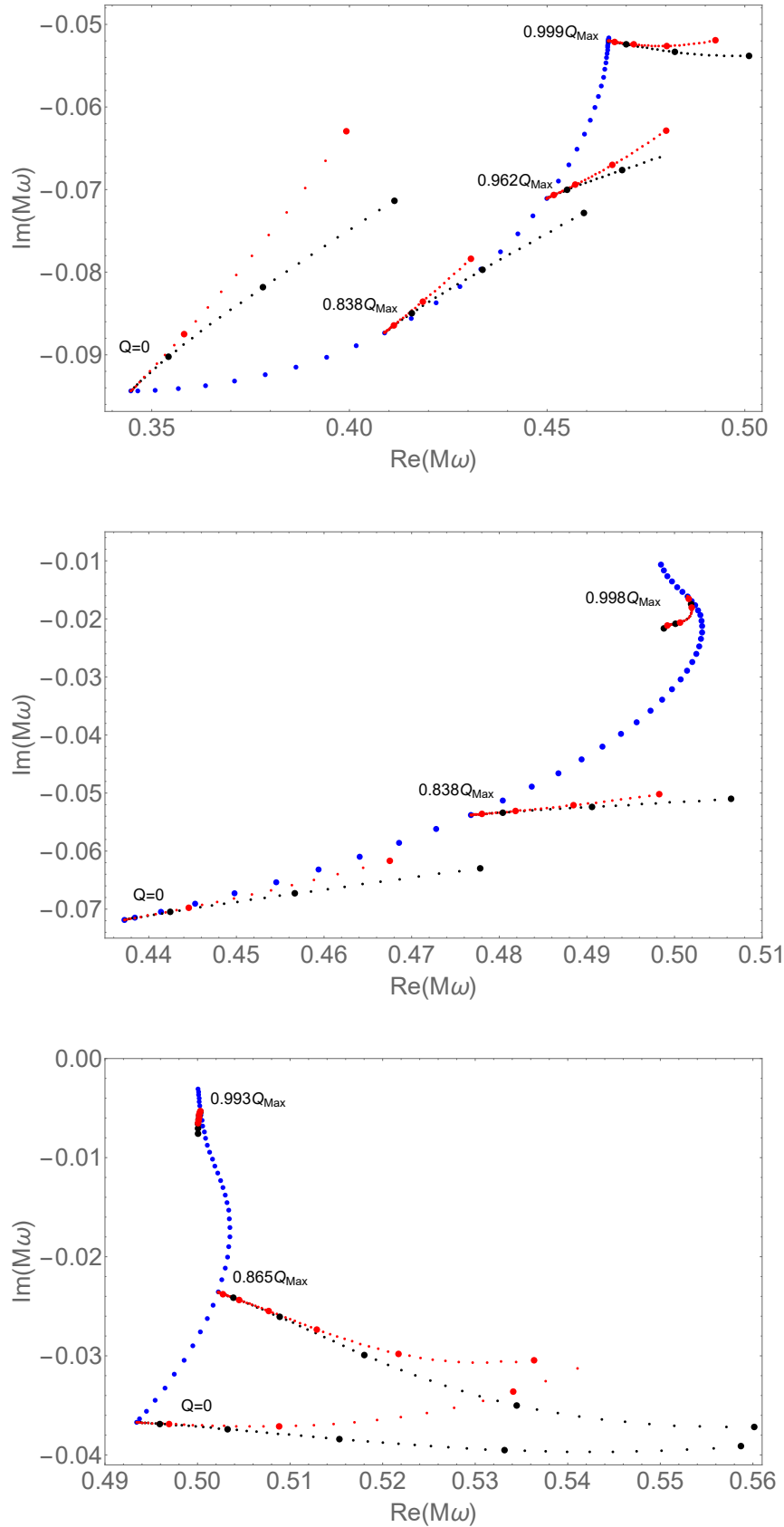


Figure 4.3.3: A comparison of the QNMs of the scalar field (red) and the scalar polarization of the Proca field (black) in the Kerr-Newman spacetime, for  $a = 0.5$  (top)  $0.9$  (middle) and  $0.99$  (bottom).

We now briefly discuss the difficulties we encountered in applying our recurrence relation, Eqs. (4.2.75)-(4.2.79). The decrease in the accuracy (which we here define as agreement with the data in [54]) of our QBS results as we move away from the peak of the superradiant instability in the complex plane raises the possibility that our recurrence relation is less reliable when  $\Im(\omega)$  is small. However, this cannot be the full story, as the data is accurate for the parameters  $S = 0, a = 0.6$  but not for  $S = +1, a = 0.99$ , where  $\Im(\omega)$  is comparable. A possibility exists that numerical error is accumulating during the Gaussian elimination step if either  $\delta_n$  or  $\varepsilon_n$  are too small. With more time to continue the project, this is the first possibility that we would consider.

Figure 4.2.7 lacks data for the odd-parity Proca QNMs when  $m = 0$ , as using our recurrence relation did not produce a smooth curve of data. We hypothesise that this is due to the failure of the argument given in Sec. 4.2.2.3 when  $m = 0$  (particularly Eq. (4.2.47)) to establish that the branch of the eigenvalue  $\nu$  that diverges in the static limit is the correct branch to take for the odd-parity mode. See also Eq. (4.2.43) for the massless eigenvalue, which for  $m = 0$  implies it is  $a^2\nu$  that tends to a constant as  $a \rightarrow 0$ , rather than  $a\nu$ , which was required to match with the non-rotating angular equation (4.2.36).

This concludes the first half of this work, on the propagation of classical bosonic fields on black hole spacetimes. We will now shift our focus to discussing the propagation of the quantum scalar field.



## Part II

# Quantum Fields



## Chapter 5

# Quantum Field Theory on Curved Spacetime

### Introduction and Overview

Throughout the next three chapters, we will be focusing entirely on the *semiclassical* theory of a scalar field  $\phi$  propagating on static, spherically symmetric spacetimes. The principles of semiclassical gravity were covered in chapter 1. Recall, in particular, that  $\phi$  is an operator on a Hilbert space of state vectors and so we wish to calculate *expectation values* of these operators. We will begin with a general discussion of quantising such a field on an arbitrary curved spacetime, before moving on to the calculation of  $\langle\phi^2\rangle$  outside of a Schwarzschild back hole. The quantity  $\langle\phi^2\rangle$  is called the *vacuum polarization* and is a prerequisite to the calculation of  $\langle T_{\mu\nu}\rangle$  while sharing a few of its important properties.

The work presented in this chapter is a summary of the relevant literature and it forms the foundation of our original numerical analysis of  $\langle\phi^2\rangle$  outside a spherically symmetric star in chapter 7. This chapter also contains the details of our own numerical implementation of the Levi and Ori method of calculating  $\langle\phi^2\rangle$  in the Boulware state outside a Schwarzschild black hole in Sec. 5.2.3. We will work in natural units, such that  $G = c = \hbar = 1$ .

## 5.1 Quantisation of a Scalar Field

### 5.1.1 Canonical Quantisation

There are many resources discussing the extension of Quantum Field Theory (QFT) from flat spacetime to curved spacetime, such as [22] and [114]. In this section we will briefly cover the fundamentals

of the topic, focusing on their application to a scalar field.

As in chapter 2, the first step of discussing a physical theory is to specify a Lagrangian density (cf. Eq. (2.1.5))

$$\mathcal{L} = -\frac{1}{2} (g^{\mu\nu} \nabla_\mu \phi \nabla_\nu \phi + (\mu^2 + \xi \mathcal{R}) \phi^2), \quad (5.1.1)$$

where  $\phi$  is a scalar field of mass  $\mu$  and coupling  $\xi$  to the Ricci scalar  $\mathcal{R}$ . From this density we can construct the Klein-Gordon equation of motion (cf. Eq. (2.1.14))

$$(\square - \mu^2 - \xi \mathcal{R}) \phi = 0, \quad (5.1.2)$$

where  $\square = g^{\mu\nu} \nabla_\mu \nabla_\nu$  is the d'Alembertian wave operator.

Two values of the coupling constant  $\xi$  are especially important: *minimal coupling*  $\xi = 0$  and *conformal coupling*  $\xi = 1/6$ . The latter is so named because under a conformal transformation of the metric

$$g_{\mu\nu} \rightarrow \tilde{g}_{\mu\nu} = \Omega^2 g_{\mu\nu}, \quad (5.1.3)$$

which also transforms the Ricci scalar

$$\mathcal{R} \rightarrow \tilde{\mathcal{R}} = \Omega^{-2} \mathcal{R} + 6\Omega^{-3} \square \Omega, \quad (5.1.4)$$

a coupling of  $\xi = 1/6$  would leave the equation of motion for a massless field invariant, as follows,

$$\left( \square - \frac{1}{6} \mathcal{R} \right) \phi \rightarrow \left( \tilde{\square} - \frac{1}{6} \tilde{\mathcal{R}} \right) \tilde{\phi} = \Omega^{-3} \left( \square - \frac{1}{6} \mathcal{R} \right) \phi, \quad (5.1.5)$$

where  $\tilde{\phi} = \Omega^{-1} \phi$ .

We can define a scalar product between two solutions of Eq. (5.1.2)

$$(\phi_1, \phi_2) = -i \int_{\Sigma} d\Sigma n^\mu \sqrt{g_\Sigma} [\phi_1 \partial_\mu \phi_2^* - (\partial_\mu \phi_1) \phi_2^*], \quad (5.1.6)$$

where  $\Sigma$  is a spacelike hypersurface with volume element  $d\Sigma$  and metric  $g_\Sigma$  and  $n^\mu$  is a future-directed unit vector orthogonal to  $\Sigma$ . If the spacetime is globally hyperbolic (which is true for all spacetimes we will consider) we can take the surface  $\Sigma$  to be a *Cauchy surface* and the inner product is independent of the Cauchy surface chosen. The condition of global hyperbolicity can be defined as the requirement that a Cauchy surface exists in the spacetime [71] and a Cauchy surface can be defined, as in [79], as “a spacelike hypersurface which every non-spacelike curve intersects exactly once”. The invariance of (5.1.6) with respect to  $\Sigma$  follows from the fact that two Cauchy surfaces  $\Sigma_1$  and  $\Sigma_2$  will enclose a volume  $\mathcal{V}$ , within which the vector field

$$J_\mu \equiv \phi_1 \partial_\mu \phi_2^* - (\partial_\mu \phi_1) \phi_2^*, \quad (5.1.7)$$

is divergence-free. The invariance of the scalar product with respect to  $\Sigma$  then follows from Gauss's theorem.

We now wish to expand the field  $\phi$  using a complete set of solutions  $f_i$  to the Klein-Gordon equation (5.1.2), in the following way

$$\phi = \sum_i \left( a_i f_i + a_i^\dagger f_i^* \right). \quad (5.1.8)$$

The index  $i$  may be discrete or continuous. In the continuous case the sum in Eq. 5.1.8 must be replaced by an integral. The  $f_i$  are chosen to be orthonormal with respect to the inner product (5.1.6)

$$(f_i, f_j) = \delta_{ij}, \quad (f_i^*, f_j^*) = -\delta_{ij}, \quad (f_i, f_j^*) = 0 \quad (5.1.9)$$

and the  $a_i^\dagger$  and  $a_i$  are the *creation* and *annihilation operators* respectively. The signs in front of the Kronecker deltas in (5.1.9) are a convention: we call the  $f_i$  the *positive frequency* modes and the  $f_i^*$  the *negative frequency* modes [114].

Finally, *canonical quantisation* can be performed by imposing commutation relations between the  $a_i$  and  $a_i^\dagger$

$$\left[ a_i, a_j^\dagger \right] = \delta_{ij}, \quad [a_i, a_j] = 0, \quad \left[ a_i^\dagger, a_j^\dagger \right] = 0 \quad (5.1.10)$$

and a vacuum state  $|0\rangle$  can be defined as a state that is annihilated by the annihilation operator,  $a_i |0\rangle = 0$  for all  $i$ .

### 5.1.2 Non-Uniqueness of the Vacuum State

It might appear at first sight that the quantisation of a scalar field in a curved spacetime proceeds very similarly to quantisation in Minkowski spacetime. Although the process is very similar, there is a crucial difference: an ambiguity arises in how we choose to expand the field  $\phi$  into modes, as in Eq. (5.1.8). This is equivalent to an ambiguity in how we choose to define what modes are to be considered positive frequency. In Minkowski space this ambiguity isn't present, as one can construct a "preferred" vacuum state that is invariant under the action of the Poincaré group and so is valid in all inertial reference frames. In a curved spacetime, the Poincaré group no longer leaves the metric line element unchanged and this "preferred" vacuum state is lost [22].

This means that when discussing the properties of a quantum field in a curved spacetime, we must specify which state we are working in. In the Schwarzschild spacetime, there are generally three vacuum states that are commonly used and they can be classified according to which surface we choose to define the positive frequency modes on [40].

- The *Boulware* state [23]: This is the vacuum state constructed using the coordinate system of an observer far from the gravitational source, i.e., on the surface  $\mathcal{I}^+ \cup \mathcal{I}^-$ . In other words, the IN and UP modes described in Sec. 3.1 (see Figs. 3.1.1 and 3.1.2) are devoid of particles. The Boulware state is considered to be the appropriate vacuum state in the spacetime of a static, spherically symmetric star. The stress-energy tensor of a quantum field  $\langle T^\mu_\nu \rangle$ , when evaluated in this state, diverges as one approaches the event horizon of the black hole.
- The *Hartle-Hawking* state [77]: This is the vacuum state measured according to a free falling observer near the black hole's event horizon, i.e., positive frequency modes are defined on the surface  $H^+ \cup H^-$ . An observer on  $\mathcal{I}^+ \cup \mathcal{I}^-$  would measure this state to contain thermal radiation, i.e., the IN and UP modes are thermally populated. The stress-energy tensor in this state is regular in the entirety of the exterior Schwarzschild spacetime, including on the event horizon and so this state is the most suitable to study black hole thermodynamics. This state models a black hole inside a thermal bath of radiation at the Hawking temperature, i.e., the black hole is in unstable equilibrium.
- The *Unruh* state [141]: Like the Hartle-Hawking state, this state is defined according to its properties on  $H^-$ . However, instead of being defined according to positive frequency modes with respect to the Schwarzschild time coordinate  $t$  it is defined with respect to the Kruskal coordinate,

$$U = -4Me^{-u/4M}, \quad u = t - r - 2M \log\left(\frac{r}{2M} - 1\right). \quad (5.1.11)$$

This state is empty at  $\mathcal{I}^-$ , but at  $\mathcal{I}^+$  it contains a flux of thermal radiation at the Hawking temperature. As such, this state is used to model an evaporating spherically symmetric black hole.

## 5.2 Calculating Vacuum Polarization

### 5.2.1 The Two Point Function and Counterterms

We wish to calculate the vacuum polarization  $\langle \phi^2 \rangle$  (i.e., the vacuum expectation value of  $\phi^2$ ) of a scalar field in the spacetime of a spherically symmetric gravitational source, be it a Schwarzschild black hole or a star. From Eqs. (5.1.8), (5.1.10) and the definition of the vacuum state  $|0\rangle$  we have

that

$$\begin{aligned}\langle \phi^2 \rangle &\equiv \langle 0 | \phi \phi | 0 \rangle = \langle 0 | \sum_{ij} \left( a_i f_i + a_i^\dagger f_i^* \right) \left( a_j f_j + a_j^\dagger f_j^* \right) | 0 \rangle \\ &= \langle 0 | \sum_i |f_i|^2 | 0 \rangle = \sum_i |f_i|^2,\end{aligned}\tag{5.2.1}$$

where in the last line we used that the vacuum state is normalised such that  $\langle 0 | 0 \rangle = 1$ .

In the Schwarzschild coordinates  $(t, r, \theta, \varphi)$  the field  $\phi$  can be decomposed into modes in the following way

$$\phi(x) = \int_0^\infty d\omega \sum_{\ell=0}^\infty \sum_{m=-\ell}^\ell \left( f_{\omega\ell m}(x) a_{\omega\ell m} + f_{\omega\ell m}^*(x) a_{\omega\ell m}^\dagger \right),\tag{5.2.2}$$

where  $a_{\omega\ell m}^\dagger$  and  $a_{\omega\ell m}$  are the creation and annihilation operators of the mode  $f_{\omega\ell m}$ , which have the commutation relations (cf. Eq. (5.1.10))

$$\left[ a_{\omega\ell m}, a_{\omega'\ell'm'}^\dagger \right] = \delta_{\ell\ell'} \delta_{mm'} \delta(\omega - \omega')\tag{5.2.3}$$

and every other commutator vanishes.

These modes can in turn be expressed through the separation of variables

$$f_{\omega\ell m}(x) = e^{-i\omega t} Y_{\ell m}(\theta, \varphi) \bar{\psi}_{\omega\ell}(r),\tag{5.2.4}$$

where the radial modes are defined  $\bar{\psi}_{\omega\ell} \equiv r^{-1} (4\pi\omega)^{-1/2} \psi_{\omega\ell}$  and  $\psi_{\omega\ell}$  are the solutions of the radial differential equation (the Regge-Wheeler equation (3.1.9), in the case of a scalar field in the spacetime of a Schwarzschild black hole) with chosen boundary conditions. It was briefly mentioned in Sec. 3.1 that the normalisation of these modes would be important in the case of quantised fields. The factor of  $\sqrt{4\pi\omega}$  ensures that the  $f_{\omega\ell m}$  are normalised with respect to the inner product (5.1.6).

Formally speaking,  $\langle \phi^2 \rangle$  diverges. More specifically, if one substitutes Eq. (5.2.4) into (5.2.2) and applies (5.2.3) to get

$$\langle \phi^2 \rangle = \int_0^\infty d\omega \sum_{\ell=0}^\infty \sum_{m=-\ell}^\ell |Y_{\ell m}(\theta, \varphi)|^2 |\bar{\psi}_{\omega\ell}(r)|^2,\tag{5.2.5}$$

(cf. Eq. (5.2.1)) one finds that the integral over  $\omega$  always diverges, whether it is performed before or after the sums over  $\ell$  and  $m$ .

The method that we will be considering to regularise this divergence is *point-splitting regularisation*, in which we define the Green's function

$$G^{(1)}(x, x') = \frac{1}{2} \langle \phi(x) \phi(x') + \phi(x') \phi(x) \rangle,\tag{5.2.6}$$

constructed out of the *two-point function* (TPF)  $\langle \phi(x) \phi(x') \rangle$ , where  $x$  and  $x'$  are different spacetime points. When  $x$  and  $x'$  are nearby, the Green's function can be written as a Hadamard series

expansion [76]

$$G^{(1)}(x, x') = \frac{\Delta^{1/2}}{(4\pi)^2} \left( \frac{2}{\sigma} + v \ln \sigma + w \right), \quad (5.2.7)$$

where  $\sigma(x, x')$  is one half of the square of the geodesic distance separating the points  $x$  and  $x'$  and  $\Delta(x, x')$  is the Van-Vleck-Morette determinant,

$$\Delta(x, x') = -|g(x)|^{-1/2} \det[-\partial_\mu \partial_{\nu'} \sigma(x, x')] |g(x')|^{-1/2}. \quad (5.2.8)$$

In this expansion,  $v(x, x')$  and  $w(x, x')$  are analytic functions of  $\sigma$ , i.e., they admit series expansions

$$v = \sum_{n=0}^{\infty} v_n \sigma^n, \quad w = \sum_{n=0}^{\infty} w_n \sigma^n. \quad (5.2.9)$$

The coefficients  $v_n$  and  $w_n$  are then found by recursion relations obtained by substituting (5.2.7) into the Klein-Gordon equation (5.1.2). This uniquely determines each of the  $v_n$  and each of the  $w_n$  for  $n \geq 1$  as long as  $w_0$  is specified [114] (for more recent work on the Hadamard renormalisation of a scalar field and in particular the calculation of these  $v_n$  and  $w_n$  coefficients, see the extension to the charged scalar field in [12]). The coefficient  $w_0$  is fixed by the global boundary conditions on the Green's function, that is to say, it is not determined locally. Hence, one can isolate the purely local part of the Green's function  $G^L$  by setting  $w_0$  to zero in (5.2.7) [5]. This is the tool that will be used to regularise the divergences: we define the *regularised Green's function*  $G_{reg}^{(1)} = G^{(1)} - G^L$  and then the vacuum polarization can be found by taking the coincidence limit

$$\langle \phi^2 \rangle_{ren} = \lim_{x' \rightarrow x} \left[ G^{(1)}(x, x') - G^L(x, x') \right] = \lim_{x' \rightarrow x} \left[ \langle \phi(x) \phi(x') \rangle - G^L(x, x') \right], \quad (5.2.10)$$

where we have now chosen to work directly with the TPF as is done in [100].

The counterterms  $G^L(x, x')$  were found in [46] through the use of a (truncated) DeWitt-Schwinger expansion of  $G^{(1)}$  and presented in [8] for an arbitrary mass  $\mu$  and curvature coupling  $\xi$ . We will refer to the counterterms expressed in this form as  $G_{DS}(x, x')$ . They are

$$G_{DS}(x, x') = \frac{1}{8\pi^2 \sigma} + \frac{\mu^2 + (\xi - 1/6) \mathcal{R}}{8\pi^2} \left[ \gamma + \frac{1}{2} \ln \left( \frac{k^2 \sigma}{2} \right) \right] - \frac{\mu^2}{16\pi^2} + \frac{1}{96\pi^2 \sigma} \mathcal{R}_{\alpha\beta} \nabla^\alpha \sigma \nabla^\beta \sigma, \quad (5.2.11)$$

where  $\gamma$  is Euler's constant,  $\mathcal{R}$  and  $\mathcal{R}_{\alpha\beta}$  are the Ricci scalar and Ricci tensor of the background spacetime and  $k$  is a *regularisation parameter*. In the case of a massive field this parameter is just the mass,  $k = \mu$ , but for a massless field the parameter is arbitrary and must be determined from experiment [8]. Regardless, we do not need to be unduly concerned about this parameter, as for a massless field in the Schwarzschild spacetime  $\mu = 0$  and  $\mathcal{R} = 0$ , so the coefficient of the term containing it vanishes.

Some care must be taken in how the points  $x$  and  $x'$  are separated. As can be seen from Eq. (5.2.11), the counterterms diverge not just when  $x = x'$ , but also for any pair of points such that

$\sigma = 0$ , i.e. when there exists a null geodesic connecting the two points. In most circumstances it is not an issue to simply assume that the two points remain either timelike or spacelike separated as they are brought together, but an interesting question presents itself, see for example [99]: can null geodesics create singularities in the TPF that the counterterms cannot account for? In Schwarzschild spacetime the answer is yes: all one has to consider are the null geodesics that leave a point  $x_i = (t_i, r_i, \theta_i, \varphi_i)$  and wrap around the black hole  $n$  times before arriving at the point  $x_n = (t_n, r_i, \theta_i, \varphi_i)$ . Then, the TPF has a singularity for the pair of points  $(x_i, x_n)$ . Understanding the location of these singularities can be important when implementing certain variants of the pragmatic mode sum regularisation method [99], to be described in Sec. 5.2.3.

It has already been mentioned that the counterterms are entirely local, but this can also be seen directly from Eq. (5.2.11):  $G_{DS}(x, x')$  depends only on the spacetime structure in the vicinity of the points  $x$  and  $x'$ , as well as the parameters of the field itself. The locality of these terms can be exploited in many calculations involving the vacuum polarization: for instance, evaluating the difference in  $\langle \phi^2 \rangle$  between two different quantum states circumvents the need to renormalise, as the counterterms are independent of the state chosen and so cancel in the subtraction [32]. The same is also true when one calculates the difference  $\Delta \langle \phi^2 \rangle$  in the vacuum polarization between two different spacetimes in the same quantum state, provided the two spacetimes are locally indistinguishable in a neighbourhood of the spacetime point  $x$  [7]. This will be explained in more detail when we come to look at QFT differences in chapter 6.

## 5.2.2 Evaluation Methods

### 5.2.2.1 WKB Methods

Evaluating the TPF  $\langle \phi(x) \phi(x') \rangle$  is not a simple task for two primary reasons: the radial functions  $\psi_{\omega\ell}$  are only known numerically and, as just discussed, the TPF contains  $\sigma^{-1}$  and  $\ln \sigma$  divergences as the points  $x$  and  $x'$  are brought together. A semi-analytical scheme to handle these problems was devised by Anderson, Hiscock and Samuel [8] following prior work by Anderson, Candelas and Howard [6, 32, 83, 84], where the vacuum polarization in Eq. (5.2.10) is rewritten in the following manner

$$\begin{aligned} \langle \phi^2(x) \rangle_{ren} &= \lim_{x' \rightarrow x} [\langle \phi(x) \phi(x') \rangle - \langle \phi_{WKB}(x) \phi_{WKB}(x') \rangle] \\ &\quad + \lim_{x' \rightarrow x} [\langle \phi_{WKB}(x) \phi_{WKB}(x') \rangle - G_{DS}(x, x')]. \end{aligned} \quad (5.2.12)$$

Here,  $\phi_{WKB}(x)$  is an analytical approximation to the singular piece of the field  $\phi(x)$ , consisting of all the high frequency modes, up to order  $\omega^{-2}$  found using the WKB method. This is then added

and subtracted from the vacuum polarization to form (5.2.12). The purpose of this construction is to split  $\langle \phi^2(x) \rangle$  into two terms: one that is calculated completely numerically (the first limit in (5.2.12)) and one that is computed analytically (the second limit in (5.2.12)). The coincidence limit of both of these terms is well defined and the mode sums in the first term will converge rapidly, as one is essentially summing the “remainder” of the TPF after the WKB approximation has been subtracted. This method was used to calculate both  $\langle \phi^2(x) \rangle$  and  $\langle T_{\mu\nu}(x) \rangle$  in an arbitrary static, spherically symmetric spacetime in [8], building on previous approximations to these quantities formed by Page, Brown and Ottewill [29] and Frolov and Zel’nikov [68].

The difficulty of implementing this scheme is in the calculation of  $\phi_{WKB}(x)$ . In the Schwarzschild metric this difficulty largely arises due to the existence of a turning point in the effective potential of the Regge-Wheeler equation  $V_\ell(r)$  ((3.1.5) with  $e = Q = 0$ ) at some critical value  $r_{turn}$ . The two WKB approximations of the radial mode, one prior to this turning point and one after this turning point, have radically different behaviors and so must be carefully matched in the vicinity of  $r = r_{turn}$ . This matching becomes harder to do the higher the order of the WKB approximations required. Even for a WKB approximation of just second order (like that required to find  $\phi_{WKB}(x)$ ) the calculation is formidable.

This motivated Anderson *et al.* to perform a *Wick rotation* of the spacetime, which is a transformation of the time coordinate  $t \rightarrow i\tau$ , such that the metric has a positive definite signature, i.e., the metric has been *Euclideanised*. This has the effect of removing the turning point from the effective potential. However, this method is only guaranteed to work if the background spacetime is static and so for spacetimes with a time dependent metric, another route must be taken. This is what motivated Levi and Ori, in [99], to develop their pragmatic mode sum approach to calculating  $\langle \phi^2(x) \rangle$ , to be detailed in Sec. 5.2.3.

The methods of Anderson *et al.*, were also used by Anderson and Fabbri in [7] to consider QFT differences between locally equivalent spacetimes, to be detailed in Sec. 6.1.

### 5.2.2.2 Counterterm Mode Sum Prescriptions

Before we discuss the pragmatic mode sum (PMR) method of Levi and Ori, note should be made of other methods that utilise mode sums. These contrast with the WKB method described in the previous subsection in that rather than regularising the entire Green’s function “all at once” by the subtraction of  $G^L$ , both the Green’s function and the counterterms are expanded as mode sums and the regularisation is done mode by mode.

One method of this type was developed by Breen and Ottewill for an arbitrary spherically

symmetric spacetime, [25, 24], where it was applied to calculate  $\langle\phi^2\rangle$  and  $\langle T^\mu{}_\nu\rangle$  in the exterior region of the “lukewarm” Reissner-Nordström-de-Sitter black hole in the Hartle-Hawking state. The distinctive feature of their method is their exploitation of the freedom to redefine the stress-energy tensor in such a way that it is independent of the renormalisation technique used, provided certain axioms are satisfied [145].

Another mode sum prescription was developed by Taylor and Breen for evaluating  $\langle\phi^2\rangle$  in the Hartle-Hawking state in an arbitrary static, spherically symmetric spacetime in any number of dimensions  $d \geq 4$ . It is presented in [135] for odd dimensions and [136] for even dimensions. Although the method also requires Euclideanising the spacetime via a Wick rotation, it does not rely on a WKB expansion. Instead, Eq. (5.2.7) is expanded in a certain set of coordinates that are referred to as “extended coordinates”. In this carefully chosen system, the counterterms  $G^L$  to be subtracted can be written as a mode sum and subtracted from  $G^{(1)}$  term by term. This method was used to calculate  $\langle\phi^2\rangle$  outside of a Schwarzschild-Tangherlini black hole with number of spacetime dimensions  $d = 4, \dots, 11$ . An interesting property of this method is that it requires separating the points  $x$  and  $x'$  in multiple of the  $d$  spacetime dimensions as opposed to the methods of [8] that required only splitting in one dimension. Splitting in more than one direction simultaneously will also be required in the “angular” variant of the pragmatic mode sum method employed by Levi and Ori, which we will cover next.

### 5.2.3 The Pragmatic Mode Sum Regularisation (PMR) of Levi and Ori

The details of this method have been outlined in a series of papers by Levi, Ori and others, including [99, 100, 97] and [98]. The primary distinction of the method is its wide range of applicability: all that is required is that the underlying spacetime have some form of symmetry. This symmetry is then utilised to decompose the DeWitt-Schwinger counterterm (5.2.11) into modes, allowing the regularisation procedure to be performed mode by mode. Hence, there are similarities between this method and that of Taylor and Breen. Though this method is not restricted to static, spherically symmetric spacetimes, it has not been generalised to spacetimes of higher dimension.

In the case of the Schwarzschild spacetime there are multiple such symmetries one could choose: utilising the staticity of the spacetime leads to a variant of the method Levi and Ori call *t-splitting*, (this is the variant of the method where an analysis of null geodesics that wrap around the black hole is very important) while utilising the spherical symmetry leads to *angular-splitting*. One could also utilise the axial symmetry, to obtain the method of *azimuthal-splitting* (This is done in the case of an evaporating Kerr black hole in [98]). We will be focusing primarily on the angular splitting

method described in [100]. Although this method is somewhat more complicated than the t-splitting variant, we found it less computationally intensive to implement.

### 5.2.3.1 Generalised Sums and Integrals

Before diving into the specifics of the method, there is an important point that must first be addressed. As mentioned underneath Eq. (5.2.5), the integral over  $\omega$  in the calculation of  $\langle \phi^2 \rangle$  does not converge. In the case of the angular-splitting method, we will find that in addition, the infinite sum over the  $\ell$  modes also fails to converge (in fact, it diverges more strongly than the integral). These divergences are not unexpected and one would hope to remove them through the subtraction of a suitable counterterm. However, at various steps in the pragmatic mode sum method, one will find that even the subtraction of counterterms is not enough to prevent certain sums and integrals from diverging. This is generally due to oscillations of the integrand or summand at large values of  $\omega$  or  $\ell$ . The full details will be given in the next subsection, but in this subsection we will detail how Levi and Ori handle these divergent sums and integrals through the use of the *generalised sum/integral*.

The generalised sum of a function  $f(\ell)$  is defined as

$$\lim_{\alpha \rightarrow 0^+} \sum_{\ell=0}^{\infty} e^{-\alpha \ell} f(\ell) \quad (5.2.13)$$

and the generalised integral of a function  $f(\omega)$  is defined as

$$\lim_{\alpha \rightarrow 0^+} \int_0^{\infty} e^{-\alpha \omega} f(\omega) d\omega. \quad (5.2.14)$$

Part of the strategy of the pragmatic mode sum method is whenever the sum or integral of a quantity would diverge in the traditional sense, to instead consider its generalised sum or integral. Throughout the following section, as in Levi and Ori's work, we will often omit the exponential factors in the integrands and summands and thus denote generalised sums/integrals as if they were "traditional" sums/integrals. This does not cause any ambiguity because if a traditional sum/integral converges, it will always agree with the result of the corresponding generalised sum/integral, as detailed in [99] and [100].

### 5.2.3.2 PMR by Angular-Splitting in a Static Spacetime

In this section we briefly describe the theory and techniques behind the PMR method applied in a static, spherically symmetric spacetime. A complete understanding of the analytical techniques is not required to numerically implement the method and so a numerical "recipe" is provided at the end of the section.

When applying the angular-splitting method, the first step is to write the metric in a manifestly spherically symmetric form. For a static, spherically symmetric spacetime this is

$$ds^2 = \Gamma(z) (-dt^2 + dz^2) + r^2(z) d\Omega^2, \quad (5.2.15)$$

for  $z$  a suitable radial coordinate.

The order of the sums and integrals in (5.2.5) should be interchanged such that the operation corresponding to the direction of the point splitting is performed last. For  $x$  and  $x'$  split in the  $\theta$  direction by an amount  $\varepsilon$ , this means the sum over  $\ell$  is performed last. Hence the expression for the vacuum polarization is

$$\begin{aligned} \langle \phi^2 \rangle_{ren} &= \lim_{\varepsilon \rightarrow 0} \left[ \sum_{\ell=0}^{\infty} \int_0^{\infty} d\omega \sum_{m=-\ell}^{\ell} Y_{\ell m}(\theta, \varphi) Y_{\ell m}^*(\theta + \varepsilon, \varphi) |\bar{\psi}_{\omega \ell}(z)|^2 - G_{DS}(x, x') \right] \\ &= \lim_{\varepsilon \rightarrow 0} \left[ \sum_{\ell=0}^{\infty} \frac{2\ell + 1}{4\pi} P_{\ell}(\cos \varepsilon) \int_0^{\infty} d\omega |\bar{\psi}_{\omega \ell}(z)|^2 - G_{DS}(x, x') \right], \end{aligned} \quad (5.2.16)$$

where in the second line the sum over  $m$  has been performed, and  $P_{\ell}$  is a Legendre polynomial.

Now we must consider the integral over  $\omega$ . Splitting the points in the  $\theta$  direction has no effect on the value of this integral and so it still diverges. Levi and Ori regulate this divergence by choosing to perform a second, additional split in the  $t$  direction by an amount  $\delta$ , such that the point  $x'$  is now given by the coordinates  $(t + \delta, z, \theta + \varepsilon, \varphi)$ . This is justified, as long as the limit of small  $\delta$  (which will regulate the integral over  $\omega$ ) is taken before the limit of small  $\varepsilon$  (which will regulate the sum over  $\ell$ ). The vacuum polarization is now

$$\langle \phi^2 \rangle_{ren} = \lim_{\varepsilon \rightarrow 0} \left[ \lim_{\delta \rightarrow 0} \sum_{\ell=0}^{\infty} \frac{2\ell + 1}{4\pi} P_{\ell}(\cos \varepsilon) \int_0^{\infty} d\omega |\bar{\psi}_{\omega \ell}(z)|^2 e^{i\omega\delta} - G_{DS}(\varepsilon) \right], \quad (5.2.17)$$

where the limit of small  $\delta$  applies only to the first term in the square brackets because  $G_{DS}$  is regular when  $\delta = 0$ , as long as  $\varepsilon > 0$ .

In (5.2.17), we see that  $G_{DS}$  is a function of  $\varepsilon$ . The form of this function needs to be found. Although  $G_{DS}$  could be expanded in simple powers of  $\varepsilon$  (and indeed, this is what Levi and Ori opt to do for the  $t$ -splitting variant of the PMR method), it will prove more useful to expand it in powers of  $\sin(\varepsilon/2)$ , as follows

$$G_{DS}(\varepsilon) = a(z) (\sin(\varepsilon/2))^{-2} + c(z) [\log(kr \sin(\varepsilon/2)) + \gamma] + d(z) + O(\varepsilon), \quad (5.2.18)$$

where  $\gamma$  is Euler's constant and the functions  $a, c$  and  $d$  will depend only on the form of the spacetime metric and on the field parameters.

The next step is to handle the integral over  $\omega$ . In the limit of small  $\delta$ , this integral diverges logarithmically, as the integrand is proportional to  $\omega^{-1}$  at leading order when  $\omega$  is large (see the

analysis in Appendix D of [100]). However, this leading order  $\omega^{-1}$  term is independent of  $\ell$ . Hence, one can regularise the integral by adding and subtracting the  $\ell = 0$  contribution to the integrand in the following way

$$\int_0^\infty d\omega |\bar{\psi}_{\omega\ell}(z)|^2 e^{i\omega\delta} = \int_0^\infty d\omega \left( |\bar{\psi}_{\omega\ell}(z)|^2 - |\bar{\psi}_{\omega 0}(z)|^2 \right) e^{i\omega\delta} + Z(\delta) \quad (5.2.19)$$

$$Z(\delta) \equiv \int_0^\infty d\omega |\bar{\psi}_{\omega 0}(z)|^2 e^{i\omega\delta}.$$

The limit as  $\delta \rightarrow 0$  of the first term of (5.2.19) can now be taken with no issue and will be denoted

$$F(\ell, z) \equiv \int_0^\infty d\omega \left( |\bar{\psi}_{\omega\ell}(z)|^2 - |\bar{\psi}_{\omega 0}(z)|^2 \right). \quad (5.2.20)$$

The vacuum polarization is now

$$\langle \phi^2 \rangle_{ren} = \lim_{\varepsilon \rightarrow 0} \left[ \sum_{\ell=0}^{\infty} \frac{2\ell+1}{4\pi} P_\ell(\cos \varepsilon) F(\ell, z) + \lim_{\delta \rightarrow 0} \left\{ \sum_{\ell=0}^{\infty} \frac{2\ell+1}{4\pi} P_\ell(\cos \varepsilon) Z(\delta) \right\} - G_{DS}(\varepsilon) \right]. \quad (5.2.21)$$

To finish this step all we need is one additional result (see Appendix B of [100]): that the following (generalised) sum vanishes for all  $\varepsilon \neq n\pi$  where  $n$  is an integer

$$\sum_{\ell=0}^{\infty} (2\ell+1) P_\ell(\cos \varepsilon) = 0. \quad (5.2.22)$$

Thus, as long as the limit of small  $\delta$  is taken before the limit of small  $\varepsilon$ , the term in curly brackets in (5.2.21) vanishes. The equation then simplifies to

$$\langle \phi^2 \rangle_{ren} = \lim_{\varepsilon \rightarrow 0} \left[ \sum_{\ell=0}^{\infty} \frac{2\ell+1}{4\pi} P_\ell(\cos \varepsilon) F(\ell, z) - G_{DS}(\varepsilon) \right] \quad (5.2.23)$$

and we are now left to consider the sum over  $\ell$ . To this end,  $G_{DS}(\varepsilon)$  must also be written as a sum over  $\ell$  and this can be accomplished through a Legendre transform. The relevant identities (proven in Appendix C of [100]) are

$$(\sin(\varepsilon/2))^{-2} = -8\pi \sum_{\ell=0}^{\infty} \frac{2\ell+1}{4\pi} h(\ell) P_\ell(\cos \varepsilon), \quad (5.2.24)$$

$$\log[\sin(\varepsilon/2)] = 2\pi \sum_{\ell=0}^{\infty} \frac{2\ell+1}{4\pi} \Lambda(\ell) P_\ell(\cos \varepsilon), \quad (5.2.25)$$

where the  $\ell^{\text{th}}$  harmonic number is defined

$$h(\ell) \equiv \sum_{k=0}^{\ell} \frac{1}{k},$$

with  $h(0) = 0$ , while  $\Lambda(\ell)$  is defined

$$\Lambda(\ell) \equiv \begin{cases} -1 & \ell = 0 \\ -\frac{1}{\ell(\ell+1)} & \ell > 0 \end{cases}.$$

Combining the Legendre transform identities with the expansion of  $G_{DS}(\varepsilon)$  in (5.2.18), the vacuum polarization can now be written in the form

$$\langle \phi^2 \rangle_{ren} = \lim_{\varepsilon \rightarrow 0} \left[ \sum_{\ell=0}^{\infty} \frac{2\ell+1}{4\pi} P_{\ell}(\cos \varepsilon) F_{reg}(\ell, z) + W(z) \right], \quad (5.2.26)$$

where

$$W(z) \equiv -[(\log(kr) + \gamma)c(z) + d(z)], \quad (5.2.27)$$

$$F_{reg}(\ell, z) \equiv F(\ell, z) - F_{sing}(\ell, z), \quad (5.2.28)$$

$$F_{sing}(\ell, z) \equiv -8\pi a(z)h(\ell) + 2\pi c(z)\Lambda(\ell). \quad (5.2.29)$$

At first glance,  $\langle \phi^2 \rangle$  as presented in (5.2.26) should now be a finite quantity, as the counterterms  $G_{DS}(\varepsilon)$  should regulate the sum over  $\ell$  in the limit of small  $\varepsilon$ . This unfortunately is not the case, due to a phenomenon that Levi and Ori refer to as a “blind spot”. This is where  $G_{DS}(\varepsilon)$  loses information about the divergences of  $\langle \phi^2 \rangle$  through the non-uniqueness of the Legendre transformation. In actuality, (5.2.24) should read

$$(\sin(\varepsilon/2))^{-2} = -8\pi \sum_{\ell=0}^{\infty} \frac{2\ell+1}{4\pi} (h(\ell) + k) P_{\ell}(\cos \varepsilon), \quad (5.2.30)$$

for  $k$  an arbitrary constant. This can contribute an extra term to  $F_{reg}$ , which we now write in the form

$$F_{reg}(\ell, z) = B(\ell, z) + A(\ell, z). \quad (5.2.31)$$

$A(\ell, z)$  contains all the “well behaved” parts of  $F_{reg}$ , such that  $\sum_{\ell=0}^{\infty} (2\ell+1) A(\ell, z) = 0$ , while  $B(\ell, z)$  is the potential “blind spot” from the arbitrary constant in (5.2.30). It has the property that

$$\sum_{\ell=0}^{\infty} (2\ell+1) B(\ell, z) P_{\ell}(\cos \varepsilon) = 0, \quad (5.2.32)$$

but taking the  $\varepsilon \rightarrow 0$  limit one would find that  $\sum_{\ell=0}^{\infty} (2\ell+1) B(\ell, z)$  diverges. This blind spot now needs to be somehow found and removed, such that we could replace  $F_{reg}$  by  $A(\ell, z)$  in (5.2.26), which would leave a  $\langle \phi^2 \rangle$  that is finally finite in the limit as  $\varepsilon \rightarrow 0$ ,

$$\langle \phi^2 \rangle_{ren} = \sum_{\ell=0}^{\infty} \frac{2\ell+1}{4\pi} A(\ell, z) + W(z). \quad (5.2.33)$$

Although there are multiple potential forms this blind spot could take, we will now specify that the blind spot will be a constant with respect to  $\ell$ ,  $B(\ell, z) = B_0(z)$ . The PMR method is applicable to other kinds of blind spots, but this is the only kind that needs to be considered in the Schwarzschild spacetime, which we will be applying this method to in the next section. The numerical method used

by Levi and Ori to remove the blind spot is to calculate the quantity  $A(\ell, z)$  somewhat indirectly, by first defining the partial sum

$$H(\ell, z) \equiv \sum_{k=0}^{\ell} \frac{2k+1}{4\pi} [F_{reg}(k, z) - F_{reg}(\ell, z)] \quad (5.2.34)$$

and then realising that the first term in (5.2.33) is nothing more than the limit of this sequence, as follows

$$\begin{aligned} \lim_{\ell \rightarrow \infty} H(\ell, z) &= \lim_{\ell \rightarrow \infty} \sum_{k=0}^{\ell} \frac{2k+1}{4\pi} [A(k, z) - A(\ell, z)] \\ &= \sum_{k=0}^{\infty} \frac{2k+1}{4\pi} A(k, z) + \lim_{\ell \rightarrow \infty} \frac{(\ell+1)^2}{4\pi} A(\ell, z) \end{aligned}$$

and the second term in the above vanishes. Hence, the final expression for the renormalised  $\langle \phi^2 \rangle$  to be evaluated numerically is

$$\langle \phi^2 \rangle_{ren} = \lim_{\ell \rightarrow \infty} H(\ell, z) + W(z). \quad (5.2.35)$$

We can summarise the complete method as a “recipe” with five steps to be followed,

1. Solve the radial mode equation to obtain  $|\bar{\psi}_{\omega\ell}(z)|^2$ . We chose to do this using the Black Hole Perturbation Toolkit [1].
2. Subtract from each  $\ell$  mode the  $\ell = 0$  contribution,  $|\bar{\psi}_{\omega 0}(z)|^2$ .
3. Integrate the result with respect to  $\omega$ . This is  $F(\ell, z)$ , as in Eq. (5.2.20).
4. Compute the coefficients  $a(z)$ ,  $c(z)$  and  $d(z)$  in the expansion of  $G_{DS}(\varepsilon)$ . From these, compute  $W(z)$ ,  $F_{sing}(\ell, z)$  and hence  $F_{reg}(\ell, z)$  from Eqs. (5.2.27), (5.2.29) and (5.2.28).
5. Compute  $H(\ell, z)$  from  $F_{reg}(\ell, z)$  using (5.2.34) and take the large  $\ell$  limit. Add this to  $W(z)$  to obtain  $\langle \phi^2 \rangle_{ren}$ .

How this method can be implemented numerically in the Schwarzschild spacetime will be covered in the next section.

### 5.2.3.3 Application to Schwarzschild

In Schwarzschild spacetime the metric can be written in the form

$$ds^2 = \left(1 - \frac{2M}{r}\right) (-dt^2 + dr_*^2) + r^2 d\Omega^2 \quad (5.2.36)$$

and so by comparison with (5.2.15) the radial coordinate  $z$  is the tortoise coordinate  $r_*$  and  $\Gamma(z) = 1 - 2M/r(r_*)$ . In practice however, it is still acceptable to use  $r$  as the radial coordinate as, in the

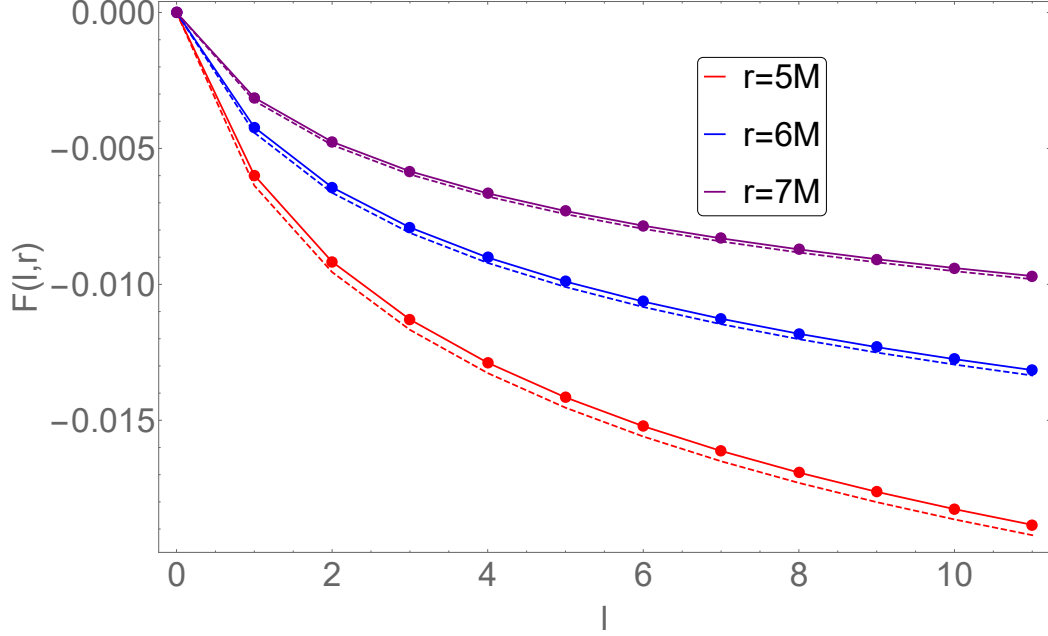


Figure 5.2.1: The solid lines show  $F(\ell, r)$ , Eq. (5.2.20), as a function of  $\ell$  for three values of  $r$ . The dashed lines show  $F_{sing}(\ell, r)$  defined in (5.2.29) and (5.2.44).

exterior region of the Schwarzschild spacetime, the function  $r(r_*)$  is monotonic. Then, the functions  $\psi_{\omega\ell} = r\sqrt{4\pi\omega}\bar{\psi}_{\omega\ell}$  in (5.2.5) are found by solving the Regge-Wheeler equation (3.1.9). As was already discussed in Sec. 3.1 we can take the IN and UP modes (the two modes that are devoid of particles in the Boulware state) to be two linearly-independent solutions to this equation, defined by the pair of boundary conditions

$$r\sqrt{4\pi\omega}\bar{\psi}_{\omega\ell}^{in}(r) = \psi_{\omega\ell}^{in}(r) = \begin{cases} A^{in}e^{-i\omega r_*} & r_* \rightarrow -\infty \\ e^{-i\omega r_*} + B^{in}e^{i\omega r_*} & r_* \rightarrow +\infty \end{cases}, \quad (5.2.37)$$

$$r\sqrt{4\pi\omega}\bar{\psi}_{\omega\ell}^{up}(r) = \psi_{\omega\ell}^{up}(r) = \begin{cases} e^{i\omega r_*} + B^{up}e^{-i\omega r_*} & r_* \rightarrow -\infty \\ A^{up}e^{i\omega r_*} & r_* \rightarrow +\infty \end{cases}. \quad (5.2.38)$$

Then, in the Boulware vacuum state,  $|\bar{\psi}_{\omega\ell}(r)|^2 = |\bar{\psi}_{\omega\ell}^{in}(r)|^2 + |\bar{\psi}_{\omega\ell}^{up}(r)|^2$ .

These functions must be computed for a wide range of values of  $\omega$  and  $\ell$ . The values we chose are  $\omega \in [0, 4]$  and  $\ell \in \{0, 1, \dots, 11\}$ . Then from each  $\ell$  mode the  $\ell = 0$  contribution is subtracted and the result can be integrated numerically with respect to  $\omega$  to find  $F(\ell, r)$ , shown in Fig. 5.2.1.

The value of  $\omega$  we choose to integrate to ( $\omega_{max} = 4$ ) is not large enough by itself to obtain the value of the integral to the accuracy we desire, but we are reluctant to take it much higher due to the increase in the required computation time. This issue can be remedied by computing an asymptotic

expansion in powers of  $\omega^{-1}$  for the  $\psi_{\omega\ell}$  functions and integrating that expansion over the remaining large frequencies. This is done in Appendix D of [100] up to an order  $\omega^{-8}$  expansion for  $|\psi_{\omega\ell}|^2$  (such that  $|\bar{\psi}_{\omega\ell}|^2 \sim \omega^{-1} |\psi_{\omega\ell}|^2$  is known to order  $\omega^{-9}$ ).

We will now briefly detail the derivation and properties of this large  $\omega$  expansion. The asymptotic behaviour of both  $\psi_{\omega\ell}^{in}$  and  $\psi_{\omega\ell}^{up}$  can be encapsulated in a single equation as follows,

$$\psi_{\omega\ell}^{in/up} = e^{\pm i\omega r_*} \sum_{k=0}^{\infty} \frac{a_k^{in/up}(r_*)}{\omega^k} + R(\omega), \quad (5.2.39)$$

where the  $+(-)$  sign is for  $\psi^{up}(\psi^{in})$  and the remainder  $R(\omega)$  contains all the terms that decay faster than a power of  $\omega^{-1}$  and thus will be discarded. Substituting this into the radial differential equation, a recurrence relation between the  $a_k$ 's can be found which can then be solved via an integral

$$a_{k+1}^{in} = -\frac{i}{2} (a_k^{in})' + \frac{i}{2} \int_{\infty}^{r_*} V_{\ell}(\bar{r}_*) a_k^{in} d\bar{r}_*, \quad (5.2.40)$$

$$a_{k+1}^{up} = \frac{i}{2} (a_k^{up})' - \frac{i}{2} \int_{-\infty}^{r_*} V_{\ell}(\bar{r}_*) a_k^{up} d\bar{r}_*, \quad (5.2.41)$$

where  $V_{\ell}(r_*)$  is the radial effective potential and  $'$  indicates a derivative with respect to  $r_*$ . The asymptotic expansion of the square of the radial function can be written in the form,

$$|\psi_{\omega\ell}|^2 = \sum_{k=0}^{\infty} \frac{b_k(r_*)}{\omega^k}, \quad (5.2.42)$$

where the coefficients  $b_k$  will be combinations of the various  $a_k$ . It is important to note that we have dropped the ‘‘in/up’’ label on both the radial function and the  $b_k$  coefficients. This is due to the first of three remarkable properties described in [100]: the  $b_k$  coefficients for the functions  $\psi_{\omega\ell}^{in}$  and  $\psi_{\omega\ell}^{up}$  are identical. The second of these properties is that  $b_k$  vanishes for any odd  $k$ , allowing us to write (5.2.42) in the form

$$|\psi_{\omega\ell}|^2 = \sum_{k=0}^{\infty} \frac{b_{2k}(r_*)}{\omega^{2k}}, \quad (5.2.43)$$

for  $k \geq 0$  an integer. These coefficients also satisfy a third interesting property: despite the  $a_k$  coefficients being written in terms of *integrals* of  $V_{\ell}(r_*)$ , the  $b_{2k}$  coefficients can be written entirely in terms of the *derivatives* of  $V_{\ell}(r_*)$ . Results up to and including  $b_8$  are presented in [100] for general  $V_{\ell}$ . To continue the expansion past this order, rather than deriving general expressions for  $b_{2k}$  we instead set  $V_{\ell}$  to be the Schwarzschild radial effective potential ((3.1.5) with  $e = Q = 0$ ) and calculate  $a_k$  up to the desired  $k$  directly from either (5.2.40) or (5.2.41). Then, considering the square of (5.2.39) allows us to find  $b_{2k}$ .

We have found that we can take  $\omega_{max} = 4$  in our numerical integration and still obtain results consistent with [100, 99] by including more terms in this asymptotic expansion, up to order  $\omega^{-14}$

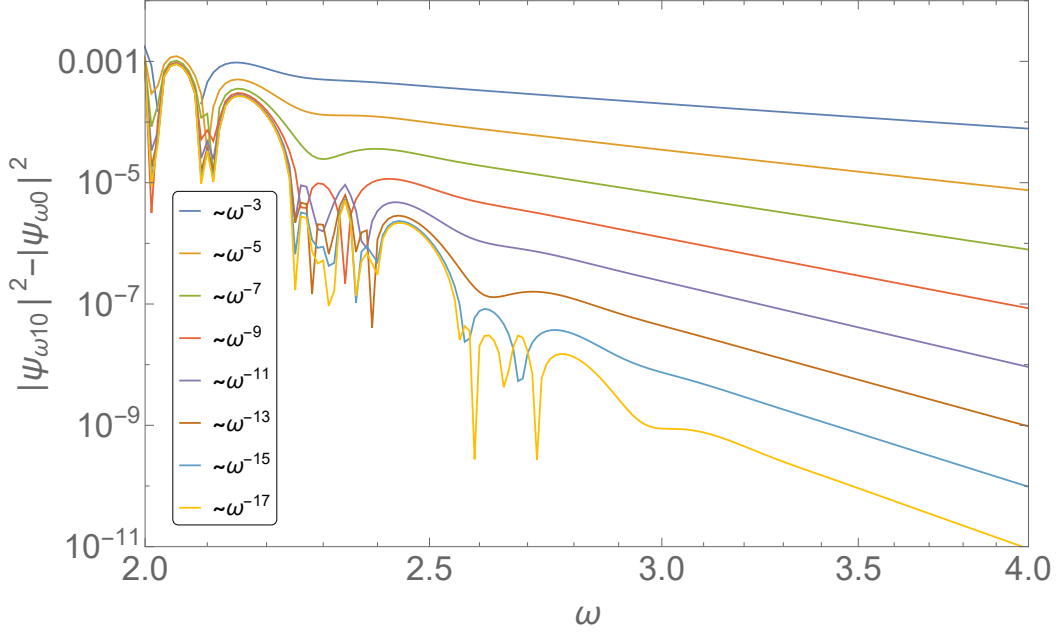


Figure 5.2.2: The top (dark blue) line in this figure is  $|\bar{\psi}_{\omega 10}(r)|^2 - |\bar{\psi}_{\omega 0}(r)|^2$  at the value  $r = 6M$ . Subsequent lines show the result of subtracting the asymptotic expansion valid for large  $\omega$  (5.2.42) term by term. The legend shows each line's scaling as a power of  $\omega$ .

(such that  $|\bar{\psi}_{\omega \ell}|^2$  is known to order  $\omega^{-15}$ ). Fortunately, additional terms in the expansion are not difficult to compute with Mathematica. This approach is justified by the excellent agreement between the expansion and the numerical data at each order, even for relatively small values of  $\omega$ , as shown in Fig. 5.2.2.

The coefficients of the expansion of the counterterm defined in (5.2.18) take relatively simple forms in the Schwarzschild spacetime

$$a(r) = \frac{1}{16\pi^2 r^2}, \quad c(r) = 0, \quad d(r) = -\frac{M}{24\pi^2 r^3}$$

and so  $W(r)$  and  $F_{sing}(\ell, r)$  are straightforward to compute

$$W(r) = \frac{M}{24\pi^2 r^3}, \quad F_{sing}(\ell, r) = -\frac{1}{2\pi r^2} h(\ell) \quad (5.2.44)$$

and so we can construct  $F_{reg}(\ell, r)$ , shown in Fig. 5.2.3 and then  $H(\ell, r)$ , shown in Fig. 5.2.4.

If  $H(\ell, r)$  fails to converge as  $\ell$  grows, this is an indication that numerical error is accumulating. An example of this is shown in Fig. 5.2.5, although for  $\ell \leq 11$  the growth with  $\ell$  is very slight. We stop evaluating  $\ell$  modes before this accumulation becomes significant, as we explain in the next subsection on error estimation.

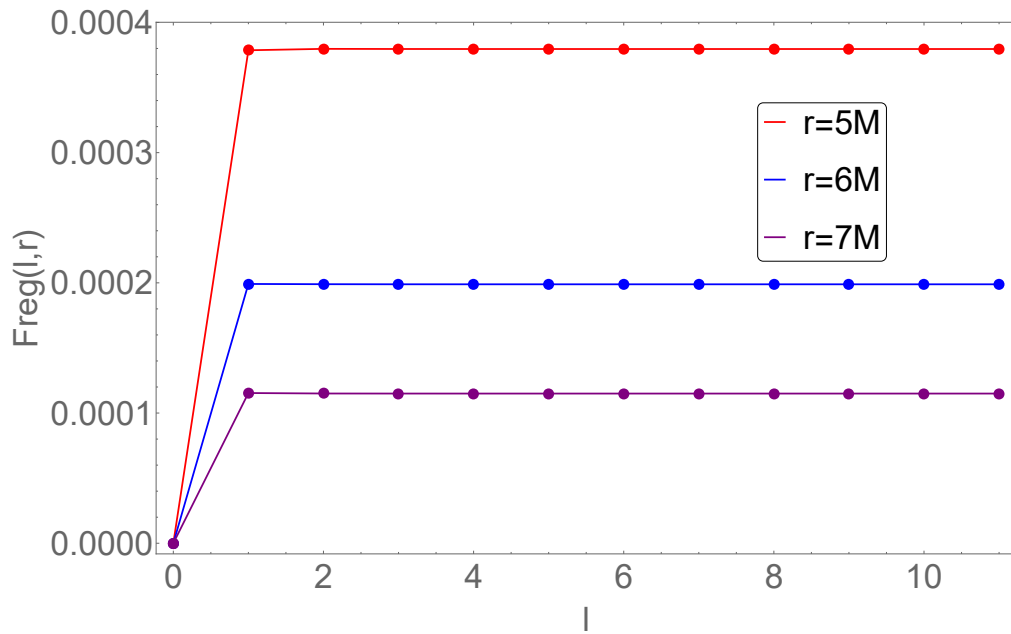


Figure 5.2.3:  $F_{reg}(\ell, r)$  (5.2.28) as a function of  $\ell$  for three values of  $r$ .

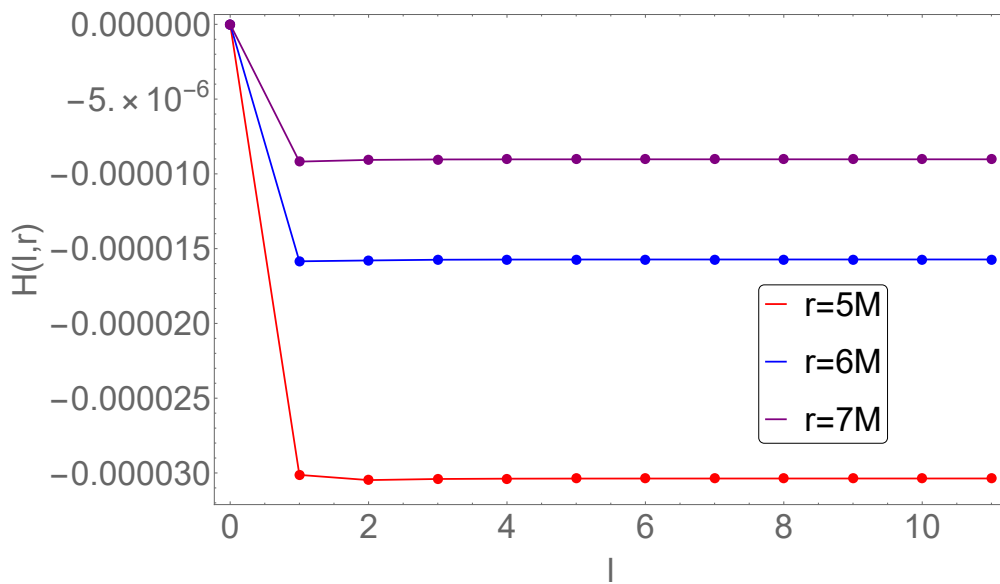


Figure 5.2.4:  $H(\ell, r)$  (5.2.34) as a function of  $\ell$  for three values of  $r$ .

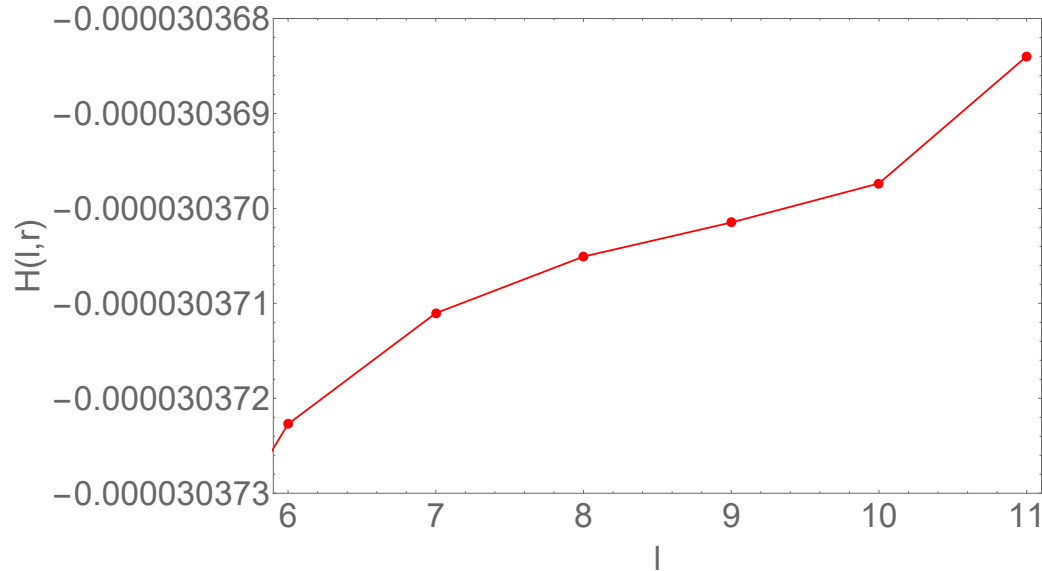


Figure 5.2.5: The  $r = 5M$  line in Fig. 5.2.4, plotted on a different scale.

#### 5.2.3.4 Error Estimation

We have identified and estimated the magnitudes of three potential sources of error in this numerical calculation,

- $\ell$  mode cutoff error:** As we can only compute a finite number of  $\ell$  modes in the sum over  $\ell$  there is an error introduced by the truncation of the sum. This error is estimated by the magnitude of the integral of the last  $\ell$  mode we include. As demonstrated in Fig. 5.2.5 it is possible that past a certain number of  $\ell$  modes the  $\ell$  cutoff error may actually increase with additional terms in the sum. This informed the decision on the number of  $\ell$  modes to calculate for each value of  $r$ .
- Large  $\omega$  tail error:** As we only numerically compute each  $\ell$  mode in the integrand in  $\langle \phi^2 \rangle$  up to a value  $\omega_{max}$ , after which we integrate the asymptotic expansion (5.2.42), this introduces an error. Our estimate of this error is simply the integral of the last term in the expansion (i.e., the term proportional to  $\omega^{-15}$  in the expansion of  $|\bar{\psi}_{\omega\ell}(r)|^2 - |\bar{\psi}_{\omega 0}(r)|^2$ ) from  $\omega_{max}$  to infinity.
- Discretisation error:** Each  $\ell$  mode of the integrand is constructed by calculating it over a grid of  $\omega$  values and then interpolating the result. This introduces an error that we estimate by re-calculating the integrand using only half as many points in the grid and then computing the difference between that and the original result.

$r/M$	$\langle\phi^2\rangle$
2.26	$(-6.7868 \pm 0.0005) \times 10^{-4}$
2.5	$(-2.4549 \pm 0.0005) \times 10^{-4}$
3.0	$(-5.705 \pm 0.009) \times 10^{-5}$
3.5	$(-1.585 \pm 0.004) \times 10^{-5}$
4.0	$(-2.878 \pm 0.025) \times 10^{-6}$
4.5	$(1.762 \pm 0.025) \times 10^{-6}$
5.0	$(3.405 \pm 0.028) \times 10^{-6}$
5.5	$(3.859 \pm 0.031) \times 10^{-6}$
6.0	$(3.821 \pm 0.031) \times 10^{-6}$

Table 5.1: Data for  $\langle\phi^2\rangle$  outside a Schwarzschild black hole as a function of  $r/M$  with error estimates.

For both the large  $\omega$  tail error and the discretisation error, the contribution to the error from each of the individual  $\ell$  modes is combined in quadrature as they are assumed to be independent of one another. We then choose to combine these three errors ( $\ell$  cutoff,  $\omega$  tail and discretisation) in quadrature to obtain an estimate of the total error, even though they are not strictly independent of one another.

Of the three errors, the discretisation error is the largest, often by multiple orders of magnitude. This implies that the total error could be best reduced by using more points in the interval of  $\omega$  values or changing how the points are distributed. In general this is not straightforward to do however, because the range of  $\omega$  that is most relevant to the integral depends on both  $r$  and  $\ell$ .

### 5.2.3.5 Results

In Table I and Fig. 5.2.6 we present the final data for  $\langle\phi^2\rangle$  in the Schwarzschild spacetime, with error bars calculated by the above prescription. This can be compared with figure 4b of [99] in which this was calculated using the  $t$ -splitting variant of the PMR method, or figure 4a of [100] calculated using the same angular splitting method we have employed here.

We will now discuss some of the properties of this data. The radial derivative of  $\langle\phi^2\rangle_{Schw}$  changes sign from positive to negative in the approach to the event horizon, such that  $\langle\phi^2\rangle_{Schw} < 0$  for  $r < r_1 \approx 4.3M$ . As such  $\langle\phi^2\rangle_{Schw}$  has a local maximum, which is located between  $r = 5.5M$  and the radius of the innermost stable circular orbit  $r = 6M$ , with a value of  $\langle\phi^2\rangle_{Schw} \approx 3.86 \times 10^{-6}$ . It is finite and negative on the radius of the light ring. Finally, as was mentioned in our discussion of the

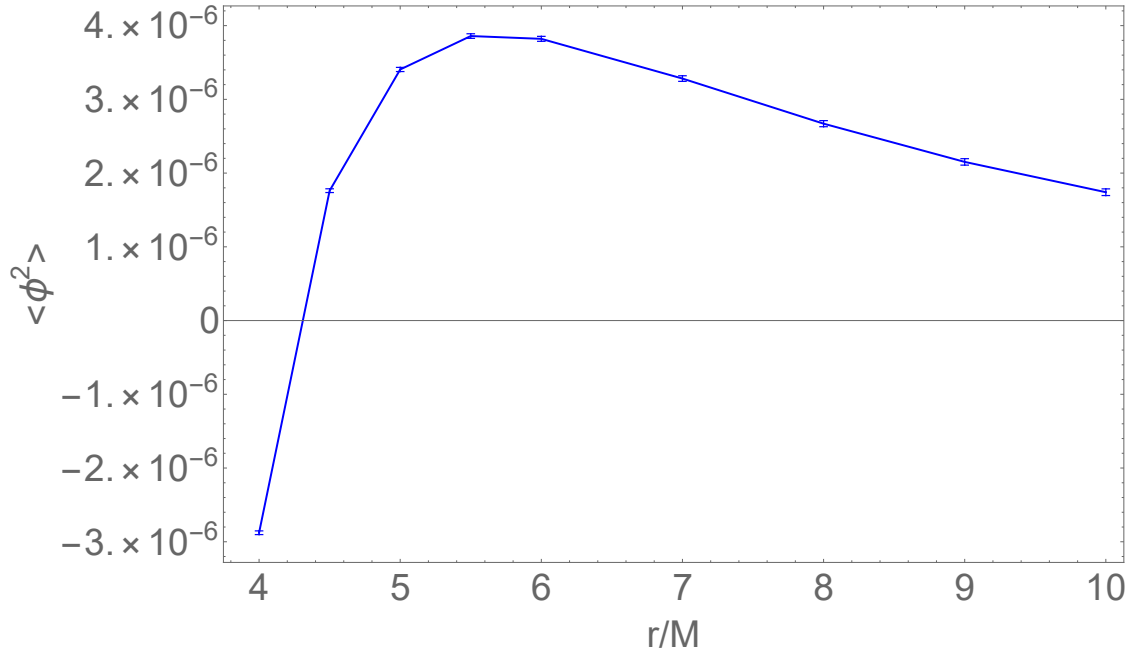


Figure 5.2.6:  $\langle \phi^2 \rangle$  outside a Schwarzschild black hole calculated using the angular-splitting PMR method, with error bars.

various different vacuum states that can be defined in the Schwarzschild spacetime, (see Sec. 5.1.2, [40] and [23]) we know that  $\langle \phi^2 \rangle_{Schw}$  diverges on the approach to the event horizon at  $r = 2M$ .

## Conclusion

In this chapter, we detailed the calculation of the vacuum polarization of a scalar field  $\langle \phi^2 \rangle$  outside of a Schwarzschild black hole, focusing specifically on the pragmatic mode sum method of Levi and Ori. We showed the individual steps of this method and their numerical results in Figs. 5.2.1-5.2.5. This data will be vital in chapter 7 when we extend the calculation of  $\langle \phi^2 \rangle$  to the spacetime of the spherically symmetric star.



## Chapter 6

# QFT Differences on Locally Equivalent Spacetimes

### Introduction and Overview

In this chapter we describe Anderson and Fabbri's work on QFT differences between locally equivalent spacetimes presented in Ref. [7], before applying it ourselves to the situation of a spherically symmetric shell in a flat spacetime. In this simple example, some results can be obtained purely analytically and we use these results to gain intuition as to how these QFT differences will behave for more realistic stellar models.

### 6.1 Mode Sum Expressions for $\Delta \langle \phi^2 \rangle$ and $\Delta \langle T^\mu{}_\nu \rangle$

#### 6.1.1 Vacuum Polarization

In Ref. [7], exact expressions for the differences in  $\langle \phi^2 \rangle$  and  $\langle T^\mu{}_\nu \rangle$  between the spacetimes of a Schwarzschild black hole and a spherically symmetric star were derived, using the scheme proposed in [8] where the spacetime is Euclideanised. These differences are denoted

$$\Delta \langle \phi^2 \rangle = \langle \phi^2 \rangle_{star} - \langle \phi^2 \rangle_{BH} \quad (6.1.1)$$

and similarly for  $\langle T^\mu{}_\nu \rangle$ . Combining these results with the PMR method to calculate these quantities for a black hole directly, one can numerically investigate the behavior of  $\langle \phi^2 \rangle$  and  $\langle T^\mu{}_\nu \rangle$  in the spacetime of a star, in the range of  $r$  that both methods are applicable, which will be the topic of chapter 7.

Before considering any specific method of calculating  $\langle \phi^2 \rangle$ , we note what we would expect to

occur upon taking the difference in (6.1.1). From (5.2.10) for  $\langle \phi^2 \rangle_{ren}$  and the knowledge that  $G^L$  depends only on the local geometry, we see that any subtraction performed in the vacuum region of both spacetimes circumvents any need to be concerned with counterterms. More specifically, the counterterms (5.2.11) depend only on the metric functions and their derivatives at the radial coordinate of interest  $r$  and by Birkhoff's theorem, the two spacetime metrics are identical in a neighborhood of that point in the vacuum region. We can see explicitly how this happens in the method of Anderson, Hiscock and Samuel. Recall Eq. (5.2.12) for  $\langle \phi^2 \rangle$  in the scheme of [8]. This is the sum of two terms, one to be calculated analytically and the other numerically

$$\langle \phi^2 \rangle = \langle \phi^2 \rangle_{numeric} + \langle \phi^2 \rangle_{analytic}. \quad (6.1.2)$$

The analytically-determined piece, constructed from  $\phi_{WKB}$  and  $G_{DS}$  (5.2.11), is identical outside the event horizon of a black hole and outside the surface of a spherically symmetric star of the same mass. This means that when taking the difference, only the numerically-calculated piece needs to be considered. This takes the form

$$\langle \phi^2 \rangle_{numeric} = \frac{1}{4\pi^2} \int_0^\infty d\omega \left[ \sum_{\ell=0}^\infty \left( (2\ell+1) C_{\omega\ell} p_{\omega\ell}(r) q_{\omega\ell}(r) - \frac{1}{\sqrt{r(r-2M)}} \right) + \frac{\omega}{1-2M/r} \right], \quad (6.1.3)$$

where  $p_{\omega\ell}$  and  $q_{\omega\ell}$  are radial modes that satisfy the differential equation

$$\frac{1}{h} \frac{d^2 \psi_{\omega\ell}}{dr^2} + \left[ \frac{2}{rh} + \frac{f'}{2fh} - \frac{h'}{2h^2} \right] \frac{d\psi_{\omega\ell}}{dr} - \left[ \frac{\omega^2}{f} + \frac{\ell(\ell+1)}{r^2} + \xi \mathcal{R}(r) \right] \psi_{\omega\ell} = 0, \quad (6.1.4)$$

with the boundary conditions that  $p_{\omega\ell}$  is regular at the event horizon of the black hole or the center of the star and  $q_{\omega\ell}$  is regular at radial infinity. Here, the functions  $f(r) = g_{tt}(r)$  and  $h(r) = g_{rr}(r)$  depend on the metric (such that in Schwarzschild spacetime  $f = 1/h = 1 - 2M/r$ ),  $\mathcal{R}$  is the Ricci scalar

$$\mathcal{R}(r) = -\frac{f''}{fh} + \frac{1}{2} \frac{(f')^2}{f^2 h} + \frac{1}{2} \frac{f'h'}{fh^2} - \frac{2f'}{rfh} + \frac{2h'}{rh^2} + \frac{2(h-1)}{r^2 h} \quad (6.1.5)$$

and  $C_{\omega\ell}$  is a normalisation constant defined via the Wronskian

$$C_{\omega\ell} \left[ p_{\omega\ell} \frac{dq_{\omega\ell}}{dr} - \frac{dp_{\omega\ell}}{dr} q_{\omega\ell} \right] = -\frac{1}{r(r-2M)}. \quad (6.1.6)$$

We will refer to the mode functions in the Schwarzschild spacetime as  $p_S$  and  $q_S$  and the mode functions in the star spacetime as  $p_*$  and  $q_*$ . As the  $q_{\omega\ell}$  function is determined by the boundary condition at infinity, which is the same for both spacetimes, we have  $q_* = q_S$ . To find  $p_*$  outside the star surface we match  $p_*$  at the star surface (found by solving (6.1.4) with  $f$  and  $h$  determined by the star's interior structure) onto a linear combination of  $p_S$  and  $q_S$  such that the function and its first derivative are continuous. Hence

$$p_* = \alpha_{\omega\ell} p_S + \beta_{\omega\ell} q_S, \quad (6.1.7)$$

where

$$\alpha_{\omega\ell} = \left. \frac{p_* q'_S - p'_* q_S}{q'_S p_S - p'_S q_S} \right|_{r=R}, \quad (6.1.8)$$

$$\beta_{\omega\ell} = \left. \frac{p_S p'_* - p'_S p_*}{q'_S p_S - p'_S q_S} \right|_{r=R} \quad (6.1.9)$$

and each of the modes are evaluated on the star surface  $r = R$ . Then, using (6.1.6) we see that  $\alpha_{\omega\ell} C_* = C_S$ . Putting all of this together, the difference in  $\langle \phi^2 \rangle$  between the two spacetimes takes the form

$$\Delta \langle \phi^2 \rangle = \frac{1}{4\pi^2} \int_0^\infty d\omega \sum_{\ell=0}^\infty (2\ell + 1) C_S \frac{\beta_{\omega\ell}}{\alpha_{\omega\ell}} q_S^2 \quad (6.1.10)$$

and this is an exact expression, as presented in [7]. It is also independent of the choice of normalization of the functions  $p_S$  and  $q_S$ .

### 6.1.2 Extension to the Stress-Energy Tensor

The methods of Anderson, Hiscock and Samuel, applicable to asymptotically flat spherically symmetric spacetimes, allow also calculation of the stress-energy tensor  $\langle T^\mu_\nu \rangle$ . The details were originally presented in [8], but schematically the method is similar to the calculation of the vacuum polarization. In particular, as shown in [7], to calculate the stress-energy difference  $\Delta \langle T^\mu_\nu \rangle$  between a star and a black hole we only need to be concerned with an entirely numerically determined piece, as the analytically determined term cancels in the subtraction. This numerical term is constructed out of five integrals labeled  $\Delta S_i$  with the index  $i \in \{1, \dots, 5\}$ ,

$$\Delta S_i = \frac{1}{4\pi^2} \int_0^\infty d\omega \sum_{\ell=0}^\infty (2\ell + 1) \Delta s_i \quad (6.1.11)$$

where

$$\Delta s_1 = \omega^2 C_{\omega\ell} \frac{\beta_{\omega\ell}}{\alpha_{\omega\ell}} q_{\omega\ell}^2, \quad (6.1.12)$$

$$\Delta s_2 = C_{\omega\ell} \frac{\beta_{\omega\ell}}{\alpha_{\omega\ell}} \left( \frac{dq_{\omega\ell}}{dr} \right)^2, \quad (6.1.13)$$

$$\Delta s_3 = \left( \ell + \frac{1}{2} \right)^2 C_{\omega\ell} \frac{\beta_{\omega\ell}}{\alpha_{\omega\ell}} q_{\omega\ell}^2, \quad (6.1.14)$$

$$\Delta s_4 = 2C_{\omega\ell} \frac{\beta_{\omega\ell}}{\alpha_{\omega\ell}} q_{\omega\ell} \left( \frac{dq_{\omega\ell}}{dr} \right), \quad (6.1.15)$$

$$\Delta s_5 = C_{\omega\ell} \frac{\beta_{\omega\ell}}{\alpha_{\omega\ell}} q_{\omega\ell}^2, \quad (6.1.16)$$

such that  $\Delta S_5 = \Delta \langle \phi^2 \rangle$ . For each of the three independent components of  $\Delta \langle T^\mu_\nu \rangle$  the construction is as follows,

$$\Delta \langle T^t_t \rangle = \frac{(2\xi + \frac{1}{2})}{1 - 2M/r} \Delta S_1 + \left( 2\xi - \frac{1}{2} \right) \left( \left( 1 - \frac{2M}{r} \right) \Delta S_2 + \frac{1}{r^2} \Delta S_3 - \frac{1}{4r^2} \Delta S_5 \right) - \frac{M\xi}{r^2} \Delta S_4, \quad (6.1.17)$$

$$\Delta \langle T^r_r \rangle = -\frac{1}{2(1 - 2M/r)} \Delta S_1 + \frac{1}{2} \left( 1 - \frac{2M}{r} \right) \Delta S_2 - \frac{1}{2r^2} \Delta S_3 + \frac{\xi}{r} \left( 2 - \frac{3M}{r} \right) \Delta S_4 + \frac{1}{8r^2} \Delta S_5, \quad (6.1.18)$$

$$\Delta \langle T^\theta_\theta \rangle = \frac{(2\xi - \frac{1}{2})}{1 - 2M/r} \Delta S_1 + \left( 2\xi - \frac{1}{2} \right) \left( 1 - \frac{2M}{r} \right) \Delta S_2 + \xi \left( \frac{2}{r^2} \Delta S_3 - \left( 1 - \frac{2M}{r} \right) \frac{1}{r} \Delta S_4 - \frac{1}{2r^2} \Delta S_5 \right). \quad (6.1.19)$$

We will use the results (6.1.10)-(6.1.19) in two ways. Firstly, in section 6.2, instead of taking the difference between a spherically symmetric star and a black hole, we will consider a toy model where we take the difference between the spacetime of a spherical shell and flat spacetime. This situation is simple enough for information about (6.1.10) to be extracted analytically without resorting to far field approximations.

Then, in chapter 7, we will perform a numerical analysis of the behavior of  $\Delta \langle \phi^2 \rangle$  and  $\Delta \langle T^\mu_\nu \rangle$  near the surface of stars with a specified internal structure and, by combining this with the results of the PMR method covered in the previous chapter, also infer the behavior of  $\langle \phi^2 \rangle_{star}$  in that same region.

### 6.1.2.1 Stress Energy Conservation

It can be shown directly from the expressions for the individual components (6.1.17)-(6.1.19) that  $\Delta \langle T^{\mu\nu} \rangle$  satisfies the conservation equation  $\nabla_\mu [\Delta \langle T^{\mu\nu} \rangle] = 0$  outside the star. We will briefly run through this calculation. First we apply the inverse metric to raise an index in each of (6.1.17), (6.1.18) and (6.1.19) and following the definition of the covariant derivative on a tensor of rank (2,0)

$$\begin{aligned} X^\nu &\equiv \nabla_\mu [\Delta \langle T^{\mu\nu} \rangle] = \partial_\mu [\Delta \langle T^{\mu\nu} \rangle] + \Gamma^\mu_{\mu\sigma} [\Delta \langle T^{\sigma\nu} \rangle] + \Gamma^\nu_{\mu\sigma} [\Delta \langle T^{\mu\sigma} \rangle] \\ &= \frac{1}{\sqrt{-g}} \partial_\mu (\sqrt{-g} \Delta \langle T^{\mu\nu} \rangle) + \Gamma^\nu_{\mu\sigma} [\Delta \langle T^{\mu\sigma} \rangle], \end{aligned} \quad (6.1.20)$$

where in the second line we have used the simplification of the Christoffel symbols that comes from contracting the upper index with one of the lower ones

$$\Gamma^\mu_{\mu\sigma} = \frac{1}{\sqrt{-g}} \partial_\sigma (\sqrt{-g}). \quad (6.1.21)$$

The only component of the vector  $X^\nu$  in Eq. (6.1.20) that does not vanish is the  $\nu = r$  component. This is due to vanishing Christoffel symbols and the fact that each component of  $\Delta \langle T^{\mu\nu} \rangle$  depends

on  $r$  only. A short calculation shows,

$$X^r = \left[ \partial_r + \frac{2}{r} - \frac{M}{r^2 f_{sch}} \right] \Delta \langle T^{rr} \rangle + \frac{M f_{sch}}{r^2} \Delta \langle T^{tt} \rangle - 2r f_{sch} \Delta \langle T^{\theta\theta} \rangle. \quad (6.1.22)$$

Using Eqs. (6.1.12)-(6.1.16) outside the star this can be written entirely in terms of  $q_S$  and its derivatives. The second derivatives of  $q_S$  can be removed using the radial equation (6.1.4) in Schwarzschild spacetime, leading to the vanishing of (6.1.22) and so conservation is satisfied.

### 6.1.3 Far Field Limit for Newtonian Stars

Some information about the form of  $\Delta \langle \phi^2 \rangle$  and  $\Delta \langle T^\mu_\nu \rangle$  far from the star or black hole can be obtained without knowledge of the nature of the gravitational source. In this region ( $\omega r \gg \ell$ ) the spacetime is asymptotically flat and the solutions of Eq. (6.1.4) are

$$p_S \rightarrow p_{flat} = \omega^{-\ell} i_\ell(\omega r), \quad (6.1.23)$$

$$q_S \rightarrow q_{flat} = \omega^{\ell+1} k_\ell(\omega r), \quad (6.1.24)$$

where  $i_\ell$  and  $k_\ell$  are the modified spherical Bessel functions of the first and second kinds respectively. This produces a normalisation constant  $C_{flat} = 2/\pi$ . The function  $q_{flat}$  can be expanded as a finite power series for large  $\omega r$  in the following manner

$$q_{flat} = \frac{\pi}{2} \omega^{\ell+1} e^{-\omega r} \left[ \frac{c_0}{\omega r} + \dots + \frac{c_\ell}{(\omega r)^{\ell+1}} \right], \quad (6.1.25)$$

where  $c_0 = 1$  and  $c_k$  are constants that depend on  $\ell$ . Taking the same approach as [7] we assume that the coefficients  $\alpha_{\omega\ell}$  and  $\beta_{\omega\ell}$  admit a series expansion around  $\omega = 0$  of the form

$$\alpha_{\omega\ell} = \alpha_{0\ell} + \omega \alpha_{1\ell} + \omega^2 \alpha_{2\ell} + \dots, \quad (6.1.26)$$

$$\beta_{\omega\ell} = \beta_{0\ell} + \omega \beta_{1\ell} + \omega^2 \beta_{2\ell} + \dots. \quad (6.1.27)$$

Then, as the sum over  $\ell$  in (6.1.10) is now a terminating sum, we swap the order of the sum and the integral and perform integration by parts. The result is a series in inverse powers of  $r$

$$\Delta \langle \phi^2 \rangle = \frac{1}{16\pi r^3} \frac{\beta_{00}}{\alpha_{00}} + O(r^{-4}) \quad (6.1.28)$$

and hence, at leading order in  $r^{-1}$  the dominant contribution to  $\Delta \langle \phi^2 \rangle$  comes from the  $\omega = \ell = 0$  piece of  $\beta/\alpha$ . By continuing this expansion to terms higher order in  $r^{-1}$  it can be seen that the first contribution from a given  $\ell$  mode is at order  $r^{-2\ell-3}$ . It is worth noting that, although Eq. (6.1.10) was independent of the normalisation of the functions  $p_{\omega\ell}$  and  $q_{\omega\ell}$ , Eq. (6.1.28) is not, as a specific normalisation was chosen in Eqs. (6.1.23) and (6.1.24).

This is as far as we can go without specifying the internal structure of the star, as knowledge of  $p_*$  is required to calculate  $\alpha_{\omega\ell}$  and  $\beta_{\omega\ell}$ . For a star that has a radius  $R \gg M$ , (a *Newtonian* star) it was shown in [7] that for general coupling  $\xi$  one has  $\beta_{00}/\alpha_{00} = -4M\xi/\pi$  and so (6.1.28) becomes

$$\Delta \langle \phi^2 \rangle = -\frac{M\xi}{4\pi^2 r^3} + O(r^{-4}). \quad (6.1.29)$$

It can be seen that, at leading order, the difference in  $\langle \phi^2 \rangle$  between a Newtonian star and a black hole depends only on the mass of the gravitational source and that for minimal coupling  $\Delta \langle \phi^2 \rangle = 0$ . This latter result is what Anderson and Fabbri call the *universality* of the vacuum polarization in the far field limit.

The same method can be applied to the difference in the stress-energy tensor, resulting in

$$\Delta \langle T^\mu{}_\nu \rangle = \frac{3}{16\pi r^5} \frac{\beta_{00}}{\alpha_{00}} \left( \xi - \frac{1}{6} \right) \text{diag}[2, -2, 3, 3] + O(r^{-6}), \quad (6.1.30)$$

$$\frac{-3M\xi}{4\pi^2 r^5} \left( \xi - \frac{1}{6} \right) \text{diag}[2, -2, 3, 3] + O(r^{-6}). \quad (6.1.31)$$

As well as vanishing in the case of minimal coupling, like  $\Delta \langle \phi^2 \rangle$  does, this also vanishes for conformal coupling  $\xi = 1/6$ .

This universality is explored further in [36] where the authors consider more exotic spacetimes such as wormholes and also in [70] for spacetimes of dimension  $D > 4$ . We will instead extend the results of Anderson and Fabbri to more general stellar structures in chapter 7.

## 6.2 Toy Model: Spherical Shell on Flat Spacetime

In the next chapter, we will be using the method of Anderson and Fabbri to numerically analyse the vacuum polarization and stress-energy differences of a scalar field between a star and a black hole near the star surface, where analytical approximations applicable in the far field (such as those discussed in the previous section) cannot be used. In preparation for this, we will first consider a toy model from which some information can be extracted analytically, even near the boundary between the interior and exterior regions of the spacetime. We will use this model to gather information about the convergence of the sums over  $\ell$  and integrals over  $\omega$  in  $\Delta \langle \phi^2 \rangle$  and  $\Delta \langle T^\mu{}_\nu \rangle$ , which we can then compare and contrast with more realistic star models.

The toy model is as follows: the spacetime will consist of two flat regions, an interior and an exterior, separated by a spherically symmetric, infinitesimally thin shell of radius  $R$ . We will impose Dirichlet boundary conditions on the shell surface. This model differs from that of a constant density star, to be described in Sec. 7.1, in multiple aspects. While the metric functions across the shell surface are smooth, (on account of being identical on both sides of the boundary) the metric

functions of a constant density star are not smooth across the star surface. In addition, the surface of the shell forms a “hard” boundary due to the Dirichlet boundary condition (only the value of  $\phi$  is fixed on the shell surface, not its derivative), as opposed to the star surface where agreement of both the radial mode and its derivative will be imposed. A hard boundary has the possibility of introducing additional divergences that would not be present otherwise.

Despite these differences, the vacuum polarization and stress-energy differences in this model will be shown to have some properties similar to their equivalents in a more realistic stellar model in the next chapter, namely, their pointwise convergence properties when we consider the sum over  $\ell$ .

### 6.2.1 Outside the Shell

We will be taking the difference of the vacuum polarization and the energy density between the flat spacetime without a spherical shell (Minkowski spacetime) and flat spacetime with a shell at radius  $r = R$  on which Dirichlet boundary conditions ( $\phi = 0$ ) are imposed. First, the linearly independent solutions on a spacetime without the shell are just the flat space solutions  $p_{flat}$  and  $q_{flat}$  from the previous section, Eqs. (6.1.23) and (6.1.24). By the same logic as presented in Sec. 6.1,  $p_{ext}$  and  $q_{ext}$  in the exterior region of the spacetime with the shell must be

$$p_{ext} = \alpha_{\omega\ell} p_{flat} + \beta_{\omega\ell} q_{flat}, \quad (6.2.1)$$

$$q_{ext} = q_{flat} \quad (6.2.2)$$

and we find the ratio of  $\alpha_{\omega\ell}$  and  $\beta_{\omega\ell}$  using the Dirichlet boundary condition  $p_{ext}(R) = 0$ ,

$$\frac{\beta_{\omega\ell}}{\alpha_{\omega\ell}} = -\frac{p_{flat}(R)}{q_{flat}(R)} = -\omega^{-2\ell-1} \frac{i_\ell(\omega R)}{k_\ell(\omega R)}. \quad (6.2.3)$$

Substituting into Eq. (6.1.10), the vacuum polarization difference is

$$\Delta \langle \phi^2 \rangle_{ext} = \frac{-1}{4\pi^2} \int_0^\infty d\omega \sum_{\ell=0}^\infty (2\ell+1) \frac{2}{\pi} \frac{i_\ell(\omega R)}{k_\ell(\omega R)} \omega k_\ell^2(\omega r). \quad (6.2.4)$$

To proceed we assume that we can look at each  $\ell$  mode individually, i.e., that the order of summation and integration can be interchanged. The  $\ell = 0$  contribution is

$$\Delta \langle \phi^2 \rangle_{ext0} = \frac{-1}{2\pi^3} \int_0^\infty d\omega \frac{i_0(\omega R)}{k_0(\omega R)} \omega k_0^2(\omega r) \quad (6.2.5)$$

and this integral converges for  $r > R$  to

$$\Delta \langle \phi^2 \rangle_{ext0} = \frac{-1}{8\pi^2 r^2} \log \left( \frac{r}{r-R} \right). \quad (6.2.6)$$

This demonstrates a logarithmic divergence on the approach to the shell surface  $r \rightarrow R$ . The large  $r$  limit of this result is

$$\begin{aligned} \lim_{r \rightarrow \infty} \Delta \langle \phi^2 \rangle_{ext0} &= \frac{-R}{8\pi^2 r^3} \sum_{n=0}^{\infty} \left(\frac{R}{r}\right)^n \frac{1}{n+1} \\ &= \frac{-R}{8\pi^2 r^3} + O(r^{-4}), \end{aligned} \quad (6.2.7)$$

which we can see has the same scaling with  $r$  as in the case of the Newtonian star, Eq. (6.1.28).

Next, we consider the energy density difference, which is the  $tt$ -component of the stress-energy difference. In a flat spacetime, Eq. (6.1.17), simplifies to

$$\Delta \langle T^t_t \rangle = \left(2\xi + \frac{1}{2}\right) \Delta S_1 + \left(2\xi - \frac{1}{2}\right) \left( \Delta S_2 + \frac{1}{r^2} \left( \left(\ell + \frac{1}{2}\right)^2 - \frac{1}{4} \right) \Delta \langle \phi^2 \rangle \right). \quad (6.2.8)$$

For  $\ell = 0$ ,  $\Delta S_1$  and  $\Delta S_2$  in the exterior can be found as follows, where we make use of the dimensionless parameter  $\rho = R/r < 1$ ,

$$\begin{aligned} \Delta S_{1ext0} &= \frac{-1}{2\pi^3} \int_0^\infty d\omega \frac{i_0(\omega R)}{k_0(\omega R)} \omega^3 k_0^2(\omega r) \\ &= \frac{-1}{32\pi^2 r^4} \left( \frac{1}{(\rho-1)^2} - 1 \right), \end{aligned} \quad (6.2.9)$$

$$\begin{aligned} \Delta S_{2ext0} &= \frac{-1}{2\pi^3} \int_0^\infty d\omega \frac{i_0(\omega R)}{k_0(\omega R)} \omega \left[ \frac{d}{dr} k_0(\omega r) \right]^2 \\ &= \frac{-1}{32\pi^2 r^4} \left( \frac{(6-5\rho)\rho}{(\rho-1)^2} - 4 \log(1-\rho) \right) \\ &\rightarrow \frac{-1}{32\pi^2 r^4} \left( \frac{1}{(\rho-1)^2} - \frac{4}{\rho-1} - 5 - 4 \log(1-\rho) + O(1-\rho) \right), \end{aligned} \quad (6.2.10)$$

$$\begin{aligned} \Delta \langle T^t_t \rangle_{ext0} &= \left(2\xi + \frac{1}{2}\right) \Delta S_{1ext0} + \left(2\xi - \frac{1}{2}\right) \Delta S_{2ext0} \\ &= \frac{-1}{16\pi^2 r^4} \left[ \frac{\rho(8\xi - 1 - (6\xi - 1)\rho)}{(\rho-1)^2} - (4\xi - 1) \log(1-\rho) \right] \\ &\rightarrow \frac{-1}{8\pi^2 r^4} \left[ \frac{\xi}{(\rho-1)^2} + \frac{1-4\xi}{2(\rho-1)} + \frac{1}{2} (1 - 6\xi - (4\xi - 1) \log(1-\rho)) + O(1-\rho) \right], \end{aligned} \quad (6.2.11)$$

where “ $\rightarrow$ ” indicates the behavior of each quantity on the approach to the shell surface  $\rho \rightarrow 1^-$ . Note that these expressions all scale like  $r^{-4}$ , which in natural units  $\hbar = c = 1$  is the correct scaling for an energy density.

We see that the external energy density difference contribution from the  $\ell = 0$  (6.2.11) mode diverges quadratically on the shell surface for non-minimal coupling and diverges linearly for minimal coupling  $\xi = 0$ . We also see that the energy density difference outside the shell is always positive for minimal coupling. We will return to discussing these divergences after examining the vacuum polarization and stress energy differences inside the shell.

Continuing to the  $\ell = 1$  mode, the vacuum polarization difference in the exterior is given by

$$\Delta \langle \phi^2 \rangle_{ext1} = \frac{-3}{2\pi^3} \int_0^\infty d\omega \frac{i_1(\omega R)}{k_1(\omega R)} \omega k_1^2(\omega r). \quad (6.2.12)$$

We perform the change of variables to  $x = \omega R$  and employ the same dimensionless parameter as before,  $\omega r = x/\rho$  where  $\rho = R/r < 1$ . The integrals over  $x$  can be performed with a computer algebra package such as Mathematica, and in each case we check that the obtained function agrees with the result obtained via a numerical integration scheme to some large  $x$ .

$$\begin{aligned} \Delta \langle \phi^2 \rangle_{ext1} &= \frac{-3}{4\pi^2 r^2} \int_0^\infty dx \frac{e^{x(1-2/\rho)} (x+\rho)^2 (x \cosh x - \sinh x)}{x^3 (x+1)} \\ &= \frac{-3}{8\pi^2 r^2} \left[ \rho(\rho-2) - 2(\rho-1)^2 e^{2/\rho-2} \text{Ei} \left( 2 - \frac{2}{\rho} \right) - \log(1-\rho) + O(1-\rho) \right] \\ &\rightarrow \frac{-3}{8\pi^2 r^2} (-1 - \log(1-\rho) + O(1-\rho)), \end{aligned} \quad (6.2.13)$$

where the last line is the limit as  $\rho \rightarrow 1^-$  and  $\text{Ei}(x)$  is the exponential integral function

$$\text{Ei}(x) \equiv \int_{-x}^\infty \frac{e^{-t}}{t} dt. \quad (6.2.14)$$

The second line of Eq. (6.2.13) has an expansion for small  $\rho$  (large  $r$ ),

$$\Delta \langle \phi^2 \rangle_{ext1} \approx \frac{-3R^3}{8\pi^2 r^5} \left( \frac{5}{6} + \frac{7}{10}\rho^2 - \frac{5}{6}\rho^3 + \dots \right) \quad (6.2.15)$$

and so, like the  $\ell = 0$  mode in Eq. (6.2.7), has the same scaling with  $r$  as the corresponding  $\ell$  mode for the Newtonian star,  $r^{-2\ell-3}$ . This expansion can also be inferred by performing a simpler integral than the one in the first line of Eq. (6.2.13) at the cost of losing knowledge of  $\Delta \langle \phi^2 \rangle_{ext1}$  outside of the small  $\rho$  regime. This is done by expanding the integrand on the first line of (6.2.13) for small  $x$  while keeping the exponential factor present such that the integral over  $x$  remains convergent. The small  $\rho$  expansion of the resulting integral then agrees with (6.2.15).

We can continue the calculation of the energy density difference by finding  $\Delta S_1$  and  $\Delta S_2$

$$\begin{aligned} \Delta S_{1ext1} &= \frac{-3}{4\pi^2 r^2 R^2} \int_0^\infty dx \frac{e^{x(1-2/\rho)} (x+\rho)^2 (x \cosh x - \sinh x)}{x(x+1)} \\ &= \frac{-3}{4\pi^2 r^2 R^2} \left[ -(\rho-1)^2 e^{2/\rho-2} \text{Ei} \left( 2 - \frac{2}{\rho} \right) + \frac{1}{8}\rho \left( -4 + \frac{1}{(\rho-1)^2} + \frac{1}{\rho-1} + 5\rho + 4 \log(1-\rho) \right) \right] \\ &\rightarrow \frac{-3}{32\pi^2 r^4} \left( \frac{1}{(\rho-1)^2} + \frac{2}{\rho-1} + 2(1 + 2 \log(1-\rho)) + O(1-\rho) \right) \end{aligned} \quad (6.2.16)$$

and we see a quadratic divergence as  $\rho \rightarrow 1^-$ . For  $\Delta S_2$  we get,

$$\begin{aligned} \Delta S_{2ext1} &= \frac{-3}{4\pi^2 r^2 R^2} \int_0^\infty dx \frac{e^{x(1-2/\rho)} (2\rho^2 + x(2\rho+x))^2 (x \cosh x - \sinh x)}{x^3 (x+1)} \\ &= \frac{3}{32\pi^2 r^2 R^2} \left[ \rho \left( 7\rho - 16\rho(\rho-1)^2 + \frac{4+\rho(8\rho-13)}{(\rho-1)^2} \right) + 8(1+2\rho(\rho-1))^2 e^{2/\rho-2} \text{Ei} \left( 2 - \frac{2}{\rho} \right) \right] \\ &\rightarrow \frac{-3}{32\pi^2 r^4} \left[ \frac{1}{(\rho-1)^2} - \frac{2}{\rho-1} - 2(9 + 4\gamma + 4 \log 2 + 4 \log(1-\rho)) + O(1-\rho) \right] \end{aligned} \quad (6.2.17)$$

and we observe the same quadratic divergence as  $\Delta S_1$  and a linear divergence of the same magnitude as  $\Delta S_1$  but with the opposite sign. This has consequences when we come to form the energy density difference

$$\begin{aligned} \Delta \langle T_t^t \rangle_{ext1} &= \left(2\xi + \frac{1}{2}\right) \Delta S_{1ext1} + \left(2\xi - \frac{1}{2}\right) \left( \Delta S_{2ext1} + \frac{2}{r^2} \Delta \langle \phi^2 \rangle_{ext1} \right) \\ &\rightarrow \frac{-3}{8\pi^2 r^4} \left[ \frac{\xi}{(\rho-1)^2} + \frac{1}{2(\rho-1)} + \frac{7}{2} + \gamma(4\xi-1) \right. \\ &\quad \left. - 4\xi(3 + \log 2) + \log 2 + \left(\frac{5}{2} - 6\xi\right) \log(1-\rho) + O(1-\rho) \right], \end{aligned} \quad (6.2.18)$$

which, like the  $\ell = 0$  mode, diverges quadratically for non-minimal coupling, diverges linearly for minimal coupling, and is positive for minimal coupling.

For the  $\ell = 2$  mode  $\Delta \langle T_t^t \rangle_{ext2}$  becomes difficult to compute analytically due to the complexity of the integrals over  $x$ , but  $\Delta \langle \phi^2 \rangle_{ext2}$  remains feasible. We omit the full analytical expression for  $\Delta \langle \phi^2 \rangle_{ext2}$  as it is somewhat unwieldy, but we present the asymptotics on the approach to the shell surface and in the far field respectively,

$$\lim_{r \rightarrow R} \Delta \langle \phi^2 \rangle_{ext2} = \frac{-5}{16\pi^2 r^2} \left( -3 - 2 \log \left( 1 - \frac{R}{r} \right) + O \left( 1 - \frac{R}{r} \right) \right), \quad (6.2.19)$$

$$\lim_{r \rightarrow \infty} \Delta \langle \phi^2 \rangle_{ext2} = \frac{-7R^5}{16\pi^2 r^7} + O(r^{-8}). \quad (6.2.20)$$

Fig. 6.2.1 shows  $\Delta \langle \phi^2 \rangle_{ext}$  for the first three  $\ell$  modes and uses numerical results to verify the analytical calculations.

### 6.2.1.1 The Far Field Limit

If we restrict ourselves to the far field limit (small  $\omega$ ), we can use the same method used by Fabbri and Anderson in [7] to get an approximate result for  $\Delta \langle \phi^2 \rangle_{ext}$  for general  $\ell$ . The ratio in Eq. (6.2.3) admits an expansion around  $\omega = 0$ , with a leading order coefficient

$$\frac{\beta_{0\ell}}{\alpha_{0\ell}} = \frac{-2R^{2\ell+1}}{4^\ell \pi (1/2)_\ell (3/2)_\ell}, \quad (6.2.21)$$

where  $(a)_n$  is a Pochhammer symbol. Combining this with Eq. (6.1.25), the integral in (6.2.4) can be evaluated for general  $\ell$  (cf. Eq. (6.2.20))

$$\lim_{r \rightarrow \infty} \Delta \langle \phi^2 \rangle_{ext\ell} = -\frac{(2\ell+1)}{\pi 2^{2\ell+4}} \frac{\Gamma(\ell+1) \Gamma(2\ell+3/2)}{\Gamma(\ell+1/2) \Gamma^2(\ell+3/2)} \frac{R^{2\ell+1}}{r^{2\ell+3}} + O(r^{-2\ell-4}) \quad (6.2.22)$$

and the sum over  $\ell$  then converges to

$$\Delta \langle \phi^2 \rangle_{ext} \approx \frac{-R}{24\pi^2 r^5} \left[ 3r^2 {}_4F_3 \left( \frac{3}{4}, 1, 1, \frac{5}{4}; \frac{1}{2}, \frac{3}{2}, \frac{3}{2}; \frac{R^2}{r^2} \right) + 5R^2 {}_4F_3 \left( \frac{7}{4}, 2, 2, \frac{9}{4}; \frac{3}{2}, \frac{5}{2}, \frac{5}{2}; \frac{R^2}{r^2} \right) \right], \quad (6.2.23)$$

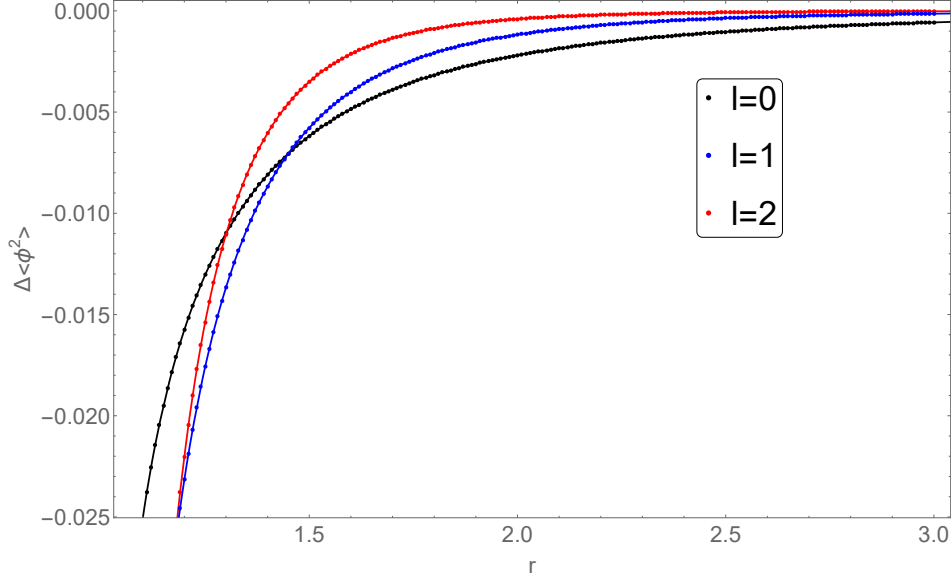


Figure 6.2.1:  $\Delta \langle \phi^2 \rangle_{ext}$  outside a thin shell of radius  $R = 1$ , for the first three  $\ell$  modes. The points were found by numerical integration while the solid curves are the analytical results, which for  $\ell = 0$  and  $\ell = 1$  are Eqs. (6.2.6) and (6.2.13) respectively.

where  ${}_pF_q(z)$  is a hypergeometric function. This method can be extended to  $\Delta \langle T_t^t \rangle_{ext}$  also. For minimal coupling and general  $\ell$  the energy density in the far field is

$$\Delta \langle T_t^t \rangle_{ext\ell} \approx -\frac{(\ell+1)(2\ell+3)\Gamma(4\ell+3)}{2^{8\ell+7}\Gamma^2(\ell+1/2)\Gamma^2(\ell+3/2)} \frac{R^{2\ell+1}}{r^{2\ell+5}},$$

which converges when summed over  $\ell$  to

$$\begin{aligned} \Delta \langle T_t^t \rangle_{ext} \approx & \frac{-R}{32\pi^2 r^7} \left[ 6r^2 {}_4F_3 \left( \frac{3}{4}, 1, 1, \frac{5}{4}; \frac{1}{2}, \frac{1}{2}, \frac{3}{2}; \frac{R^2}{r^2} \right) \right. \\ & \left. + 25R^2 {}_4F_3 \left( \frac{7}{4}, 2, 2, \frac{9}{4}; \frac{3}{2}, \frac{3}{2}, \frac{5}{2}; \frac{R^2}{r^2} \right) + 10R^2 {}_5F_4 \left( \frac{7}{4}, 2, 2, 2, \frac{9}{4}; 1, \frac{3}{2}, \frac{3}{2}, \frac{5}{2}; \frac{R^2}{r^2} \right) \right]. \end{aligned} \quad (6.2.24)$$

Both (6.2.23) and (6.2.24) are regular everywhere outside the shell and so we conclude that even though each individual  $\ell$  mode may diverge on the approach to the shell surface, we still have pointwise convergence of the sum over  $\ell$  far from the shell. We will find in Sec. 7.3 that this divergence of each  $\ell$  mode individually as  $r \rightarrow R$  is a property that does not hold for a more realistic stellar model, although the sum over  $\ell$  in this limit will remain divergent. This would appear to imply that at  $r = R$ , the divergence of each individual  $\ell$  mode is a product of the hard boundary of the shell model, but the divergence of the sum over  $\ell$  is caused by something more fundamental. We will return to discussing this in Sec. 7.3.

### 6.2.2 Inside the Shell

In the interior region of the shell spacetime, the roles of  $p$  and  $q$  are swapped compared to the exterior, as follows

$$q_{int} = \alpha_{\omega\ell} p_{flat} + \beta_{\omega\ell} q_{flat}, \quad (6.2.25)$$

$$p_{int} = p_{flat}, \quad (6.2.26)$$

such that  $\beta C_{shell} = C_{flat}$ . This is because inside the shell the boundary condition on  $p$  is known (regularity at the origin) and so it is  $q$  that now must be fixed on the shell surface. We find the ratio of  $\alpha_{\omega\ell}$  and  $\beta_{\omega\ell}$  by imposing the Dirichlet boundary condition  $q_{int}(R) = 0$  on the shell surface. The vacuum polarization difference is

$$\begin{aligned} \Delta \langle \phi^2 \rangle_{int} &= \frac{1}{4\pi^2} \int_0^\infty d\omega \sum_{\ell=0}^\infty (2\ell+1) C \frac{\alpha}{\beta} p^2 \\ &= \frac{-1}{4\pi^2} \int_0^\infty d\omega \sum_{\ell=0}^\infty (2\ell+1) \frac{2}{\pi} \frac{k_\ell(\omega R)}{i_\ell(\omega R)} \omega i_\ell^2(\omega r), \end{aligned} \quad (6.2.27)$$

or for  $\ell = 0$

$$\Delta \langle \phi^2 \rangle_{int0} = \frac{-1}{2\pi^3} \int_0^\infty d\omega \frac{k_0(\omega R)}{i_0(\omega R)} \omega i_0^2(\omega r) \quad (6.2.28)$$

and this integral converges whenever  $r < R$ . To perform the integral, we change variables once more to  $x = \omega R$ , set  $\omega r = \bar{\rho}x$  where  $\bar{\rho} = 1/\rho = r/R < 1$  and write the integral in terms of hyperbolic functions

$$\Delta \langle \phi^2 \rangle_{int0} = \frac{-1}{4\pi^2 r^2} \int_0^\infty \frac{dx}{x} (\coth x - 1) \sinh^2(\bar{\rho}x). \quad (6.2.29)$$

Despite the simplicity of this integrand, evaluating the integral must be done in multiple steps.

First we expand the integrand in powers of  $\bar{\rho}$

$$\Delta \langle \phi^2 \rangle_{int0} = \frac{-1}{4\pi^2 r^2} \int_0^\infty dx \sum_{n=1}^\infty \frac{\bar{\rho}^{2n}}{(3/2)_{n-1} (2)_{n-1}} (\coth x - 1) x^{2n-1}. \quad (6.2.30)$$

This can be integrated term by term to get

$$\begin{aligned} \Delta \langle \phi^2 \rangle_{int0} &= \frac{-1}{4\pi^2 r^2} \sum_{n=1}^\infty \frac{\zeta(2n)}{2n} \bar{\rho}^{2n} \\ &= \frac{-1}{8\pi^2 r^2} \log(\pi \bar{\rho} \csc \pi \bar{\rho}), \end{aligned} \quad (6.2.31)$$

where  $\zeta(x)$  is the Riemann zeta function. In this calculation and in the calculation of the energy density difference below, whenever we evaluate an integral via an expansion in powers of  $\bar{\rho}$  we check the final result against numerical integration for a range of  $\bar{\rho}$  up to  $\bar{\rho} = 0.999$  and find good agreement.

Now to extend this to the energy density difference. The only important integrals are  $\Delta S_1$  and  $\Delta S_2$ , like the exterior.

$$\Delta S_{1int0} = \frac{-1}{4\pi^2 r^2 R^2} \int_0^\infty x (\coth x - 1) \sinh^2(\bar{\rho}x) dx \quad (6.2.32)$$

and this integral is comparatively straightforward to evaluate without requiring an expansion in  $\bar{\rho}$ ,

$$\begin{aligned} \Delta S_{1int0} &= \frac{-1}{32\pi^2 r^4} \left( \bar{\rho}^2 \pi^2 \left( \csc^2 \pi \bar{\rho} - \frac{1}{3} \right) - 1 \right) \\ &\rightarrow \frac{-1}{32\pi^2 r^4} \left( \frac{1}{(\bar{\rho} - 1)^2} + \frac{2}{\bar{\rho} - 1} + O(\bar{\rho} - 1) \right), \end{aligned} \quad (6.2.33)$$

where “ $\rightarrow$ ” means taking the limit on the approach to the shell surface,  $\bar{\rho} \rightarrow 1^-$ . The second integral however is more involved and is handled as follows,

$$\begin{aligned} \Delta S_{2int0} &= \frac{-1}{4\pi^2 r^4} \int_0^\infty \frac{dx}{x} (\coth x - 1) (\sinh \bar{\rho}x - \bar{\rho}x \cosh \bar{\rho}x)^2 \\ &= \frac{-1}{4\pi^2 r^4} \int_0^\infty dx \sum_{n=1}^\infty \frac{n}{9(5/2)_{n-1}(4)_{n-1}} \bar{\rho}^{2n+4} (\coth x - 1) x^{2n+3} \\ &= \frac{-1}{4\pi^2 r^4} \left[ \sum_{n=1}^\infty \frac{n(2n+3)}{4(n+2)} \zeta(2n+4) \bar{\rho}^{2n+4} \right] \\ &= \frac{-1}{32\pi^2 r^4} \left( \frac{1}{3} \pi^2 \bar{\rho}^2 + \pi \bar{\rho} (4 \cot \pi \bar{\rho} + \pi \bar{\rho} \csc^2 \pi \bar{\rho}) + 4 \log(\pi \bar{\rho} \csc \pi \bar{\rho}) - 5 \right) \\ &\rightarrow \frac{-1}{32\pi^2 r^4} \left( \frac{1}{(\bar{\rho} - 1)^2} + \frac{6}{\bar{\rho} - 1} + \frac{2}{3} (\pi^2 - 6 \log(1 - \bar{\rho})) + O(\bar{\rho} - 1) \right), \end{aligned} \quad (6.2.34)$$

where in the second line we have expanded the integrand in powers of  $\bar{\rho}$  and in the third line the integral has been evaluated after interchanging it with the sum. Finally, the energy density is

$$\begin{aligned} \Delta \langle T^t_t \rangle_{int0} &= \left( 2\xi + \frac{1}{2} \right) \Delta S_{1int0} + \left( 2\xi - \frac{1}{2} \right) \Delta S_{2int0} \\ &= \frac{-1}{16\pi^2 r^4} \left[ 1 - \frac{1}{6} \pi^2 \bar{\rho}^2 - 6\xi - \pi \bar{\rho} (1 - 4\xi) \cot \pi \bar{\rho} + 2\pi^2 \bar{\rho}^2 \xi \csc^2 \pi \bar{\rho} - (1 - 4\xi) \log(\pi \bar{\rho} \csc \pi \bar{\rho}) \right] \\ &\rightarrow \frac{-1}{8\pi^2 r^4} \left[ \frac{\xi}{(\bar{\rho} - 1)^2} + \frac{8\xi - 1}{2(\bar{\rho} - 1)} + \frac{1}{12} (4\xi - 1) (\pi^2 - 6 \log(1 - \bar{\rho})) + O(\bar{\rho} - 1) \right]. \end{aligned} \quad (6.2.35)$$

This diverges quadratically for non-minimal coupling and linearly for minimal coupling, in which case the energy density difference is negative.

## 6.2.3 The Total Energy Difference

### 6.2.3.1 Analytical Calculation: $\ell = 0$

For  $\ell = 0$ , we have an expression for the energy density difference both inside and outside the shell. Hence, we can obtain a total energy difference by integrating the energy density over the full

spacetime. For general coupling the expansions of  $\Delta \langle T_t^t \rangle$  near the shell, are (see Eqs (6.2.11) and (6.2.35))

$$\Delta \langle T_t^t \rangle_{ext0} \rightarrow \frac{-1}{8\pi^2 r^4} \left[ \frac{\xi}{(\rho-1)^2} + \frac{1-4\xi}{2(\rho-1)} + \frac{1}{2} (1-6\xi - (4\xi-1) \log(1-\rho)) \right], \quad (6.2.36)$$

$$\Delta \langle T_t^t \rangle_{int0} \rightarrow \frac{-1}{8\pi^2 r^4} \left[ \frac{\xi}{(\bar{\rho}-1)^2} - \frac{1-8\xi}{2(\bar{\rho}-1)} + \frac{1}{12} (4\xi-1) (\pi^2 - 6 \log(1-\bar{\rho})) \right]. \quad (6.2.37)$$

We now perform the integral of the exterior energy density over the exterior region of the spacetime

$$\int_{R+\varepsilon}^{\infty} dr 4\pi r^2 \Delta \langle T_t^t \rangle_{ext0} = -\frac{\xi}{2\pi\varepsilon} + \frac{2\xi - (4\xi-1) \log\left(\frac{R}{\varepsilon}\right)}{4\pi R} + O(\varepsilon) \quad (6.2.38)$$

and the integral of the interior energy density over the interior region of the spacetime

$$\int_0^{R-\varepsilon} dr 4\pi r^2 \Delta \langle T_t^t \rangle_{int0} = -\frac{\xi}{2\pi\varepsilon} + \frac{1}{24\pi R} \left( \pi^2 - 12\xi + 6(4\xi-1) \log\left(\frac{R}{\varepsilon}\right) \right) + O(\varepsilon). \quad (6.2.39)$$

It is intriguing that the coupling  $\xi$  continues to play a role in the expressions for  $\Delta \langle T_t^t \rangle$ , even though the Ricci tensor should vanish everywhere except on the infinitesimally thin shell. Indeed, for non-minimal coupling we see that the total energy difference retains a  $\varepsilon^{-1}$  style divergence. Conversely, for minimal coupling, we obtain a finite result for the energy in the  $\ell = 0$  mode, due to the cancellation of the logarithmically divergent terms when (6.2.38) and (6.2.39) are summed,

$$E_0 = \frac{\pi}{24R} \quad (6.2.40)$$

and this has the expected scaling with  $R$  for an energy in natural units.

### 6.2.3.2 Numerical Verification: $\ell = 0$

We can use numerical results to verify this analytical calculation. Fig. 6.2.2 shows  $\Delta \langle T_t^t \rangle_{ext0}$  and  $\Delta \langle T_t^t \rangle_{int0}$  for minimal coupling, indicating agreement between the analytical and numerical results both inside and outside the shell. Other than  $r = R$  the only other point where a numerical result cannot be obtained is at  $r = 0$ , where we instead interpolate over the remaining small values of  $r$ .

To find the total energy numerically we subtract a counterterm from the data in Fig. 6.2.2 motivated by the form of the linear divergence of  $4\pi r^2 \Delta \langle T_t^t \rangle$ , that also has a vanishing integral over all positive  $r$  such that the total energy isn't affected. The counterterm is, for general  $\ell$ ,

$$f_c(r) = \frac{2\ell+1}{4\pi} \frac{2}{(r+R)} \frac{1}{(r-R)}, \quad (6.2.41)$$

such that the total energy difference for general  $\ell$  is

$$E_\ell = \int_0^\infty (4\pi r^2 \Delta \langle T_t^t \rangle_\ell - f_c(r)) dr + \int_0^\infty f_c(r) dr, \quad (6.2.42)$$

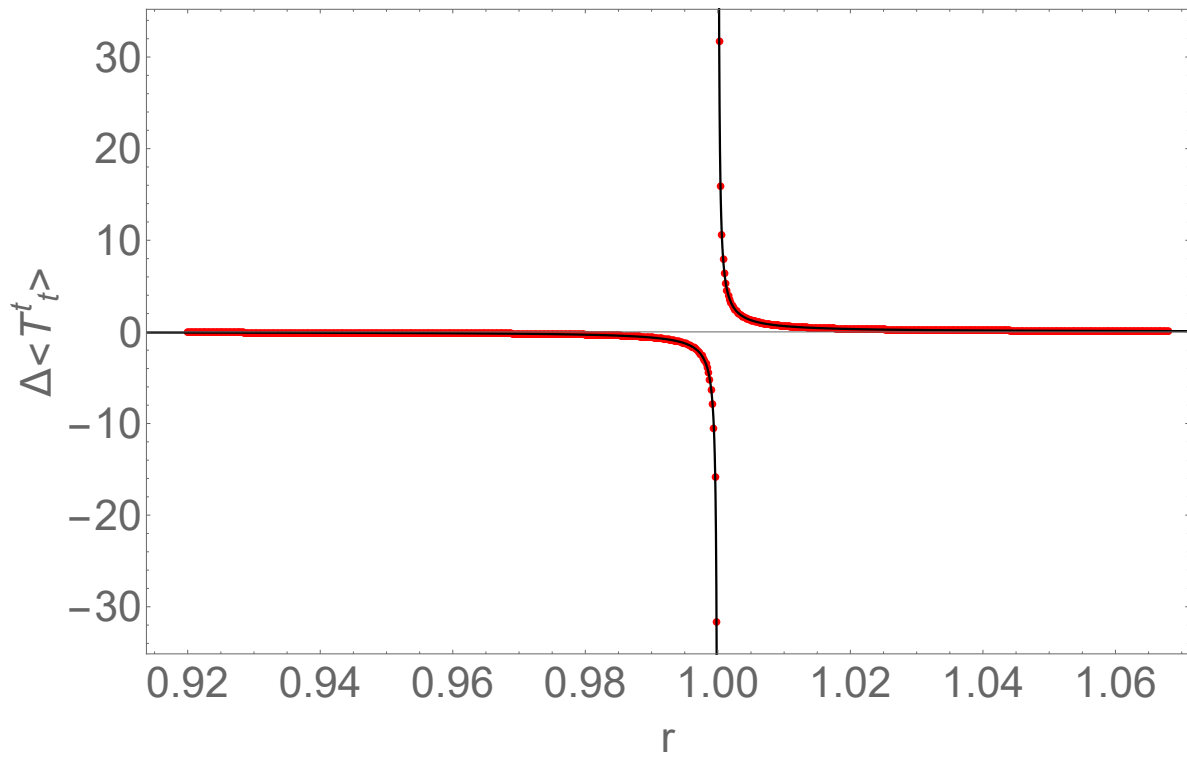


Figure 6.2.2:  $\Delta \langle T_t^t \rangle$  for minimal coupling  $\xi = 0$  both inside and outside a shell of radius  $R = 1$  for  $\ell = 0$ . The points were found by numerical integration while the solid curves are the analytical results from Eqs (6.2.11) and (6.2.35).

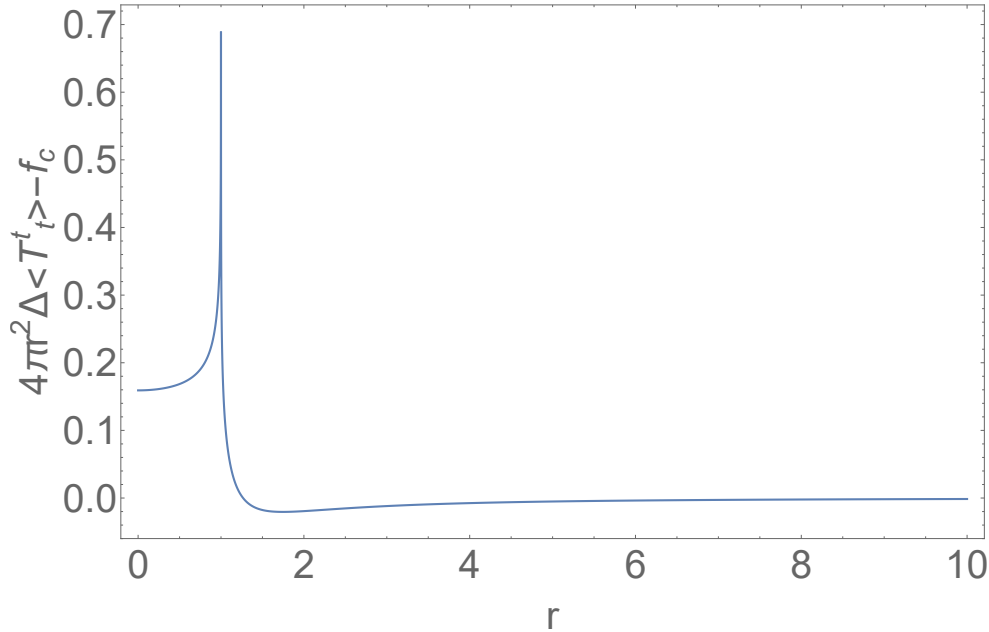


Figure 6.2.3: The regularised energy density  $4\pi r^2 \Delta \langle T_t^t \rangle - f_c(r)$  for a thin shell of radius  $R = 1$ , minimal coupling  $\xi = 0$  and  $\ell = 0$ .

where the second integral vanishes.

The expression in the first integrand of (6.2.42) produces the data in Fig. 6.2.3, which retains a logarithmic divergence at  $r = R$ . To integrate this data over all positive  $r$  numerically we approximate the behaviour of the energy density for  $r > r_{max}$  (typical values of  $r_{max}$  range from 20 to 40) by a function of the form  $ar^{-5} + br^{-6}$  with constants  $a$  and  $b$  found via numerical fitting. Additionally, to reduce potential numerical error near the logarithmic divergence at  $r = R$ , we integrate the analytical expression of Eq. (6.2.11) from  $r \in (R - \varepsilon, R)$  and the expression of Eq. (6.2.35) from  $r \in (R, R + \varepsilon)$  where  $\varepsilon$  is of order  $10^{-4}$ . The numerical verification produces a result that agrees with the analytical expression for the total energy (6.2.40) to at least six significant figures.

### 6.2.3.3 Numerical Calculation: $\ell > 0$

For  $\ell > 0$  we don't have an analytical expression for  $\Delta \langle T_t^t \rangle$  both inside and outside the shell, so we can only obtain a result for the full energy numerically using the process described above. This also means we cannot attempt to reduce numerical error near the shell surface by integrating analytics. We can estimate this error by performing a similar process to the one performed in the far field: for a shell of radius  $R = 1$  we approximate the near shell behavior by the function  $a_{ext} + b_{ext} \log(1 - \frac{1}{r}) + c_{ext}(r - 1)$  outside the shell and  $a_{int} + b_{int} \log(1 - r) + c_{int}(r - 1)$  inside the

$\ell$	$E_\ell$
0	$0.1309 \pm 0.0032$
1	$1.132 \pm 0.010$
2	$3.132 \pm 0.020$
3	$6.13 \pm 0.04$
4	$10.13 \pm 0.07$

Table 6.1: The total energy difference, found by integrating inside and outside a shell for the first five  $\ell$  modes, with error bars.

shell. We combine this error in quadrature with the magnitude of the integral of the approximate function in the far field  $ar^{-2\ell-5} + br^{-2\ell-6}$  from  $r_{max}$  to  $\infty$  and the magnitude of the interpolation over the small values of  $r$  to obtain the error values in Table (6.1).

This table indicates that, while the contribution to the total energy from each individual  $\ell$  mode is finite, the terms in the sum over  $\ell$  are increasing and so the sum diverges. However, there is a clear pattern in the results, consistent with the form

$$E_\ell = \frac{\pi}{24R} + \frac{\ell(\ell+1)}{2R} \quad (6.2.43)$$

and so this raises the possibility of employing a regularisation scheme in which we subtract this expression from each numerically found  $E_\ell$  and sum together any potentially remaining small terms. We would expect such a result to be somehow comparable to the known Casimir zero-point energy of the scalar field induced by a spherical shell on a flat spacetime, see [106]. However, what is left after the numerical subtraction of (6.2.43) from the data in Table 6.1 has large enough error bars that the result is consistent with zero, so we cannot ignore the possibility that the  $E_\ell$  of Eq. (6.2.43) is the exact result.

## Conclusion

After summarising the method of Anderson and Fabbri to calculate QFT differences between locally equivalent spacetimes, we applied the method to a toy model consisting of a scalar field on the spacetime of a thin spherical shell, with flat exterior and interior regions. We completed a fully analytical calculation of  $E_0$ , the  $\ell = 0$  contribution to the total energy difference of the minimally coupled scalar field with a Dirichlet boundary condition on the shell surface. We extended the calculation semi-analytically to  $E_\ell$  for  $\ell > 0$  and found a clear pattern in the final results. Each  $E_\ell$

is finite due to the cancellation of the divergences in each  $\ell$  mode of the energy density difference  $\Delta \langle T^t_t \rangle$  on the interior and exterior of the shell surface (a cancellation that does not occur if the coupling is non-minimal), but the resulting sum of  $E_\ell$  over  $\ell$  is clearly divergent. We will contrast this in the next chapter with the more realistic model of a star sitting in a Schwarzschild spacetime.

# Chapter 7

## Numerical Analysis of QFT Differences

### Introduction and Overview

One of the goals of this chapter is to perform a numerical calculation of  $\langle\phi^2\rangle$  on the spacetime of a spherically symmetric star. To perform this calculation we will be utilising the results for  $\langle\phi^2\rangle$  outside a Schwarzschild black hole from chapter 5 and work performed by Anderson and Fabbri in Ref. [7] on the topic of QFT differences described in the previous chapter. We compare and contrast the results for different star radii and different coupling to the scalar curvature. We also perform a numerical calculation of the stress-energy difference between a star and a black hole near the star surface.

Within Ref. [7] is also an analysis of vacuum polarization differences and stress-energy differences in the far field limit of Newtonian stars and black holes, which we described in Sec. 6.1.3. In the next section we show how these analytical approximations can be extended to more general spherically symmetric stars. We test these approximations numerically in Sec. 7.4.

### 7.1 Approximation in the Far Field Limit

#### 7.1.1 Constant Density Stars

A simple stellar model is that of a constant density star, whose (Euclideanised) spacetime is specified by the *interior Schwarzschild metric* [132]

$$g_{tt}(r) \equiv f_*(r) = \left( \frac{3}{2} \sqrt{1 - \frac{2M}{R}} - \frac{1}{2} \sqrt{1 - \frac{2Mr^2}{R^3}} \right)^2, \quad (7.1.1)$$

$$g_{rr}(r) \equiv h_*(r) = \left( 1 - \frac{2Mr^2}{R^3} \right)^{-1}, \quad (7.1.2)$$

in the region  $r < R$  where  $R$  is the radius of the star. For  $r > R$  the metric is simply specified by the standard Schwarzschild metric, such that the metric functions of the full spacetime are continuous, i.e., the complete metric line element for the star spacetime is

$$ds^2 = \left[ \theta(R-r) f_*(r) + \theta(r-R) \left( 1 - \frac{2M}{r} \right) \right] dt^2 + \left[ \theta(R-r) h_*(r) + \theta(r-R) \left( 1 - \frac{2M}{r} \right)^{-1} \right] dr^2 + r^2 d\Omega^2, \quad (7.1.3)$$

where  $\theta(x)$  is the Heaviside step function.

Now, according to (6.1.28), we want to consider the “static” ( $\omega = 0$ ) behavior of (6.1.4). In the exterior Schwarzschild spacetime this equation has solutions in terms of Legendre functions, which we write as

$$p_{static} = \frac{\pi}{2M} \frac{1}{N} P_\ell \left( \frac{r}{M} - 1 \right), \quad (7.1.4)$$

$$q_{static} = N Q_\ell \left( \frac{r}{M} - 1 \right), \quad (7.1.5)$$

where the constant  $N$  is

$$N = \frac{2^{2\ell}}{M^{\ell+1}} \frac{\Gamma(\ell + 1/2) \Gamma(\ell + 3/2)}{\Gamma(\ell + 1)}. \quad (7.1.6)$$

This normalisation is chosen such that the  $C_{\omega\ell}$  calculated from (6.1.6) is equal to  $2/\pi$ , so that we can compare our results directly with Eq. (6.1.28) and also such that  $q_{static}$  and  $q_{flat}$  will agree in the far field to leading order in  $r^{-1}$ ,

$$\lim_{\omega \rightarrow 0} \frac{q_{static}}{q_{flat}} = 1 + O\left(\frac{M}{r}\right). \quad (7.1.7)$$

Now we need to find  $p_*$ . An approximate solution can be found by constructing a Frobenius series around the singular point at the origin, of the form

$$p_*(r) = r^\ell \sum_{k=0}^{\infty} a_{2k} r^{2k} \quad (7.1.8)$$

and  $a_0 = 1$ . This is substituted into (6.1.4) with the metric functions (7.1.1) and (7.1.2) and the coefficients  $a_{2k}$  for  $k \geq 1$  are found by solving the equation term by term in powers of  $r$ . The first of these coefficients is

$$a_2 = \frac{M\ell(R(21 + 10\ell - 3X(2\ell + 5)) - 18M(\ell + 2)) - 6M\xi(18M + R(9X - 11))}{(1 - 3X)^2(2\ell + 3)R^4} \quad (7.1.9)$$

and we have defined

$$X = \sqrt{1 - \frac{2M}{R}}. \quad (7.1.10)$$

These  $a_{2k}$  coefficients grow in complexity rapidly and so it is often easier and less computationally intensive to specify the parameters  $\ell$  and  $\omega$  in the radial differential equation (6.1.4) and calculate the  $a_{2k}$  for each set of parameters individually to the order  $k$  we desire.

The functions  $p_{static}$ ,  $q_{static}$  and  $p_*$  are then substituted into (6.1.8) and (6.1.9) to get  $\alpha_{0\ell}$  and  $\beta_{0\ell}$  as a power series in  $M/R$ . To calculate such an expansion to order  $R^{-n}$  requires us to compute (7.1.8) to order  $k = n + 2\ell + 1$ .

All that is needed to get an expression for  $\Delta \langle \phi^2 \rangle$  at leading order in  $r^{-1}$  according to (6.1.28) is to perform this process for  $\ell = 0$ . The result is

$$\Delta \langle \phi^2 \rangle = -\frac{M\xi}{4\pi^2 r^3} \mathcal{S}_0 \left( \frac{M}{R} \right) + O(r^{-4}), \quad (7.1.11)$$

where we have defined the  $\ell = 0$  structure function

$$\mathcal{S}_0(x) = 1 - \frac{6}{5}(2\xi + 1)x + \frac{12}{35}(17\xi^2 + 10\xi - 4)x^2 + O(x^3). \quad (7.1.12)$$

As we approach the limit of a small compactness parameter  $M/R$  (i.e. as  $R \rightarrow \infty$ ), we see that (7.1.11) reduces to the result for a Newtonian star in (6.1.29). As for the Newtonian star, it can be seen from (7.1.11) that  $\Delta \langle \phi^2 \rangle$  vanishes for minimal coupling only. For any non-zero value of coupling the vacuum polarization far from the star is sensitive to its mass at leading order and to its internal structure at subsequent orders in  $M/R$ .

It is straightforward to combine our knowledge of  $\beta_{00}/\alpha_{00}$  with Eq. (6.1.30) to generalise  $\Delta \langle T^\mu_\nu \rangle$  to a constant density star also,

$$\Delta \langle T^\mu_\nu \rangle = -\frac{3M\xi}{4\pi^2 r^5} \left( \xi - \frac{1}{6} \right) \mathcal{S}_0 \left( \frac{M}{R} \right) \text{diag} [2, -2, 3, 3] + O(r^{-6}). \quad (7.1.13)$$

Although only the  $\ell = 0$  contribution is needed at leading order in  $r^{-1}$ , we can also find the leading order contributions to  $\Delta \langle \phi^2 \rangle$  for general  $\ell \geq 0$ , which takes the form,

$$\Delta \langle \phi^2 \rangle_\ell^{static} = \frac{2\ell + 1}{4\pi^2} \frac{2}{\pi} \frac{\beta_{0\ell}}{\alpha_{0\ell}} \int_0^\infty \omega^{2\ell+2} k_\ell^2(\omega r) d\omega \quad (7.1.14)$$

and the general expression for the integral over  $\omega$  for  $r > 0$  is given by

$$\int_0^\infty \omega^{2\ell+2} k_\ell^2(\omega r) d\omega = \frac{\pi^2 \Gamma(\ell + 1) \Gamma(2\ell + 3/2)}{8\Gamma(\ell + 3/2)} r^{-2\ell-3}. \quad (7.1.15)$$

The static contribution to the ratio of  $\beta$  to  $\alpha$  is

$$\frac{2}{\pi} \frac{\beta_{0\ell}}{\alpha_{0\ell}} = -\frac{3(2\ell + 3)MR^{2\ell}\xi}{2^{2\ell+1}\pi\Gamma^2(\ell + 5/2)} \mathcal{S}_\ell \left( \frac{M}{R} \right), \quad (7.1.16)$$

where  $\mathcal{S}_\ell(x) = 1 + O(x)$  is the structure function for general  $\ell$ . As such, Eq. (7.1.14) can be written in a form that emphasises the scaling with respect to  $R$  and  $r$ ,

$$\Delta \langle \phi^2 \rangle_\ell^{static} = M \xi A_\ell r^{-3} \left( \frac{R}{r} \right)^{2\ell} \mathcal{S}_\ell \left( \frac{M}{R} \right), \quad (7.1.17)$$

with a coefficient  $A_\ell$  given by

$$A_\ell = -\frac{3(2\ell+3)(\ell!)\Gamma(2\ell+3/2)}{2^{2\ell+5}\pi\Gamma(\ell+1/2)\Gamma^2(\ell+5/2)}. \quad (7.1.18)$$

Equation (7.1.17) implies that the scaling of the static contributions is  $(M/r^3)(R/r)^{2\ell}$ . This agrees with the general scaling as that predicted by [130], for  $\langle \phi^2 \rangle$  outside a star in the “weak field” limit, which is a star with a constant density (as we have assumed here, but will no longer assume in Sec. 7.1.3) but with  $R \gg M$  (which we have not assumed).

Calculating the terms in the structure function series  $\mathcal{S}_\ell$  for general  $\ell$  is time consuming, but it is straightforward to calculate terms for a specified  $\ell$ . For example, for  $\ell = 1$  Eq. (7.1.16) reads

$$\frac{2}{\pi} \frac{\beta_{01}}{\alpha_{01}} = -\frac{8M\xi R^2}{15\pi^2} \left( 1 - \frac{2(2\xi^2 + 11\xi - 1)}{7\xi} \frac{M}{R} + \frac{(108\xi^3 + 600\xi^2 + 655\xi - 100)}{315\xi} \frac{M^2}{R^2} + \dots \right), \quad (7.1.19)$$

such that the structure function  $\mathcal{S}_1$  can be read off as

$$\mathcal{S}_1(x) = 1 - \frac{2(2\xi^2 + 11\xi - 1)}{7\xi} x + \frac{(108\xi^3 + 600\xi^2 + 655\xi - 100)}{315\xi} x^2 + \dots \quad (7.1.20)$$

### 7.1.2 Ultra Compact Objects

For a fixed mass  $M$  there is a minimum radius attainable by a static, spherically symmetric matter configuration (such as a constant density star), referred to as the *Buchdahl limit* [30]. At this limit, the central pressure (i.e., the pressure at the origin  $r = 0$ ) as a function of the compactness  $R/M$  diverges. This imposes the following inequality, (in natural units)

$$R > \frac{9}{4}M. \quad (7.1.21)$$

We could also infer this limit from the Frobenius expansion of the scalar field inside the star. For  $\ell = \omega = 0$ , the coefficients  $a_k$  in the Frobenius series for  $p_*$  (7.1.8) dramatically simplify. The first two even order coefficients become (after simplification)

$$a_2 = \frac{M\xi(18M + R(3X - 7))}{R^3(9M - 4R)}, \quad (7.1.22)$$

$$a_4 = \frac{M^2\xi[54M(8X - 5 + 6\xi(X - 1)) + R(23(6\xi + 5) - 9X(18\xi + 23))]}{10R^6(3X - 1)(9M - 4R)}, \quad (7.1.23)$$

with  $X$  defined in (7.1.10). These coefficients diverge at the Buchdahl limit  $R = \frac{9}{4}M$ , as does every following non-zero  $a_k$ .

In the numerical analysis of  $\Delta \langle \phi^2 \rangle$  and  $\Delta \langle T^\mu{}_\nu \rangle$  to follow in Sec. 7.2 onwards, we will consider the case of an *Ultra Compact Object* (UCO), a constant density star with a radius  $R$  close to Buchdahl limit, chosen to be  $R = 2.26M$ .

### 7.1.3 Different Stellar Models

The method we used to arrive at the far field result in (7.1.11) can be applied to different stellar models. To select an additional example, we refer to the analysis of Delgaty and Lake [50], in which 127 static, spherically symmetric, perfect fluid solutions to Einstein's equations are presented. In each circumstance, they performed a series of tests to determine the physical validity of the solution. The interior Schwarzschild solution passes all their chosen tests except one, that the speed of sound should be subluminal, i.e.,  $dp/d\rho < 1$  where  $p$  is the internal pressure and  $\rho$  is the density. As such, to demonstrate our method further we will choose a stellar structure that, at the very least, passes the same tests as the interior Schwarzschild metric.

The metric we choose is given the label ‘‘Tolman IV’’ by [50], originally presented in [139]. This passes each physical test, including having a subluminal sound speed. It is given in the Euclideanised form

$$g_{tt}(r) = B^2 (1 + r^2/A^2), \quad (7.1.24)$$

$$g_{rr}(r) = \frac{1 + 2r^2/A^2}{(1 - r^2/C^2)(1 + r^2/A^2)}, \quad (7.1.25)$$

where  $A, B$  and  $C$  are integration constants (we have used  $C$  instead of the symbol  $R$  used in [50] and [139] so as to not confuse this integration constant with the radius of the star). The density  $\rho(r)$  and pressure  $p(r)$  can be found through Einstein's equations and are given by

$$8\pi\rho = \frac{1}{A^2} \frac{1 + 3A^2/C^2 + 3r^2/C^2}{1 + 2r^2/A^2} + \frac{2}{A^2} \frac{1 - r^2/C^2}{(1 + 2r^2/A^2)^2}, \quad (7.1.26)$$

$$8\pi p = \frac{1}{A^2} \frac{1 - A^2/C^2 - 3r^2/C^2}{1 + 2r^2/A^2}. \quad (7.1.27)$$

In particular, the density is not constant, unlike for the interior Schwarzschild metric.

The radius of the star,  $R$ , can then be found by finding the value of  $r$  at which the pressure vanishes. This is

$$R = C \sqrt{\frac{1}{3} \left( 1 - \frac{A^2}{C^2} \right)}. \quad (7.1.28)$$

The mass of the star  $M$  is found by matching the  $g_{rr}$  component of the Tolman IV metric to the corresponding component of the exterior Schwarzschild metric at the star radius  $r = R$ . This gives

$$M = \frac{R}{2} \left[ 1 - \frac{(1 - R^2/C^2)(1 + R^2/A^2)}{1 + 2R^2/A^2} \right], \quad (7.1.29)$$

while performing the same matching for the  $g_{tt}$  component specifies the constant  $B$ ,

$$B^2 = (1 - R^2/C^2) / (1 + 2R^2/A^2). \quad (7.1.30)$$

This provides enough information to re-write the metric components entirely in terms of  $M$  and  $R$

$$g_{tt}(r) = 1 + \frac{M(r^2 - 3R^2)}{R^3}, \quad (7.1.31)$$

$$g_{rr}(r) = \frac{R^3(2Mr^2 - 3MR^2 + R^3)}{(R^3 - Mr^2)(R^3 + M(r^2 - 3R^2))}. \quad (7.1.32)$$

This stellar model has its own equivalent of the Buchdahl limit, although rather than  $\frac{9}{4}M$  being the limiting value of  $R$  we instead find that we must impose  $R > 3M$ . This is because when  $R = 3M$ ,  $g_{rr}$  diverges at  $r = 0$  and it can be shown by a calculation of the square of the Riemann tensor  $R^{abcd}R_{abcd}$  that this is a curvature singularity. This singularity persists when  $R < 3M$  but moves to larger values of  $r$  while still remaining inside the star.

From here, we find the solution  $p_*(r)$  inside the star using a Frobenius series of the same form as Eq. (7.1.8). As before,  $a_k = 0$  for all odd  $k$ . The first two even-order coefficients for  $\ell = \omega = 0$  are  $a_2 = M\xi/R^3$  and

$$a_4 = \frac{M^2\xi [(9M^2 + R^2)(3\xi + 4) - 6MR(3\xi + 5)]}{10R^6(R - 3M)^2}. \quad (7.1.33)$$

We note every non-zero coefficient from  $a_4$  onward diverges when the star radius is at the light ring  $R = 3M$ , in accordance with the existence of the curvature singularity discussed above.

The final expressions for  $\Delta \langle \phi^2 \rangle$  and  $\Delta \langle T^\mu{}_\nu \rangle$  at leading order in  $r^{-1}$  take the same form as Eq. (7.1.11) and (7.1.13) respectively, with the modified structure function

$$\mathcal{S}_{Tol0}(x) = 1 - \frac{6}{5}(2\xi + 1)x + \frac{6}{35}(34\xi^2 + 18\xi - 9)x^2 + O(x^3). \quad (7.1.34)$$

This structure function agrees with the one obtained from the interior Schwarzschild metric (7.1.12) up to first order in the parameter  $x = M/R$ , but differs thereafter. This makes sense, as the metric coefficients in the interior Schwarzschild and Tolman IV metrics also agree to first order after an expansion in this parameter.

## 7.2 Outline of the Numerical Method

The remainder of this chapter will be focused on the numerical computation of  $\Delta \langle \phi^2 \rangle$  and  $\Delta \langle T^\mu_\nu \rangle$ , which proceeds in the following manner: first we solve the radial mode equation (6.1.4) in the exterior Schwarzschild spacetime with the required boundary conditions to find  $p_S$  and  $q_S$  and then in the interior star spacetime to find  $p_*$ . We then construct the integrands in (6.1.10) for each  $\ell$  mode, integrate them with respect to  $\omega$  and then perform the sum over  $\ell$ . Here, we describe each step in detail.

To find  $q_S$  we transform the radial mode equation using the independent variable  $s = 1/r$ ,

$$s^4 f \frac{d^2 q_S}{ds^2} + s^4 \frac{df}{ds} \frac{dq_S}{ds} - \left[ \frac{\omega^2}{f} + s^2 \ell(\ell+1) \right] q_S(s) = 0. \quad (7.2.1)$$

This equation must be solved with the boundary condition that  $q_S$  decays exponentially as  $s \rightarrow 0$  ( $r \rightarrow \infty$ ). To aid numerical computation we transform the dependent variable in the manner  $q_S = e^Q$  as is performed in Ref. [81], to produce a non-linear equation for  $Q(s)$

$$s^4 f \frac{d^2 Q}{ds^2} + s^4 \left[ f \frac{dQ}{ds} + \frac{df}{ds} \right] \frac{dQ}{ds} - \left[ \frac{\omega^2}{f} + s^2 \ell(\ell+1) \right] = 0. \quad (7.2.2)$$

We then impose initial data for the solution at  $s = \delta_q$  for  $\delta_q \ll M^{-1}$  and integrate inwards towards the surface of the star. The initial data for  $q_S$  takes the form of an asymptotic series expansion (with  $b_0 = 1$ )

$$q_S = s^\rho e^{-\frac{\Omega}{s}} \sum_{k=0}^{\infty} b_k s^k \quad (7.2.3)$$

and so the logarithm of this forms the initial data for  $Q$ . The coefficients  $\Omega, \rho$  and  $b_k$  for  $k \geq 1$  are found by substituting (7.2.3) into (7.2.1) and solving the equation term by term in powers of  $s$ . This gives  $\Omega = \omega$ ,  $\rho = 1 + 2M\omega$ , and the first two non-trivial  $b_k$  coefficients are

$$b_1 = \frac{\ell(\ell+1)}{2\omega} + 4M^2\omega, \quad (7.2.4)$$

$$b_2 = \frac{(\ell-1)\ell(\ell+1)(\ell+2)}{8\omega^2} + \frac{M}{2\omega} + 2\ell(\ell+1)M^2 + 4M^3\omega + 8M^4\omega^2. \quad (7.2.5)$$

The function  $p_S$  is found similarly. Defining the ‘‘shifted’’ radial variable  $x = r - 2M$  the radial mode equation is transformed to

$$\frac{d^2 p_S}{dx^2} + \left[ \frac{1}{x} + \frac{1}{x+2M} \right] \frac{dp_S}{dx} - \left[ \omega^2 \left( 1 + \frac{2M}{x} \right)^2 + \frac{\ell(\ell+1)}{x(x+2M)} \right] p_S(x) = 0 \quad (7.2.6)$$

and the boundary condition of regularity at the black hole horizon is imposed at  $x = \delta_p$  for  $\delta_p \ll M$  by the Frobenius series ansatz (with  $a_0 = 1$ )

$$p_S = x^\nu \sum_{k=0}^{\infty} a_k x^k. \quad (7.2.7)$$

The coefficients  $\nu$  and  $a_k$  for  $k \geq 1$  are then found by substituting (7.2.7) into (7.2.6) and solving the equation term by term in powers of  $x$ . This gives  $\nu = \pm 2M\omega$ , of which we choose the positive root so that  $p_S$  satisfies the boundary condition of regularity on the black hole event horizon. The first two non-trivial  $a_k$  coefficients are

$$a_1 = \frac{\ell(\ell+1) - 2M\omega + 8M^2\omega^2}{2M + 8M^2\omega}, \quad (7.2.8)$$

$$a_2 = \frac{(\ell-1)\ell(\ell+1)(\ell+2) + (4-8\ell(\ell+1))M\omega + 8(1+2\ell(\ell+1))M^2\omega^2 - 16M^3\omega^3 + 64M^4\omega^4}{16M^2(1+2M\omega)(1+4M\omega)}. \quad (7.2.9)$$

The Schwarzschild radial equation is then integrated outwards from  $x = \delta_p$  up to  $r = R$ , where the surface of the star would be in the star spacetime.

The initial data imposing regularity of the function  $p_*$  at the center of the star is the same as that in Eq. (7.1.8). This is imposed at  $r = \delta_*$  for  $\delta_* \ll M$  and the interior Schwarzschild radial equation (Eq. (6.1.4) with  $f$  and  $h$  specified by Eqs. (7.1.1) and (7.1.2)) is integrated from  $\delta_*$  up to the star surface.

We chose to take each of the three initial data series to an order of  $k_{max} = 10$  and impose them at  $\delta_p = \delta_q = \delta_* = 10^{-3}$ . Each of the three functions  $p_S, q_S$  and  $p_*$  (and from these, the integrand in (6.1.10)) are numerically calculated for a range of values of  $\omega \in (0, \omega_{max})$  and  $\ell \in \{0, 1, \dots, \ell_{max}\}$ . Appropriate choices of internal parameters will be discussed in the next section.

We must also choose how to divide the range of  $\omega$  into a grid of points for the evaluation of the integrand in Eq. (6.1.10). An example integrand is plotted in Fig. 7.2.1. It is clear that the small frequency behavior provides a much larger contribution to the integral than the large frequency behaviour and so we choose to cluster the grid of points more tightly when  $\omega$  is small. For  $\omega < 0.1$  we choose a spacing  $d\omega = 0.001$  and for  $\omega > 0.1$  we choose a spacing  $d\omega = 0.004$ . We will also assess these choices in the subsection on error estimation.

In the static case  $\omega = 0$ , we do not find the functions  $p_S$  and  $q_S$  numerically. Instead they are known exactly in terms of Legendre polynomials, as in Eqs. (7.1.4) and (7.1.5).

A logarithmic plot of the integrand for each of the  $\ell$  modes for chosen values of  $R$  and  $r$  is shown in Fig. 7.2.2. It can be seen that as  $\omega$  approaches  $\omega_{max}$  the gradient approaches a constant, i.e., the integrand is decaying exponentially. This motivates the following analytical approximation: for  $\omega > \omega_{max}$  we integrate a function of the form  $a_\ell e^{-b_\ell \omega}$ , where the constants  $a_\ell$  and  $b_\ell$  are found by numerical fitting.

Finally, we repeat this process for multiple values of  $r$  and  $\xi \in \{0, 1/10, 1/6\}$ . The results are shown in Fig. 7.2.3. The figure shows that there is an approximately linear dependence of  $\Delta \langle \phi^2 \rangle$  on

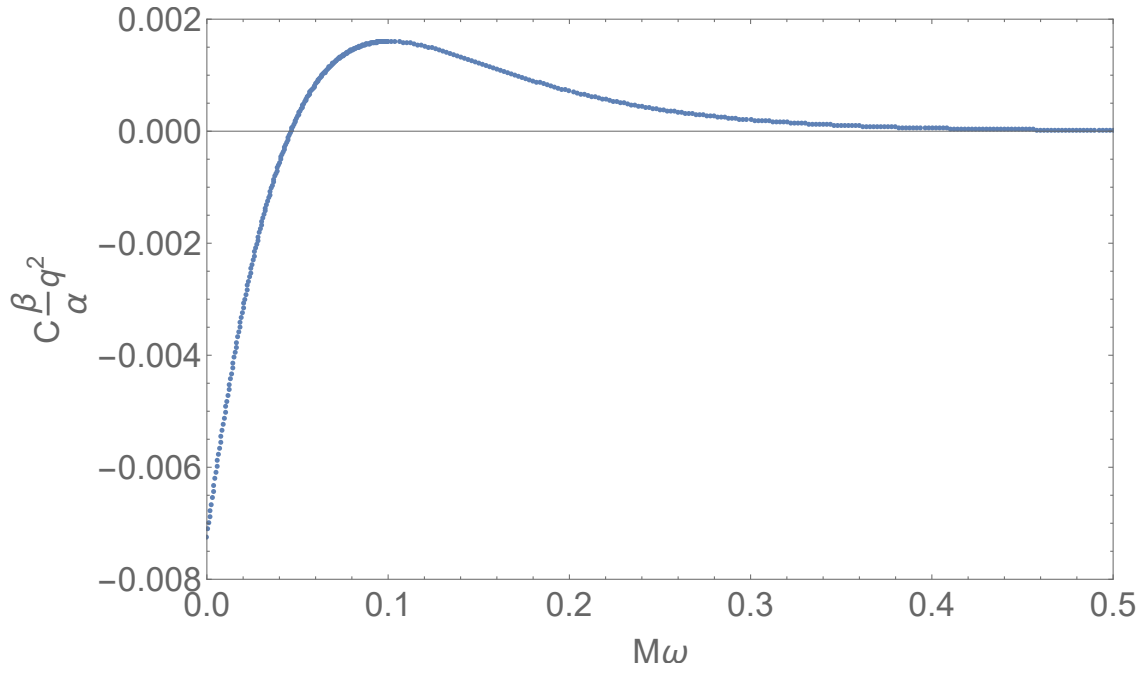


Figure 7.2.1: The integrand of Eq. (6.1.10) for the parameters  $R = 4M, r = 6M, \xi = 1/6, \ell = 0$ .

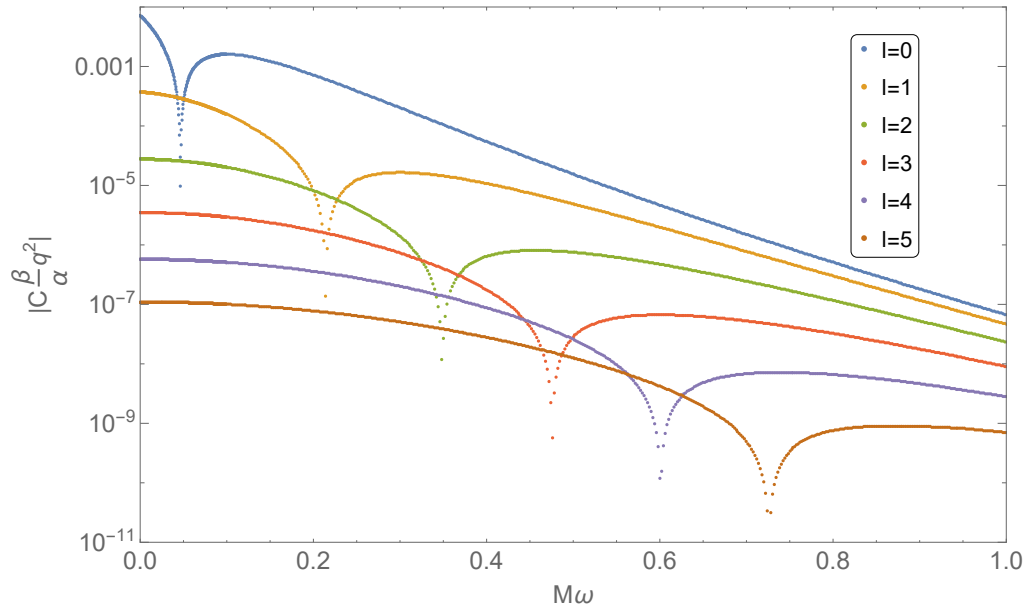


Figure 7.2.2: The (absolute value of the) integrand of Eq. (6.1.10) for  $R = 4M, r = 6M, \xi = 1/6$  and each  $\ell$  value from 0 to  $\ell_{max} = 5$ .

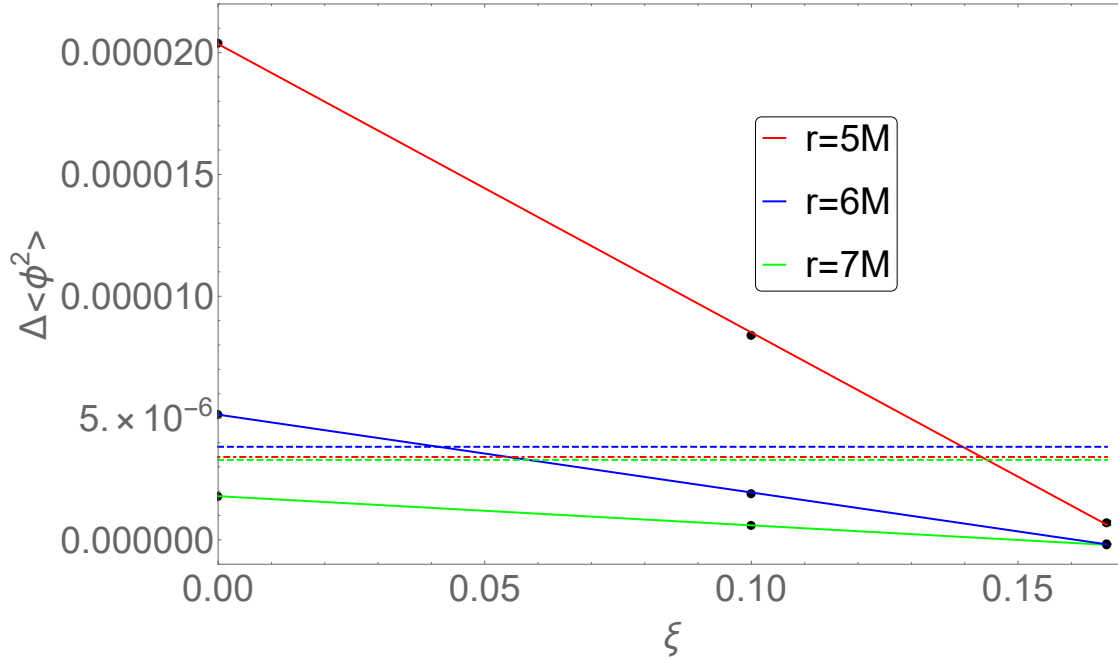


Figure 7.2.3:  $\Delta \langle \phi^2 \rangle$  for  $R = 4M$  and various values of  $r$  and  $\xi$ . Error bars are included, but are too small to be visible. The solid lines are found by a least squares fit. The dashed lines are the corresponding values of  $\langle \phi^2 \rangle$  in the Schwarzschild spacetime at the same  $r$  values.

the coupling  $\xi$  and the coefficient of proportionality decreases with increasing  $r$ . These two traits are shared by the behaviour of  $\Delta \langle \phi^2 \rangle$  in the limit of large  $r$ , see Eq. (7.1.11).

The three main sources of error in this calculation are the  $\ell$  cutoff,  $\omega$  tail and discretisation errors described in the calculation of  $\langle \phi^2 \rangle$  in the Schwarzschild spacetime (see Sec. 5.2.3.4) and they are estimated through the same methods. The primary difference in the results is the relative orders of magnitude of the different errors. Far from the star, the discretisation error is the largest error by multiple orders of magnitude, while still being small compared to the value of  $\Delta \langle \phi^2 \rangle$ . As we approach the star surface, the  $\ell$  cutoff and  $\omega$  tail errors grow until they are larger than the discretisation error and the total error relative to  $\Delta \langle \phi^2 \rangle$  becomes larger. Hence, near the surface of the star, the calculation could be best improved by including additional  $\ell$  modes in the sum and including larger  $\omega$  values in the integral. In the next section, we will now present this numerical data, with error bars included.

## 7.3 Numerical Analysis Near the Star Surface

### 7.3.1 Vacuum Polarization Near a Compact Object

The vacuum polarization outside of a constant density star  $\langle\phi^2\rangle_{Star}$  is simply the sum of the vacuum polarization outside a Schwarzschild black hole  $\langle\phi^2\rangle_{Schw}$  and the difference  $\Delta\langle\phi^2\rangle$  between a black hole and a constant density star. We numerically calculated  $\langle\phi^2\rangle_{Schw}$  in chapter 5 and described the method used to numerically calculate  $\Delta\langle\phi^2\rangle$  in the previous section.

Typical values for the highest  $\ell$  mode considered and the largest frequency  $\omega$  for each mode are  $\ell_{max} = 5$  and  $M\omega_{max} = 1$ . We will consider two values of the compactness parameter,  $R/M = 4$  and  $R/M = 2.26$ . The first value models a compact neutron star, but not so compact that a light ring has formed. The second models an ultra compact object with a radius just larger than the Buchdahl bound, Eq. (7.1.21). Outside this ultra compact object a light ring exists at  $R = 3M$ .

#### 7.3.1.1 $R = 4M$ (Compact Neutron Star)

The results for  $\langle\phi^2\rangle_{Schw}$ ,  $\Delta\langle\phi^2\rangle$  and  $\langle\phi^2\rangle_{Star}$  for conformal and minimal coupling are shown respectively in Figs. 7.3.1 and 7.3.2. For conformal coupling it can be seen that  $\Delta\langle\phi^2\rangle < 0$  for  $r > r_1 \approx 5.5M$ , a similar radius to where  $\langle\phi^2\rangle_{Schw}$  has its maximum. In addition,  $\Delta\langle\phi^2\rangle < \langle\phi^2\rangle_{Schw}$  for  $r > r_2 \approx 4.8M$ . We see that, unlike  $\langle\phi^2\rangle_{Schw}$ ,  $\langle\phi^2\rangle_{Star}$  is everywhere positive and monotonically increasing on the approach to the star surface. The error bars grow in size as  $r$  decreases because the contributions from modes with  $\ell > \ell_{max}$  become more relevant, as do the contributions to each individual  $\ell$ -mode from the large frequencies  $\omega > \omega_{max}$ .

For minimal coupling,  $\Delta\langle\phi^2\rangle$  is everywhere positive. In the region  $r < 10M$  plotted in Fig. 7.3.2 it can be seen that  $\Delta\langle\phi^2\rangle$  dominates over  $\langle\phi^2\rangle_{Schw}$  and hence, so does  $\langle\phi^2\rangle_{Star}$ . In other words, replacement of the black hole by a compact neutron star has drastically changed the vacuum polarization.

The value of  $\langle\phi^2\rangle_{Star}$  at a radius  $r = 4.5M$  is  $(7.5 \pm 0.06) \times 10^{-5}$  for minimal coupling and  $(6.6 \pm 0.6) \times 10^{-6}$  for conformal coupling respectively, such that the ratio of the minimal value to the conformal value is  $(11.4 \pm 1.0)$ . This shows that the coupling term plays a large role in determining the magnitude of the vacuum polarization near a compact neutron star: see also Fig. 7.2.3 that demonstrates that this relationship to the coupling is approximately linear.

The values of  $\Delta\langle\phi^2\rangle$  and  $\langle\phi^2\rangle_{Star}$  on the surface of the neutron star are not shown in either figure. This is because we have numerical evidence that these two quantities diverge at  $r = R$ , but remain finite for  $r > R$ . This evidence is presented in Fig. 7.3.3. It can be seen that when  $r = R$

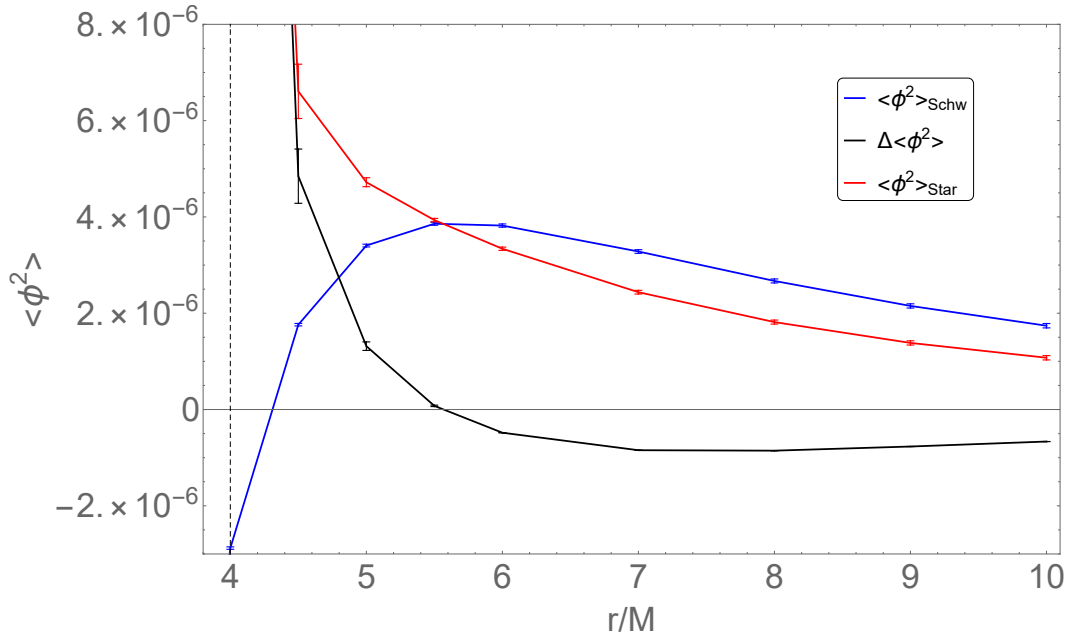


Figure 7.3.1:  $\langle \phi^2 \rangle$  outside a Schwarzschild black hole, outside a compact neutron star and  $\Delta \langle \phi^2 \rangle$  for conformal coupling  $\xi = 1/6$ . The vertical dashed line indicates the star surface at  $R = 4M$ .

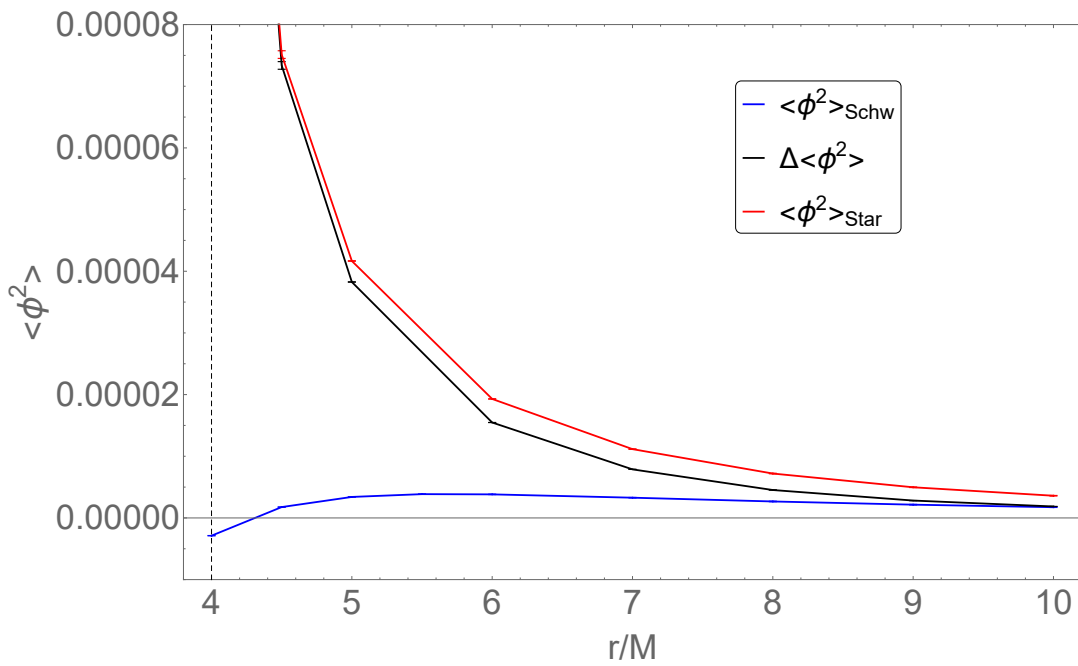


Figure 7.3.2:  $\langle \phi^2 \rangle$  outside a Schwarzschild black hole, outside a compact neutron star and  $\Delta \langle \phi^2 \rangle$  for minimal coupling  $\xi = 0$ . The vertical dashed line indicates the star surface at  $R = 4M$ .

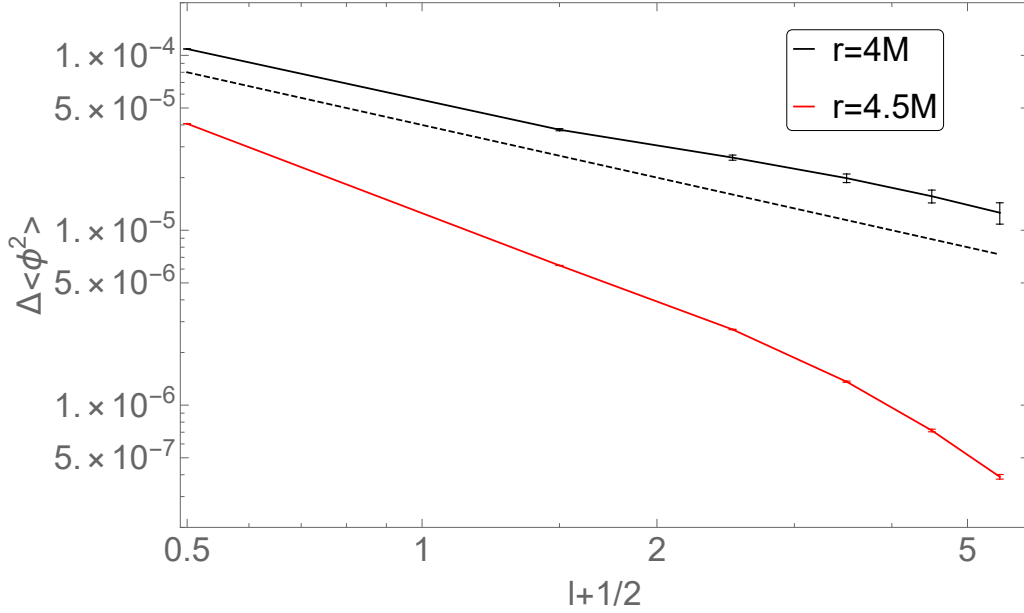


Figure 7.3.3: The magnitude of the contribution of each  $\ell$  mode to  $\Delta \langle \phi^2 \rangle$  outside a  $R = 4M$  compact neutron star for minimal coupling. The black dashed line is proportional to  $(\ell + 1/2)^{-1}$ .

the contribution to  $\Delta \langle \phi^2 \rangle$  from each  $\ell$  mode does not decay faster than  $(\ell + 1/2)^{-1}$ , which implies that the sum over the  $\ell$  modes does not converge, while for  $r > R$  the terms do decay fast enough for a convergent sum. This is similar behaviour to the shell model studied in Sec. 6.2, with the exception that each  $\ell$  mode contribution is itself finite on the star surface. A potential reason for this divergence of the sum over  $\ell$  could be a breakdown of our method to calculate  $\Delta \langle \phi^2 \rangle$  on the star surface caused by the violation of one of the assumptions made. Namely, that the spacetime of the star and the spacetime of the black hole are locally equivalent in a neighborhood of the point  $\Delta \langle \phi^2 \rangle$  is to be found.

### 7.3.1.2 $R = 2.26M$ (Ultra Compact Object)

Analogous results for an ultra compact object are presented in Figs. 7.3.4 and 7.3.5 for conformal and minimal coupling respectively. In both cases,  $\Delta \langle \phi^2 \rangle$  is everywhere positive and in the region  $r < 7M$  shown  $\Delta \langle \phi^2 \rangle$  once again dominates over  $\langle \phi^2 \rangle_{Schw}$ . In the case of conformal coupling  $\langle \phi^2 \rangle_{Star}$  once again monotonically increases on the approach to the UCO surface. Unlike the case of the larger compact object above, in the case of minimal coupling  $\langle \phi^2 \rangle_{Star}$  does not monotonically increase. Instead the radial derivative vanishes at approximately  $r \approx 3.5M$  before becoming negative. For the range of radii  $r_1 < r < r_2$  where  $r_1 \approx 2.4M$  and  $r_2 \approx 2.8M$ , we find that  $\langle \phi^2 \rangle_{Star} < 0$  with a

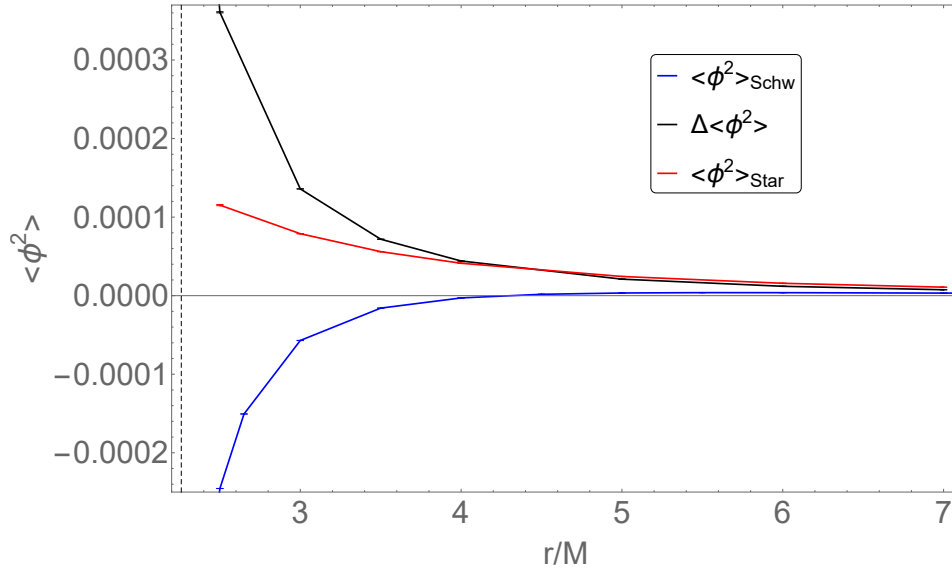


Figure 7.3.4:  $\langle \phi^2 \rangle$  outside a Schwarzschild black hole, outside an ultra compact object and  $\Delta \langle \phi^2 \rangle$  for conformal coupling  $\xi = 1/6$ . The vertical dashed line indicates the star surface at  $R = 2.26M$ .

local minimum at  $r \approx 2.5M$ . We cut off the plot of  $\langle \phi^2 \rangle_{Star}$  here, as it then sharply increases in the same manner that  $\Delta \langle \phi^2 \rangle$  does, which we believe is the consequence of a divergence on the star surface, which we will address shortly.

By comparing the two figures it can be seen that  $\Delta \langle \phi^2 \rangle$  is of the same order of magnitude for both minimal and conformal coupling. It would seem that for the ultra compact object the coupling term plays a much less important role in determining the magnitude of  $\langle \phi^2 \rangle_{Star}$ . This could perhaps be understood if we consider that by decreasing the radius  $R$  of the compact object we bring it closer to the Schwarzschild radius  $R_S = 2M$  at which point we would expect the behaviour of  $\langle \phi^2 \rangle$  to approach the behaviour of  $\langle \phi^2 \rangle_{Schw}$  which is independent of coupling. Another potential explanation comes from the fact that the coupling term is proportional to the Ricci scalar  $\mathcal{R}$  and so its influence on the value of  $\langle \phi^2 \rangle$  is proportional to the size of the spacetime region for which  $\mathcal{R} \neq 0$ , i.e., the region inside the star. Naturally, the size of this region shrinks as the star radius is decreased.

Once again, the value of  $\Delta \langle \phi^2 \rangle$  on the surface of the compact object is not shown, as we have numerical evidence that the sum over  $\ell$  when  $r = R$  does not converge, see Fig. 7.3.6.

Finally, we plot a direct comparison of  $\langle \phi^2 \rangle_{Star}$  between the minimal and conformal coupling cases for the compact neutron star in Fig. 7.3.7 and for the ultra compact object in Fig. 7.3.8. It is clear to see that for the neutron star,  $\langle \phi^2 \rangle_{Min} > \langle \phi^2 \rangle_{Con}$  while for the ultra compact object the

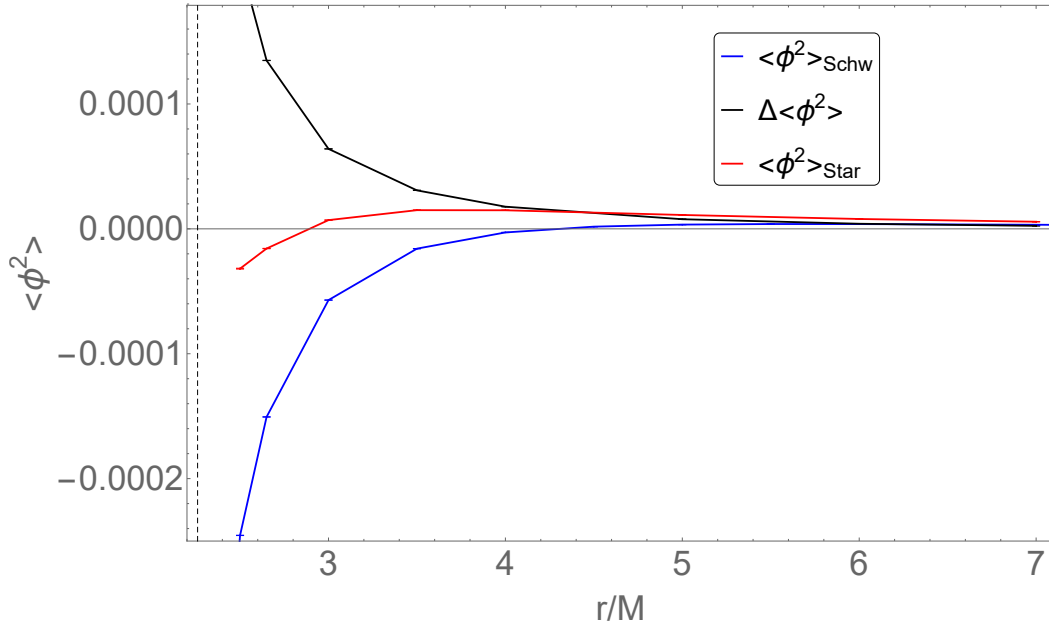


Figure 7.3.5:  $\langle \phi^2 \rangle$  outside a Schwarzschild black hole, outside an ultra compact object and  $\Delta \langle \phi^2 \rangle$  for minimal coupling. The vertical dashed line indicates the star surface at  $R = 2.26M$ .

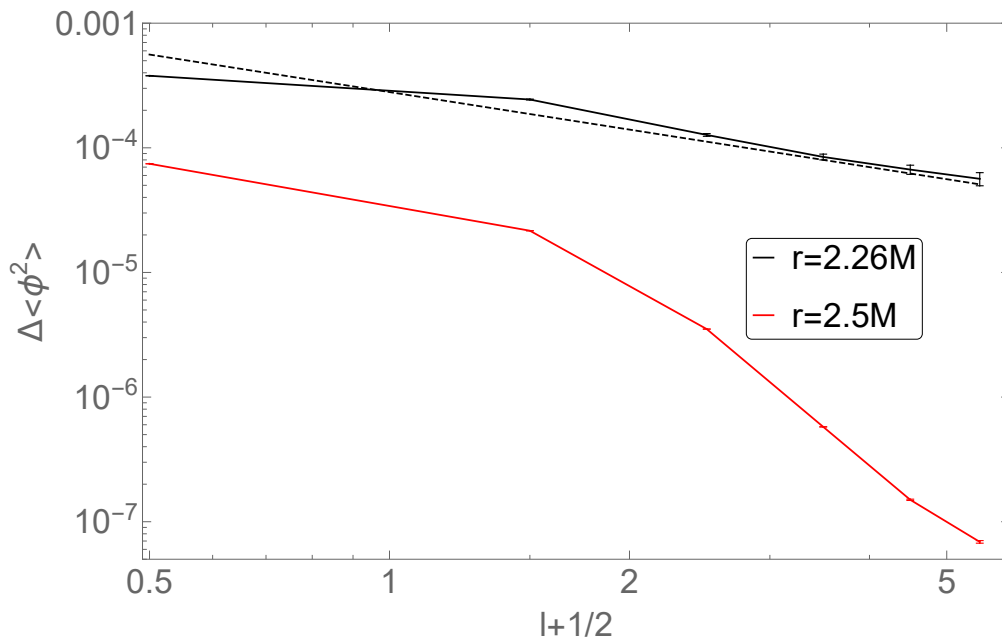


Figure 7.3.6: The magnitude of the contribution of each  $\ell$  mode to  $\Delta \langle \phi^2 \rangle$  outside a  $R = 2.26M$  ultra compact object for minimal coupling. The black dashed line is proportional to  $(\ell + 1/2)^{-1}$ .

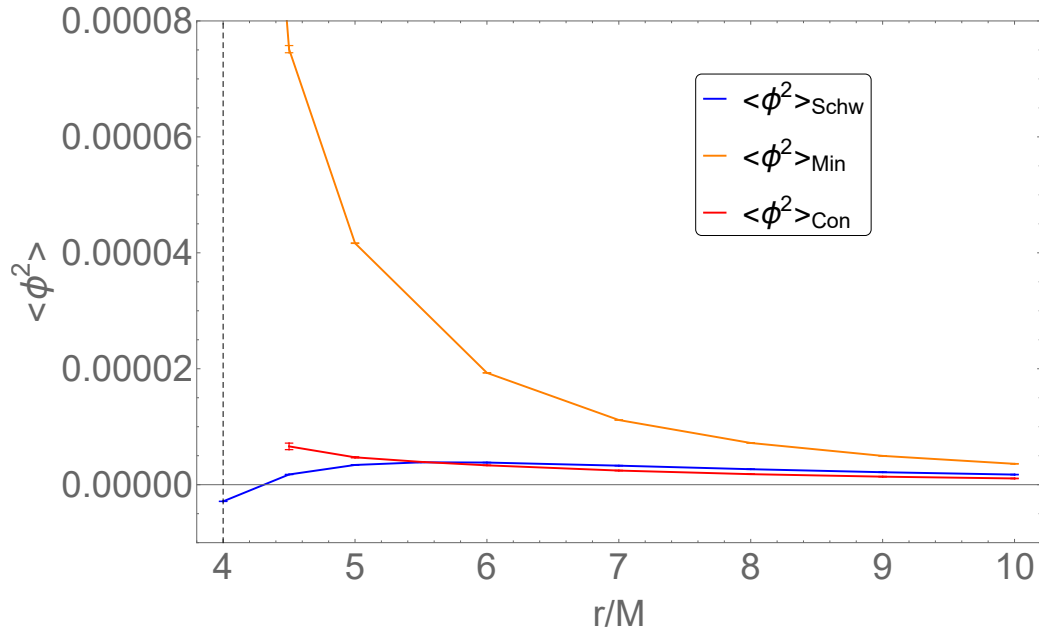


Figure 7.3.7:  $\langle \phi^2 \rangle$  outside a Schwarzschild black hole and outside a compact neutron star for minimal and conformal coupling. The vertical dashed line indicates the star surface at  $R = 4M$ .

opposite is true.

## 7.3.2 Stress-Energy Tensor Near a Compact Object

### 7.3.2.1 $R = 4M$ (Compact Neutron Star)

We now repeat the analysis of the previous section, but applied to the stress-energy difference  $\Delta \langle T^\mu_\nu \rangle$ . The three non-trivial, independent components of the stress-energy difference (given by Eqs. (6.1.17)-(6.1.19)) outside a compact neutron star for conformal and minimal coupling are shown in Fig. 7.3.9 and Fig. 7.3.10 respectively. In the conformal coupling case, the temporal and radial components are positive while the angular components are negative. In the minimal coupling case, the radial component is positive while the temporal and angular components are negative and further from the star we have the approximate relation  $\Delta \langle T^t_t \rangle \approx -\Delta \langle T^r_r \rangle$ . We will revisit this relation in Sec. 7.4 when we consider  $\Delta \langle T^\mu_\nu \rangle$  in the far field numerically.

We take particular note of the behaviour of  $\Delta \langle T^t_t \rangle$ . The sign of this component depends on the value of coupling chosen, unlike the other two components whose signs remain the same. This is another property that we will revisit when we come to discuss the far field limit numerically.

As  $\Delta \langle \phi^2 \rangle$  diverges on the star surface, it is unsurprising to find that  $\Delta \langle T^\mu_\nu \rangle$  does also, as shown

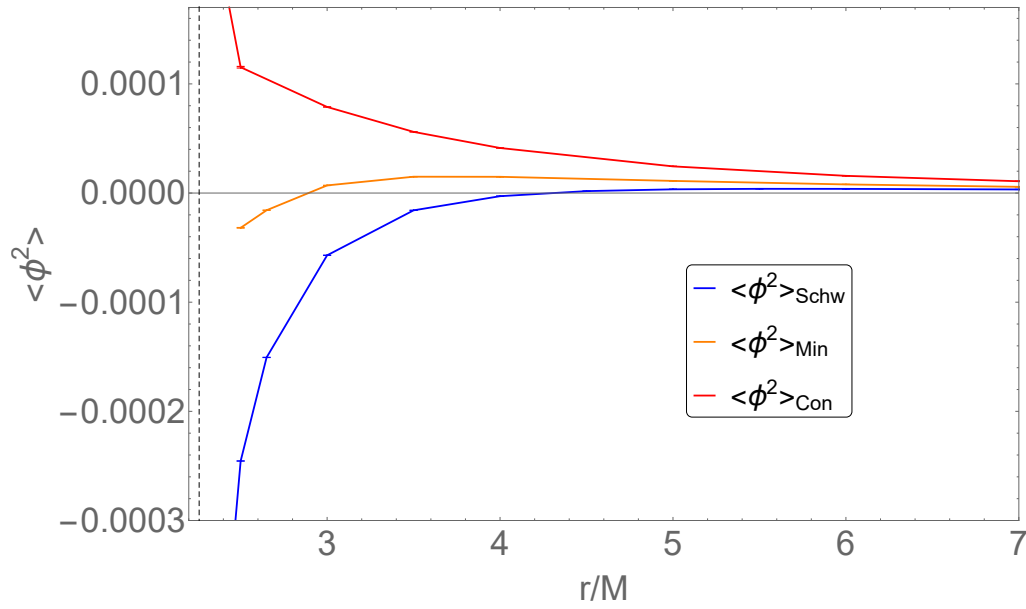


Figure 7.3.8:  $\langle \phi^2 \rangle$  outside a Schwarzschild black hole and outside an ultra compact object for minimal and conformal coupling. The vertical dashed line indicates the star surface at  $R = 2.26M$ .

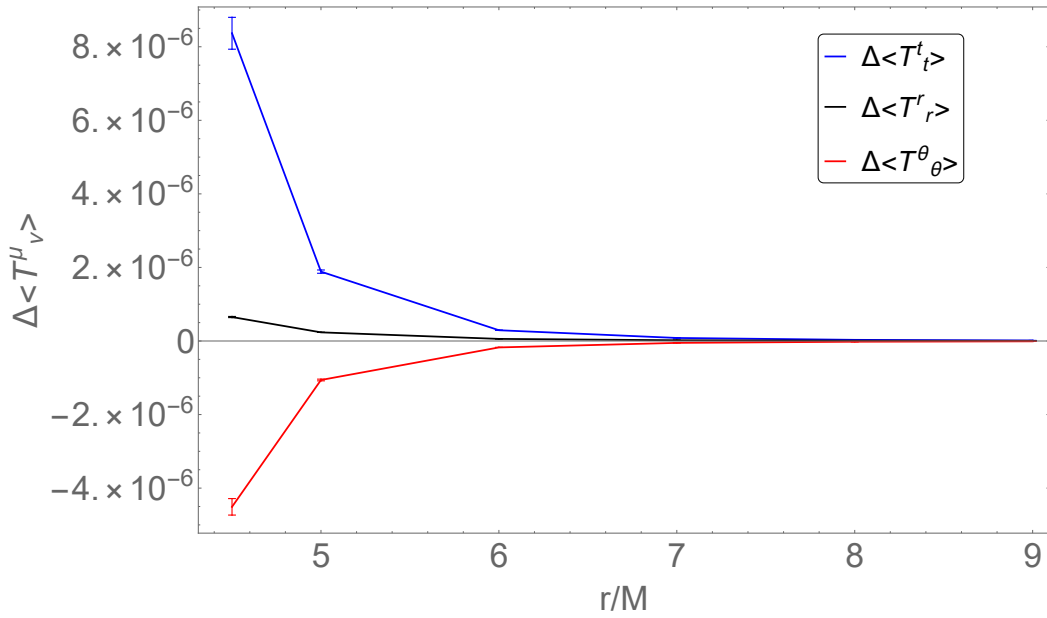


Figure 7.3.9:  $\Delta \langle T^\mu{}_\nu \rangle$  outside a compact neutron star of radius  $R = 4M$  for conformal coupling  $\xi = 1/6$ .

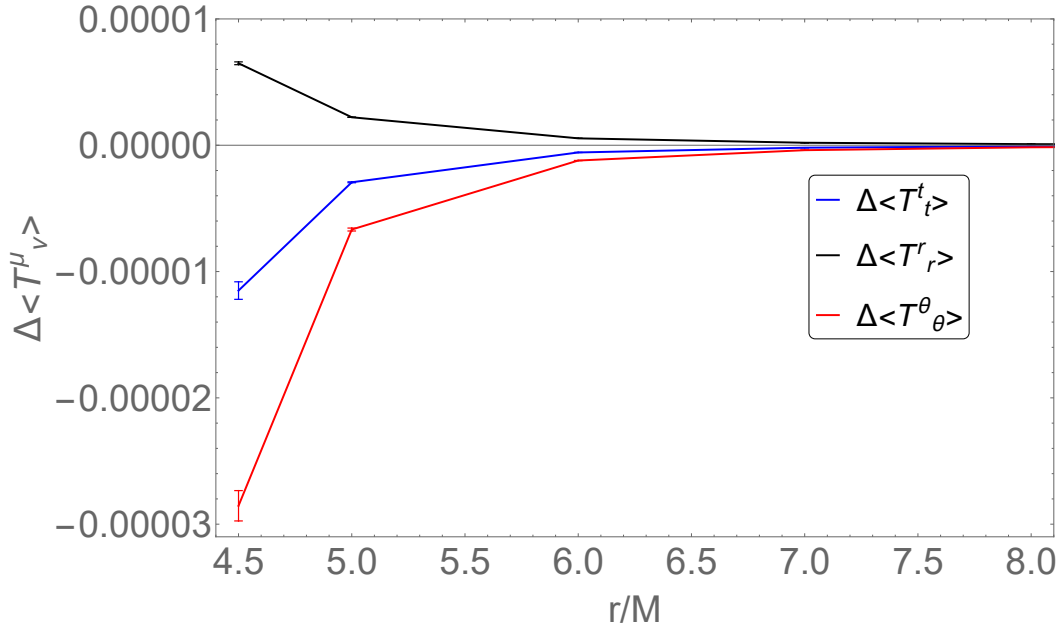


Figure 7.3.10:  $\Delta\langle T^\mu_\nu\rangle$  outside a compact neutron star of radius  $R = 4M$  for minimal coupling.

in Fig. 7.3.11. The divergence is much more severe than that of  $\Delta\langle\phi^2\rangle$ . In fact, the numerical evidence indicates that the individual terms of the sum over  $\ell$  are not decreasing.

This can be explained by considering each of the five integrals that form  $\Delta\langle T^\mu_\nu\rangle$  individually, Eqs. (6.1.12)-(6.1.16), in particular we note that  $\Delta s_3 = (\ell + 1/2)^2 \Delta s_5$  will diverge like  $\ell + 1/2$  on the star surface. We will look closer at this in the next subsection, where we present results for the ultra compact object.

### 7.3.2.2 $R = 2.26M$ (Ultra Compact Object)

$\Delta\langle T^\mu_\nu\rangle$  outside an ultra compact object for conformal and minimal coupling are shown in Fig. 7.3.12 and Fig. 7.3.13 respectively. For conformal coupling, swapping the compact neutron star for an ultra compact object has changed the sign of  $\Delta\langle T^r_r\rangle$  near the star surface, while this is not the case for minimal coupling. We look closer at this in the next subsection.

Another effect of decreasing  $R$ , for conformal coupling only, is that the temporal and radial components no longer have a fixed sign. In the direction of decreasing  $r$ , the temporal component's sign changes from negative to positive between  $r = 5M$  and  $r = 4M$  while the angular component's sign changes from positive to negative between  $r = 4M$  and  $r = 3.5M$ . This cannot be seen in Fig. 7.3.12, but is shown in Table 7.1.

Next, in Fig. 7.3.14 we show the contributions from each  $\ell$  mode to  $\Delta\langle T^t_t\rangle$  both on the UCO

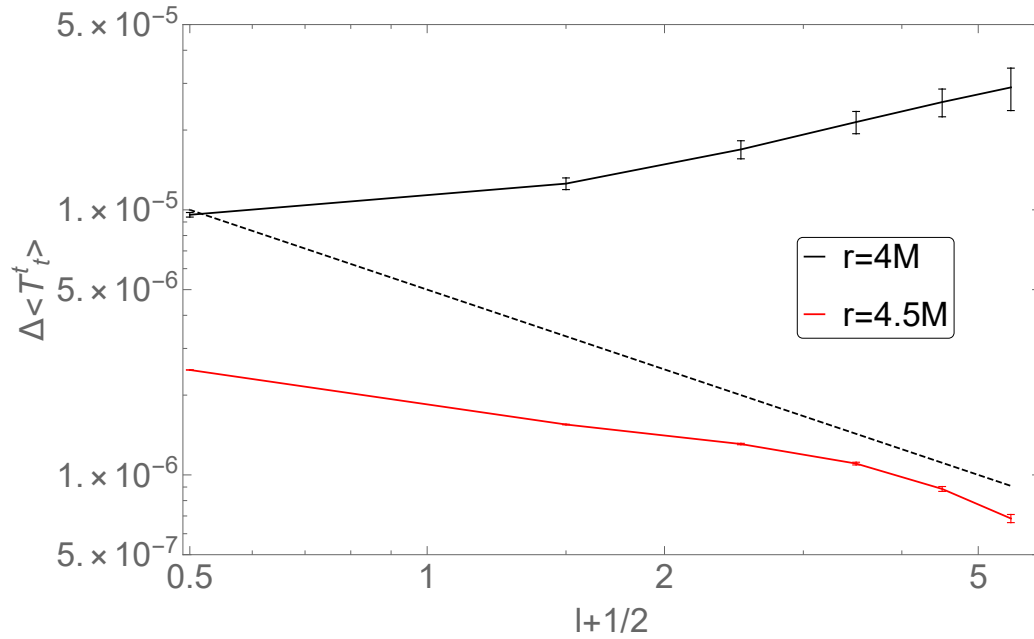


Figure 7.3.11: The magnitude of the contribution of each  $\ell$  mode to  $\Delta\langle T^t_t \rangle$  outside a  $R = 4M$  compact neutron star for minimal coupling. The black dashed line is proportional to  $(\ell + 1/2)^{-1}$ .

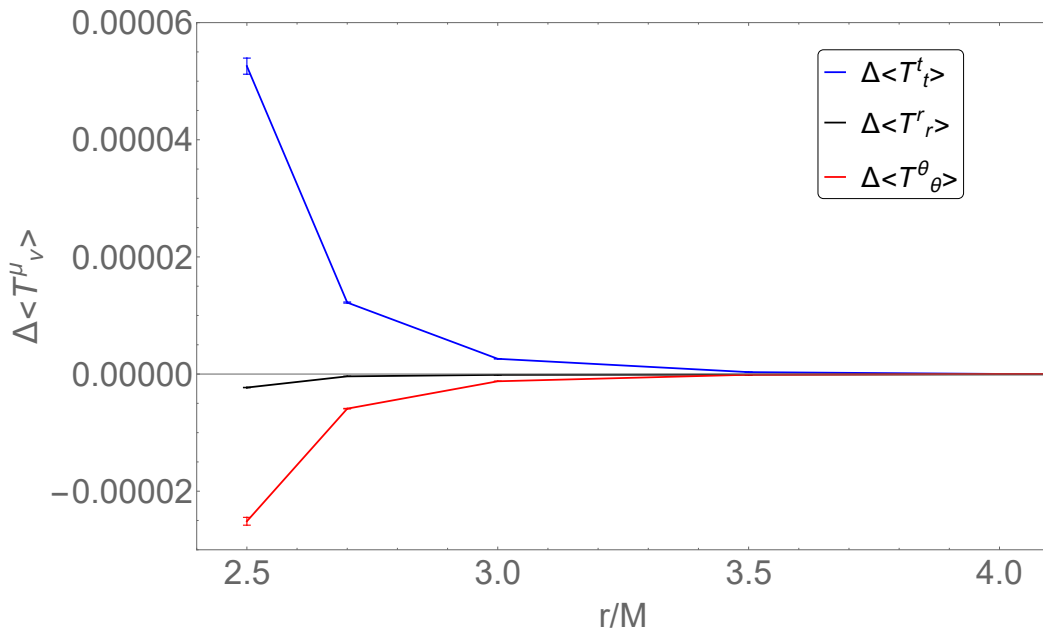


Figure 7.3.12:  $\Delta\langle T^\mu_\nu \rangle$  outside a constant density ultra compact object of radius  $R = 2.26M$  for conformal coupling  $\xi = 1/6$ .

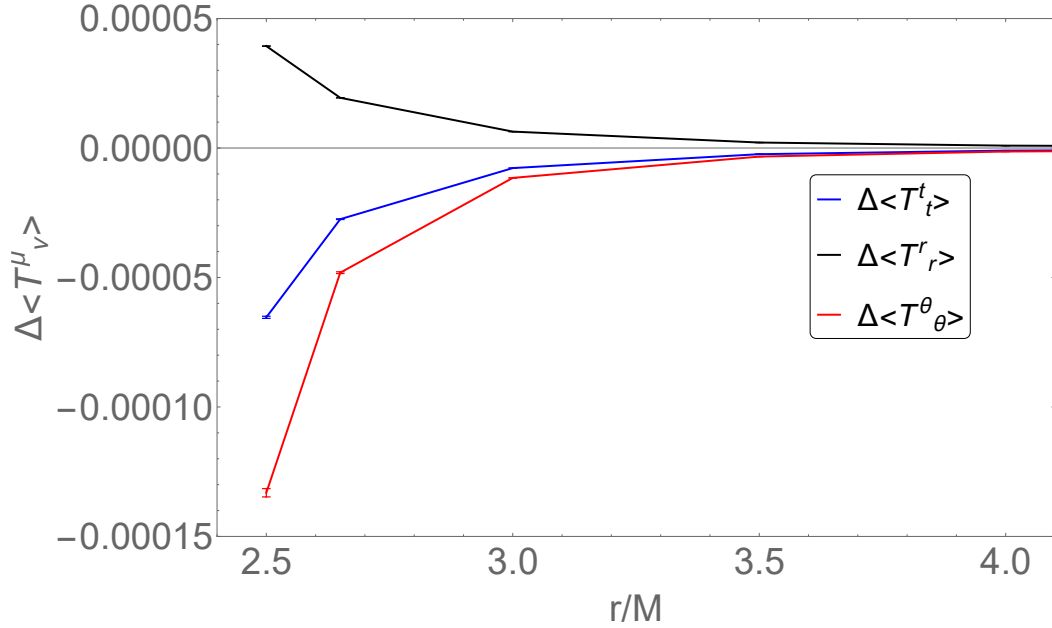


Figure 7.3.13:  $\Delta \langle T^\mu_\nu \rangle$  outside a constant density ultra compact object of radius  $R = 2.26M$  for minimal coupling.

$r/M$	$\Delta \langle T^t_t \rangle$	$\Delta \langle T^r_r \rangle$	$\Delta \langle T^\theta_\theta \rangle$
2.5	$(2.47 \pm 0.14) \times 10^{-5}$	$(-1.08 \pm 0.04) \times 10^{-6}$	$(-1.18 \pm 0.07) \times 10^{-5}$
2.7	$(3.80 \pm 0.10) \times 10^{-6}$	$(-1.219 \pm 0.010) \times 10^{-7}$	$(-1.84 \pm 0.05) \times 10^{-6}$
3.0	$(5.10 \pm 0.05) \times 10^{-7}$	$(-2.7133 \pm 0.0035) \times 10^{-8}$	$(-2.414 \pm 0.023) \times 10^{-7}$
3.5	$(3.672 \pm 0.009) \times 10^{-8}$	$(-1.0524 \pm 0.0004) \times 10^{-8}$	$(-1.310 \pm 0.005) \times 10^{-8}$
4.0	$(1.575 \pm 0.004) \times 10^{-9}$	$(-4.6460 \pm 0.0014) \times 10^{-9}$	$(1.5354 \pm 0.0023) \times 10^{-9}$
5.0	$(-1.26459 \pm 0.00007) \times 10^{-9}$	$(-1.0688 \pm 0.0004) \times 10^{-9}$	$(1.16672 \pm 0.00015) \times 10^{-9}$
6.0	$(-4.91403 \pm 0.00019) \times 10^{-10}$	$(-3.0482 \pm 0.0013) \times 10^{-10}$	$(3.9811 \pm 0.0006) \times 10^{-10}$
7.0	$(-1.88586 \pm 0.00007) \times 10^{-10}$	$(-1.0345 \pm 0.0006) \times 10^{-10}$	$(1.46019 \pm 0.00025) \times 10^{-10}$

Table 7.1: The three independent components of  $\Delta \langle T^\mu_\nu \rangle$  and their error estimates outside a radius  $R = 2.26M$  ultra compact object for conformal coupling  $\xi = 1/6$ .

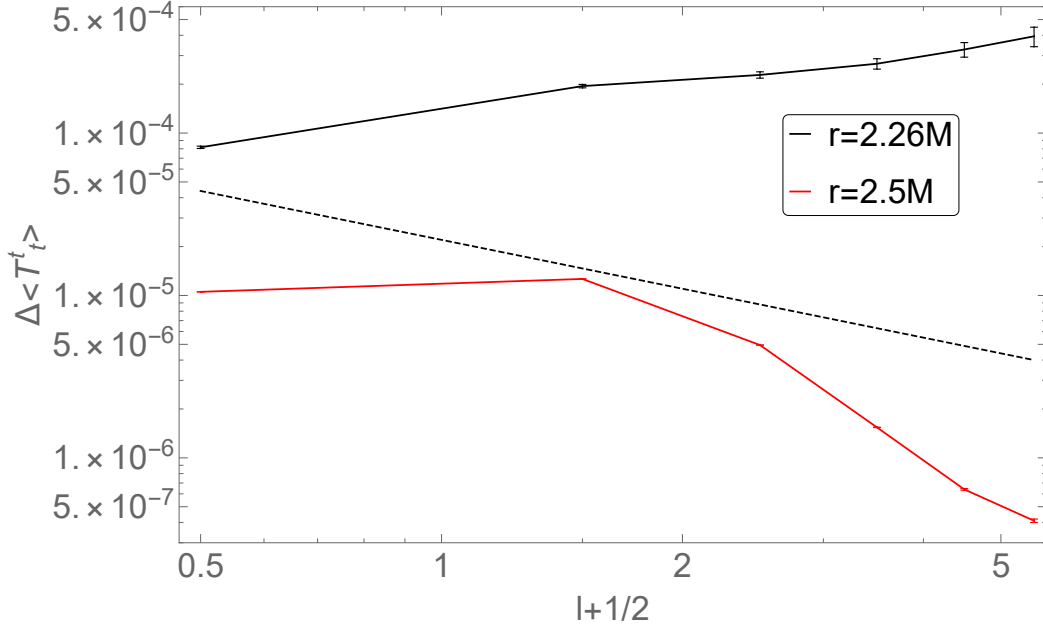


Figure 7.3.14: The magnitude of the contribution of each  $\ell$  mode to  $\Delta \langle T_t^t \rangle$  outside a  $R = 2.26M$  ultra compact object for minimal coupling. The black dashed line is proportional to  $(\ell + 1/2)^{-1}$ .

surface and near the surface. The behaviour is qualitatively similar to the case of a  $R = 4M$  star (Fig. 7.3.11), where the terms in the summand increase in magnitude with  $\ell$  on the star surface and decrease off the star surface.

To look closer at the source of this divergence of the sum over  $\ell$  on the star surface, we consider  $\Delta s_3$ , defined in Eq.(6.1.14), in the case of minimal coupling, plotted in the small  $\omega$  regime in Fig. 7.3.15. We have scaled the frequency axis by  $(\ell + 1/2)^{-1}$  to bring the peak of each integrand into a similar position. We can see that for  $\omega/(\ell + 1/2) > \omega_{peak} \approx 0.15$  the integrands appear to asymptotically approach a “universal curve” as  $\ell$  increases. This also holds for  $\Delta s_1$  and  $\Delta s_2$ : the other two summands with terms that increase as  $\ell$  increases. This is not the case for  $\Delta s_4$  and  $\Delta s_5$ , the summands with terms that decrease with  $\ell$ , but not fast enough to ensure convergence.

### 7.3.2.3 Comparison

Of the four cases considered (two values of  $R$ , two values of  $\xi$ ), the fact that  $\Delta \langle T_r^r \rangle < 0$  on the approach to the star surface only for the compact neutron star with conformal coupling, see Fig. 7.3.12, warrants further examination. Equation (6.1.18) expresses  $\Delta \langle T_r^r \rangle$  in terms of the five integrals labeled  $\Delta S_i$ . Since this expression is a linear combination of the  $\Delta S_i$  with coefficients that are independent of  $\omega$  we can instead consider it as a single integral. This integrand for  $\xi = 1/6$

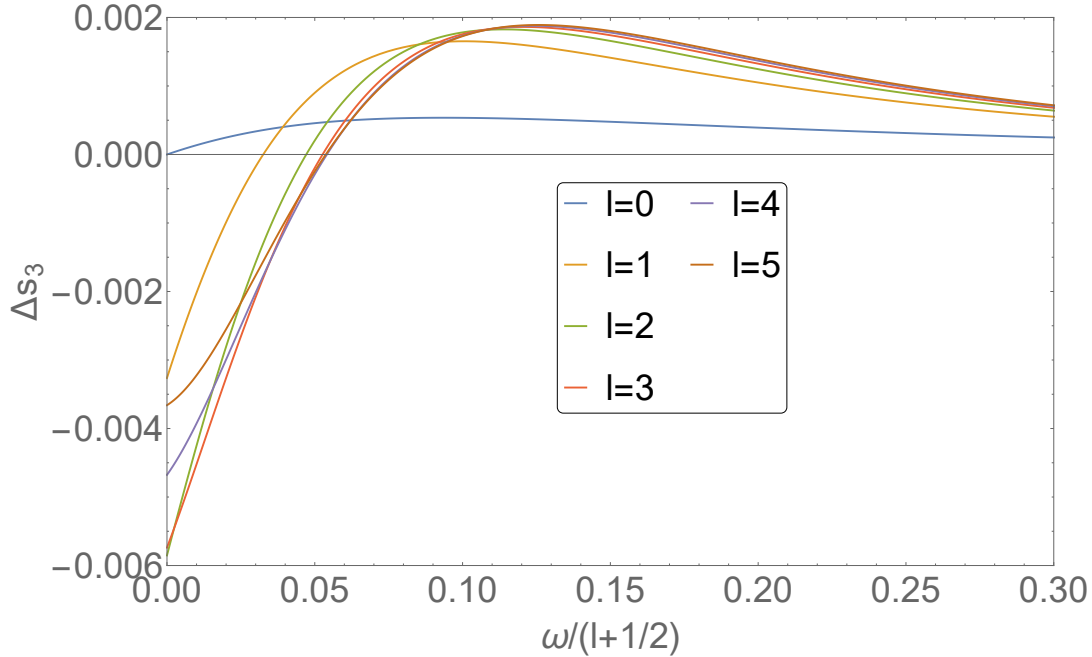


Figure 7.3.15:  $\Delta s_3$  on the surface of a  $R = 2.26M$  ultra compact object with minimal coupling, as a function of  $\omega/(\ell + 1/2)$  for various  $\ell$ .

is plotted in Figs. 7.3.16 and 7.3.17 for the compact neutron star and the ultra compact object respectively. Directly comparing the two, we can see that the change of sign in  $\Delta \langle T_r^r \rangle$  comes almost entirely from a drastic change in behaviour of the  $\ell = 0$  mode when the star radius is decreased.

## 7.4 Numerical Analysis Far From the Star Surface

### 7.4.1 Vacuum Polarization

The numerical method described in Sec. 7.2 is applicable to all ranges of  $r$  and so can also be used to calculate  $\Delta \langle \phi^2 \rangle$  and  $\Delta \langle T^\mu_\nu \rangle$  far from the star. We will use this to test the validity of the approximate expressions given in Eqs. (7.1.11) and (7.1.13). In particular, we only need to numerically calculate the  $\ell = 0$  contribution to both quantities, as this was all that was required to generate the leading order analytical approximation. For  $\Delta \langle \phi^2 \rangle$  these results are presented for the compact neutron star of radius  $R = 4M$  in Fig. 7.4.1 and for the ultra compact object of radius  $R = 2.26M$  in Fig. 7.4.2. On both figures data is shown for both minimal and conformal coupling.

It can be seen that for  $\xi = 0$ ,  $\Delta \langle \phi^2 \rangle$  scales like  $r^{-4}$  in the far field. This is numerical evidence that the universality result reported by [7] (i.e., the vanishing of  $\Delta \langle \phi^2 \rangle$  for minimal coupling) is only valid to leading order in  $r^{-1}$ . For  $\xi = 1/6$ , outside of both a compact neutron star and an ultra

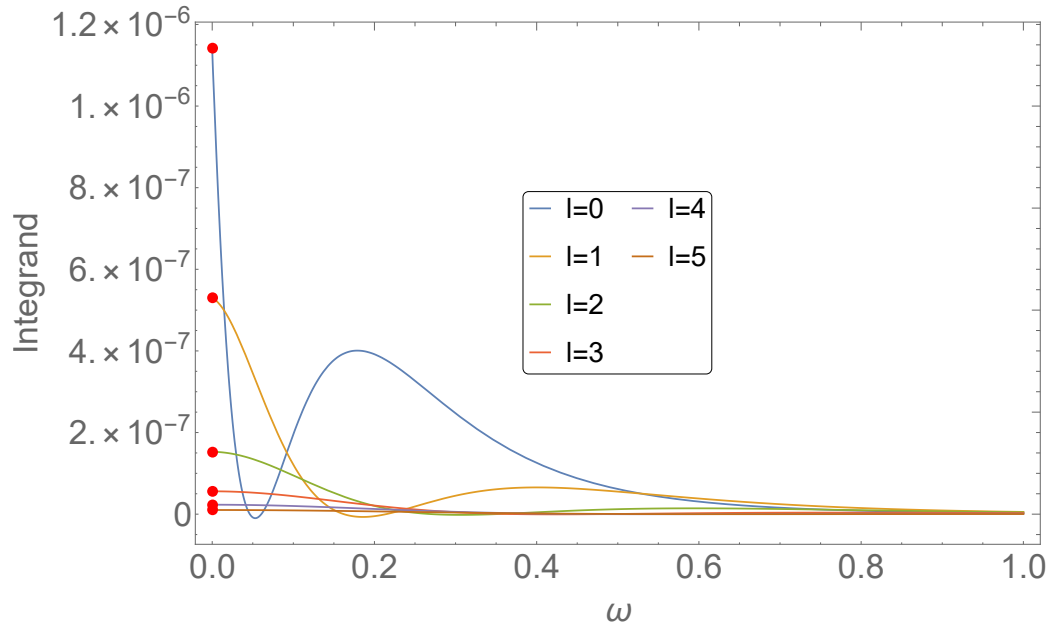


Figure 7.3.16: The integrand of Eq. (6.1.18) for  $R = 4M, r = 5M, \xi = 1/6$ . The solid red dots are the  $\omega = 0$  values of the integrand, calculated using the known static solutions for  $p_S$  and  $q_S$  in terms of Legendre functions, Eqs. (7.1.4) and (7.1.5).

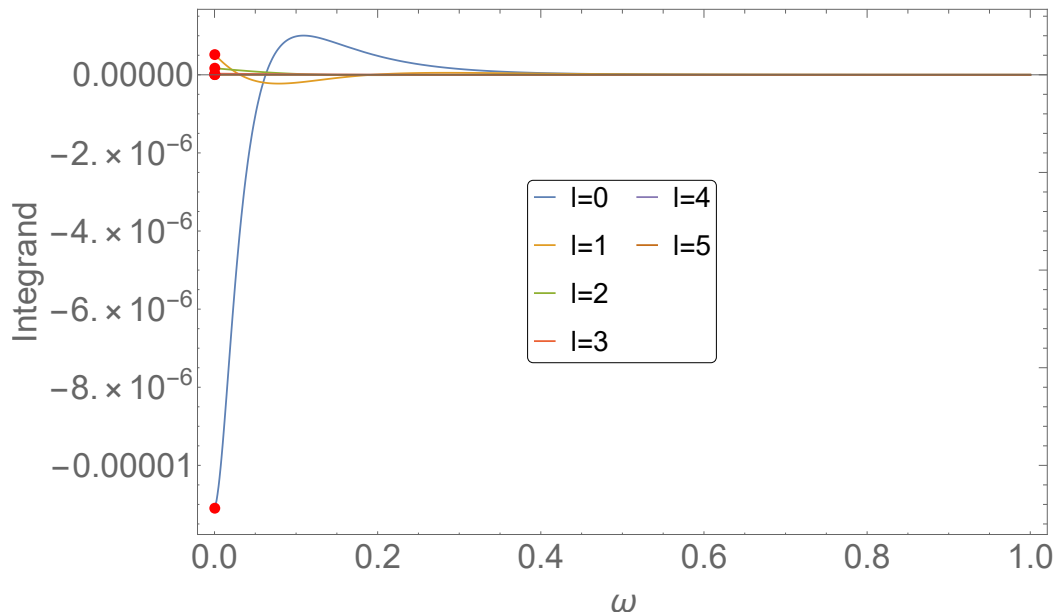


Figure 7.3.17: The integrand of Eq. (6.1.18) for  $R = 2.26M, r = 3M, \xi = 1/6$ . The solid red dots are the  $\omega = 0$  values of the integrand, calculated using the known static solutions for  $p_S$  and  $q_S$  in terms of Legendre functions, Eqs. (7.1.4) and (7.1.5).

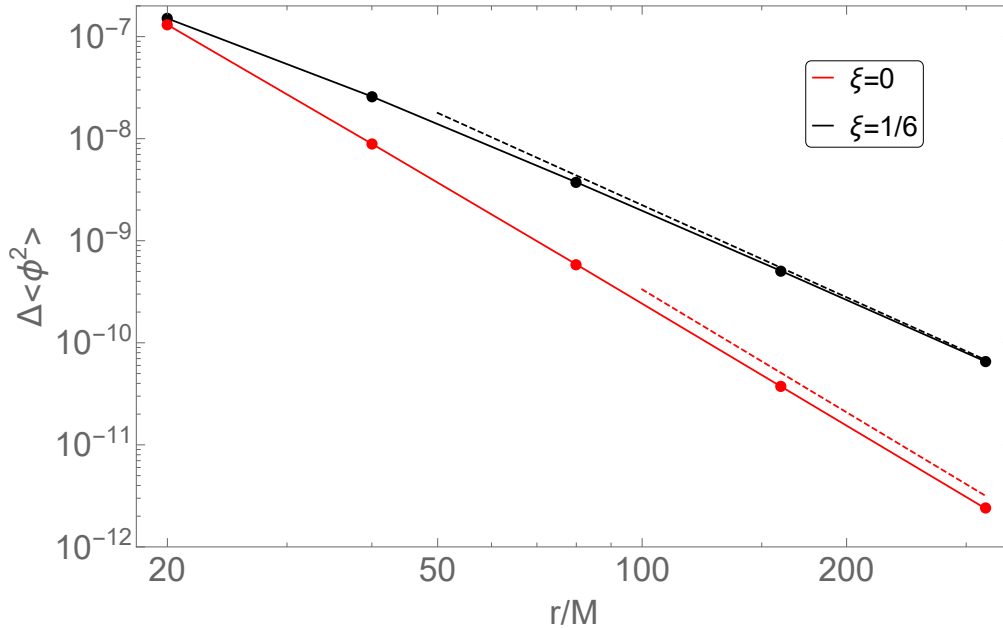


Figure 7.4.1: The  $\ell = 0$  contribution to  $\Delta \langle \phi^2 \rangle$  outside a  $R = 4M$  star, for minimal and conformal coupling. The black dashed line is determined by Eq. (7.1.11) with seven terms in the structure function series. The red dashed line is proportional to  $r^{-4}$ .

compact object  $\Delta \langle \phi^2 \rangle$  scales like  $r^{-3}$  (as [7] originally predicted).

For  $R = 4M$  the  $r^{-3}$  coefficient matches well with our new result in Eq. (7.1.11). In fact, this agreement seems to hold for any  $R$  that is sufficiently large, as shown in Fig. 7.4.3.

On the other hand, Eq. (7.1.11) does not accurately predict the  $r^{-3}$  coefficient of  $\Delta \langle \phi^2 \rangle$  far from an ultra compact object. Considering the behaviour of the structure function, Eq. (7.1.12), for different values of its argument  $M/R$  helps to highlight why. The partial sums of the terms in the structure function are shown in Fig. 7.4.4 and for the ultra compact object it is unclear if the sum converges. We hypothesise that the underlying problem is that the derivation of Eq. (7.1.11) requires the evaluation of the function  $q_{static}$  on the star surface, see Eqs. (6.1.8) and (6.1.9). However, the validity of  $q_{static}$  (see Eq. (7.1.5)) as an approximate solution when  $r = R$  to the static, radial differential equation in Schwarzschild spacetime (Eq. (6.1.4) with  $\omega = 0$  and  $f = h^{-1} = 1 - 2M/r$ ) breaks down when  $R$  is too small. Hence, our result in Eq. (7.1.11) also becomes invalid if  $R$  is too small.

We can continue this analysis beyond the leading order in  $r^{-1}$  by looking at higher order  $\ell$  modes. The analytical approximation in the far field for these modes comes from Eqs. (7.1.17), (7.1.18) and for  $\ell = 1$ , Eq. (7.1.20). An example comparison is plotted in Fig. 7.4.5, showing the expected  $r^{-5}$

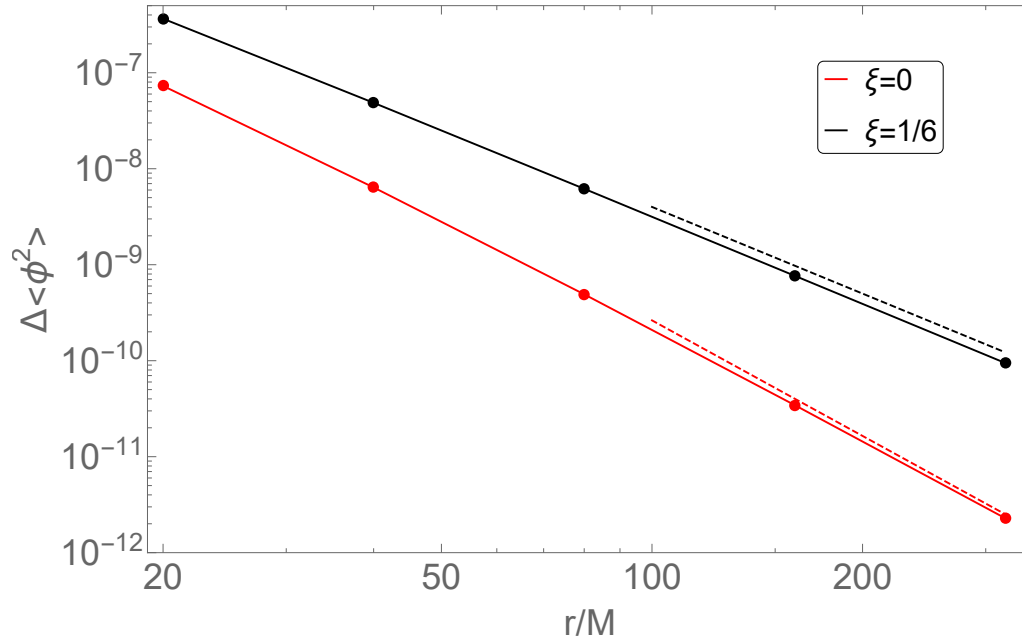


Figure 7.4.2: The  $\ell = 0$  contribution to  $\Delta \langle \phi^2 \rangle$  outside a  $R = 2.26M$  ultra compact object, for minimal and conformal coupling. The black dashed line is proportional to  $r^{-3}$  and the red dashed line is proportional to  $r^{-4}$ .

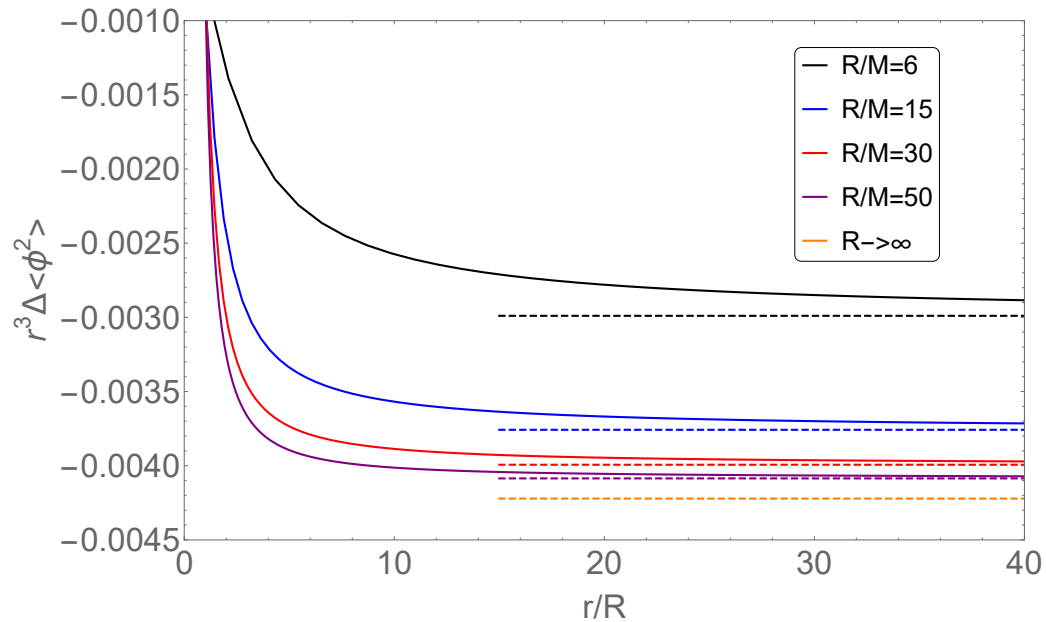


Figure 7.4.3: The  $\ell = 0$  mode of  $\Delta \langle \phi^2 \rangle$ , for  $\xi = 1/6$  and for various values of  $R$ . The solid lines are obtained by the numerical method, the dashed lines are the analytical approximations of Eq. (7.1.11).  $R \rightarrow \infty$  indicates the weak field limit derived in [7], see Eq. (6.1.29).

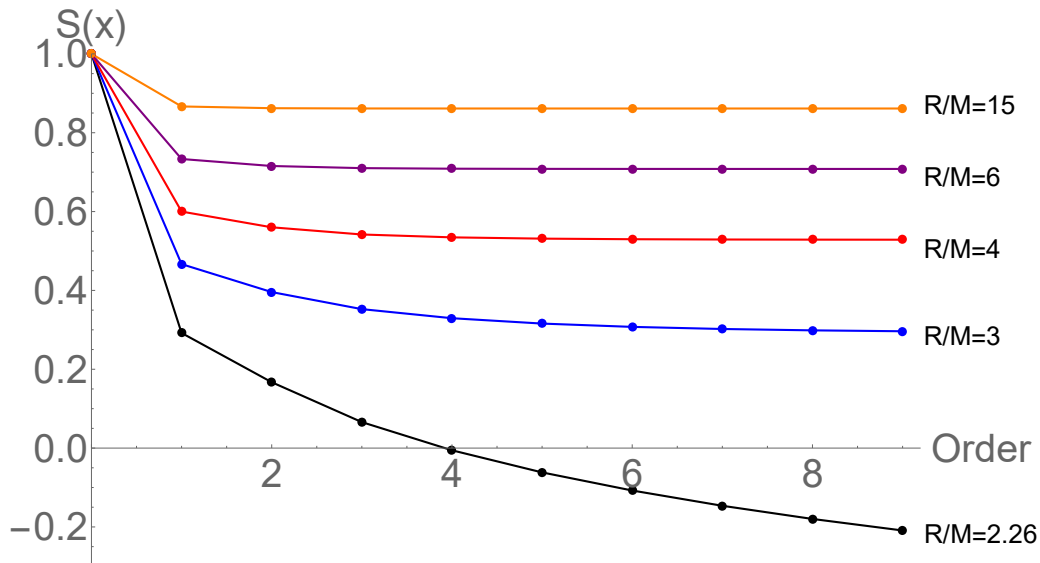


Figure 7.4.4: The value of the structure function  $\mathcal{S}_0(x)$  in Eq. (7.1.12) as we increase the number of terms in the series, for various star radii.

scaling for large  $r$ .

## 7.4.2 Stress-Energy Tensor

We now consider the far field behaviour of the stress-energy difference  $\Delta \langle T^\mu_\nu \rangle$ . In Fig. 7.4.6 all three independent components of the difference are shown in the far field limit for a compact neutron star of radius  $R = 4M$ , for a coupling that is neither minimal nor conformal ( $\xi = 1/12$ ) so that our result in Eq. (7.1.13) can be used. We see that  $\Delta \langle T^\mu_\nu \rangle$  scales like  $r^{-5}$  in a manner that agrees with (7.1.13). We also tested this for the single component  $\Delta \langle T^t_t \rangle$  on the spacetimes of larger radii stars, with the results shown in Fig. 7.4.7.

For the two special values  $\xi = 0$  and  $\xi = 1/6$  the far field asymptotic approximation of Eq. (7.1.13) vanishes.  $\Delta \langle T^\mu_\nu \rangle$  for both minimal and conformal coupling far away from a  $R = 4M$  compact neutron star is plotted in Figs. 7.4.8 and 7.4.9 respectively and it can be seen that in both cases it scales like  $r^{-6}$ . This means that, as found for the vacuum polarization, universality of the stress-energy in the far field is only valid to leading order in  $r^{-1}$ .

In the case of minimal coupling we note that  $\Delta \langle T^t_t \rangle = -\Delta \langle T^r_r \rangle$  and it is clear to see why this is from Eqs. (6.1.17) and (6.1.18) when  $\xi = \ell = 0$ . The data also shows, for minimal coupling, that as  $r$  grows,  $\Delta \langle T^\theta_\theta \rangle \rightarrow 2\Delta \langle T^t_t \rangle$  and so we can write down the general behaviour of the stress-energy difference for minimal coupling in the far field limit:  $\Delta \langle T^\mu_\nu \rangle \approx -0.075r^{-6} \text{diag}[1, -1, 2, 2]$ . This contrasts with the behaviour for when the coupling is not equal to zero or  $1/6$ , which was

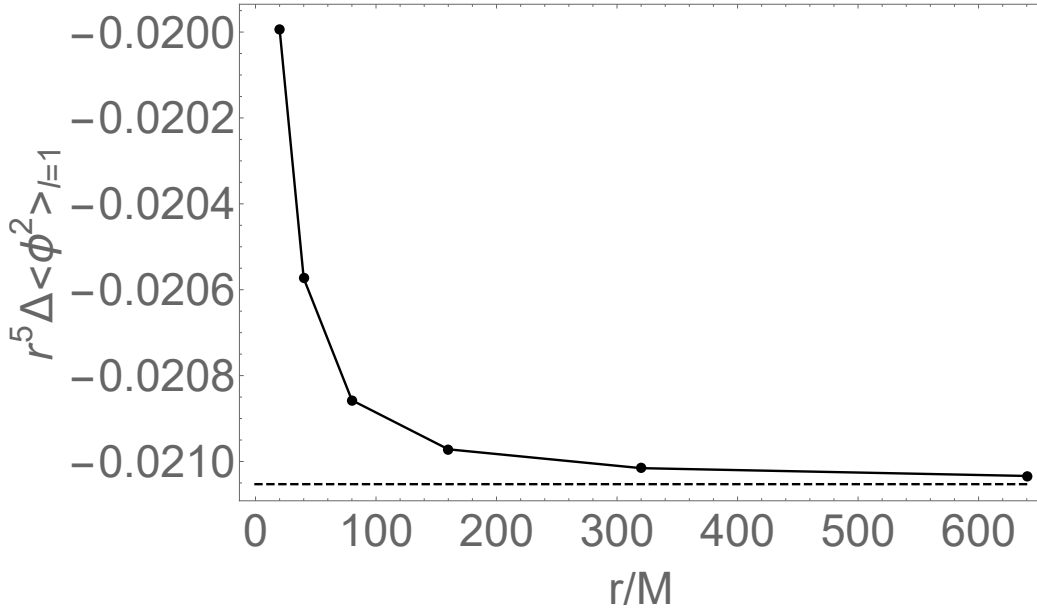


Figure 7.4.5: The  $\ell = 1$  contribution to  $\Delta \langle \phi^2 \rangle$  (solid line) for  $\xi = 1/6$  and  $R = 4M$ , compared with the analytical approximation in the far field (dashed line) obtained from (7.1.17), (7.1.18) and (7.1.20), with eight terms in the structure function series.

$$\Delta \langle T^\mu_\nu \rangle \sim -r^{-5} \text{diag}[2, -2, 3, 3].$$

For conformal coupling there isn't a clear integer-multiple relationship between the components in the far field like there was for minimal coupling. We do however, notice that the sign of  $\Delta \langle T^t_t \rangle$  depends on the choice of coupling, like it did near the star surface in Figs. 7.3.9 and 7.3.10. The  $r^{-6}$  coefficient in the far field is approximately  $0.002 \times \text{diag}[9, 1, -5, -5]$ .

## Conclusion

Vacuum polarization differences and stress-energy differences between spherically symmetric stars and black holes were considered numerically both near the star surface and in the far field limit. In the latter case, the numerical results were compared to analytical approximations and good agreement was found when  $R \geq 3M$ , i.e. when the star radius was not close to the Buchdahl limit  $R = \frac{9}{4}M$ .

We found that the magnitude of  $\langle \phi^2 \rangle$  near the surface of a star becomes more dependent on coupling  $\xi$  as the size of the star increases. For an ultra compact object, the surface values of  $\langle \phi^2 \rangle$  for both minimal and conformal coupling were of the same order of magnitude, although the qualitative

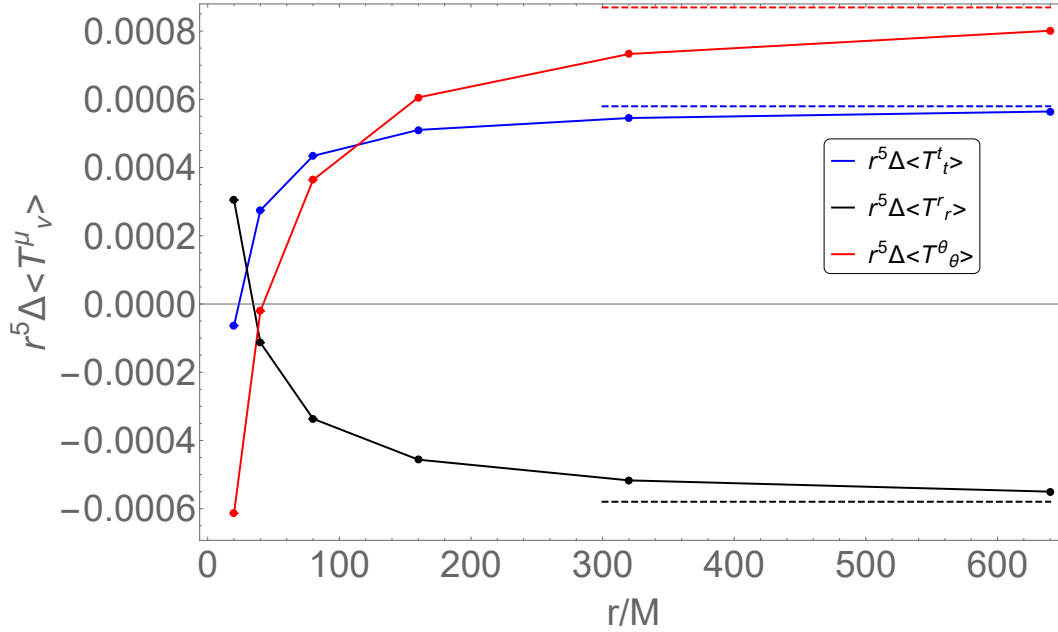


Figure 7.4.6: The  $\ell = 0$  contribution to  $\Delta \langle T^\mu_\nu \rangle$  outside a  $R = 4M$  compact neutron star, for  $\xi = 1/12$ . The dashed lines are determined from Eq.(7.1.13) with seven terms in the structure function series.

features on the approach to the star surface were different, see Fig. 7.3.8.

In addition, it was shown that the universality results proven by Anderson and Fabbri in [7] only hold to leading order in  $r^{-1}$ , by performing a numerical calculation in the far field limit for values of  $\xi$  such that the leading order result vanishes.

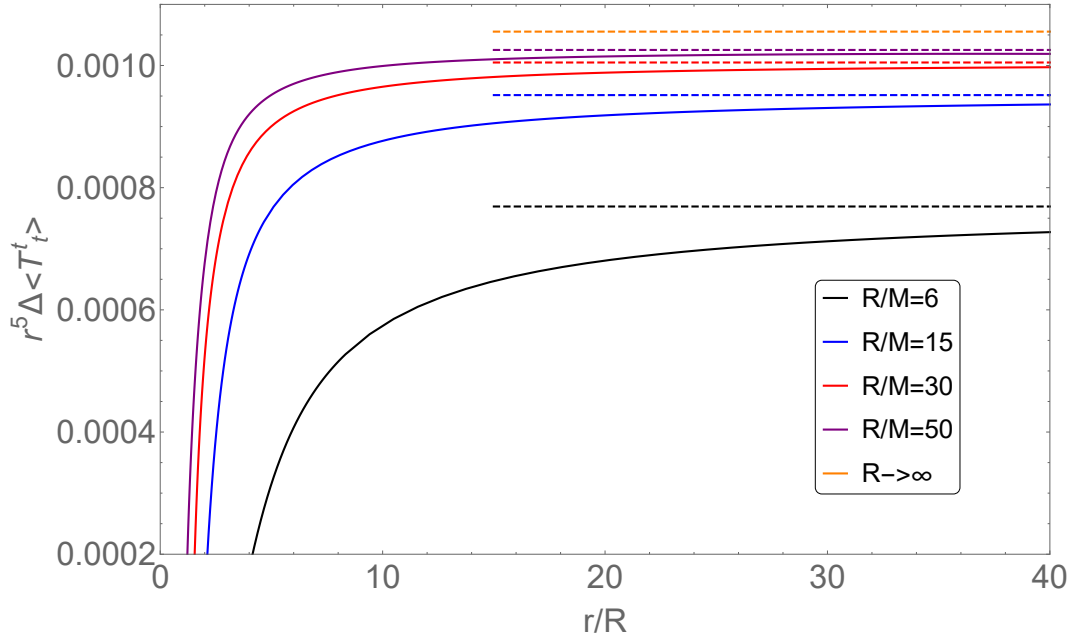


Figure 7.4.7: The  $\ell = 0$  mode of  $\Delta \langle T_t^t \rangle$ , for  $\xi = 1/12$  and for various values of  $R$ . The solid lines are obtained by the numerical method, the dashed lines are the analytical approximations of Eq. (7.1.13).  $R \rightarrow \infty$  indicates the weak field limit derived in [7], see Eq. (6.1.31).

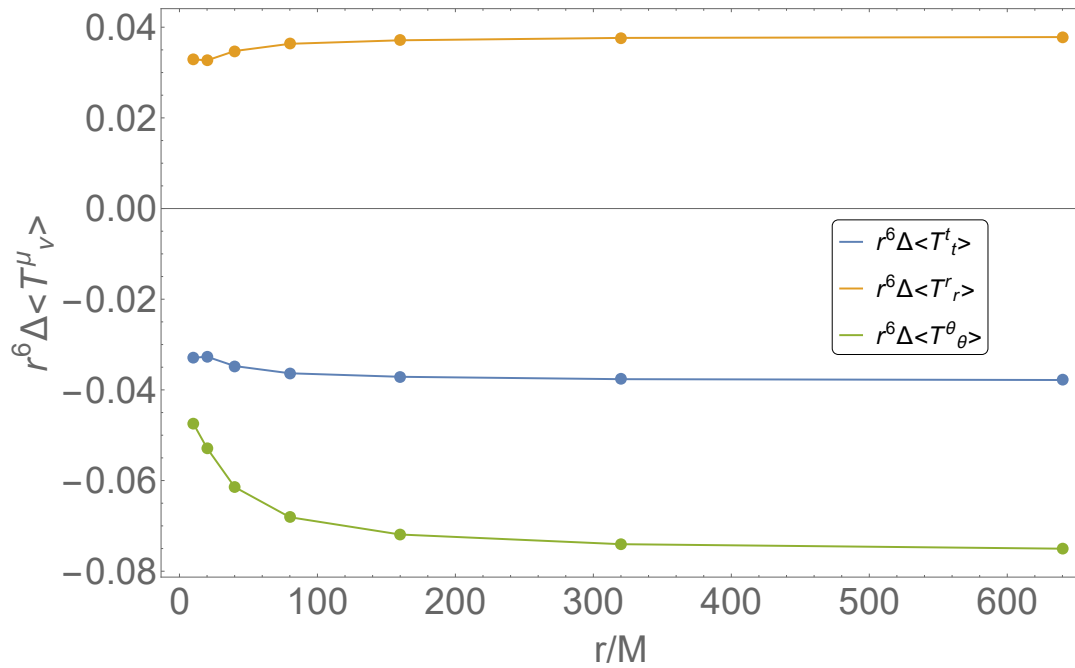


Figure 7.4.8: The  $\ell = 0$  contribution to  $\Delta \langle T^\mu_\nu \rangle$  outside a  $R = 4M$  compact neutron star for minimal coupling.

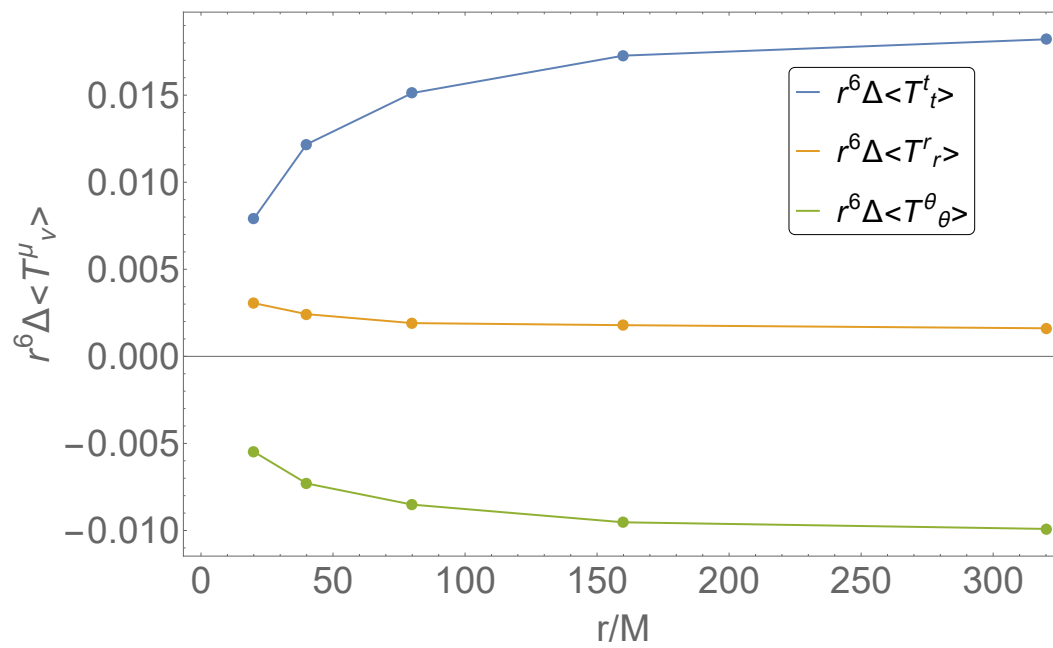


Figure 7.4.9: The  $\ell = 0$  contribution to  $\Delta \langle T^\mu_\nu \rangle$  outside a  $R = 4M$  compact neutron star for conformal coupling  $\xi = 1/6$ .

# Chapter 8

## Conclusion and Outlook

This thesis has covered our research concerning both classical and quantum bosonic fields on black hole spacetimes. In this chapter we will summarise our primary results and suggest possible avenues of further study.

### 8.1 Summary of Results

#### 8.1.1 Classical Fields

We presented our original work on the application of Leaver's method to the charged Proca field on the Reissner-Nordström spacetime in Sec. 3.4.2. We found a new four-term recurrence relation, presented in Eqs. (3.4.3)-(3.4.6), arising from the radial ODE of the decoupled, odd-parity component of the charged Proca field on the Reissner-Nordström spacetime. We applied the continued fraction method to solve this recurrence relation and find the QBSs and QNMs of this odd-parity polarization of the Proca field, presented in Figs. 3.4.1-3.4.5. We compared the QBS frequencies to known analytical approximations and to previously collected data and found good agreement.

Following the relatively recent LFKK method [66] of separating the Proca equation on the Kerr and Kerr-Newman spacetimes, we found a new five term recurrence relation presented in Eqs. (4.2.75)-(4.2.79) from the resulting radial ODE. This recurrence can be used to find QNMs of the Proca field for all three polarization states after a careful consideration of the angular eigenvalue  $\nu$  via the method of spectral decomposition, detailed in [54]. Our original results for the QNMs are presented for the Kerr spacetime in Figs. 4.2.5-4.2.10 and for the Kerr-Newman spacetime in Figs. 4.3.2-4.3.3. This recurrence can also be used to find QBSs for at least two of the three polarization states of the Proca field, the results of which are presented in Figs. 4.2.2-4.2.4. We found good agreement in the real part with the known QBS data in these cases, with agreement in the

imaginary part dependent on the mass of the field.

### 8.1.2 Quantum Fields

We investigated, numerically and analytically, a recently proposed method of calculating differences in QEVs evaluated in the same quantum state in locally equivalent spacetimes. This method was described by Anderson and Fabbri in [7] for the difference in the vacuum polarization and stress-energy tensor of a scalar field in the Boulware vacuum state between a Schwarzschild black hole and a Newtonian star,  $\Delta \langle \phi^2 \rangle$  and  $\Delta \langle T^\mu_\nu \rangle$  respectively. We first used the method to perform a complete analytical calculation of the  $\ell = 0$  contribution to the energy density difference  $\Delta \langle T^t_t \rangle$  between the spacetime of a spherically symmetric shell and flat spacetime, Eq. (6.2.40). We then explored the higher  $\ell$  modes via a combination of numerics and analytics. We found a surprising pattern in the results for the integral of the energy density difference over the entire shell spacetime, presented in Table (6.1).

We extended Anderson and Fabbri's far field analytical approximations of  $\Delta \langle \phi^2 \rangle$  and  $\Delta \langle T^\mu_\nu \rangle$  between the spacetimes of a Schwarzschild black hole and a Newtonian star, Eqs. (6.1.29) and (6.1.31), to more general stellar models. For the interior Schwarzschild metric and the Tolman metric these results are given in Eqs. (7.1.11) and (7.1.34). These far field results depend on the internal matter distribution of the star through a structure function  $\mathcal{S}(M/R)$  which was obtained as a series expansion. We saw that two metrics specifying the star interior that agreed to first order in an expansion for small impact parameter  $x = M/R$  had structure functions  $\mathcal{S}(x)$  that also agreed to this order. The results for the interior Schwarzschild metric were compared to numerics in the far field and found to agree well for values of coupling where the leading order term does not vanish (Fig. 7.4.6). The expected sub-leading order scaling with  $r^{-1}$  was found in the cases where the leading order term did vanish (Figs. 7.4.8 and 7.4.9).

The results of our own numerical implementation of Levi and Ori's PMR method [100] to the calculation of  $\langle \phi^2 \rangle$  for a massless scalar field outside a Schwarzschild black hole are presented in Table (5.1) and Fig. 5.2.6 and agree with previously collected data to within the quoted numerical error bars. We combined this with a new numerical exploration of  $\Delta \langle \phi^2 \rangle$  and  $\Delta \langle T^\mu_\nu \rangle$  near the star surface for a variety of star radii and couplings  $\xi$  to the scalar curvature to find  $\langle \phi^2 \rangle$  near the surface of a spherically symmetric star. The results are presented throughout Sec. 7.3.

## 8.2 Further Study

On the Reissner-Nordström spacetime we have only applied the recurrence relation method to the decoupled odd-parity polarization of the Proca field. In theory, it would be possible to apply an extension of the method using matrix-valued continued fractions, as was done in [126] for the uncharged Proca field, to the other two polarizations.

Our recurrence relation method appears to be less reliable when calculating QBS frequencies for field masses much smaller than the mass value of the most unstable superradiant mode. This is most noticeable for the  $S = +1$  polarization where no reliable data could be obtained. We were also unable to obtain reliable data for the QNMs of the odd-parity mode of the Proca field in the specific case when  $m = 0$ . Possible reasons for these difficulties were discussed at the end of chapter 4. These issues warrant further investigation to see if these difficulties can be remedied.

The techniques we used in Sec. 7.1 to extend Anderson and Fabbri's method to more general stellar structures has room to be explored further. In particular it would be interesting to see if a more detailed link between the interior metric functions and the form of the structure function could be established.

We currently have no explanation for the interesting pattern in the values for the total energy difference presented in Table 6.1. We hypothesise that there should exist a regularisation scheme that can make the sum over  $\ell$  finite and the final result should be in some way comparable to the value of the Casimir energy around a spherical shell, see for example [106].

A full treatment of  $\langle T^\mu_\nu \rangle$  via the angular splitting PMR method has yet to be published. As such, we did not numerically compute  $\langle T^\mu_\nu \rangle$  for a scalar field outside a Schwarzschild black hole. However, there is scope to combine our numerical calculation of the difference  $\Delta \langle T^\mu_\nu \rangle$  with data for  $\langle T^\mu_\nu \rangle$  outside a Schwarzschild black hole calculated using the  $t$ -splitting variant of the PMR method [97] to obtain data for  $\langle T^\mu_\nu \rangle$  outside a spherically symmetric star.



# Appendix A

## Quasibound States of a Scalar Field

In this appendix we cover the matched asymptotic expansion techniques used to approximate the QBS frequencies of a scalar field, in both static and rotating black hole spacetimes. The corresponding calculations for the vector field were covered in Secs. 3.1.2 and 4.2.3 respectively. At the end of this section, we briefly discuss some previous numerical work testing these approximations.

### A.1 Non-rotating Spacetimes

Although the work of Furuhashi and Nambu for a charged, massive, scalar field in [69] was conducted in the Kerr-Newman spacetime, it is found that the leading order approximation to the bound state frequencies is independent of the black hole rotation  $a$ . Hence this approximation is also valid for the Schwarzschild and Reissner-Nordström spacetimes and we detail the general method here.

Furuhashi and Nambu begin by assuming that each of the parameters  $M\omega$ ,  $M\mu$  and  $eQ$  are small,

$$O(M\omega) = O(M\mu) = O(eQ) \equiv O(\alpha) \ll 1 \quad (\text{A.1.1})$$

and then considering the radial differential equation (3.1.9) with the effective potential (3.1.5) in the region far from the black hole  $r \gg r_+$

$$\frac{d^2\psi}{dr^2} + \left[ \omega^2 - \mu^2 + \frac{2(2M\omega^2 - M\mu^2 - eQ\omega)}{r} - \frac{\ell(\ell+1) + \alpha^2}{r^2} \right] \psi = 0. \quad (\text{A.1.2})$$

Here the radial function is

$$\psi(r) = \sqrt{\Delta} R(r) = \sqrt{\Delta} \frac{u(r)}{r}, \quad (\text{A.1.3})$$

where  $u(r)$  is the same function in the mode decomposition (3.1.2) and  $\Delta = r^2 f_{rn}$  is the horizon function of Reissner-Nordström spacetime. It is worth noting that this equation takes the exact same form even when  $a \neq 0$ : very far from the black hole the effects of the rotation are minimal

(This is unsurprising given the Kerr metric (2.2.9) reduces to the Schwarzschild metric in the large  $r$  limit for fixed  $a$ ). This must be solved with the regular boundary condition at infinity, i.e., we must use the  $-$  sign in Eq. (3.2.12). This equation has a solution for  $u(r)$  in terms of the confluent hypergeometric function

$$u(r) = (2qr)^{\ell+1} e^{-qr} U(\ell + 1 + \chi + \alpha^2, 2\ell + 2 + 2\alpha^2, 2qr), \quad (\text{A.1.4})$$

where  $\chi$  is as in (3.2.15). Although this solution is, strictly speaking, only valid far from the black hole, the behavior of the solution in the limit of small  $r$  is known, with leading order terms proportional to  $(2qr)^{\ell+1}$  and  $(2qr)^{-\ell}$  such that  $R(r) = u(r)/r$  has leading order terms proportional to  $r^\ell$  and  $r^{-\ell-1}$ . This can be taken to be the behavior of the solution in an ‘‘overlap’’ region neither close to nor far from the black hole.

A similar analysis is then performed near the horizon of the black hole. Defining a new radial variable  $z$

$$z = \frac{r - r_+}{r - r_-}, \quad (\text{A.1.5})$$

the radial equation can be cast in the form for  $r \ll \ell$

$$\left(z \frac{d}{dz}\right)^2 (\Delta^{-1}R) + \left[\rho^2 - \ell(\ell + 1) \frac{z}{(1-z)^2}\right] (\Delta^{-1}R) = 0, \quad (\text{A.1.6})$$

where the index  $\rho$  is the same as that in (3.2.15). This equation has a solution in terms of the Gauss hypergeometric function

$$\Delta^{-1}R = z^{i\rho} (1-z)^{\ell+1} {}_2F_1(\ell + 1, \ell + 1 + 2i\rho, 1 + 2i\rho, z), \quad (\text{A.1.7})$$

whose behavior in limit as  $z \rightarrow 1$  (limit of large  $r$ ) is known. Once again it is found that in the overlap region,  $R(r)$  has two leading order terms, proportional to  $r^\ell$  and  $r^{-\ell-1}$ .

The behavior of the two solutions in this overlap region can be matched up and this provides conditions on the bound state frequency  $\omega$ , see equation 15 of [69]. What is learned is that the real part of the spectrum of  $\omega$  is approximately *hydrogenic*, i.e., it is comparable to the allowed energies of the electron orbitals around a hydrogen atom,

$$\Re(\omega) \approx \mu \left[ 1 - \frac{1}{2} \left( \frac{M\mu - eQ}{\ell + n + 1} \right)^2 \right]. \quad (\text{A.1.8})$$

For a non-rotating black hole there are no further relevant corrections to the real part of the bound state spectrum. The next-to-leading order correction is entirely imaginary,

$$\Im(\omega) = \mu \delta \nu \frac{(M\mu - eQ)^2}{(\ell + 1 + n)^3}, \quad (\text{A.1.9})$$

where  $\delta\nu$  is defined in equation 24 of [69],

$$\begin{aligned} \delta\nu &= 2i\rho^{(0)} \left[ \frac{2(M\mu - eQ)}{\ell + n + 1} \mu (r_+ - r_-) \right]^{2\ell+1} \\ &\times \frac{(2\ell + n + 1)!}{n!} \left[ \frac{\ell!}{(2\ell)! (2\ell + 1)!} \right]^2 \prod_{k=1}^{\ell} (k^2 + 4\rho^{(0)2}). \end{aligned} \quad (\text{A.1.10})$$

Here,  $\rho^{(0)}$  is the first order approximation to  $\rho$  found by substituting the hydrogenic approximation to  $\Re(\omega)$ , Eq. (A.1.8) into (3.2.15) in place of  $\omega$ . Hence, the total scaling of  $\Im(\omega)$  as a power of the mass is  $\mu^{4\ell+6}$ .

From Eq. (A.1.9) we can recognise that to remain consistent with the boundary condition at infinity, a bound state can only occur when

$$\Im \left( \sqrt{\Re(\omega)^2 - \mu^2} \right) = \frac{M\mu - eQ}{\ell + n + 1} > 0, \quad (\text{A.1.11})$$

requiring  $M\mu > eQ$ .

Superradiance will occur when  $\Im(\omega) > 0$ , which is when  $\rho^{(0)} > 0$ . This condition can be written as

$$\frac{1}{2\kappa} \left( e\Phi_H - \omega^{(0)} \right) > 0, \quad (\text{A.1.12})$$

where the surface gravity and electromagnetic potential of the black hole have been introduced

$$\kappa = \frac{1}{2} \left( \frac{1}{r_+} - \frac{r_-}{r_+^2} \right), \quad \Phi_H = \frac{Q}{r_+}. \quad (\text{A.1.13})$$

This form is useful when comparing the superradiance condition in Reissner-Nordström spacetime to that in the Kerr spacetime in chapter 4, but it is easy to show that in Reissner-Nordström spacetime this is just the same superradiance condition we wrote down in Sec. 3.1,  $\omega < eQ/r_+$ .

As  $\omega \approx \mu$  the superradiance condition can also be phrased as  $\mu < eQ/r_+$ . However, this is incompatible with the bound state condition  $M\mu > eQ$ . We can conclude that, while superradiance does occur for a charged scalar field around a Reissner-Nordström black hole, there can be no superradiant instabilities.

## A.2 Rotating Spacetimes

### A.2.1 Analytical Methods

In this section we will discuss a massive, charged scalar field around a Kerr-Newman black hole with charge  $Q$ , as including a mass  $\mu$  and a charge  $e$  on the field doesn't cause any issues for

the separability of the solution (for an earlier discussion of the uncharged scalar field on the Kerr spacetime, see [26]). The angular and radial equations are then given by [51] and [69]

$$\left[ \frac{1}{\sin\theta} \frac{d}{d\theta} \left( \sin\theta \frac{d}{d\theta} \right) + a^2 (\omega^2 - \mu^2) \cos^2\theta - \frac{m^2}{\sin^2\theta} + \lambda \right] S = 0, \quad (\text{A.2.1})$$

$$\Delta \frac{d}{dr} \left( \Delta \frac{d\psi}{dr} \right) + \left\{ -\Delta (\mu^2 r^2 + \lambda) + [(r^2 + a^2)\omega - am - eQr]^2 \right\} \psi = 0, \quad (\text{A.2.2})$$

where we are using the radial function  $\psi(r) = \sqrt{\Delta} R(r) = \sqrt{\Delta} u(r)/r$  as we did in the non-rotating case (A.1.3) (where  $\Delta$  was defined in (2.2.5)) and have absorbed some terms into the angular eigenvalue

$$\lambda \equiv \tilde{\lambda} + 2ma\omega - a^2\omega^2. \quad (\text{A.2.3})$$

A comparison to the known equations in the non-rotating limit, in particular the potential in Eq. (3.1.5), allows us to infer that as  $a \rightarrow 0$ ,  $\lambda = \tilde{\lambda} = \ell(\ell + 1)$ .

### A.2.1.1 Leading Order

Both [51] and [69] perform asymptotic matching arguments on the radial differential equation (A.2.2). The far field analysis for  $r \gg r_+$ , to leading order, is identical to the non-rotating case in the previous section (Eq. (A.1.2)) as any terms involving the rotation  $a$  are contained in the  $\alpha^2$ . In the near-horizon region, the index  $\rho$  in Eq. (3.2.15) now depends on  $a$

$$\rho = \frac{(r_+^2 + a^2)\omega - ma - eQr_+}{r_+ - r_-}. \quad (\text{A.2.4})$$

Recall the expression for the imaginary part of  $\omega$  obtained from this analytic method in Eq. (A.1.9). In particular, superradiance occurs for  $\rho^{(0)} > 0$ , a condition which now reads

$$\frac{1}{2\kappa} (m\Omega_H + e\Phi_H - \Re(\omega)) > 0, \quad (\text{A.2.5})$$

with the surface gravity,  $\kappa$ , angular velocity  $\Omega_H$  and electromagnetic potential  $\Phi_H$

$$\kappa = \frac{1}{2} \left( \frac{r_+ - r_-}{a^2 + r_+^2} \right), \quad \Omega_H = \frac{a}{a^2 + r_+^2}, \quad \Phi_H = \frac{Qr_+}{a^2 + r_+^2}. \quad (\text{A.2.6})$$

(For more on the superradiance of a massive, charged scalar field on the spacetime of a Kerr-Newman black hole, see [20]). In particular, the most unstable mode occurs when  $\Im(\omega)$  scales with the smallest possible power of  $M\mu$ , when  $\ell = m = 1$  and  $n = 0$

$$\Im(\omega) = \frac{\mu^4}{24} (M\mu - eQ)^5 (a^2 + r_+^2)^3 (\Omega_H + e\Phi_H - \mu) \left( \kappa^2 + (\Omega_H + e\Phi_H - \mu)^2 \right). \quad (\text{A.2.7})$$

In the Kerr spacetime this reduces to

$$\Im(\omega) = \frac{a}{M^2} \frac{(M\mu)^9}{24} \quad (\text{A.2.8})$$

and so we see this is more unstable than the fastest growing mode of the scalar field in the Schwarzschild or Reissner-Nordström spacetimes (see Eq. (A.1.9, which scales like  $\mu^{10}$  when  $\ell = 1$ )) but not as unstable as the fastest growing vector mode in the Kerr spacetime (see Eq. (4.2.61) where the fastest scaling is  $\mu^7$ ).

### A.2.1.2 Higher Orders

We now refer to the more recent work of [18], where they study the massive (uncharged) scalar field in the Kerr spacetime. They, like Furuhashi and Nambu in [69], assume that  $M\mu = \alpha \ll 1$  and expand all quantities in the radial and angular differential equations (A.2.2) and (A.2.1) in terms of this parameter. In this notation the leading order hydrogenic approximation already stated is  $\omega \approx \mu (1 - \alpha^2/2N^2)$  where  $N = \ell + n + 1$ . Schematically, the radial function is expanded as

$$R = \sum_k \alpha^k R_k, \quad (\text{A.2.9})$$

that satisfies a differential equation

$$\left[ \square^{(0)} + \alpha \square^{(1)} + \alpha^2 \square^{(2)} + \dots \right] [R_0 + \alpha R_1 + \alpha^2 R_2 + \dots] = 0, \quad (\text{A.2.10})$$

where each  $\square$  represents a differential operator. This expansion is performed on both the near-horizon and far-field differential equations. To extend the asymptotic matching argument described above to higher orders they rearrange this into an in-homogeneous equation

$$\square^{(0)} R_i = - \sum_{k=0}^{i-1} \square^{(i-k)} R_k \equiv J_i, \quad (\text{A.2.11})$$

that can be solved order by order for each  $R_i$ . The process is quite involved and requires them to consider the cases  $\ell = 0$  and  $\ell \neq 0$  separately, but the final result is valid for all  $\ell \geq 0$ . It is

$$\Re(\omega) = \mu \left( 1 - \frac{\alpha^2}{2N^2} - \frac{\alpha^4}{8N^4} + \frac{f_{N\ell}}{N^3} \alpha^4 + \frac{h_\ell}{N^3} m \alpha^5 + \dots \right), \quad (\text{A.2.12})$$

$$f_{N\ell} = -\frac{6}{2\ell + 1} + \frac{2}{N}, \quad (\text{A.2.13})$$

$$h_\ell = \frac{16}{2\ell(2\ell + 1)(2\ell + 2)}. \quad (\text{A.2.14})$$

The term proportional to  $f_{N\ell}$  is referred to as the *fine structure* correction and the term proportional to  $h_\ell$  is the *hyper-fine structure* correction. Note that there is no hyper-fine correction in the case where  $\ell = 0$ , as this forces us to set  $m = 0$ .

### A.2.2 Numerical Methods

The validity of these analytical results was tested through direct integration of the radial differential equation in [69]. Using the tortoise coordinate  $r_*$  suitable for the Kerr(-Newman) spacetime

$$r_* = \int dr \frac{r^2}{\Delta} = r + \frac{1}{r_+ - r_-} [r_+^2 \log(r - r_+) - r_-^2 \log(r - r_-)] \quad (\text{A.2.15})$$

and the radial function  $u(r) = rR(r)$ , the solutions near the horizon and far from the black hole can be written as

$$u_{near}(r_*) = \exp \left[ -i \left( \frac{2M\omega - eQ}{r_+} - \frac{am + Q^2\omega}{r_+^2} \right) r_* \right], \quad (\text{A.2.16})$$

$$u_{far}(r_*) = r_*^{(M\mu^2 - eQ\omega)/q} e^{-qr_*}. \quad (\text{A.2.17})$$

Then, these two solutions are used as the starting data for two numerical integrations, one going outwards from the horizon and one going inwards from infinity. This gives two mode solutions  $u^{(1)}$  and  $u^{(2)}$ . We want these solutions to be the same solution up to a constant factor, i.e., we want them to be linearly dependent. This occurs when the Wronskian  $W(\omega)$  of the two solutions is zero (see Eq. (3.1.14)) and so the Wronskian forms a merit function that can be minimised over the complex frequency plane. The imaginary part of the frequency that minimises this merit function is the field instability rate for the parameters  $(a, \mu, e)$  chosen.

For a given black hole rotation and charge the  $(\mu, e)$  parameter space can be scanned to find the largest instability rate. For example, [69] report that for a black hole with parameters  $a = 0.98M$ ,  $Q = 0.01M$  the largest instability magnitude  $\Im(M\omega) \approx 1.13 \times 10^{-7}$  occurs at  $M\mu = 0.35$  and  $eQ = -0.08$ . The asymptotic matching approximation method picked out the location of the instability correctly, but not the magnitude. This shortcoming of the predictions of the asymptotic matching method is also present for the vector field, see Fig. 4.2.3.

Similar results were presented for the uncharged scalar field on the Kerr spacetime in [52], but they also calculated the QNMs as well as the QBSs. Rather than asymptotic matching they derived a three-term recurrence relation using the same method as was described in the non-rotating case in Sec. 3.2.2 (as direct integration is not a suitable numerical scheme for finding QNMs, see Sec. 3.4.1), which they then solve using continued fractions. See also [53] where the superradiant instabilities of the scalar field are studied in the time domain (as opposed to the frequency domain).

# Bibliography

- [1] Black Hole Perturbation Toolkit. ([bhptoolkit.org](http://bhptoolkit.org)).
- [2] AAD, G., ABAJYAN, T., ABBOTT, B., ABDALLAH, J., ABDEL KHALEK, S., ABDELALIM, A., ABDINOV, O., ABEN, R., ABI, B., ABOLINS, M., AND ET AL. Observation of a new particle in the search for the Standard Model Higgs boson with the ATLAS detector at the LHC. *Phys. Lett. B* **716**, 1 (2012), 1–29.
- [3] ABBOTT, B., ABBOTT, R., ABBOTT, T., ABERNATHY, M., ACERNESE, F., ACKLEY, K., ADAMS, C., ADAMS, T., ADDESSO, P., ADHIKARI, R., AND ET AL. Observation of gravitational waves from a binary black hole merger. *Phys. Rev. Lett.* **116**, 6 (2016), 061102.
- [4] ABBOTT, R., ABBOTT, T., ABRAHAM, S., ACERNESE, F., ACKLEY, K., ADAMS, A., ADAMS, C., ADHIKARI, R., ADYA, V., AFFELDT, C., AND ET AL. GWTC-2: Compact binary coalescences observed by LIGO and Virgo during the first half of the third observing run. *Phys. Rev. X* **11**, 2 (2021), 021053.
- [5] ADLER, S. L., LIEBERMAN, J., AND NG, Y. J. Regularization of the stress-energy tensor for vector and scalar particles propagating in a general background metric. *Ann. Phys. (N.Y.); (United States)* **106**, 2 (1977), 279–321.
- [6] ANDERSON, P. R. A method to compute  $\varphi^2$  in asymptotically flat, static, spherically symmetric spacetimes. *Phys. Rev. D* **41**, 4 (1990), 1152–1162.
- [7] ANDERSON, P. R., AND FABRI, A. Apparent universality of semiclassical gravity in the far field limit. *Phys. Rev. D* **75**, 4 (2007), 044015.
- [8] ANDERSON, P. R., HISCOCK, W. A., AND SAMUEL, D. A. Stress-energy tensor of quantized scalar fields in static spherically symmetric spacetimes. *Phys. Rev. D* **51**, 8 (1995), 4337–4358.
- [9] ASHBY, N. Relativity and the global positioning system. *Physics Today* **55**, 5 (2002), 41–47.

- [10] BAIBHAV, V., BERTI, E., CARDOSO, V., AND KHANNA, G. Black hole spectroscopy: Systematic errors and ringdown energy estimates. *Phys. Rev. D* **97**, 4 (2018), 044048.
- [11] BAKER, K., CANTATORE, G., CETIN, S. A., DAVENPORT, M., DESCH, K., DÖBRICH, B., GIES, H., IRASTORZA, I. G., JAECKEL, J., LINDNER, A., AND ET AL. The quest for axions and other new light particles. *Annalen der Physik* **525**, 6 (2013), A93–A99.
- [12] BALAKUMAR, V., AND WINSTANLEY, E. Hadamard renormalization for a charged scalar field. *Class. Quant. Grav.* **37**, 6 (2020), 065004.
- [13] BALAKUMAR, V., WINSTANLEY, E., BERNAR, R. P., AND CRISPINO, L. C. Quantum superradiance on static black hole space-times. *Phys. Lett. B* **811** (2020), 135904.
- [14] BARDEEN, J. M., CARTER, B., AND HAWKING, S. W. The four laws of black hole mechanics. *Comm. Math. Phys.* **31**, 2 (1973), 161–170.
- [15] BARDEEN, J. M., AND PRESS, W. H. Radiation fields in the Schwarzschild background. *J. Math. Phys.* **14**, 1 (1973), 7–19.
- [16] BARYAKHTAR, M., LASENBY, R., AND TEO, M. Black hole superradiance signatures of ultralight vectors. *Phys. Rev. D* **96**, 3 (2017), 035019.
- [17] BAUMANN, D., CHIA, H. S., AND PORTO, R. A. Probing ultralight bosons with binary black holes. *Phys. Rev. D* **99**, 4 (2019), 044001.
- [18] BAUMANN, D., CHIA, H. S., STOUT, J., AND TER HAAR, L. The spectra of gravitational atoms. *J. Cos. Astro. Phys.* **2019**, 12 (2019), 006.
- [19] BECKER, K., BECKER, M., AND SCHWARZ, J. H. *String Theory and M-Theory: A Modern Introduction*. Cambridge University Press, 2006.
- [20] BENONE, C. L., AND CRISPINO, L. C. B. Massive and charged scalar field in Kerr-Newman spacetime: Absorption and superradiance. *Phys. Rev. D* **99**, 4 (2019), 044009.
- [21] BERTI, E., CARDOSO, V., AND STARINETS, A. O. Quasinormal modes of black holes and black branes. *Class. Quant. Grav.* **26**, 16 (2009), 163001.
- [22] BIRRELL, N. D., AND DAVIES, P. C. W. *Quantum Fields in Curved Space*. Cambridge Monographs on Mathematical Physics. Cambridge University Press, 1982.

- [23] BOULWARE, D. G. Spin- $\frac{1}{2}$  quantum field theory in Schwarzschild space. *Phys. Rev. D* **12**, 2 (1975), 350–367.
- [24] BREEN, C., AND OTTEWILL, A. C. Hadamard renormalization of the stress energy tensor in a spherically symmetric black hole space-time with an application to lukewarm black holes. *Phys. Rev. D* **85**, 8 (2012), 084029.
- [25] BREEN, C., AND OTTEWILL, A. C. Hadamard renormalization of the stress energy tensor on the horizons of a spherically symmetric black hole space-time. *Phys. Rev. D* **85**, 6 (2012), 064026.
- [26] BRILL, D. R., CHRZANOWSKI, P. L., PEREIRA, C. M., FACKERELL, E. D., AND IPSER, J. R. Solution of the scalar wave equation in a Kerr background by separation of variables. *Phys. Rev. D* **5**, 8 (1972), 1913–1915.
- [27] BRITO, R., CARDOSO, V., AND PANI, P. Black holes as particle detectors: evolution of superradiant instabilities. *Class. Quant. Grav* **32**, 13 (2015), 134001.
- [28] BRITO, R., CARDOSO, V., AND PANI, P. *Superradiance*. Springer International Publishing, 2020.
- [29] BROWN, M. R., OTTEWILL, A. C., AND PAGE, D. N. Conformally invariant quantum field theory in static Einstein space-times. *Phys. Rev. D* **33**, 10 (1986), 2840–2850.
- [30] BUCHDAHL, H. A. General relativistic fluid spheres. *Phys. Rev.* **116**, 4 (1959), 1027–1034.
- [31] BUCHER, M., AND NI, W.-T. General relativity and cosmology. *Int. J. Mod. Phys. D* **24**, 14 (2015), 1530030.
- [32] CANDELAS, P. Vacuum polarization in Schwarzschild spacetime. *Phys. Rev. D* **21**, 8 (1980), 2185–2202.
- [33] CARDOSO, V., DIAS, Ó. J., HARTNETT, G. S., MIDDLETON, M., PANI, P., AND SANTOS, J. E. Constraining the mass of dark photons and axion-like particles through black-hole superradiance. *J. Cos. Astro. Phys* **2018**, 03 (2018), 043–043.
- [34] CARDOSO, V., MIRANDA, A. S., BERTI, E., WITEK, H., AND ZANCHIN, V. T. Geodesic stability, Lyapunov exponents, and quasinormal modes. *Phys. Rev. D* **79**, 6 (2009), 064016.
- [35] CARDOSO, V., AND YOSHIDA, S. Superradiant instabilities of rotating black branes and strings. *J. High En. Phys* **2005**, 07 (2005), 009–009.

- [36] CARLSON, E. D., ANDERSON, P. R., FABBRI, A., FAGNOCCHI, S., HIRSCH, W. H., AND KLYAP, S. A. Semiclassical gravity in the far field limit of stars, black holes, and wormholes. *Phys. Rev. D* **82**, 12 (2010), 124070.
- [37] CARROLL, S. M. *Spacetime and Geometry: An Introduction to General Relativity*. Cambridge University Press, 2019.
- [38] CARTER, B. Global structure of the Kerr family of gravitational fields. *Phys. Rev.* **174**, 5 (1968), 1559–1571.
- [39] CASALS, M., DOLAN, S., OTTEWILL, A. C., AND WARDELL, B. Self-force calculations with matched expansions and quasinormal mode sums. *Phys. Rev. D* **79**, 12 (2009), 124043.
- [40] CASALS, M., DOLAN, S. R., NOLAN, B. C., OTTEWILL, A. C., AND WINSTANLEY, E. Quantization of fermions on Kerr space-time. *Phys. Rev. D* **87**, 6 (2013), 064027.
- [41] CAYUSO, R., DIAS, O. J. C., GRAY, F., KUBIZŃÁK, D., MARGALIT, A., SANTOS, J. E., SOUZA, R. G., AND THIELE, L. Massive vector fields in Kerr-Newman and Kerr-Sen black hole spacetimes. *J. High En. Phys* **2020**, 4 (2020), 159.
- [42] CHANDRASEKHAR, S. The solution of Dirac’s equation in Kerr geometry. *Proc. Roy. Soc. Lon. A. Math. Phys. Sci.* **349**, 1659 (1976), 571–575.
- [43] CHANDRASEKHAR, S. *The Mathematical Theory of Black Holes*. Springer Netherlands, Dordrecht, 1984.
- [44] CHANG, J. F., AND SHEN, Y. G. Massive charged quasinormal modes of a Reissner-Nordström black hole. *Int. J. Theo. Phys.* **46**, 6 (2007), 1570–1583.
- [45] CHIA, H. S. *Probing particle physics with gravitational waves*. PhD thesis, Amsterdam U., 2020.
- [46] CHRISTENSEN, S. M. Vacuum expectation value of the stress tensor in an arbitrary curved background: The covariant point-separation method. *Phys. Rev. D* **14**, 10 (1976), 2490–2501.
- [47] CHRUŚCIEL, P. T., COSTA, J. L., AND HEUSLER, M. Stationary black holes: Uniqueness and beyond. *Liv. Rev. in Rel.* **15**, 1 (2012), 7.
- [48] COOK, G. B., AND ZALUTSKIY, M. Gravitational perturbations of the Kerr geometry: High-accuracy study. *Phys. Rev. D* **90**, 12 (2014), 124021.

- [49] DÉCANINI, Y., FOLACCI, A., AND OULD EL HADJ, M. Waveforms in massive gravity and neutralization of giant black hole ringings. *Phys. Rev. D* **93**, 12 (2016), 124027.
- [50] DELGATY, M., AND LAKE, K. Physical acceptability of isolated, static, spherically symmetric, perfect fluid solutions of Einstein's equations. *Comp. Phys. Comm.* **115**, 2 (1998), 395–415. Computer Algebra in Physics Research.
- [51] DETWEILER, S. Klein-Gordon equation and rotating black holes. *Phys. Rev. D* **22**, 10 (1980), 2323.
- [52] DOLAN, S. R. Instability of the massive Klein-Gordon field on the Kerr spacetime. *Phys. Rev. D* **76**, 8 (2007), 084001.
- [53] DOLAN, S. R. Superradiant instabilities of rotating black holes in the time domain. *Phys. Rev. D* **87**, 12 (2013), 124026.
- [54] DOLAN, S. R. Instability of the Proca field on Kerr spacetime. *Phys. Rev. D* **98**, 10 (2018), 104006.
- [55] DOLAN, S. R. Electromagnetic fields on Kerr spacetime, Hertz potentials and Lorenz gauge. *Phys. Rev. D* **100**, 4 (2019), 044044.
- [56] DOLAN, S. R., AND OTTEWILL, A. C. On an expansion method for black hole quasinormal modes and Regge poles. *Class. Quant. Grav* **26**, 22 (2009), 225003.
- [57] DRAY, T. The relationship between monopole harmonics and spin-weighted spherical harmonics. *J. Math. Phys.* **26**, 5 (1985), 1030–1033.
- [58] DUFFY, L. D., AND VAN BIBBER, K. Axions as dark matter particles. *New J. Phys.* **11**, 10 (2009), 105008.
- [59] EAST, W. E. Superradiant instability of massive vector fields around spinning black holes in the relativistic regime. *Phys. Rev. D* **96**, 2 (2017), 024004.
- [60] EAST, W. E., AND PRETORIUS, F. Superradiant instability and backreaction of massive vector fields around Kerr black holes. *Phys. Rev. Lett.* **119**, 4 (2017), 041101.
- [61] ENDLICH, S., AND PENCO, R. A modern approach to superradiance. *J. High En. Phys.* **2017**, 5 (2017), 52.

- [62] FRIEMAN, J. A., TURNER, M. S., AND HUTERER, D. Dark energy and the accelerating universe. *Ann. Rev. Astron. Astrophys* **46**, 1 (2008), 385–432.
- [63] FROLOV, V., AND NOVIKOV, I. *Black hole physics: basic concepts and new developments*, vol. 96 of *Fundamental Theories of Physics*. Springer Science & Business Media, 2012.
- [64] FROLOV, V. P., KRTOUŠ, P., AND KUBIZŇÁK, D. Black holes, hidden symmetries, and complete integrability. *Liv. Rev. in Rel.* **20**, 1 (2017), 6.
- [65] FROLOV, V. P., KRTOUŠ, P., AND KUBIZŇÁK, D. Separation of variables in Maxwell equations in Plebański-Demiański spacetime. *Phys. Rev. D* **97**, 10 (2018), 101701.
- [66] FROLOV, V. P., KRTOUŠ, P., KUBIZŇÁK, D., AND SANTOS, J. E. Massive vector fields in rotating black-hole spacetimes: separability and quasinormal modes. *Phys. Rev. Lett.* **120**, 23 (2018), 231103.
- [67] FROLOV, V. P., AND ZELNIKOV, A. *Introduction to black hole physics*. Oxford Univ. Press, Oxford, 2011.
- [68] FROLOV, V. P., AND ZEL'NIKOV, A. I. Killing approximation for vacuum and thermal stress-energy tensor in static space-times. *Phys. Rev. D* **35**, 10 (1987), 3031–3044.
- [69] FURUHASHI, H., AND NAMBU, Y. Instability of massive scalar fields in Kerr-Newman spacetime. *Prog. Theo. Phys* **112**, 6 (2004), 983–995.
- [70] GARBARZ, A., GIRIBET, G., AND MAZZITELLI, F. D. Conformal invariance and apparent universality of semiclassical gravity. *Phys. Rev. D* **78**, 8 (2008), 084014.
- [71] GEROCH, R. Domain of dependence. *J. of Math. Phys.* **11**, 2 (1970), 437–449.
- [72] GIESLER, M., ISI, M., SCHEEL, M. A., AND TEUKOLSKY, S. A. Black hole ringdown: The importance of overtones. *Phys. Rev. X* **9**, 4 (2019), 041060.
- [73] GOEBEL, C. J. Comments on the “vibrations” of a black hole. *Astrophys. J.* **172** (1972), L95.
- [74] GOLDBERG, J. N., MACFARLANE, A. J., NEWMAN, E. T., ROHRLICH, F., AND SUDARSHAN, E. C. G. Spin-s spherical harmonics and  $\delta$ . *J. Math. Phys* **8**, 11 (1967), 2155–2161.
- [75] GUNTER, D. L. A study of the coupled gravitational and electromagnetic perturbations to the Reissner–Nordstrom black hole: The scattering matrix, energy conversion, and quasi-normal modes. *Proc. Roy. Soc. Lon. A. Math. Phys. Sci.* **296**, 1422 (1980), 497–526.

- [76] HADAMARD, J. *Lectures on Cauchy's Problem in Linear Partial Differential Equations*. Yale University Press, 1923.
- [77] HARTLE, J. B., AND HAWKING, S. W. Path-integral derivation of black-hole radiance. *Phys. Rev. D* **13**, 8 (1976), 2188–2203.
- [78] HAWKING, S. W. Particle creation by black holes. *Comm. Math. Phys.* **43**, 3 (1975), 199–220.
- [79] HAWKING, S. W., AND ELLIS, G. F. R. *The Large Scale Structure of Space-Time*. Cambridge Monographs on Mathematical Physics. Cambridge University Press, 1973.
- [80] HERDEIRO, C., SAMPAIO, M. O. P., AND WANG, M. Hawking radiation for a Proca field in  $D$  dimensions. *Phys. Rev. D* **85**, 2 (2012), 024005.
- [81] HEWITT, M. *Vacuum polarisation on higher dimensional black hole spacetimes*. PhD thesis, U. of Sheffield, 2015.
- [82] HOD, S. Stationary scalar clouds around rotating black holes. *Phys. Rev. D* **86**, 10 (2012), 104026.
- [83] HOWARD, K. W. Vacuum  $T_{\mu}^{\nu}$  in Schwarzschild spacetime. *Phys. Rev. D* **30**, 12 (1984), 2532–2547.
- [84] HOWARD, K. W., AND CANDELAS, P. Quantum stress tensor in Schwarzschild spacetime. *Phys. Rev. Lett.* **53**, 5 (1984), 403–406.
- [85] HUANG, Y., LIU, D.-J., ZHAI, X.-H., AND LI, X.-Z. Instability for massive scalar fields in Kerr-Newman spacetime. *Phys. Rev. D* **98**, 2 (2018), 025021.
- [86] HUI, L., OSTRIKER, J. P., TREMAINE, S., AND WITTEN, E. Ultralight scalars as cosmological dark matter. *Phys. Rev. D* **95**, 4 (2017), 043541.
- [87] KERR, R. P. Gravitational field of a spinning mass as an example of algebraically special metrics. *Phys. Rev. Lett.* **11**, 5 (1963), 237–238.
- [88] KODAMA, H., ISHIBASHI, A., AND SETO, O. Brane world cosmology: Gauge-invariant formalism for perturbation. *Phys. Rev. D* **62**, 6 (2000), 064022.
- [89] KOKKOTAS, K. D., AND SCHMIDT, B. G. Quasinormal modes of stars and black holes. *Liv. Rev. in Rel.* **2**, 1 (1999), 2.

- [90] KONOPLYA, R., AND ZHIDENKO, A. Decay of massive scalar field in a Schwarzschild background. *Phys. Lett. B* **609**, 3-4 (2005), 377–384.
- [91] KONOPLYA, R. A. Decay of a charged scalar field around a black hole: Quasinormal modes of RN, RNAdS, and dilaton black holes. *Phys. Rev. D* **66**, 8 (2002), 084007.
- [92] KONOPLYA, R. A. Massive vector field perturbations in the Schwarzschild background: Stability and quasinormal spectrum. *Phys. Rev. D* **73**, 2 (2006), 024009.
- [93] KONOPLYA, R. A., AND ZHIDENKO, A. Quasinormal modes of black holes: From astrophysics to string theory. *Rev. Mod. Phys.* **83**, 3 (2011), 793–836.
- [94] LANDAU, L. D., AND LIFSHITZ, E. M. *The Classical Theory of Fields: Volume 2*. Course of theoretical physics. Elsevier Science, 1975.
- [95] LEAVER, E. An analytic representation for the quasinormal modes of Kerr black holes. *Proc. Roy. Soc. Lond. A* **A402**, 1823 (1985), 285–298.
- [96] LEAVER, E. W. Quasinormal modes of Reissner-Nordstrom black holes. *Phys. Rev. D* **41**, 10 (1990), 2986–2997.
- [97] LEVI, A. Renormalized stress-energy tensor for stationary black holes. *Phys. Rev. D* **95**, 2 (2017), 025007.
- [98] LEVI, A., EILON, E., ORI, A., AND VAN DE MEENT, M. Renormalized stress-energy tensor of an evaporating spinning black hole. *Phys. Rev. Lett.* **118**, 14 (2017), 141102.
- [99] LEVI, A., AND ORI, A. Pragmatic mode-sum regularization method for semiclassical black-hole spacetimes. *Phys. Rev. D* **91**, 10 (2015), 104028.
- [100] LEVI, A., AND ORI, A. Mode-sum regularization of  $\phi^2$  in the angular-splitting method. *Phys. Rev. D* **94**, 4 (2016), 044054.
- [101] LUNIN, O. Maxwells equations in the Myers-Perry geometry. *J. High En. Phys* **2017**, 12 (2017), 138.
- [102] MANN, R. B. *An introduction to particle physics and the standard model*. CRC Press, Boca Raton, FL, 2010.
- [103] MEINEL, R. Constructive proof of the Kerr–Newman black hole uniqueness including the extreme case. *Class. Quant. Grav* **29**, 3 (2012), 035004.

- [104] MISNER, C., THORNE, K., WHEELER, J., AND KAISER, D. *Gravitation*. Princeton University Press, 2017.
- [105] MORRIS, M. S., THORNE, K. S., AND YURTSEVER, U. Wormholes, time machines, and the weak energy condition. *Phys. Rev. Lett.* **61**, 13 (1988), 1446–1449.
- [106] NESTERENKO, V. V., AND PIROZHENKO, I. G. Simple method for calculating the Casimir energy for a sphere. *Phys. Rev. D* **57**, 2 (1998), 1284–1290.
- [107] NEUPANE, I. P., AND SCHERER, C. Inflation and quintessence: Theoretical approach of cosmological reconstruction. *J. Cosm. Astro. Phys* **2008**, 05 (2008), 009.
- [108] NEWMAN, E., AND PENROSE, R. An approach to gravitational radiation by a method of spin coefficients. *J. Math. Phys* **3**, 3 (1962), 566–578.
- [109] NEWMAN, E. T., COUCH, E., CHINAPARED, K., EXTON, A., PRAKASH, A., AND TORRENCE, R. Metric of a rotating, charged mass. *J. Math. Phys* **6**, 6 (1965), 918–919.
- [110] NORDSTRÖM, G. On the energy of the gravitation field in Einstein’s theory. *Roy. Aca. of Wetenschappen Proc. Phys. Sci. B* **20** (1918), 1238–1245.
- [111] OHASHI, A., AND AKI SAKAGAMI, M. Massive quasinormal mode. *Class. Quant. Grav* **21**, 16 (2004), 3973–3984.
- [112] PANI, P., CARDOSO, V., GUALTIERI, L., BERTI, E., AND ISHIBASHI, A. Black hole bombs and photon-mass bounds. *Phys. Rev. Lett.* **109**, 13 (2012), 131102.
- [113] PANI, P., CARDOSO, V., GUALTIERI, L., BERTI, E., AND ISHIBASHI, A. Perturbations of slowly rotating black holes: Massive vector fields in the Kerr metric. *Phys. Rev. D* **86**, 10 (2012), 104017.
- [114] PARKER, L., AND TOMS, D. *Quantum Field Theory in Curved Spacetime: Quantized Fields and Gravity*. Cambridge Monographs on Mathematical Physics. Cambridge University Press, 2009.
- [115] PENROSE, R. Gravitational collapse: The role of general relativity. *Riv. Nuovo Cim.* **1** (1969), 252–276.
- [116] PENROSE, R., AND FLOYD, R. M. Extraction of rotational energy from a black hole. *Nat. Phys. Sci* **229**, 6 (1971), 177–179.

- [117] PERCIVAL, J., AND DOLAN, S. R. Quasinormal modes of massive vector fields on the Kerr spacetime. *Phys. Rev. D* **102**, 10 (2020), 104055.
- [118] POISSON, E. *A Relativist's Toolkit: The Mathematics of Black-Hole Mechanics*. Cambridge University Press, 2004.
- [119] PRESS, W., AND TEUKOLSKY, S. Floating orbits, superradiant scattering and the black hole bomb. *Nature* **238**, 5361 (1972), 211–212.
- [120] PRESS, W., TEUKOLSKY, S., VETTERLING, W., AND FLANNERY, B. *Numerical Recipes 3rd Edition: The Art of Scientific Computing*. Cambridge University Press, 2007.
- [121] PRESS, W. H., AND TEUKOLSKY, S. A. Evaluating continued fractions and computing exponential integrals. *Comp. Phys* **2**, 5 (1988), 88–89.
- [122] PRICE, R. H. Nonspherical perturbations of relativistic gravitational collapse. ii. integer-spin, zero-rest-mass fields. *Phys. Rev. D* **5**, 10 (1972), 2439–2454.
- [123] REGGE, T., AND WHEELER, J. A. Stability of a Schwarzschild singularity. *Phys. Rev.* **108**, 4 (1957), 1063–1069.
- [124] REISSNER, H. On the self-gravity of the electric field according to Einstein's theory. *Annalen der Physik* **355**, 9 (1916), 106–120.
- [125] ROBINSON, D. C. Uniqueness of the Kerr Black Hole. *Phys. Rev. Lett.* **34**, 14 (1975), 905–906.
- [126] ROSA, J. A. G., AND DOLAN, S. R. Massive vector fields on the Schwarzschild spacetime: Quasinormal modes and bound states. *Phys. Rev. D* **85**, 4 (2012), 044043.
- [127] SAMPAIO, M. O. P., HERDEIRO, C., AND WANG, M. Marginal scalar and Proca clouds around Reissner-Nordström black holes. *Phys. Rev. D* **90**, 6 (2014), 064004.
- [128] SANTOS, N. M., BENONE, C. L., CRISPINO, L. C. B., HERDEIRO, C. A. R., AND RADU, E. Black holes with synchronised Proca hair: linear clouds and fundamental non-linear solutions. *J. High En. Phys* **2020**, 7 (2020), 010.
- [129] SANTOS, N. M., AND HERDEIRO, C. A. R. Stationary scalar and vector clouds around Kerr-Newman black holes. *Int. J. of M. Phys. D* **29**, 11 (2020), 2041013.
- [130] SATZ, A., MAZZITELLI, F. D., AND ALVAREZ, E. Vacuum polarization around stars: Nonlocal approximation. *Phys. Rev. D* **71**, 6 (2005), 064001.

- [131] SCHUTZ, B. F., AND WILL, C. M. Black hole normal modes - A semianalytic approach. *Astrophys. J.* **291** (1985), L33–L36.
- [132] SCHWARZSCHILD, K. On the gravitational field of a sphere of incompressible fluid according to Einstein's theory. *Sitzungsber. Preuss. Akad. Wiss. Berlin (Math. Phys. )* **1916** (1916), 424–434.
- [133] SIMMENDINGER, C., WUNDERLIN, A., AND PELSTER, A. Analytical approach for the floquet theory of delay differential equations. *Phys. Rev. E* **59**, 5 (1999), 5344–5353.
- [134] SIMONE, L. E., AND WILL, C. M. Massive scalar quasinormal modes of Schwarzschild and Kerr black holes. *Class. Quant. Grav.* **9**, 4 (1992), 963–978.
- [135] TAYLOR, P., AND BREEN, C. Mode-sum prescription for the vacuum polarization in odd dimensions. *Phys. Rev. D* **94**, 12 (2016), 125024.
- [136] TAYLOR, P., AND BREEN, C. Mode-sum prescription for vacuum polarization in black hole spacetimes in even dimensions. *Phys. Rev. D* **96**, 10 (2017), 105020.
- [137] TEUKOLSKY, S. A. Rotating black holes: Separable wave equations for gravitational and electromagnetic perturbations. *Phys. Rev. Lett.* **29**, 16 (1972), 1114–1118.
- [138] TEUKOLSKY, S. A. Perturbations of a rotating black hole. 1. Fundamental equations for gravitational electromagnetic and neutrino field perturbations. *Astrophys. J.* **185** (1973), 635–647.
- [139] TOLMAN, R. C. Static solutions of Einstein's field equations for spheres of fluid. *Phys. Rev.* **55**, 4 (1939), 364–373.
- [140] UNRUH, W. Separability of the neutrino equations in a Kerr background. *Phys. Rev. Lett.* **31**, 20 (1973), 1265–1267.
- [141] UNRUH, W. G. Notes on black-hole evaporation. *Phys. Rev. D* **14**, 4 (1976), 870–892.
- [142] VISSER, M. Gravitational vacuum polarization. IV. Energy conditions in the Unruh vacuum. *Phys. Rev. D* **56**, 2 (1997), 936–952.
- [143] VISSER, M. The Kerr spacetime: A brief introduction. In *Kerr Fest: Black Holes in Astrophysics, General Relativity and Quantum Gravity* (2007).
- [144] WALD, R. *General Relativity*. University of Chicago Press, 2010.

- [145] WALD, R. M. Axiomatic renormalization of the stress tensor of a conformally invariant field in conformally flat spacetimes. *Annals of Physics* **110**, 2 (1978), 472–486.
- [146] WEINBERG, S. *The quantum theory of fields: volume 3, supersymmetry*. Cambridge university press, 2005.
- [147] WILL, C. M. The confrontation between General Relativity and experiment. *Living Reviews in Relativity* **17**, 1 (2014), 4.
- [148] WITEK, H., CARDOSO, V., ISHIBASHI, A., AND SPERHAKE, U. Superradiant instabilities in astrophysical systems. *Phys. Rev. D* **87**, 4 (2013), 043513.